TWISTED AND COILED POLYMER ACTUATORS:

DESIGN, MECHANICS, AND BIOMIMETICS

By Diego R. Higueras-Ruiz

A Dissertation

Submitted in Partial Fulfillment

of the Requirements for the Degree of

Doctor of Philosophy

in Bioengineering

Northern Arizona University

December 2021

Approved:

Michael W. Shafer, Ph.D., Co-chair

Heidi P. Feigenbaum, Ph.D., Co-chair

Kiisa C. Nishikawa, Ph.D.

Timothy A. Becker, Ph.D.

Zachary F. Lerner, Ph.D.

ABSTRACT

TWISTED AND COILED POLYMER ACTUATORS:

DESIGN, MECHANICS, AND BIOMIMETICS

DIEGO R. HIGUERAS-RUIZ

In the past few decades, interest in novel soft actuators that can mimic the compliant nature of biological muscles has grown fast. Such actuation technologies have the potential to improve current human-machine interactions in applications such as smart exoskeletons and prosthetics, wearables, intelligent surgical tools, and even humanoids. To this end, it was recently shown that inexpensive drawn polymer monofilaments, such as nylon fishing lines, can be used to create thermally driven linear or torsional soft actuators. These actuators are called twisted polymer actuators (TPAs), and their actuation mechanism relies on the anisotropic microstructure of the virgin material used for fabrication, specifically, the axial thermal contraction and radial thermal expansion. In the past few years, researchers have attempted to model the actuation response of TPAs; however, it has been shown that such actuation is moisture-content- and time-dependent (viscoelastic), which have limited the accuracy of actuation models for TPAs. Furthermore, the thermal activation of TPAs is generally an inefficient and time-consuming (particularly during cooling) driver.

This Ph.D. work first presents a literature review on soft actuators and a comparison to biological muscles, focusing on those properties that make biological muscles highly adaptable systems. This study helps better understand the current accomplishments of each soft actuation technology, the remaining challenges, and future directions that are required for soft actuation technologies to be used as successful muscle substitutes.

Next, a study on the hygroscopic behavior and moisture content effects of TPAs actuation performance is presented. This study found that TPAs made from drawn monofilaments of nylon 66 are hygroscopic and moisture-content-dependent. Moreover, the hygroscopic properties of TPAs are strongly affected by temperature changes, and temperature changes are required for actuation, which makes TPAs challenging to model and therefore control in environments with different relative humidity levels. As a result of the previously mentioned shortcomings of thermally activated twisted polymer actuators, the rest of this Ph.D. work focuses on the conception, characterization, modeling, and initial optimization of a new soft actuation technology inspired by TPAs named cavatappi artificial muscles. Cavatappi artificial muscles use an actuation mechanism that relies upon specific processing of inexpensive polymer tubes to develop microstructural anisotropy, which mimics the anisotropic mechanical properties of the precursor monofilaments used to fabricate TPAs. These tubes can be configured as torsional actuators when twisted or linear actuators when helically coiled, similar to TPAs. After drawing and twisting, hydraulic or pneumatic pressure applied inside the tube results in localized untwisting of the helical microstructure. This untwisting manifests as a contraction of the helical pitch for the coiled configuration. Given the hydraulic or pneumatic activation source and the constant material temperature, these new devices have been shown to outperform TPAs with regard to actuation bandwidth, efficiency, modeling, and practical implementation. Since cavatappi can generate high forces and power, this technology could be used in bioengineering and robotics applications. Cavatappi show contractions greater than 50% of their initial length, mechanical contractile efficiencies of about 45%, and specific work and power metrics ten and five times higher than human skeletal muscles, respectively. Finally, this dissertation also presents an actuation model that uses the material properties of the precursor structure to predict the actuation response of cavatappi artificial muscles and validation using experimental actuation data.

ACKNOWLEDGEMENTS

TABLE OF CONTENTS

LIST OF TABLES

LIST OF FIGURES

xiv

xvi

xvii

PREFACE

This section provides information about the research scope of this Ph.D. work. The dissertation outline is divided into chapters in the following paragraphs, where the chapter's topics are briefly summarized. Furthermore, chapters 2–5 were written to appear as articles in journals, and, as a result, some redundancy should be expected from combining these articles within the university formatting requirements.

Chapter 1 is divided into the following four subsections: motivation, aim of research, hypothesis, and dissertation outline. This chapter articulates the motivation of the research, voids to be filled, established hypothesis, and the impact of this Ph.D. work on the field of soft actuation. Finally, this section presents a research timeline where the reader is provided the work progress that has been required to culminate this Ph.D.

Chapter 2 presents a literature review that compares the current soft actuation technologies to skeletal muscles. This chapter provides a comparative study between soft actuators and biological muscles using specific performance metrics and those properties of biological muscles that make them highly adaptable systems (tunable compliance and impedance, morphological computation, self-sensing, muscle synergy, etc.) As a result, this chapter presents the remaining significant challenges for soft actuators to be used as muscle substitutes and future directions.

Chapter 3 provides a study on the moisture impact on twisted polymer actuation. This chapter presents two moisture-related matters: moisture content impact on the thermal actuation of TPAs and the capability of TPAs to actuate as a function of moisture absorption at room temperature.

Chapter 4 introduces a fluid-driven muscle-like actuator fabricated from inexpensive polymer tubes and inspired by twisted polymer actuators. These new soft actuators

are called cavatappi artificial muscles based on their resemblance to the Italian pasta. This chapter presents the fabrication procedure, a full characterization of the actuation response, and their initial implementation in some basic bioinspired applications.

Chapter 5 establishes a model framework for predicting the actuation response of cavatappi using the thick-wall pressure vessel stress analysis and the spring theory. The presented model uses the linear elastic mechanical properties of the precursor drawn material used for fabrication to predict the artificial muscles contraction under different external loads. Thus, the elastic precursor material properties are also characterized in this chapter.

Chapter 6 presents the conclusions and future directions of this dissertation.

CHAPTER 1

INTRODUCTION

1.1 Motivation and Research Impact

Traditional electric and fluidic actuators operate effectively in many tasks where high accuracy, repeatability, reliability, high specific power, and efficiency are required [96, 145, 148, 269], yet their rigid configuration and lack in tunable compliance and impedance often limits their deployment in areas such as biomimetic and bio-inspired applications. This has led many in search of new compliant and flexible actuators under the name of soft actuators or soft robots to fill this void [42, 71, 97, 150, 195, 203, 220]. The goal of new soft actuators is to mimic the adaptable muscle-like actuation response and properties found in biological muscles, which could enable safe human-machine interactions with minimal control.

This actuation field is emerging fast as new low-cost soft actuators with similar performance to biological muscles are being reported every year and successfully implemented in bio-inspired applications such as smart exoskeletons [57, 334], wearables [10], intelligent surgical tools [48], and even humanoids [25, 52]. Some of these soft actuators include thermally driven twisted polymer actuators (TPAs) [127, 128], electromechanical carbon nanotubes (CNTs) [34, 35], dielectric elastomer actuators (DEAs) [92, 362], hydraulically amplified self-healing electrostatic actuators (HASELs) [8, 167], electrostatic bellow muscles (EBMs) [303], electro-ribbon actuators and electro-origami robots [317], fluid-based soft actuation technologies such as, Mckibben actuators [66], fluid-driven origami-inspired artificial muscles (FOAMs) [189], origami-based vacuum pneumatic artificial muscles (OV-PAMs) [185], and others like water-responsive and photo-responsive actuators [176, 256].
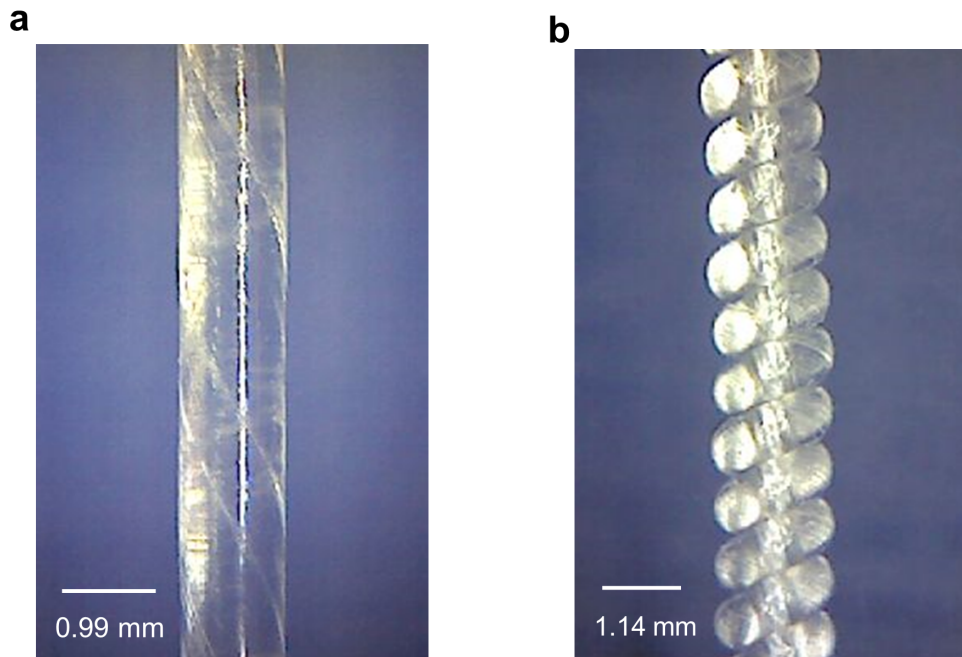
FIGURE 1.1: Twisted polymer actuators. (a) Torsional actuator, a.k.a. straight twisted polymer actuator (STPA).(b) Linear polymer actuators, a.k.a. twisted coiled polymer actuators (TCPAs)

As a result of the aforementioned need for exploring new soft actuation technologies that can mimic the actuation response in biological muscles, this work initially focused on twisted polymer actuators (TPAs) due to their extreme performance and affordability. TPAs were initially discovered by Haines et al. [128] and inspired by twisted/coiled carbon nanotube actuators [105, 196, 197]. Haines et al. showed that drawn polymer monofilaments, such as fishing line and sewing threads, can actuate when configured in a coiled shape as a result of over-twisting the straight monofilament around its central axis [127, 128]. These linear actuators are called "twisted coiled polymer actuators" (TCPAs) (Fig. 1.1(b)). These same drawn polymers can torsionally actuate when they are set in a twisted configuration but remain straight; this torsional actuator is known as "straight twisted polymer actuators" (STPAs) (Fig. 1.1(a)) [28, 295].

The actuation phenomenon in TCPAs and STPAs (collectively called twisted polymer actuators) is thought to be a result of the untwist that occurs about the monofilament's
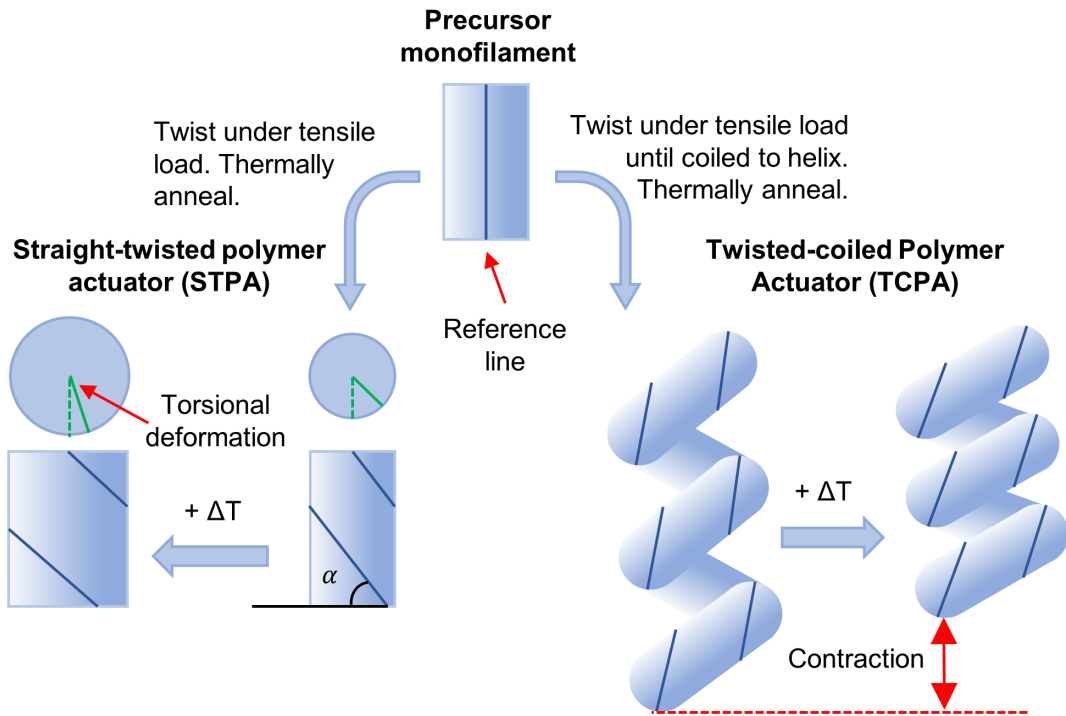
FIGURE 1.2: Thermal actuation mechanisms of STPAs and TCPAs

axis due to anisotropic thermal expansions [128]. Specifically, the actuation mechanism is thought to result from the thermal expansion in the direction perpendicular to the internal fibers (i.e., radial direction) and the thermal contraction along the internal fibers (i.e., axial direction). After being twisted, the expansion/contraction perpendicular to and along the internal fibers (i.e., polymer chains) remains relatively unchanged, but the internal fibers are no longer axially aligned. Thus, upon heating, the twisted fibers of the STPA untwist, and torsional actuation occurs (see left diagram in Fig. 1.2). In a TCPA, the coiling causes the untwist to manifest as an axial contraction of the helix (see right diagram in Fig. 1.2).

The actuation mechanism might be better understood by looking at the micro-structure models published by Prevorsek et al. [268], Choy et al. [68], Elad and Schultz [98], and Bukosek et al. [47]. These authors present similar microstructural models of drawn polymer monofilaments, including crystalline and amorphous regions connected in series

3

and aligned with the draw direction (axial direction), known as microfibrillar regions. These regions are connected by bridges and/or inter-fibril tie molecules (a.k.a. internal fibers), more extended regions aligned with the draw direction. Bruno et al. [45] indicate that negative thermal expansion along the drawn direction is due to the tension caused by atomic vibrations in the interfibrillar molecules. Simultaneously, this effect contributes to the expansion perpendicular to the microfibrillar region (radial direction). This negative thermal expansion is maintained along the now helically aligned internal fibers for a twisted monofilament with a helical orientation of its internal fibers. So too is the positive thermal expansion perpendicular to the internal fiber direction. The thermal anisotropy of the precursor monofilaments and their helical reorientation causes untwist in STPAs and contraction in TCPAs.

In order to create actuation models, initial efforts focused on modeling STPAs, because they represent the elemental unit of TCPAs. Modeling these soft actuators is crucial for future control; thus, accurate mathematical models are required. To do so, our research group focused on a kinematic closed-form material-based radial dependent model presented by Shafer et al. that uses the thermal material properties of the precursor monofilament to predict the untwist of STPAs under free torsion as a function of temperature [296].

To this end, Swartz et al. compared torsional actuation predictions generated by the aforementioned material-based model with experimental results. Swartz et al. also presented an area-weighted average of the Shafer et al. to eliminate the radial dependence in the predictions. The results in this work suggested that inter-layer stresses could lead to inaccuracies in the actuation predictions [315]. This was thought because the Shafer et al. model does not account for internal stresses in the material. Next, Higueras-Ruiz et al. simulated a straight twisted polymer actuator (STPA) using a finite element (FE)

4

model [137] to study the internal stresses in TPAs. To do so, the linear elastic mechanical properties of the untwisted monofilament as a function of temperature were obtained experimentally, as they are needed as inputs to the FE model. Here, FE results were compared with experimental actuation responses and the Shafer et al. model predictions. The simulations and experiments use STPAs to generate torsional actuation under free torsion. Under these conditions, it was shown that interlayer stresses are not the main driver for the torsional actuation of STPAs and the FE model predicts experimental data about as well as closed-form models. Additionally, this work interpreted the internal stresses to understand the actuation mechanism of TPAs better and evaluate their effects on STPAs' torsional actuation under free torsion conditions. As a result, it was found that most of the untwist produced in STPAs occur at the outer layers, being the center of the monofilament a constraint for untwisting (torsional actuation); thus, hypothetically, a hollowed filament could help to increase the performance of TPAs. This insight was later used in this Ph.D. work to conceive cavatappi artificial muscles, later explained in this section. Finally, and as part of this Ph.D. work, Higueras et al. presented that the precursor monofilaments used for TPAs fabrication were highly hygroscopic and moisture content in their microstructure causes changes in their material properties and, in turn, in the actuation response of these soft actuators, making them moisture content dependent [138]. Additionally, it was also shown that TPAs could generate actuation due to moisture content at room temperature.

As a result of the difficulties presented in creating reliable models that can predict the actuation response of TPAs under real-life actuation conditions and external environment along with the current need for new biomimetic soft actuation systems, this Ph.D. work focuses on (i) comparing the current soft actuation technologies with the performance and properties of biological muscles, (ii) studying the moisture effects on TPAs fabricated with nylon 66, and (iii) exploiting TPAs actuation mechanism to create a new fluid-driven

actuator named cavatappi artificial muscle and an actuation model for future control.

1.2   Aim of research

This work both studies the limitations found in TPAs, and presents a new, low-cost, flexible, fluidic, and soft actuation technology named cavatappi artificial muscles that sidesteps the limitations found in TPAs. The term "*cavatappi*" is based on their resemblance to the Italian pasta (Fig. 1.3(a)). The design and development of cavatappi is originally inspired by the mechanics of twisted polymer actuators, particularly the idea of exploiting the material's anisotropy to generate actuation. As previously mentioned, TPAs are thermally driven linear or torsional actuators, whose actuation response is a result of the anisotropic thermal properties of the precursor (untwisted) material, which experiences axial thermal contraction, and radial thermal expansion [128]. They are inexpensive, often fabricated from fishing lines, and have been demonstrated in areas such as robotics [353], medical devices [202], and active textiles [127]. However, their modeling using the precursor material properties is a complex task as a result of the material dependencies such as viscoelasticity [295, 315], hygroscopicity, which causes their response/performance to depend on moisture content (also part of this work) [138]. Moreover, the viscoelastic and hygroscopic properties of TPAs are strongly affected by the temperature changes, and temperature changes are required for actuation, which makes TPAs challenging to model, and therefore control [28, 137, 165, 296, 297, 315, 356]. Additionally, as previously mentioned, thermal activation generally leads to low efficiency $\sim 1\%$ and slow actuation (particularly during cooling).

The extreme performance and shortcomings of TPAs have led this dissertation to explore new actuation modalities that mitigate inherent drawbacks yet take advantage of their strengths by mimicking their actuation mechanism. Initially, it was surmised that internal

6
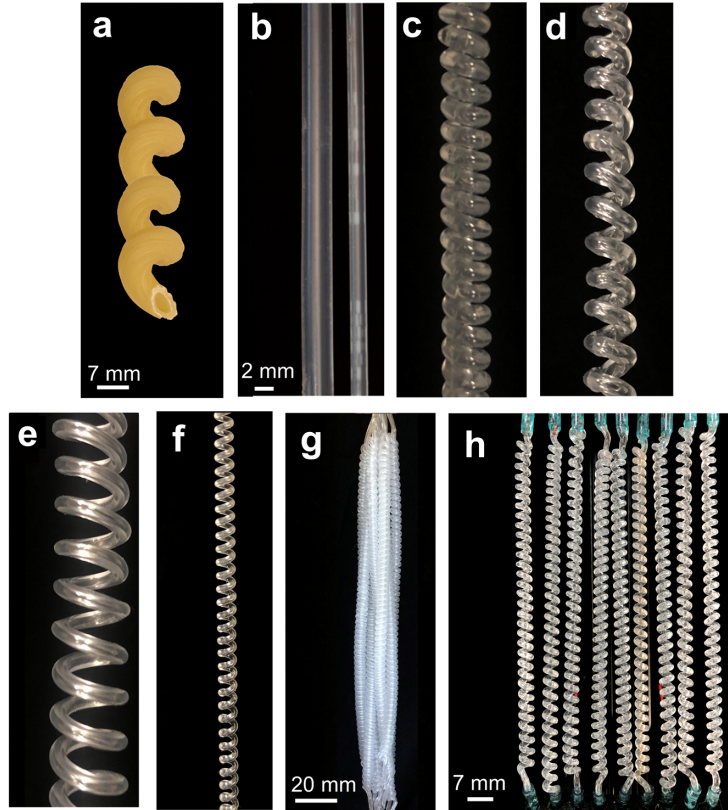
FIGURE 1.3: Cavatappi pasta, cavatappi artificial muscles and precursor tubes. (a) Cavatappi pasta is shaped as a helical tube. (b) Precursor undrawn tube (left) and precursor drawn tube (right). (c) Cavatappi made from drawn tube in Fig. 1B. (d) Cavatappi in b which has been pre-stretched and annealed after fabrication in order to increase the helix pitch. (e) Cavatappi made from the drawn precursor tube shown in b and coil ID of 7 mm. (f) Mini-cavatappi made from a 0.7 mm OD/0.25 mm ID tube. (g) Bundle of cavatappi artificial muscles that simulate a human skeletal muscle bundle. (h) Linear-parallel configuration of nine cavatappi from Fig 1c. The scale in Fig. 1 b is used for b-f, and the scales for a, g, and h are shown in the figures.

pressure in a tube could be used to develop similar anisotropic expansion seen during TPA heating. Pressure testing showed that soft polyvinyl chloride (PVC) tubing (Fig. 1.3(b-left)) could generate radial expansion similar to TPAs, yet the tubing developed axial expansion, which it was known from previous TPA modeling works would reduce actuation performance when twisted [296, 315]. The PVC microstructure was set out to mitigate this axial expansion by enhancing anisotropy by cold-drawing Fig. 1.3(b-right). Fig. 1.3(b-right) shows the precursor tube (left - 3.18 mm OD, 1.58 mm ID) and the same
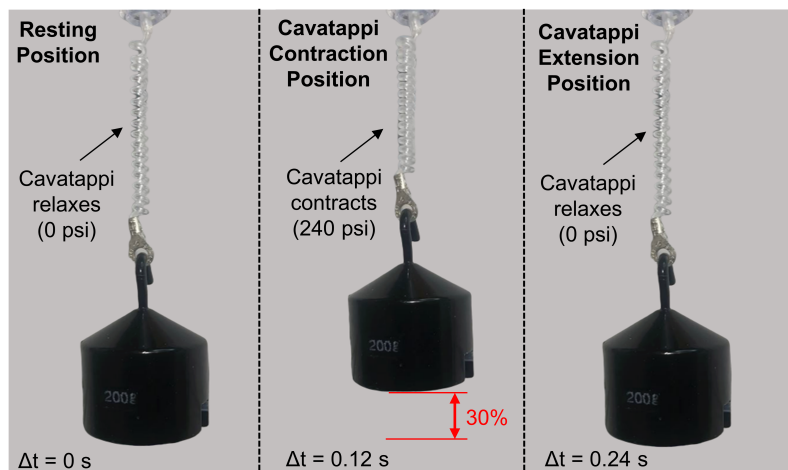
FIGURE 1.4: Cavatappi actuation response under an isotonic load of 0.2 kg.

tube (right - 1.8 mm OD, 0.85 mm ID) after the cold-drawing necessary to increase axial stiffness relative to radial stiffness. Note the significant change in diameter that occurs during the drawing process. After drawing, the internal pressurization induced positive radial and negative axial strains that mimicked heated TPA precursor fibers. Next, twists in the drawn tubes were inserted to reorient the high-stiffness molecular chains into a helical configuration around the central tube axis while maintaining the tube's ability to expand radially. Such a straight-twisted tube configuration would generate an untwisting when pressurized (torsional actuation). The twisted tubes were then helically coiled Fig. 1.3(c-h) so that the localized untwisting would manifest as linear actuation by reducing the coil's pitch (Fig. 1.4).

The fluidic activation source and the constant material temperature in cavatappi artificial muscles lead these new devices to outperform TPAs with regard to actuation bandwidth, efficiency, modeling, and practical implementation. Initial testing has shown that cavatappi can perform contractions greater than 50% of their initial length, mechanical contractile efficiencies of about 45%, and total energy conversion efficiencies of approximately 23%. Furthermore, cavatappi artificial muscles can exhibit specific work and power metrics ten and five times higher than human skeletal muscles, respectively, and

continued development will lead to even higher performance in the future.

The flexibility of cavatappi could be used on applications over corners/joints such as knees, elbows, or ankles since they can be placed under a curved deformation and still actuate. Since cavatappi are fabricated from soft PVC tubing, the same tube length could consist of sections where the drawn precursor tube is coiled-twisted, straight-twisted, or kept as the original straight drawn configuration. As such, a single tube length, with a coiled section in the middle, could serve as (i) the plumbing from the pressure source, (ii) the actuator, and (iii) the tendon running to the point of the force application. Such an implementation would decrease the overhead mass and complexity from fittings, increase reliability by eliminating leaks, and decrease maintenance operations.

Compared to TPAs, cavatappi artificial muscles have the potential to present better controllability and accuracy since modeling the actuation response of cavatappi artificial muscle is significantly simpler as only the mechanical properties of the precursor tube are needed, and there is no need to collect mechanical properties as a function of temperature. Furthermore, the soft polyvinyl chloride used for cavatappi presents small moisture absorption [344]; thus, moisture dependencies do not need to be included in actuation models. TPAs, by comparison, show a high affinity for moisture, and their mechanical properties depend heavily on moisture, and temperature [138].

While cavatappi present similar characteristics and metrics as other soft actuators, they are inexpensive solid-state actuators (0.20 $/ft) of easy and low-cost fabrication, whose affordability and simplicity will contribute to their fast investigation and implementation. Under pneumatic or hydraulic actuation, they are initially shown to actuate in milliseconds and rapidly recover to their initial position; this feature is not shown in other actuators like TPAs or SMAs due to their thermally driven actuation mechanism. The high ratio between the work they can deliver and their size and their negligible

changes in volume during actuation will allow them to be combined to create new configurations leading to an increase in their lifting force capacity. These configurations can be approached by stringing tubes together. Some promising examples are smart textiles used to assist individuals with disabilities in basic motions or smart prosthetics implemented to substitute amputated limbs fully. Furthermore, cavatappi might benefit those fields where small, lightweight, and strong actuators are required, such as microrobotics or microfluidics.

1.3   Hypothesis

Based on the actuation mechanism presented in thermally driven twisted polymer actuators, I hypothesize that new pneumatically or hydraulically driven soft actuators can be developed using twisted and coiled extruded/drawn tubes. More specifically, I propose using the anisotropic mechanical properties (high axial and low radial stiffness) of extruded/drawn polymer tubes to create new soft torsional and linear actuators. In doing so, the right material's properties' selection along with the reorientation of the polymeric chains by twisting the precursor structures while remaining straight will allow the creation of torsional actuators (elemental units of a cavatappi artificial muscle). Furthermore, twisting and coiling the precursor structure around a mandrel will allow to create linear actuators (cavatappi artificial muscles).

To validate the aforementioned hypothesis, I will characterize the actuation behavior and metrics of cavatappi artificial muscles, as well as build several applications that use cavattapi to demonstrate their easy implementation in the biorobotics. Next, I will compare such actuation behavior, metrics, and implementation capacities with other soft actuation technologies to establish and show the potential impact of this new technology on the soft actuation field.

In addition, and as part of this dissertation, I also hypothesize that the actuation response of cavatappi artificial muscles can be predicted within a reasonable margin of error by using analytical material-based models. I will formulate a model that will predict the actuation contraction of cavatappi artificial muscles under tensile loads to support my hypothesis. The proposed model will use the mechanical properties of the precursor structure used for fabrication, the pitch angle of the internal fibers (fiber's reorientation), and internal pressure as inputs. As part of this work, the model will be validated using experimental actuation responses collected during the actuation characterization of cavatappi. To use this work's model, the mechanical properties of the precursor tube will need to be characterized; thus, a complete characterization will also be presented in this work. The predictions will be expected to follow the same trend as the experimental results and provide valuable qualitative and quantitative data that can be used to accurately predict and optimize the actuation behavior of cavatappi without previous testing thereof.

1.4   Dissertation Outline and Research Timeline

To present the scope of research and timeline, Fig. 1.5 shows a Gantt chart that provides information about the evolution of this Ph.D. research. This timeline shows the main research tasks, start date, number of days for the task to be completed, and a graphical representation of the research progress and completion. Along with the research tasks, the reader can find the journal publications for each task. In this Gantt chart (Fig. 1.5), the literature review has been a continuous process during this Ph.D. work; thus, this research task starts in Fall 18 and ends in Fall 2021. Next, initial TPAs modeling is also included here. This research task was initially started during a previous M.S. conducted by the author of this dissertation and ended during the first two semesters of this Ph.D. work. As a result of inaccuracies in the initial TPAs modeling, research on moisture's impact on TPAs conducted better to understand the effects of moisture content in TPAs

Research Task Description	Progress	Start	No. Days
Literature Review	100%	9/1/2018	1,150
Initial TPAs Modeling	100%	9/1/2018	210
Moisture's Impact on TPAs	100%	1/1/2019	375
Extrusions Testing for Cavatappi Actuator Conception	100%	7/15/2019	170
Cavatappi Actuation Characterization	100%	1/1/2020	250
Cavatappi Modeling and Optimization	100%	9/1/2020	120
Polymer Precursor Drawn Tubes Characterization	100%	1/1/2021	90
Actuation Model Validation	100%	4/1/2021	180

FIGURE 1.5: Research Gantt chart.

actuation and find potential solutions regarding this matter. This research task started in Spring 2018 and ended in mid Spring 2020. Next, extruded polymer tubes testing, cavatappi conception, and full actuation characterization were completed by Fall 2020. Finally, for the total completion of this Ph.D., cavatappi modeling and initial optimization, drawn polymer tubes properties characterization, and actuation model validation were completed by the beginning of Fall 2021. The proposed work in the timeline was planned to be completed by the beginning of Fall 2021; thus, the main focus of Fall 2021 was to finish writing the dissertation and preparing the dissertation defense.

CHAPTER 2

WHAT IS AN ARTIFICIAL MUSCLE? A COMPARISON OF SOFT ACTUATORS TO BIOLOGICAL MUSCLES

Abstract. Interest in emulating the properties of biological muscles that allow for fast adaptability and control in unstructured environments has motivated researchers to develop new soft actuators, often referred to as 'artificial muscles'. The field of soft robotics is evolving rapidly as new soft actuator designs are published every year. In parallel, recent studies have also provided new insights for understanding biological muscles as 'active' materials whose tunable properties allow them to adapt rapidly to external perturbations. This work presents a comparative study of biological muscles and soft actuators, focusing on those properties that make biological muscles highly adaptable systems. In doing so, we briefly review the latest soft actuation technologies, their actuation mechanisms, and advantages and disadvantages from an operational perspective. Next, we review the latest advances in understanding biological muscles. This presents insight into muscle architecture, the actuation mechanism, and modeling, but more importantly, it provides an understanding of the properties that contribute to adaptability and control. Finally, we conduct a comparative study of biological muscles and soft actuators. Here, we present the accomplishments of each soft actuation technology, the remaining challenges, and future directions. Additionally, this comparative study contributes to providing further insight on soft robotic terms, such as biomimetic actuators, artificial muscles, and conceptualizing a higher level of performance actuator named artificial supermuscle. In conclusion, while soft actuators often have performance metrics such as specific power, efficiency, response time, and others similar to those in muscles, significant challenges remain when finding suitable substitutes for biological muscles, in terms of other factors such as control strategies, onboard energy integration, and thermoregulation.

Glossary of Terms and Definitions

Actuator efficiency: The energy conversion efficiency between the energy activation driver input and the mechanical work output ignoring elastic strain and/or electrostatic energy.

Adaptive dynamic response: The ability of an actuator to actively change its inherent stiffness/compliance, damping, or both in order to adjust its time-variant dynamics.

Embedded control: Actuator level sensing and feedback control, excluding supervisory controller (brain, etc.).

Integration: The capacity to merge actuation elements like onboard energy source and sensor in the actuator's architecture.

Lifetime: The maximum number of actuation cycles that a soft actuator or a biological muscle can perform without failure or degradation.

Maximum actuation strain: The maximum deformation that an actuator is capable of performing divided by the initial length of the actuator, usually measured under non-loaded conditions.

Maximum actuation stress: The maximum stress that an actuator is capable of performing divided by the cross section area of the actuator, usually measured under blocked force conditions.

Morphological computation: The capacity to provide a quick controlled response by using the adaptive dynamics and morphology of the muscles or soft actuators themselves when external perturbations occur in an uncontrolled environment.

Multi-element actuator: An actuator whose inherent stiffness and/or damping force capacity is on the order of its blocked (isometric) actuation force capacity.

Muscle synergy: The ability to activate specific groups of muscles synergistically to produce a particular movement, thereby reducing the dimensionality of muscle control and improving actuation timing, control, and efficiency.

Off-board energy: The energy located outside the actuator architecture that allows for long duration actuation or more actuation cycles than the onboard energy. For muscles, an example of this type of energy is oxygen supplied by the circulatory system for synthesis of ATP. For soft actuators, examples are external batteries (electro-activation) or pressurized tanks (fluid-driven).

Onboard energy: The energy integrated into the actuator's architecture that allows for short duration actuation or a limited number of actuation cycles. In biological muscle, this includes ATP, creatine phosphate, glycogen, and fat droplets stored within the muscle itself. In soft actuators, this level of energy integration is under development.

Performance: The level achieved by an actuator for a particular action that results from the actuator's properties, i.e. metrics.

Properties: The inherent or embedded attributes of the actuator.

Scalability: The ability of an actuator to work at multiple length scales due to series and parallel operation.

Soft actuator: An actuator whose physical form and flexible material allow for actuation (axial, radial, torsion, bending, and/or combinations of these) even under physical perturbations (bending, pinching, or pulling) when energy input is applied.

Specific average power: The average power developed by an actuator divided by its mass.

Specific peak power: The maximum peak power developed by an actuator divided by its mass.

Specific work: The work capacity of the actuator divided by its mass.

Stiffness: A quantity that represents resistance to deformation under load.

Total efficiency: The ratio of mechanical work output to chemical/electrical/etc. energy input to the system (robotic/biological) hosting the actuator ignoring elastic strain and/or electrostatic energy.

Tunable-element actuator: An actuator whose inherent stiffness and/or damping characteristics can be actively or passively adjusted.

Tunable compliance: The degree to which an actuator can change length (strain) in response to externally applied forces (stresses) when an energy input is applied. Note that compliance is the inverse of stiffness. Tunable compliance is when compliance can be adjusted by an input signal, e.g. activation in the case of biological muscles.

Variable recruitment: The ability to selectively recruit motor units in series and parallel to grade the force generated by a muscle.

2.1   Introduction

For the past few decades, human-machine interactions (HMIs) [13, 111, 182, 194, 272] in applications such as smart exoskeletons and prosthetics [57, 334], wearables [10], intelligent surgical tools [48], and even humanoid robots [25, 52] have led scientists to study new soft actuation technologies that feature properties similar to biological muscles. These new soft actuators mimic the compliant nature of biological muscles and their use aims to overcome the drawbacks of conventional actuators in bio-inspired applications [204, 209, 329]. Conventional actuators, such as electric motors and hydraulic or pneumatic cylinder actuators, are widely used in robotics because they feature high accuracy, repeatability, reliability, high specific power, and efficiency [96, 145, 148, 269]. However, their rigidity, weight, and lack of essential properties for adaptable muscle-like actuation make them unsuitable for many HMIs [31, 50, 150]. As a result, new bioinspired soft actuators are being developed and incorporated into various bioinspired robotic systems [29, 212]. These soft actuators can be fully synthetic [42, 71, 97, 150, 195, 203, 220] or a hybrid between synthetic and biological materials, known as biohybrid or bio-syncretic robotics [112, 274, 311, 372]. Among soft robotics, biohybrid robots constructed by the integration of living cells such as cardiomyocytes [16, 108], skeletal muscles [199, 227], and microorganisms [291, 301, 357] along with flexible materials can provide similar actuation to that one found in nature. Although biohybrid robotics is an attractive solution

16
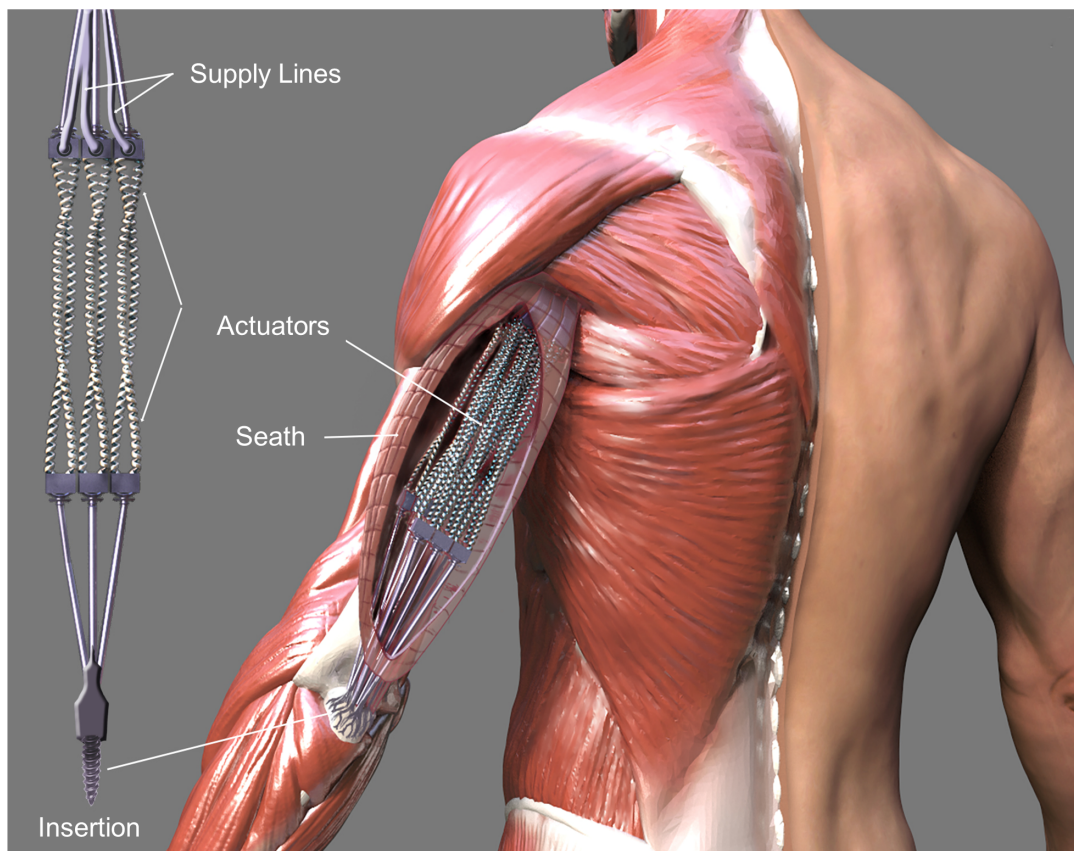
FIGURE 2.1: Integration concept of soft actuators (cavatappi artificial muscles) in a biological system (human body). Figure produced by Victor O. Leshyk.

to mimic the actuation response of biological muscles, in this work, we intend to compare fully synthetic soft actuators with biological muscles because biohybrid robotic actuators can inherently mimic biological muscles properties due to their biological composition. For further information about biohybrid robotics, we direct the reader to recent publications that review several decades of this work [112, 274, 311, 372].

A cursory study of fully synthetic soft actuators highlights a number of qualitative similarities to biological muscles, but quickly reveals deeper questions. What defines an 'artificial muscle' and more importantly, what properties of biological muscles distinguish them from engineered systems? This work compares both the performance and properties of soft engineered actuators to biological muscle in order to answer these questions.
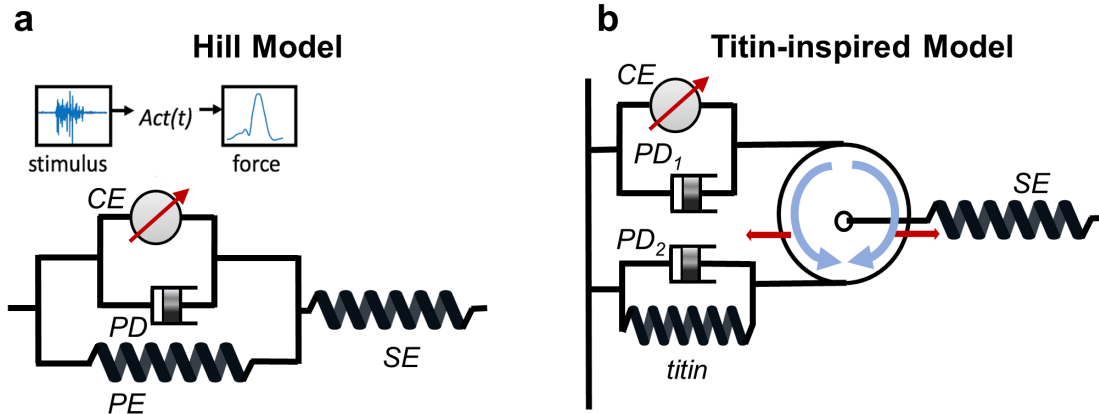
FIGURE 2.2: Muscle models. (a) Traditional model based on 'muscles-as-motors' has been in widespread use for decades [323]. This model consists of a transfer function *Act(t)* that converts an input stimulus into muscle force, plus modules that represent muscle properties including passive tension, force-length and force-velocity relationships. (b) Models based on 'muscles-as-tunable-materials' are a relatively new development [318]. In these models, activation rotates a movable pulley in one direction, and the pulley rotates back in the other direction during deactivation (blue arrows) to simulate time- and length-dependent activation dynamics. The pulley translates along the long axis of a muscle when stretched or shortened by external or internal forces (red arrows). The length-dependent force is given by superposition of pulley rotation and translation. SE = series elastic element. PD = parallel damping element. PE = parallel elastic element. CE = contractile element.

Many recent reviews have provided updates on soft actuators [42, 71, 97, 150, 195, 203, 220] and some of these compare performance of soft actuators with biological muscles. Our comparison focuses not only on performance criteria but also on investigating the unique properties of biological muscles and comparing these inherent properties with synthetic actuator technologies. In this work, we compare both worlds, soft and biological actuators, to better benchmark the new technologies and determine where advances are needed. In doing so, we refine the definitions of terms including artificial muscle and biomimetic actuator, which have at times been applied to soft actuators regardless of their similarities to their biological brethren. Additionally, understanding the unique properties of biological muscles that contribute to efficient and adaptive control of human movement [242, 246] may inspire new technologies capable not only of safe HMIs but also of seamless integration with humans (Fig. 2.1).
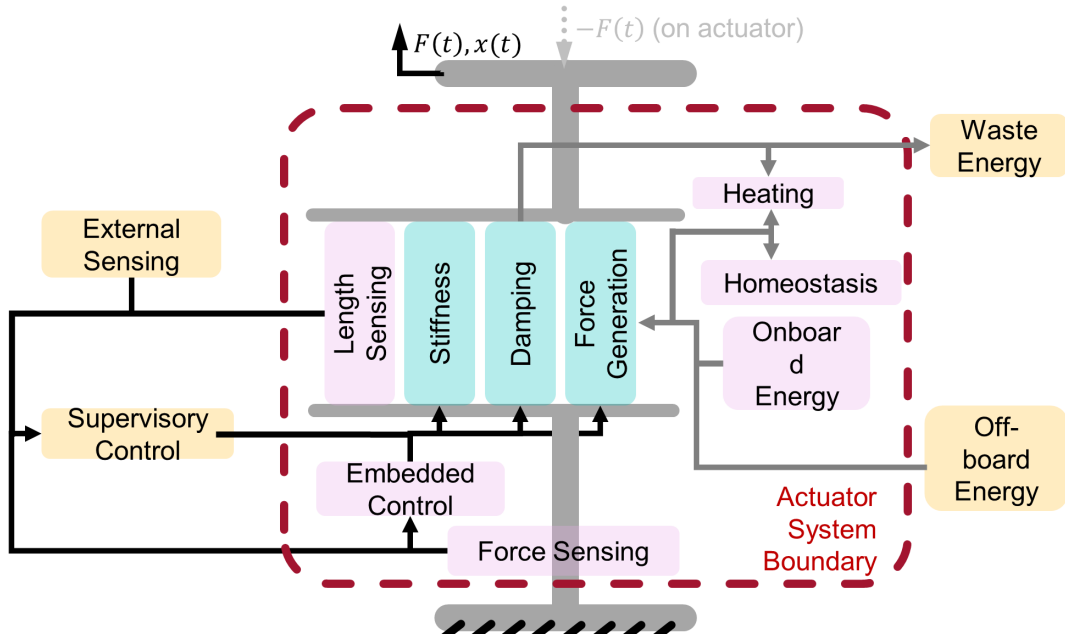
FIGURE 2.3: The control volume for the 'actuator system' is defined by the red dashed line boundary. Because internal elements are the focus of this work, this boundary was chosen to include only features and functions that occur within the actuator. Sensor and control mechanisms are shown with black arrows, while energy flow is shown with gray arrows. Biological and engineered actuators develop internal forces that, with inherent and tunable stiffness and damping, can affect the dynamic response of the system (adaptive dynamic response). Supervisory inputs affect both force generation and tuning. The integration of force and length sensing, embedded, control and onboard energy storage make biological muscles a highly integrated system. Some of this integration is available in engineered systems. All actuation systems require some external control and rate of energy transfer for operation. The external energy sources may be used for actuator work output or for maintaining environmental requirements for in-range operation (temperature, moisture, removal of waste products, etc.). Inefficiencies and damping contribute to actuator heating and cooling (waste energy flow) requirements.

Traditionally, muscles have been viewed as motors (Fig. 2.2(a)) that convert activation input into a force output via a transfer function Act(t) [293]. The transfer functions typically range from 1st to 3rd order systems of differential equations [186, 323, 339]. While muscle models based on this principle perform reasonably well at predicting the force of isolated muscles in laboratory experiments [157], recent studies demonstrate that they perform poorly at predicting muscle force during natural movements of humans [86] and animals [186], especially at faster speeds [339] where the adaptive dynamic response

of muscles is particularly important.

Recent models instead describe muscles as tunable active materials, similar to many soft actuators, that produce force when deformed by applied loads [235, 243, 318]. These models (Fig. 2.2(b)) emulate the adaptive dynamic response of muscles [241], based on activation-dependent changes in stiffness and equilibrium length of a spring [95]. The new models capture length-dependence of activation dynamics [72], and adapt automatically to changes in speed and terrain [318]. At the same time that biologists were evolving their view of muscles away from force generators to that of tunable active materials, engineers began exploring how synthetic actuation could be achieved through material deformation (soft actuation), an interesting convergence. A consequence is that the evolving view of muscles as tunable materials may provide inspiration for the design and control of soft actuators with a similar adaptive dynamic response that could provide versatility and safety of HMIs.

To compare soft actuators and muscles, we found it useful to define an 'actuation system volume' in order to better classify actuator features and delineate a system boundary for the scope of this work. In this volume (Fig. 2.3), energy flow and sensory feedback are included, as both are critical to the resulting system performance. We exclude consideration of features external to the actuator but necessary for operation, such as off-board energy storage (e.g. lipid reserves), external sensing (e.g. vision), and supervisory control (e.g. brain control). Other items within the actuator system boundary may not be present for many engineered systems. For example, onboard energy storage and embedded control are generally non-existent in synthetic actuators and are features to strive toward. Conversely, the energy required for homeostasis is an inherent cost of biological muscles that is not present in most synthetic actuators. This systemic view of the actuator includes features not often considered when comparing synthetic actuator designs, which often simply consider force generation capacity and occasionally, length

and force sensing. Despite containing elements that may not be present in all actuation systems, the volume presented in Fig. 2.3 helps to classify features and thus provide a basis for comparison between disparate actuation modalities.

Based on this definition of the actuation system volume (Fig. 2.3), we compare biological and engineered soft actuators. We begin by reviewing the latest muscle-like soft actuators in Section 2.2, including the design, actuation mechanism, and some operational advantages and disadvantages. In Section 2.3, we review the structure, actuation mechanism, models, and inherent properties that endow biological muscles with tunable compliance and adaptive dynamic response. This introduction to biological muscles also presents an engineering perspective of the muscle system as a tunable-element actuator [236, 241] to facilitate comparing the performance and properties of muscles and current soft actuators (Section 2.4). Section 2.4 first compares performance metrics of conventional actuators, soft actuators, and biological muscles. Next, we compare those properties that provide biological muscles with tunable compliance and adaptability to the soft actuators presented in Section 2.2. Finally, Section 2.5 summarizes the current state of soft actuators in terms of performance and properties, and uses this comparative study to provide additional insight on soft robotic terms including biomimetic actuator, artificial muscle, and artificial supermuscle.

2.2 Soft Actuation Technology

The high accuracy and repeatability deployed by conventional, rigid electromechanical and fluidic actuators have been key for their widespread use in industry for the last century [126, 348]. However, their complexity and rigidity limit their deployment in areas such as biorobotics and compliant structures. This has led many scientists and engineers to search for new soft actuators that can adapt their dynamic response in a similar manner

to actuation systems found in nature. The compliance of these new 'soft' actuators [42, 71, 209, 329] (ranging from $\sim$0.1 to 10 MPa^{-1}) is similar to the passive compliance of biological muscles [247]. While new soft actuation technologies are continually being developed, we present a review of soft technologies that have significantly impacted this field and have similar performance to biological muscles. The soft actuators in this section are grouped using their actuation drivers, including electrostatic, thermal, and fluidic soft actuators. Finally, this section also briefly mentions other promising novel technologies for artificial muscles, including electrostatic bellow muscles (EBM), electro-ribbon actuators and electro-origami robots, water-responsive actuators (WRA), photo-responsive actuators (PRA), and eukaryotic DNA inspired artificial muscles.

2.2.1 Electrostatic Actuators

2.2.1.1 Carbon Nanotubes (CNTs)

Carbon Nanotubes act as electrodes or counter electrodes, or both, when they are immersed in an electrolyte (Fig. 2.4). During actuation, electrostatic forces are generated by an asymmetric swelling or contraction of the CNT structure as a result of ion transport in the material matrix (Fig. 2.4(a)) [34]. CNTs can be fabricated from a single-walled sheet of graphite (Single-Walled Nanotubes, SWNT) rolled into a cylinder with a diameter in the nanometer scale (Fig. 2.4(b)-left). They can also be found in a nested configuration with more than one layer (Multi-Walled Nanotubes, MWNT, Fig. 2.4(b)-right) or a hybrid configuration with other materials such as nylon fibers (Fig. 2.4(c)). Despite the different configurations, they all share the same actuation mechanism.

CNT actuators are composed of many nanotubes in the form of films and yarns. The porosity of this material enables fast ion transport which translates into fast actuation, strain rates, and specific power [201]. However, the mechanical properties that make

22
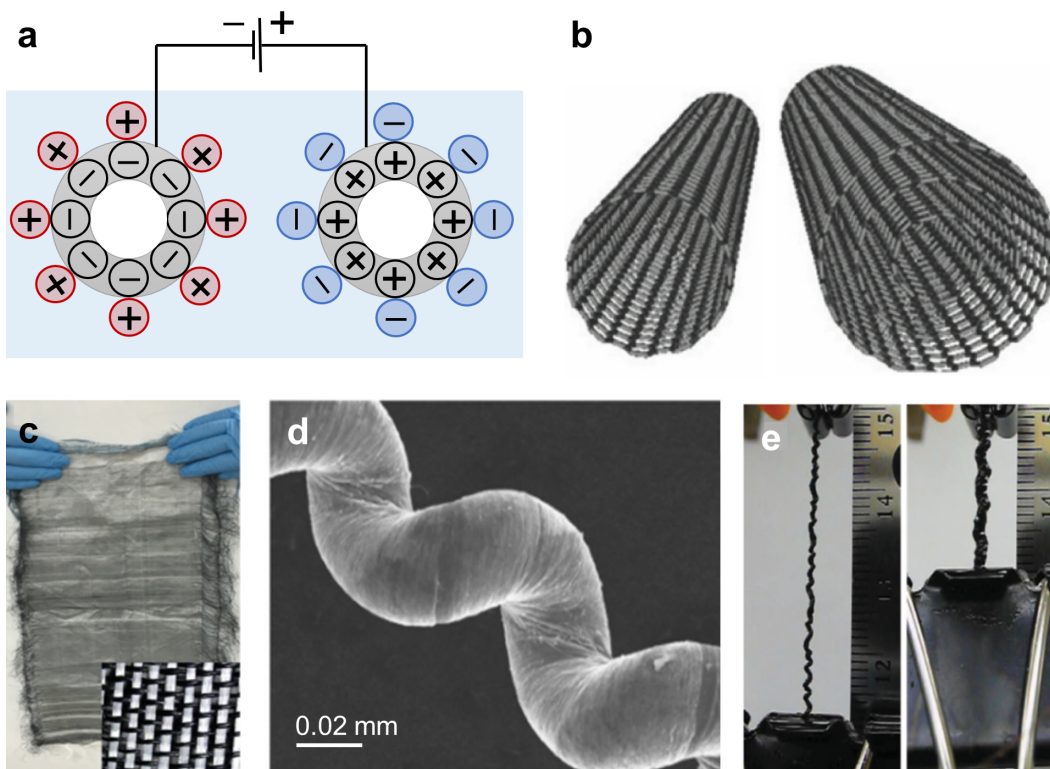
FIGURE 2.4: Carbon Nanotube Actuators (CNTs). (a) Schematic illustration of charge injection in a nanotube-based electromechanical actuator. An applied potential injects charge of opposite sign in the two pictured nanotube electrodes, which are in a liquid or solid electrolyte (light blue background). The different charges in each electrode are balanced by ions from the electrolyte (denoted by the charged spheres on each nanotube cylinder). Each illustrated single nanotube electrode represents an arbitrary number of nanotubes in each electrode that act mechanically and electrically in parallel. Depending on the potential and the relative number of nanotubes in each electrode, the opposite electrodes can provide either in-phase or out-of-phase mechanical deformations [34]. (b) Left: Single-Walled Nanotube, SWNT. Right: Multi-Walled Nanotube, MWNT [229]. (c) Fabric knitted using nylon fibers as weft and CNT fibers as warp. The inset shows the pattern details of the fabric [84]. (d) Chemically actuated thin coiled silicone–CNT hybrid yarn. (e) A 500 µm thick coiled yarn contracts by 50% under 2 MPa tensile stress when exposed to hexane. The tensile stress is with respect to the non-coiled diameter of hybrid yarn before solvent absorption [196].

CNTs strong and stiff (tensile modulus of 1 TPa and tensile strength from 20-40 GPa [220, 285, 365]) do not allow for high deformations, leading to a limitation in their strain [220]. Although strains are increased in twisted and coiled CNT actuators (Fig. 2.4(d) and (e)), similar to the twisted polymer actuators discussed in Section 2.2.2.1, their actuation response time also increases, making them much slower than biological muscles

23
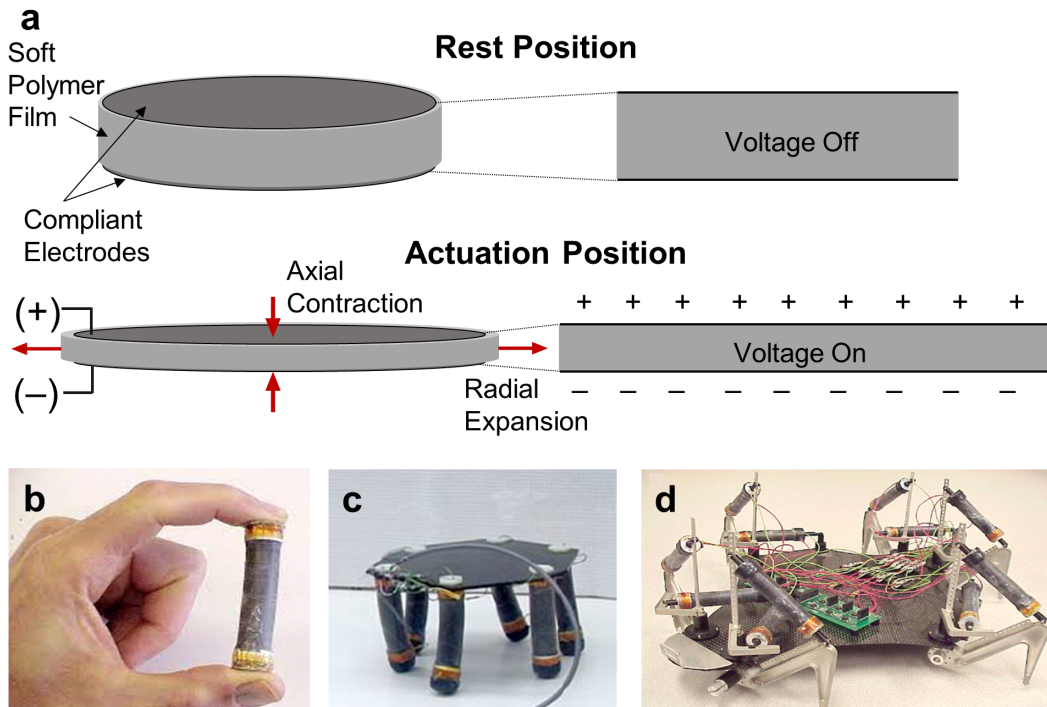
FIGURE 2.5: Electro-Active Polymers (EAPs). (a) Operating principle of dielectric elastomer actuators (DEAs). When a bias voltage is applied across an elastomer (soft polymer) film coated on both sides with compliant electrodes, Coulombic forces compress the film in the axial direction and expand it radially [43]. (b) One degree of freedom multifunctional electroelastomer roll (MER) actuator fabricated with two pre-strained films rolled around a compressed central spring (the spring is located at the center of the roll and covered by the films). (c) MERbot, a robot using a 2-DOF MER for each of its six legs [258]. (d) FLEX 2 robot using MER actuators from b [259].

[105, 196]. In this work, we focus on single fiber CNTs as they have been most studied and utilized in applications [219, 220]. Single fibers have been combined to form smart textiles, which have been used to assist individuals with limited mobility [84]. Finally, it is important to mention that extraction of carbon nanotube fibers is currently difficult, and the fabrication process makes these actuators expensive [35].

2.2.1.2 Electro-Active Polymers (EAPs)

Electroactive polymers are capable of developing high mechanical strain in response to electrical stimuli [30]. EAP materials exhibit some beneficial features for biomimetic

implementations such as high strain and power density, versatility, and scalability [258]. EAPs are normally designed in a sandwich configuration with a soft insulating elastomer membrane between two compliant electrodes. Actuation is driven by an electric field generated by the voltage applied between the electrodes. While there are many different types of EAPs, here, we focus on Dielectric Elastomer Actuators (DEAs) because these display the best performance in terms of linear actuation [92, 362]. DEAs can generate high deformations as a result of electrostatic interactions between the electrodes. The actuation mechanism in DEAs is based on the principle of capacitors. When an external voltage is applied, opposite charges attract in the electric field direction and repel in the perpendicular direction. The generated Maxwell stress creates compressive forces on the dielectric material (polyurethanes, silicones, or acrylics) along the direction of the applied voltage, leading to an expansion of the dielectric material in the other two directions (see Fig. 2.5(a)). The elastomers of DEAs are usually silicone or acrylic materials which achieve large deformation due to their low elastic modulus (1 to 10 MPa). Additionally, they also have a fast actuation response, making them suitable candidates for bioinspired applications. Walking robots like MERbot and FLEX 2 (Fig. 2.5(c) and (d)) have been actuated using DEAs in a roll configuration (Fig. 2.5(b)) [55, 164, 236, 258, 259, 259, 362]. However, the high voltages required for actuation can create challenges for practical implementation of their power electronics.

2.2.1.3   Hydraulically Amplified Self-healing Electrostatic Actuators (HASELs)

Hydraulically Amplified Self-healing Electrostatic actuators are electrohydraulic activated muscle-mimetic actuators fabricated from an elastomeric shell partially covered by a pair of opposing electrodes and filled with a dielectric liquid. The use of hydraulic principles in HASEL actuators results in the capability to scale actuation force and strain; features also used in other device classes such as microhydraulic systems [283] and hydrostatically

25
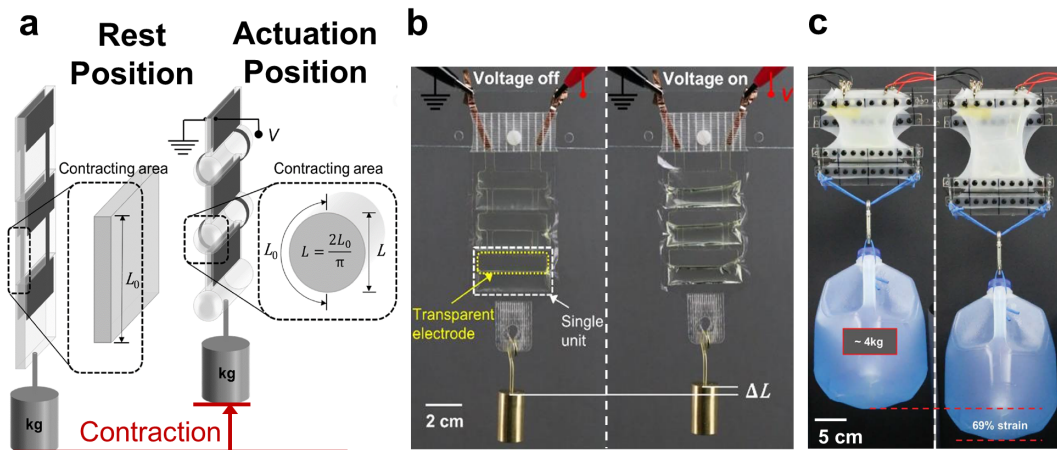
FIGURE 2.6: Hydraulically Amplified Self-healing Electrostatic Actuators (HASELs). (a) Actuation mechanism of Peano-HASEL actuators. Each unit consists of a flexible rectangular pouch filled with liquid dielectric. Electrodes are placed over a portion of the pouch on either side. When the voltage (V) increases, electrostatic forces displace the liquid dielectric, causing the electrodes to progressively close. This forces fluid into the uncovered portion of the pouch, causing a transition from a flat cross section to a more circular one, which leads to a contractile force [167]. (b) Three-unit Peano-HASEL actuator shown lifting 20 g on application of 8 kV across the electrodes [167]. (c) Contractile linear actuation of six Planar-HASEL actuators lifting a gallon of water [8].

coupled DE actuators [53]. Upon voltage application, the induced electric field generates an electrostatic Maxwell stress that pressurizes and displaces the liquid dielectric, leading to contraction (Fig. 2.6(a)). HASELs have been developed in different configurations: Planar-HASELs (Fig. 2.6(c)), Peano-HASELs (Fig. 2.6(b)), Donut-HASELs and bio-inspired designs such as a scorpion tail that can contract, curl, and twist [8, 167, 223]. However, their actuation relies on the same mechanism in which a pouch is designed and fabricated to develop the desired actuation response under internal pressurization created by the generated Maxwell stresses.

In this work, we mainly focus on Planar- and Peano-HASELs as their contraction actuation is similar to biological muscles in almost all their metrics (Table 2.1) [8, 167]. In addition, HASELs also have an inherent strain sensing property; measured capacitance is

low when the actuator is fully flexed and high when fully extended. This self-sensing capacity of HASELs can be a useful feature for control, similar to the mechanical impedance of biological muscle [144, 206]. Unlike traditional solid DEAs, which would be permanently damaged due to a high electric field, the use of a liquid dielectric enables HASEL actuators to self-heal from a dielectric breakdown. The self-healing property improves the durability and stability of HASELs. Finally, it is important to mention that HASELs require high voltage (>5 kV) for activation, which could lead to the risk of electroshock of users. Although high voltage requirements usually translate into voluminous power electronics [8, 167], new research has shown HASEL applications with portable electronics and batteries (3.7 V, 500 mAh lithium polymer battery with a 5 V power booster); however, the duration and efficiency of such set-ups has not been reported [223].

2.2.2 Thermal Actuators

2.2.2.1 Twisted Polymer Actuators (TPAs)

Twisted coiled polymer actuators are thermally driven linear actuators with a specific work and power 64 and 84 times that of biological muscles [128, 202]. The actuation response of TPAs results from the anisotropic thermal properties of the untwisted precursor material (Fig. 2.7(a) and (d)), which experiences axial thermal contraction and radial thermal expansion (similar to the asymmetric response of carbon nanotubes to ion transport). The thermal anisotropy of the precursor monofilament translates into shear strain on the twisted elemental unit (Fig. 2.7(b)) and, in turn, axial contraction on the coil-shaped TPA upon heating (Fig. 2.7(c) and (e)). These actuators are fabricated by twisting a drawn polymer monofilament until the monofilament buckles in twist and coils, or by wrapping the twisted monofilament around a mandrel to create a coil. TPAs are spring-shaped (Fig. 2.7(e)), and can be assembled in groups to form braided structures

(Fig. 2.7(f) and (g)) [128]. TPAs are inexpensive, often fabricated from fishing line or sewing thread, and have been deployed in robotics (Fig. 2.7(h)) [202, 309, 360], medical devices [202], and active textiles [143]. Although TPAs outperform skeletal muscles in many metrics, including specific work/power and maximum stress/strain (see Table 2.1), thermal activation is generally inefficient and slow. Additionally, most of the drawn polymers used in TPA fabrication are highly viscoelastic [295, 315] and hygroscopic, which causes their actuation response and performance to depend on moisture content of the material [138]. Moreover, the temperature changes required for actuation affect the viscoelasticity and hygroscopic properties of TPAs, which leads to modeling challenges, and therefore, a lack of accurate control algorithms [137, 297, 315, 352, 356].

2.2.3   Fluidic Actuators

2.2.3.1   Pleated Pneumatic Artificial Muscles (PPAMs)

Among fluid-based muscle-like actuators, Pleated Pneumatic Artificial Muscles—an recent version of McKibben actuators—develop contractile actuation by inflating an unstretchable membrane surrounded by numerous pleats in the axial direction [74]. In all McKibbens (regular and thin), the macroscopic anisotropy causes the device to contract in length and expand radially when pneumatically loaded [65, 177]. Upon inflation, the pleated membrane unfolds without straining the material, producing radial growth and axial contraction of the actuator (Fig. 2.8(a) and (b)). PPAMs have the highest performance metrics, which makes them potential candidates for HMIs (Fig. 2.8(d)) [36, 300] and other bioinspired applications (Fig. 2.8(c) and (e)) [79, 335]. The pleated configuration of McKibbens was developed to eliminate their multi-component nature that causes frictional losses and hysteresis, which also limited their controllability [65, 129]. PPAMs can outperform many metrics such as specific work, average specific power, and actuation
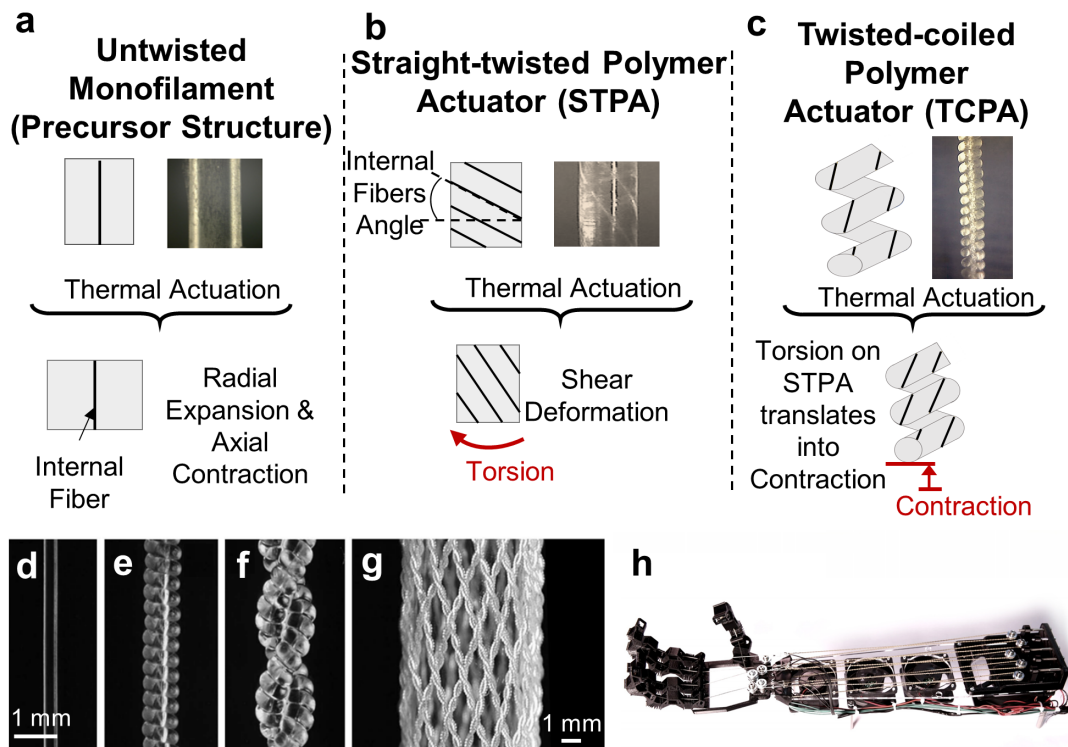
FIGURE 2.7: Twisted Polymer Actuators (TPAs). Actuation response under thermal loading of (a) an untwisted straight monofilament (precursor structure), (b) straight twisted polymer actuator (torsional actuator), and (c) twisted and coiled polymer actuator (axial actuator). Optical images of: (d) a non-twisted 0.3 mm diameter monofilament, (e) a TPA after coiling by twist insertion a 0.3 mm diameter monofilament, (f) a two-ply muscle formed, (g) a braid formed from 32 two-ply, coiled, 102 µm diameter fibers [128]. (h) A robot hand constructed using TPAs to execute various grasping maneuvers using open loop control [360].

stress compared to biological muscles [74, 336]. To maintain low mass, PPAMs typically deploy air as the working fluid for actuation. Due to gas compressibility, low pumping efficiency, and the relatively large amount of fluid required for operation, they generally achieve low total efficiency [213, 215, 216]. It is also important to note that the substantial radial growth resulting from inflation limits the parallel operation of PPAMs, making them useful only in volumetrically inefficient configurations. This limitation prevents variable recruitment in bioinspired applications.
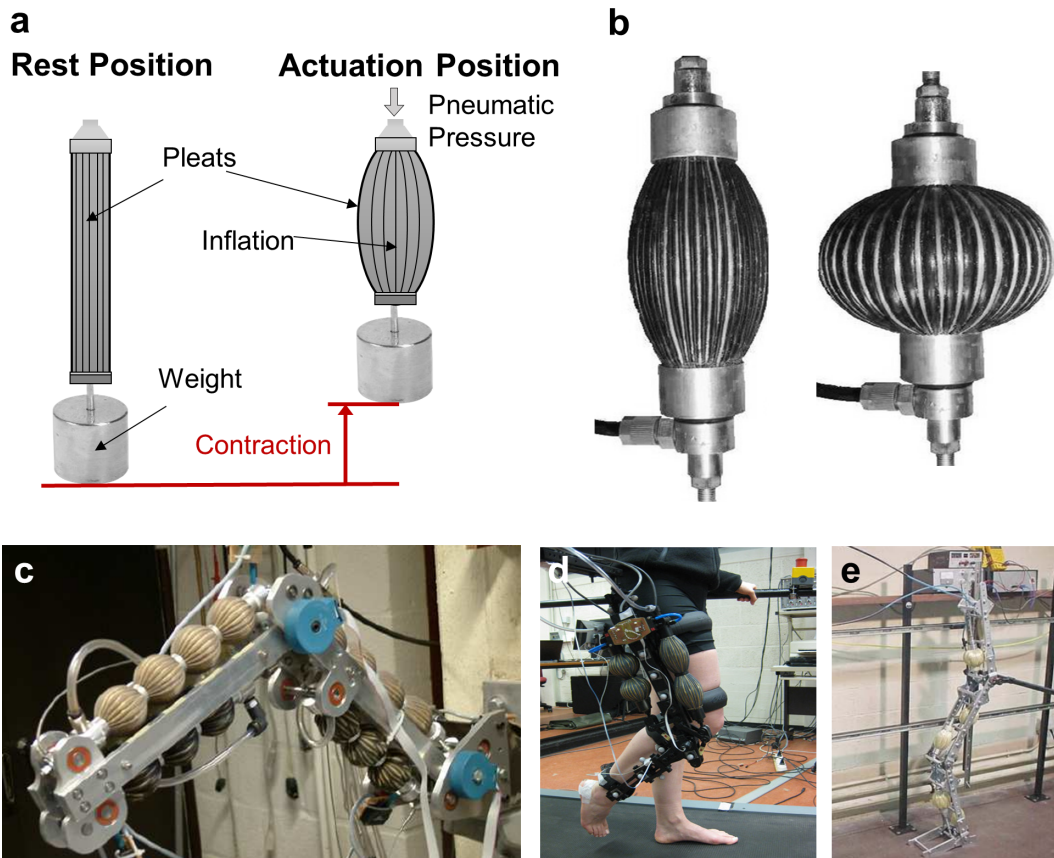
FIGURE 2.8: Pleated Pneumatic Artificial Muscles (PPAMs). (a) Schematic illustration of the actuation response of a PPAM when inflated. (b) PPAM shown at two different actuation stages: at rest (left) and at maximum contraction (right) [336]. (c) Robotic manipulator actuated by serially arranged PPAMs [79]. (d) KNEXO, a knee exoskeleton prototype powered by PPAMs [39]. (e) Right half of the 'lucy leg' attached to a sliding mechanism [335].

2.2.3.2 Flexible Elastomeric Actuators (FEAs)

Flexible Elastomeric Actuators are fluid-driven continuum solid structures pre-designed and programmed to mimic the motion found in some biological systems such as octopuses (Fig. 2.9(c)) or starfish (Fig. 2.9(b)). Their working principle is inspired by the venus flytrap, whose flexible membranes are pressurized with fluid leading to a quick trap closure (100 ms) [106]. FEAs are usually programmed to develop bending as their actuation response, but other deformations such as elongation, contraction, and torsion are also possible; however, in this work we focus on bending and contractile FEAs (Fig. 2.9(a)).

30

Different subgroups of FEAs include Soft Pneumatic Actuators (SPAs) [298] and Flexible-fluidic Actuators (FFAs) [110], but they all rely on the same actuation principle. They are normally fabricated using 3D printing and modeling techniques, making them easy to fabricate and affordable. In their fabrication, arrangements of extensible and inextensible regions are conveniently designed to create specific bending, torsion, elongation, and contraction that translates into motion when fluid pressure is applied, which allows control of their topology. Their materials and design are the source for their actuation properties (mechanical compliance, topology and geometry, maximum stress and strain, efficiency, etc.), which means they can be designed to perform specific tasks (single-tasking) such as walking, grasping, pulling, or twisting.

FEAs can change their compliance as a function of internal pressure [298], generating high strains and block forces [42]. However, as is also true for all polymer-based soft actuators, some of these metrics can be affected by environmental conditions such as temperature and humidity, as the mechanical properties of the precursor materials depend on such [42], which can hinder control. The mechanical properties of these materials and their arrangements lead to non-linearities during actuation which are enhanced during pneumatic activation due to compressibility [99]. Although liquid-based devices can exhibit more linear behavior than those driven pneumatically [134], creating closed-form models for these actuators is still an arduous task, and finite element methods are usually applied when predicting their actuation response [228], limiting their broad adoption. The applications include medical devices, bio-inspired applications, or HMIs where inherent compliance and adjustable stiffness are needed [110, 210, 298, 345].

2.2.3.3 Fluid-driven Origami-inspired Artificial Muscles (FOAMs)

Fluid-driven Origami-inspired Artificial Muscles are origami-based vacuum-driven actuators consisting of a repeated zigzag-pattern skeleton within a sealed bag. When negative
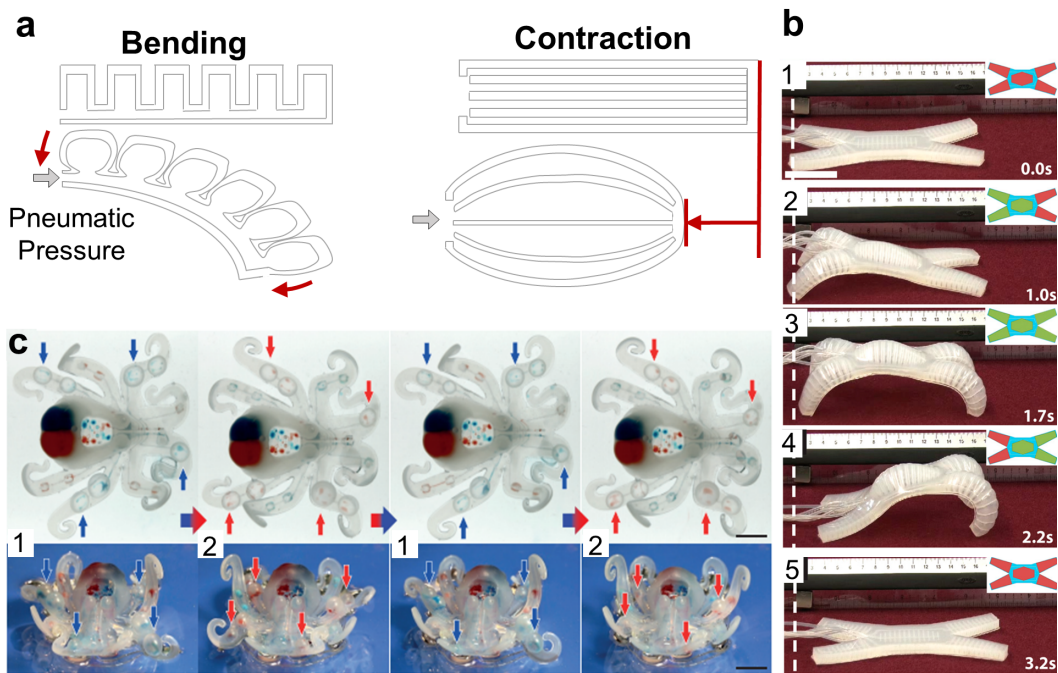
FIGURE 2.9: Flexible Elastomeric Actuators (FEAs). (a) FEA designs and actuation principles: bending actuator (top-left), contractile actuator (top-right). All FEAs actuate upon inflation as a result of their design and flexible materials. (b) Walking cycle of a multigait soft robot inspired by animals (e.g., squid, starfish, worms). This soft robot uses the pressurization of the legs' internal membranes to create an undulation deformation that translates into a walking motion of the entire structure. A particular leg's pressurization is shown (Insets) in green, and inactive legs are shown (Insets) in red. Scale bar, 4 cm [298]. (c) Operation of an octobot autonomously alternating between actuation states (two actuation cycles). During actuation, alternating groups of tentacles are actuated separately, blue ('1') and red ('2'). When the inflatable chambers in the tentacles are internally pressurized with fluid, the tentacles rise and when pressure is released, they lay down. Scale bars, 10 mm [345].

pressure is applied to the actuator, the air inside the bag exits and the zigzag pattern leads to contraction (Fig. 2.10(a)). The internal skeleton found in FOAMs can be designed to develop many different actuation responses in addition to the single-degree-of-freedom contractile motion as shown in Fig. 2.10(c). FOAMs have been fabricated at small scales (Fig. 2.10(b)), shown to perform under water, designed to dissolve when in contact with hot water, and onboard energy and sensors have been integrated into their skeletons [189]. These actuators develop high strains, specific work and average power, and have high fluidic-to-contractile energy conversion efficiencies. Although they have been shown
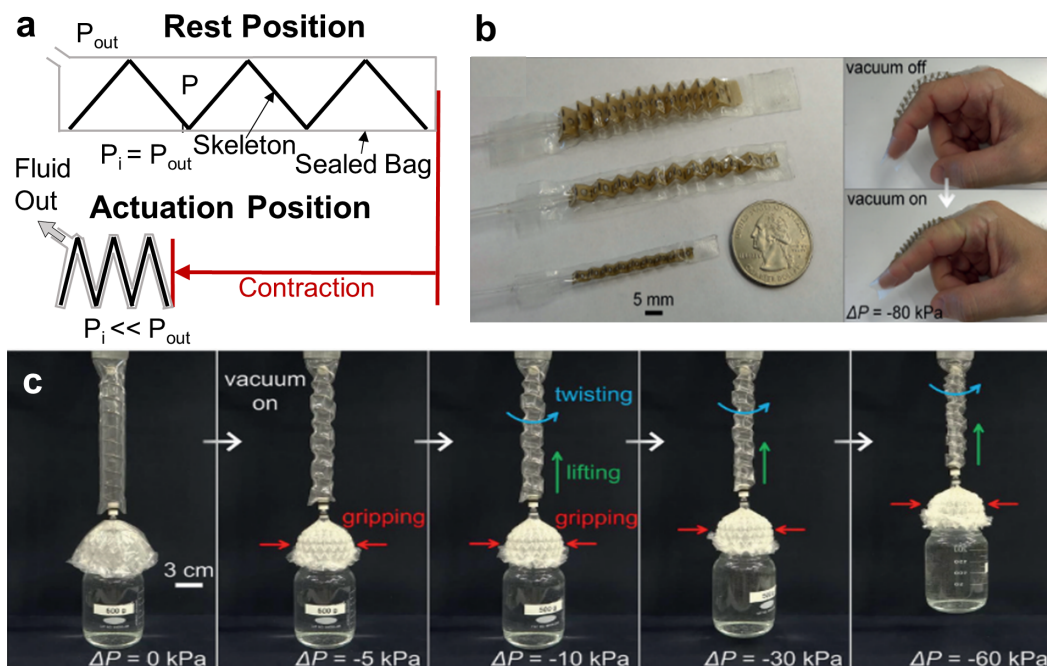
FIGURE 2.10: Fluid-driven Origami-inspired Artificial Muscles (FOAMs). (a) Actuation mechanism. Upon application of negative pressure ($P_{in} \ll P_{out}$), the zigzag-pattern skeleton folds as a result of air exiting from the sealed bag. (b) Miniature linear actuators use polyethyl ether ketone (PEEK) zigzag origami structures as skeletons and PVC films as skins. (c) A bottle of water is gripped, lifted, and twisted by a single-channel vacuum-driven robotic arm [189].

to perform well in portable applications using small vacuum pumps, their negative pressure rate source is usually low, which leads to a slow response. Furthermore, the large strains generated by FOAMs significantly decrease with small load increments, similar to the muscle-length force dependence found in biological muscles [189]. Finally, as is true for all vacuum-driven actuators, there is a theoretical limit to the stress generated in these devices based on the difference between the pump's vacuum capacity and the local atmospheric pressure. Positive pressure actuators do not suffer from such a limit.

2.2.3.4 Origami-Based Vacuum Pneumatic Artificial Muscles (OV-PAMs)

Similar to FOAMs, Origami-Based Vacuum Pneumatic Artificial Muscles consist of a sealed chamber made from polyvinyl chloride connecting a top and a bottom plate with
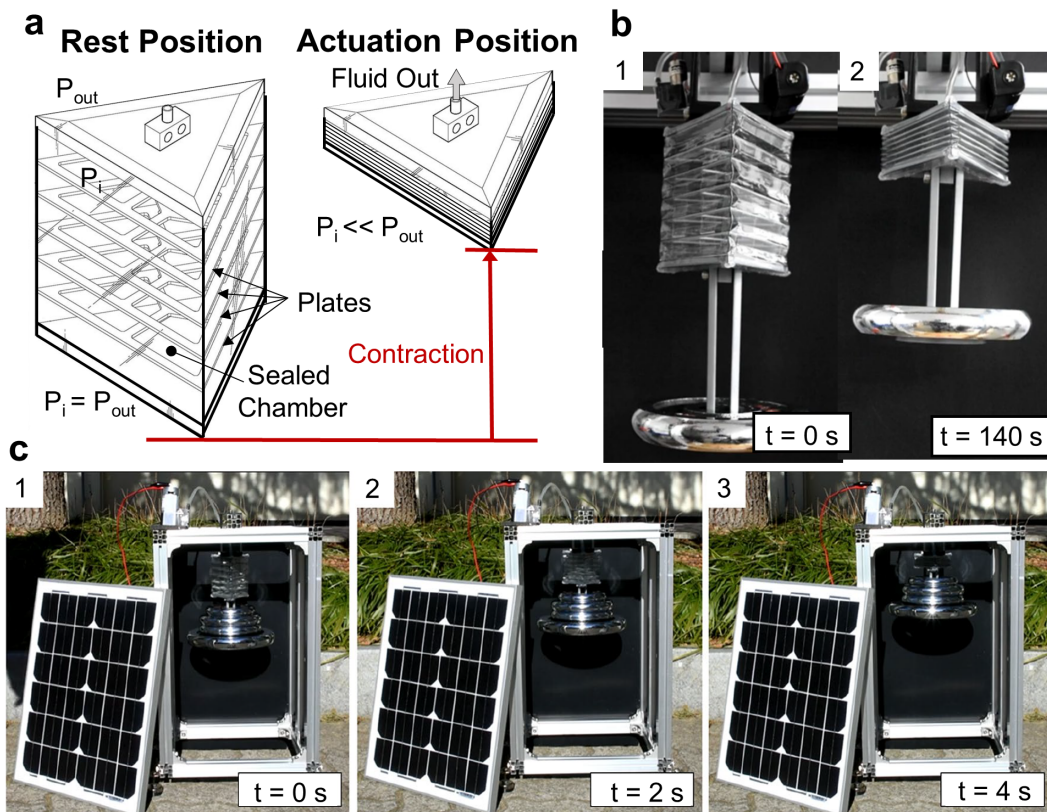
FIGURE 2.11: Origami-Based Vacuum Pneumatic Artificial Muscles (OV-PAMs). (a) Actuation mechanism. Upon applied negative pressure, the air inside the actuator chamber exits and the actuator contracts [185]. (b) Folding of the corners of the actuator and contraction [184]. (c) Portable actuation module powered by solar energy [184].

evenly spaced transverse reinforcements (Fig. 2.11(a) and (b)), rather than using an internal foldable skeleton like FOAMs. Negative pressure inside the chamber causes the PVC film to fold and the transverse reinforcements to stack up, leading to contraction. OV-PAMs have excellent efficiency close to one. However, their specific power and maximum strain are approximately ten times less than those of biological muscles [184, 185]. OV-PAMs can maintain a strain close to 100% while generating their maximum force, which allows these actuators to generate force independently of their length, unlike FOAMs and biological muscles. Similar to FOAMs, OV-PAMs are also vacuum activated, and their actuation response is usually slow when using portable vacuum pumps (Fig. 2.10(c)),

34

resulting in low specific power. Additionally, OV-PAMs are voluminous, and their narrow degree of flexibility could limit their implementation in small and flexible robotic applications [184, 185].

2.2.3.5 Cavatappi Artificial Muscles

Cavatappi artificial muscles use a similar actuation mechanism as Twisted Polymer Actuators (TPAs), but bypass the inefficient thermal actuation driver. These devices use anisotropic mechanical properties of drawn polymer tubes to develop contraction but employ internal pressurization rather than temperature changes for actuation. These tubes can be configured as torsional actuators when twisted or as linear actuators when helically coiled with similar shape to cavatappi pasta (Fig. 2.12(c) and (d)). After drawing (Fig. 2.12(a)) and twisting (Fig. 2.12(b)), hydraulic or pneumatic pressure applied inside the tube results in localized untwisting of the helical microstructure. This untwisting manifests as a contraction of the helical pitch for the coiled configuration (Fig. 2.12(c)).

As a result of their hydraulic or pneumatic activation and the more constant material temperature, these devices outperform TPAs in terms of actuation bandwidth, efficiency, and practical implementation. Cavatappi can exhibit contractions $\gtrsim 50\%$ of their initial length, mechanical contractile efficiencies near 45%, and specific work and power metrics ten and five times higher than biological muscles, respectively [140]. Small-scale cavatappi have also been designed with an outer diameter of less than one millimeter. Activation by internal pressurization allows configuration in parallel, and scalability similar to biological muscle fibers without the need to isolate individual actuators to avoid interference by the activation energy source (uncontrolled heat transfer in TPAs). In principle, these parallel configurations (Fig. 2.12(e) and (f)) could perform variable recruitment and muscle synergy, and be used in bio-inspired muscle-like applications. Despite the minimal amount of fluid required for actuation (low flow rates), one drawback of cavatappi is the
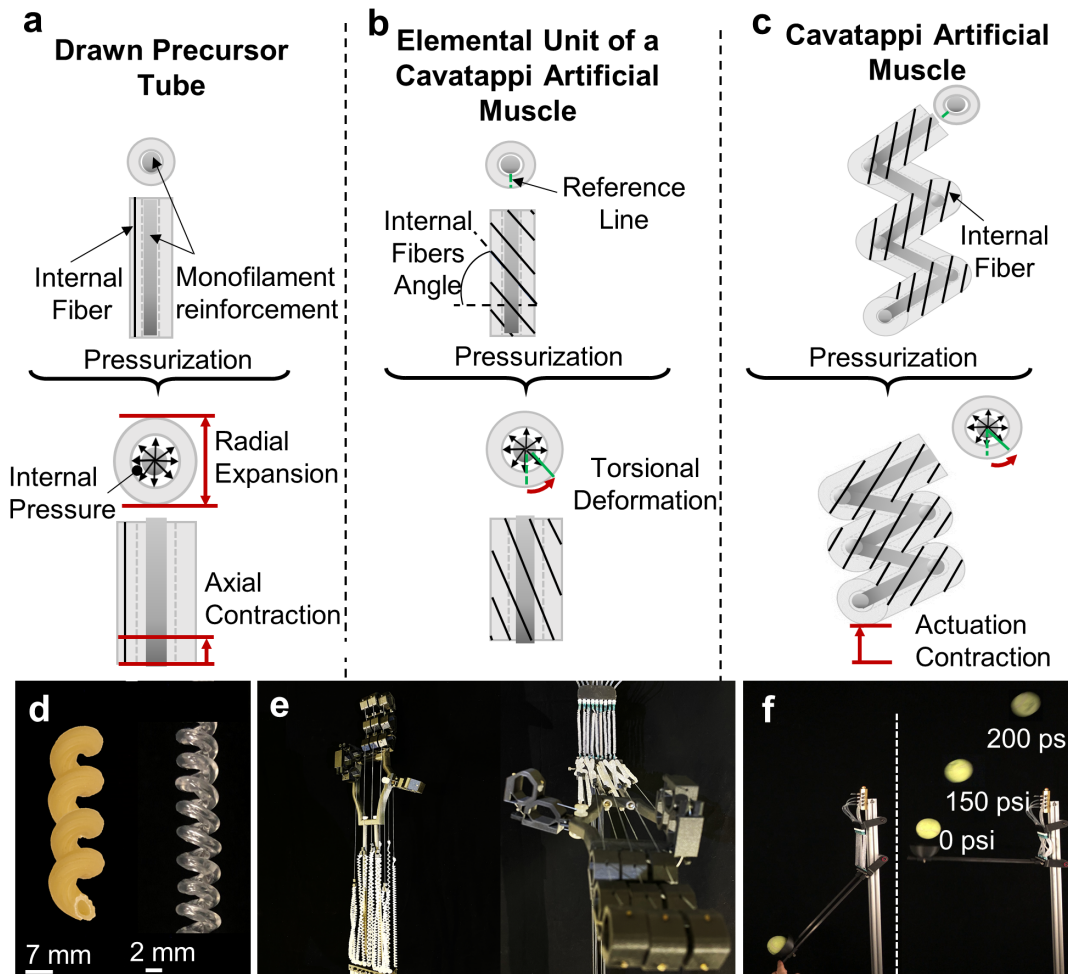
FIGURE 2.12: Cavatappi artificial muscles. Actuation response of Cavatappi artificial muscles. (a) Internal pressurization produces axial contraction and radial expansion in the drawn precursor tube, (b) untwist in the cavatappi elemental unit, and (c) linear contraction in the cavatappi artificial muscle (coiled structure). (d) The helical pasta-like shape of Cavatappi gives inspiration to the actuator's name, and a cavatappi artificial muscle (right) made from a 1.8 mm OD/0.85 mm ID drawn tube, which has been pre-stretched and annealed after fabrication in order to increase the helix pitch. (e) Robotic hand and arm system with cavatappi artificial muscles in place. (f) Cavatappi used to catapult a ball to demonstrate the potential elastic energy storage capacity of cavatappi [140].

high pressure needed for actuation ($\sim$1.5 MPa). Although small high-pressure pumps are available, they are expensive and reduce the economy of cavatappi in many applications.

36

2.2.4 Other Promising Soft Actuation Technologies

In addition to those actuators described in the previous sections, there are several other technologies whose actuation principles and designs might provide useful insights to achieve successful muscles substitutes. Although the actuators described in this section are promising in the field of artificial muscles, they still do not meet most of the performance metrics of biological muscles or they have not been investigated yet in depth.

Along with DEAs and HASELs, other electrostatic actuators have been reported in the past years. Electrostatic bellow muscles (EBMs) have used the previously mentioned electrostatic actuation principles along with thin films, liquid dielectrics, and rigid polymeric stiffening elements to form a circular shaped actuator capable of out-of-shape contraction [303]. These actuators are simple-to-make and low-cost and can deploy fast actuation strain (actuation contractions and strain rates greater than 40% and 1200%/s, respectively) and efficiency similar to biological muscles. Furthermore, they can also work as harvesting systems during inactive actuation phases which can be used to increase the energy efficiency of the actuator. However, at the EBMs current state, some of their key metrics are orders of magnitudes lower than those found in biological muscles. These metrics are specific work (0.0012 kJ/kg), specific power (0.015 kW/kg), and maximum actuation stress (0.004–0.006 MPa) [303]. Electro-ribbon actuators and electro-origami robots use an origami fold whose opposing sides are oppositely charged. At the fold hinge, an electric field is developed exerting an electrostatic force. Such electrostatic force is amplified by using a small bead of high permittivity and breakdown strength liquid dielectric, which in turn, enable useful work while the hinge closes [317]. Multiple actuator configurations are possible using this actuation mechanism; however, the performance metrics of these actuators strongly depend on the actuator design. For example, the designs for high specific energy (0.007 kJ/kg) and high peak specific power (0.1 kW/kg) are

different. Thus, while a specific electro-ribbon actuator might achieve high performance in one of these metrics, there is not a generic or standard actuator that can meet all the performance metrics of biological muscles [317].

Others have focused their effort on soft actuators that generate mechanical motion in response to changes in the moisture content in their natural or synthetic material structure, the driver being usually the external relative humidity (RH) [256]. These soft actuators are called water-responsive (WR) actuators and have been found to be great candidates for energy-related applications. Some of these applications are weather-responsive architectural systems that can autonomously adjust their openings upon changes in local RH [146, 217] or smart textiles that open and close in response to human body's sweating to facilitate comfort [161, 230, 343]. The same actuation mechanism has been deployed in actuation systems. Overall, these actuators can perform similar actuation performance metrics as biological muscles; however, most of these actuation technologies require of long times to generate an actuation cycle [12, 161, 173, 354]. Additionally, environmental relative humidity is a driver difficult to control, which makes these actuators face multiple challenges in some bioinspired applications.

Photoresponsive materials have also been used to generate actuation [176]. In this soft actuation subfield, photochemical transformation and photothermal heat generation are the most exploited actuation mechanisms. Although these have been shown to be promising in fields like micro-robotics [371], similar limitations as the ones found for WR actuators are presented when they are deployed as artificial muscles. Their timescale of deformation typically on the order of seconds or longer due to light propagation, interplay between isomerization kinetics, and mechanical properties of the matrix [176]. Furthermore, photoactuation on smaller length scales for the miniaturization of photomechanical devices remains a challenge as a result of limitations in light delivery in such scale [176].

Finally, the thousandfold contraction mechanism of eukaryotic DNA into the cell nucleus was used to create artificial muscles under the name's work: dual high-stroke and high-work capacity artificial muscles inspired by DNA supercoiling [305]. These soft fiber actuators could generate contractions close to 90% and maximum specific works 36 times higher than biological muscles when immersing the actuators in base and acid solutions [305]. However, and similar to WR and photoresponsive soft actuators, their actuation response is slow and their driver is difficult to use in some bio-inspired applications.

In conclusion, the above soft actuation technologies have not been extensively reviewed in this work because there are still challenges present to meet some of the key metrics of biological muscles as such technologies are found in their early stages. However, the aforementioned soft actuators might help to inspired future soft actuation technologies.

2.3   Biological Muscles

Animal and human muscles and the bodies that contain them integrate multiple components, such as power source (ATP), actuators, strain and force sensors [144, 206], and control circuits in the spinal cord and brain, into a relatively compact material architecture [242]. The unique structure of biological muscles provides these actuators with several properties that are usually limited in conventional actuators. Therefore, compared to robots, animals exhibit remarkably agile, versatile, adaptable and efficient movements [87]. In terms of versatility, any muscle can function as a motor, brake, strut or spring depending on the activation and strain that it experiences during movement. In terms of adaptability, muscles instantaneously adjust their material properties in response to unexpected perturbations [246], becoming less stiff and more damped when stepping into a hole [78], and more stiff and less damped when encountering an obstacle in the path of movement [77]. This section presents a top-down, multi-scale introduction to biological
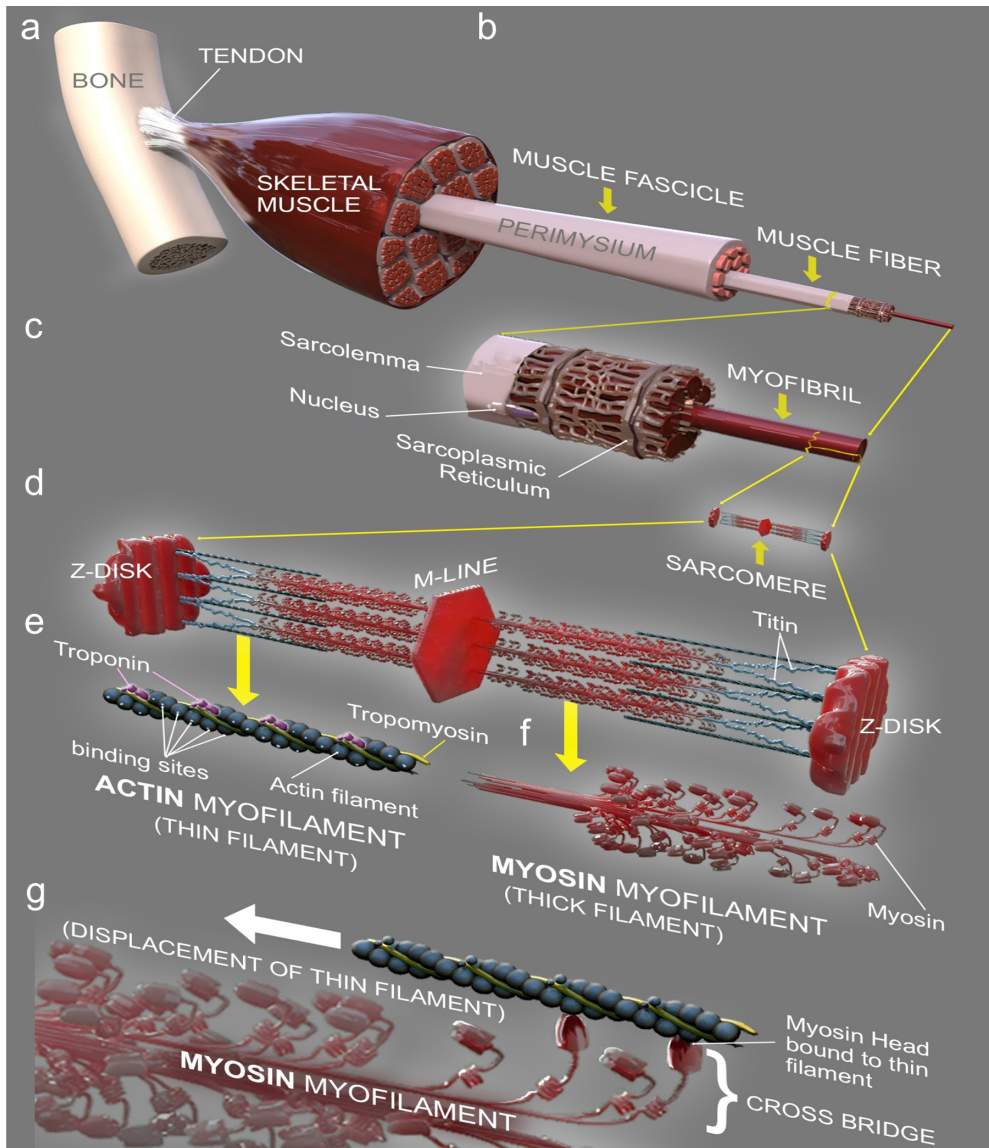
FIGURE 2.13: Structure of biological muscles. (a) In vertebrate animals and humans, skeletal muscles are connected to bones via tendons. (b) Most of the cross-sectional area of muscles is composed of muscle fibers consisting of numerous sarcomeres (c) arranged in series. (d) Sarcomeres are organized into near-crystalline arrays of actin (e) and myosin (f) filaments.(g) Displacement of the thin filament. Figure produced by Victor O. Leshyk.

muscle structure and function, actuation mechanism, control, and key properties that make muscles unique and would be useful to incorporate in soft actuators.

2.3.1 Structure and Function

Skeletal muscles of vertebrate animals and humans are connected to bones by collagen fibers that form tendons or aponeuroses (Fig. 2.13(a)). When a muscle is activated, its force is transmitted through the tendons to the bones to produce a torque about a joint. When this torque overcomes opposing loads (antagonistic muscles and external loads), actuation is achieved by changing the distance between the anchor points. Although nerves, blood, and lymphatic vessels are woven throughout, muscles mainly consist of bundles of fibers, 5 - 100 µm in diameter, connected in parallel (Fig. 2.13(b); [289]). Muscle fibers can reversibly contract by up to 50% in isolation and 30% during natural movements. Muscle fibers are composed of mitochondria, which supply the sarcomeres with energy for contraction in the form of adenosine triphosphate (ATP), and parallel subunits called myofibrils (Fig. 2.13(c)), typically about 2 µm in diameter, which extend from one end of a muscle fiber to the other and consist of longitudinally repeated units called sarcomeres. The scalability property allows biological muscles to function as actuators at scales ranging from micrometres (sarcomeres) to meters (elephant trunks). The sarcomere is the functional unit of actuation in biological muscles (Fig. 2.13(d)). This core unit contains thick and thin filaments packed at high density into a nearly crystalline lattice [132]. The high specific work and power of muscles comes largely from the dense packing of actin and myosin proteins into muscle sarcomeres. The thin filaments (Fig. 2.13(e)) consist largely of actin, troponin and tropomyosin proteins. The thick filaments (Fig. 2.13(f)) consist mainly of myosin. The myosin protein has a pair of heads, 5 nm in diameter, which protrude from the thick filament backbone. Early studies from electron microscopy demonstrated that the myosin and actin filaments slide past each other during muscle contraction [151, 153]. Later studies showed that myosin heads form cross bridges with adjacent thin filaments during muscle contraction. Swinging of myosin cross bridges attached to actin associated with hydrolysis of ATP was identified as the

mechanism of filament sliding [152, 207], and was consistent with a simple model linking muscle energetics and mechanics [142].

2.3.2 Actuation Mechanism

When an action potential, generated by a motor neuron in the brainstem or spinal cord, arrives at a muscle fiber, a burst of Ca^{++} is released from the sarcoplasmic reticulum. The Ca^{++} binds to troponin, which rotates the tropomyosin molecule to expose sites on the thin filaments to which cross bridges can bind. Rotation of the myosin heads, initially charged with ATP, pulls the thin filaments toward the thick filaments [273], resulting in actuation via muscle contraction. As the myosin heads rotate, they generate tensile force from the chemical energy released as ATP splits into ADP (adenosine diphosphate) and Pi (inorganic phosphate). The ADP and Pi are then released from the myosin head, and the cross bridge remains bound to the thin filament until a new ATP molecule binds to start the cycle over again. The total force generated by a muscle is determined by the number of attached cross bridges. However, the number of cross bridges that can attach to actin at a given instant depends on muscle length, the so-called 'force-length relationship' [122]. As sarcomeres are stretched, overlap between thick and thin filaments is progressively reduced. Cross bridge attachment also depends on the availability of Ca^{++}, which increases in response to an action potential and "activates" the thin filaments. The sliding-filament swinging-crossbridge theory of muscle contraction led to the view of muscles as actuators that produce a force when activated; analogous to how an electric motor that, given an input voltage, produces a torque [294] or how elemental units of cavatappi articial muscles or twisted polymer actuators generate a torque when internally pressurized or heated, respectively. [128, 140]. An important feature of biological muscles, not explained by traditional cross-bridge theories, is that their viscoelastic properties (stiffness and damping) depend not only on the level of activation, but also on strain history [7]. Muscles develop

more force during and after active stretching (force enhancement), and less force during and after active shortening (force depression), than the "isometric" force that develops at the same final length. Force enhancement and depression allow for instantaneous adjustments of muscle impedance during unexpected perturbations, such as stepping on a stone or into a hole, when a muscle's force and stiffness change instantaneously, long before reflex feedback or supervisory commands from the nervous system can change the level of muscle activation [76–78, 246]. The importance of strain history in muscle force production has led to the idea that a critical element might be missing from theories of muscle contraction and models based on them [198], specifically a viscoelastic element whose stiffness and free length depend on activation [241, 245]. Recent research suggests that the giant titin protein (Fig. 2.13(d)) is the missing tunable spring [95, 198, 241]. This giant protein forms a continuous fiber from one end of a half-sarcomere to the other and transmits cross-bridge forces from the myosin filaments to the actin filaments in the Z-disk [198]. New evidence demonstrates that titin binds to actin in the presence of Ca^{++}, increasing stiffness and decreasing equilibrium length [95]. This mechanism can explain the strain-history dependence of muscle force production [240] as well as the adaptive dynamics response of muscles to unexpected perturbations [246]. The emerging view of titin as a tunable viscoelastic element leads to a different view of muscle as an active, composite material that actuates movement by developing force in response to combined effects of activation—which tunes the muscle's viscoelastic properties—and deformation by applied loads caused by interactions with the environment [235]. From this viewpoint, titin is a viscoelastic element in muscle sarcomeres that computes, morphologically, the effects of activation and deformation. By using 'morphological computation' to adjust viscoelastic properties, titin plays an important role in tuning impedance and stabilizing unexpected perturbations. This view of muscle as an active material with tunable stiffness and equilibrium length [241] provides new ideas for bio-inspired design of soft actuators.

2.3.3 Control

Control of actuation by biological muscles occurs at three levels: 1) supervisory feedforward commands from the brain (supervisory control); 2) embedded control provided by sensory feedback loops, between proprioceptive length and force sensors in the muscles and tendons, and pattern-generating circuits in the spinal cord; and 3) the adaptive dynamic response provided by the tunable material properties of the muscles themselves. Neuromechanics is the study of how muscles, sense organs, motor pattern generators, and the brain interact to produce controlled movement under varying environmental conditions [242]. Accurate control and adaptability of movement result from direct coupling between the neural system and the muscles. These systems communicate by a series of transformations of information, from brain and spinal cord to muscles to body, and back to brain. The control depends on the transformation of information (transfer function) and, in turn, on the dynamic behavior of each subsystem. To better explain how the interplay between the neural and mechanical systems occurs at all levels of biological organization, we use the example of a "goalkeeper catching a ball". Our goalkeeper must accomplish many tasks to catch the ball, including running toward the ball, adopting a suitable position for catching the ball, and eventually catching the ball. All of these tasks involve the interplay between sensorimotor properties of the nervous system and mechanical properties of the musculoskeletal system during locomotion. The higher level supervisory functions plan the sequence of movements required to intercept the ball, whereas embedded control via feedback from length and force sensors in the muscles and tendons themselves [237] regulates mechanical impedance by coactivating antagonist muscles that actuate the same joint [206, 242], while the adaptive dynamic response via tunable compliance at the level of the muscle itself provides versatility and adaptability, for example associated with unexpected changes in terrain (e.g., when the goalkeeper steps on a bump or into a hole on the playing field).

Muscle synergy: Whereas the brain plans sequences of movement relative to a goal or task, spinal reflexes and sensory feedback loops activate specific groups of muscles synergistically to produce a desired movement. A muscle synergy is a pattern of activation of a group of muscles that work together to produce a particular movement, such as knee flexion. For example, when the goalkeeper crouches to prevent a goal by the opposite team, the muscles at the ankle and knee joints that work together to flex the knee are activated in a particular pattern called a 'muscle synergy'. Reflex loops and central pattern generators in the spinal cord produce the synergies, which provide actuation timing and control of the group of muscles as a unit, which improves coordination and efficiency [32, 63, 102, 190, 306, 320]. A single muscle can be part of multiple muscle synergies, and a single synergy can activate various muscles. Muscle synergy leads to a reduction in the dimensionality of muscle control, akin to asking an orchestra to play a particular song rather than telling each musician which notes to play. The force can also be modulated by varying the number of fibers that are activated in parallel (variable recruitment). This grading of force enables efficiency to be maximized over a wide range of loads and contraction velocities, in addition to enabling control of acceleration and force.

Morphological Computation: In biological muscles, the giant titin protein enables the adaptive dynamic response of muscles by morphologically summing the effects of activation (i.e., commands from the nervous systembrain) and strain (i.e., deformations produced by interactions with the environment). These morphological computations underpin the embedded control which lead to the versatility and adaptability of biological muscles. As a result of this morphological computation, muscles have a tunable compliance. Compliance tuning is the way soft structures (natural or artificial) interact adaptively with their environment. Common examples include octopus arms—which can bend

around objects, squeeze through small gaps, or stiffen selectively when used as a modifiable skeleton or strut—and elephant trunks function similarly to transmit high forces, for example when lifting a tree. Tongues in general and human lips are other examples. To perform these different functions, muscles have the ability to adapt their impedance (i.e., stiffness and viscosity) instantaneously when loading conditions change [242]. Returning to our example of the goalkeeper, morphological computation by the muscles themselves can be seen when the goalkeeper catches a soccer ball that contains high momentum. The adaptive dynamic response inherent in the tunable compliance of biological muscles will provide the arm of the goalkeeper with time-varying compliance to adapt the ball's impact and modulate its momentum. Low compliance of arm muscles would lead to a large impulse as the ball makes contact, providing less time to grasp the ball, while a very compliant arm would not bring the momentum to zero and stop the ball. Conventional actuators could perform similarly, when using control strategy with fast feedback control, but would not benefit from the computational efficiencies achieved through morphological computation. By instantaneously adjusting their stiffness and damping, muscles perform more work when an obstacle is encountered in the path of movement, whereas more energy is dissipated (damping) when muscles are rapidly unloaded [78, 87]. The tunable material properties of biological muscles [241] provide adaptive control of impedance without requiring sensing or feedback [242, 246], in contrast to conventional robots in which the impedance of every joint output torque is typically sensed and controlled using feedback. In biological systems, muscle synergy, morphological computation and adaptive dynamic response offload some of the computations normally attributed to supervisory control, reducing requirements for sensing and information transfer, and thereby off-loading computational burden from the nervous system. Although this offloading is computationally efficient for the supervisory controller (brain), it is not without drawbacks. Training muscle synergies requires learning over developmental or evolutionary time scales. For example, human babies typically require two years of learning to develop the synergies

necessary for walking and while most ungulate species are able to walk quickly after birth, eons of evolutionary learning bestow them with pre-programmed movement sequences. In both cases, the efficiency and adaptability inherent to biological muscles requires time to learn and points to learned actuation response as an important area for continued research in the field of soft actuation [58, 264].

2.3.4 Energy Sources and Temperature Control

In biological muscles, actuator, power source (mitochondria), and fuel (ATP, creatine phosphate, glycogen) are found within the same structure, which more or less exempts organisms from carrying voluminous fuel reservoirs. This self-contained power source capability allows biological muscles to exhibit high overall specific work (0.04 kJ/kg) and power (0.28 kW/kg; [163]) since their power source weight is low compared to those of conventional and soft robotic actuators [195]. However, the energy source for work and power of biological muscles depends on the intensity and duration of activity [33]. For short duration, high intensity, anaerobic activities like sprinting, energy comes from onboard supplies of ATP and creatine phosphate, which can fuel cross-bridge cycling without requiring oxygen or glucose (onboard energy). As the duration of sustained activity increases, muscles depend increasingly on de novo ATP synthesis by mitochondria, which additionally requires oxygen supplied by the circulatory system, and glucose from breakdown of fat droplets and glycogen stored within the muscles or liver (off-board energy). If glycogen and fat stores become depleted, for example when "hitting the wall" during a marathon race, glucose must be delivered from the circulatory system in addition to oxygen. The definition of metrics such as specific power, specific work, and even efficiency become less clear at the systems level. For example, the specific work, power metrics, and efficiency of isolated muscles is similar to the overall efficiency of human walking (∼0.2 -0.4) but the efficiency achieved during running is substantially higher

($\sim$0.5-0.65) due to increased storage and recovery of elastic energy by the muscles and tendons [347]. The circulatory system plays additional roles in removing waste products that accumulate during exercise, as well as in temperature regulation. When waste products, such as inorganic phosphate and lactic acid, accumulate in muscles faster than they can be removed by the circulatory system, muscles experience fatigue, a decline in force for a given level of activation [104]. Fatigue of biological muscles is a major limitation compared to artificial muscles. In addition to providing oxygen and fuel and removing waste products such as carbon dioxide and lactate, the circulatory system of animals also provides temperature control for muscles, which like conventional actuators and artificial muscles produce heat as a byproduct of oxidizing fuel. While muscles function well over a fairly wide range of temperatures [156], their function can decline rapidly if they become too hot or too cold. Like biological muscles, many soft actuators also exhibit temperature dependence of their actuation performance metrics (Section 2.4.2).

2.3.5   Limitations of Biological Muscles as Actuators

The length- and velocity-dependence of biological muscles and their slow actuation response times are often cited as limitations [109]. As noted previously, the force, work and power of biological muscles depends on their length and velocity [7, 18, 142]. Biological muscles produce maximum force at intermediate lengths that represent optimal overlap of the thick and thin filaments in muscle sarcomeres [122], and the force of biological muscles falls faster with shortening velocity than that of electric motors [50, 142]. In contrast, conventional actuators such as electric motors with feedback control can deploy a constant maximum torque and/or stress during actuation independent of their joint angle and are capable of maintaining useful stress and power as a function of velocity [96]. Additionally, conventional actuators are bidirectional and symmetric, in contrast to biological muscles. However, the asymmetrical function of biological muscles is critical to their versatility.

They function as struts when their length is constant, as brakes or springs when stretched actively, and as motors or shock absorbers during active shortening. Models of biological muscle actuation have been shown to provide accurate predictions using springs and dampers. The combination of elastic and viscous elements makes them produce actuation forces slowly compared to electric motors under isometric (constant length) conditions. However, their response time depends on both strain and strain rate, decreasing during stretch and increasing during shortening [72], making biological muscles suitable for any application where fast actuation is required. Most electrical and fluidic soft actuators are built from viscoelastic materials with relatively slower actuation response times, but most of them can also perform fast actuation responses [8, 140].

2.4 Comparative Study

The latest research conducted on the actuation of biological muscles [203, 234] sets standards useful for evaluating the actuation performance requirements of suitable muscle analogs. From the conventional robotic and soft robotic literature, it has been established that artificial muscle technologies need to meet several crucial prerequisites, such as flexibility (soft), durability, and light weight [31, 42, 50, 71, 150, 203]. However, soft actuators could also mimic other properties of biological muscles such as morphological computation, adaptive control, adaptive dynamics response, self-contained power source capacities (onboard energy), scalability, muscle synergy and variable recruitment [87, 144, 206, 242, 243].

As engineered systems, soft actuators may even be able to outperform muscle in areas such as time response, specific power, efficiency, fatigue, aging, etc. [211, 244]. However, the performance of soft actuators can vary widely depending on the conditions of operation. This section evaluates actuation performance for a set of conventional actuators,

soft actuators, and biological muscles (Section 2.4.1). We compare key metrics, including average and peak specific power, specific work, maximum actuation strain and stress, lifetime, power cost, actuation driver and magnitude, actuator and total efficiency, and response time. In Section 2.4.2, we use the inherent properties of biological muscles to develop a comparative study of soft actuators and biological muscles. Section 2.4.2 presents the latest advances in the soft actuation field regarding self-sensing, modeling, adaptive dynamic response, morphological computation, variable recruitment and scalability, energy source and temperature control, and length and velocity dependence. Additionally, Section 2.4.2 also briefly describes why conventional actuators cannot achieve such properties.

2.4.1 Performance metrics

For any soft actuator to qualify as an artificial muscle, it should achieve similar performance metrics to biological muscles. However, this is not the only requirement (see Section 2.4.2). To contextualize their performance, soft actuators are compared to each other, conventional actuators, and biological muscles. Table 2.1 compares non-dimensional and specific actuation metrics for some conventional actuators (electro-mechanical and piston-cylinder actuators), soft robotic technologies (see Section 2.2), and biological muscles (see Section 2.3). The metrics include average and peak specific power, specific work, maximum strain and stress, lifetime, material cost per power unit, activation method (driver) and magnitude, efficiency, and response time. Although the scope of this work is limited to the actuator system (see Fig. 2.3), Table 2.1 also includes a "total-system efficiency" metric that considers off-board energy storage to output work, as some literature only reports these values. For soft-actuators, this is the electrical energy to mechanical work conversion, and for biological muscles this is chemical free energy to mechanical work.

As a point of reference, electric motor and piston-cylinder actuators (Table 2.1) have high specific power metrics, high efficiencies of 80% (excluding pneumatic piston-cylinder actuators), and actuation stress of 0.6 MPa [96, 148, 204, 226]. Many soft actuators also possess advantageous metrics (Table 2.1). Electro-Active Polymers (EAPs) exhibit excellent metrics, including specific work and power, maximum actuation strain and stress, and efficiency [43, 174, 203, 362]. Earlier prototypes were prone to wear or damage as a result of dielectric breakdown when operating in high electric fields, which initially limited the lifetime of these actuators. However, recent EAPs have life spans up to millions of cycles [80, 91, 281]. It remains uncertain whether DEAs can achieve a lifespan of billions of cycles as biological muscles do. Carbon nanotubes (CNT) have maximum actuation stresses of 26 MPa, actuation response times <10 ms, strain rates of 19%/s, and specific power of 0.270 kW/kg [201, 220, 285]. However, they exhibit low strain (3%) and low total efficiencies (0.5%), which are key factors in developing suitable artificial muscles [197, 203]. Additionally, CNTs are difficult to extract and fabricate, which makes this technology expensive (high purity samples cost about \$750/g) [35]. As a basis of comparison, TPAs and cavatappi cost about \$0.005/g and \$0.05/g, approximately 100,000x and 10,000x less expensive, respectively. HASELs can generate high strains ($\sim$60%) and full-cycle system efficiency of 21%. Finally, and this is true for all soft actuators, the time response depends on the power source, system, and energy deployed for actuation. With this consideration, in Table 2.1, we report a qualitative assessment of time response based on their actuation drivers.

Twisted polymer actuators (TPAs) develop specific work of 2.5 kJ/kg and average specific power of 27.1 kW/kg. However, thermal activation requirements limit their response time, control, and efficiency [128, 202]. The electrical-mechanical energy conversion efficiency for TPAs is thought to be similar to that of shape-memory metals, which is approximately 1-2% [128].

Fluid-based actuation has been investigated extensively for the last 70 years and is a potential candidate for significant applications in human-mimetic robots. McKibben actuators, the grandfather of muscle-like fluidic actuators, are pneumatically or hydraulically driven artificial muscles (PAMs or HAMs) widely used in robotics and wearables [36, 249, 279, 330]. Pleated Pneumatic Artificial Muscles (PPAMs) are a recently improved embodiment of conventional McKibben actuators that can develop a specific work of 1.1 kJ/kg and contractions of 38% [215, 336]. The design of PPAMs has also improved efficiency by limiting frictional losses and actuation hysteresis characteristic of conventional McKibbens. However, all McKibbens suffer from inefficient volumetric growth during inflation limiting parallel operation and scaling.

TABLE 2.1: Comparison of metric for various conventional actuators (three first columns or blue columns), soft actuators (next eight columns or orange columns), and skeletal muscles (last column or green columns). Electro-mechanical actuators (EMA) [4, 148, 204], Hydraulic Cylinder (HC) [2, 148, 226], pneumatic cylinder (PC) [4, 148, 226], Electro-Active Polymers (EAPs) [43, 80, 174, 203, 218, 281, 362], carbon nanotube (CNT) [34, 35, 197, 201, 203, 220, 220, 285, 322], Twisted polymer actuators (TPAs) [128], Pleated Pneumatic Artificial Muscles (PPAMs) [74, 215, 336], Flexible Elastomers Actuators (FEAs) [42, 88, 345, 377], Fluid-driven Origami-inspired Artificial Muscles (FOAMs) [189], Origami-Based Vacuum Pneumatic Artificial (OV-PAM) [184, 185], Cavatappi [140], Hydraulically amplified self-healing electrostatic actuators (HASELs) [8, 167], and biological muscles [163, 203, 234]. Time actuation response is qualitatively evaluated using Harvey balls. Bolded metrics outperform those metrics of skeletal muscles.

Metrics	EMA	HC	PC	EAP	CNT	TPA	PPAM	FEA	FOAM	OV-PAM	Cavatappi	HASEL	Skeletal Muscle*
Avg/Peak Specific Power† (kW/kg)	**0.3-5** /—	**20-200** /—	**2-20** /—	~0.4 /0.1-0.6	~0.1 /0.27	**27** /50	**1** /—	**1** /—	~1 /~2	0.02 /0.02	**0.8** /1.42	**0.36** /0.59	0.05 /0.28
Specific Work (kJ/kg)	—	**0.09**	**0.15**	**0.1-0.75**	**0.7-2**	**2.48**	**1.1**	—	~0.25	0.19	0.11-0.38	**0.07**	0.04
Maximum Actuation Strain (%)	—	~35	~35	**>100**	~5	**49**	38	~30	**90**	**>90**	~50	~60	>40
Maximum Actuation Stress (MPa)	—	**50**	**0.7**	**5**	**26**	~100	0.16	1.5	~0.6	0.04	~0.70	0.3	0.35
Power Cost (USD/W)	~3	~0.02	~0.03	~7	~6.5×10³	~3×10⁻⁴	~5	~0.02	~0.2	~1.25	~0.06	~0.055	—
Actuator Efficiency (%)	—	90–98	30–40	—	—	—	~57‡‖	25-46	59§‖	~99‡‖	~45§‖	—	—
Total System Efficiency (%)	**50-90**	**40-45**	3-4	**25-80**	~0.5	~1	~5‡‖	**11-23**	2-5§‖	16‡‖	**10-22§‖**	21§¶††	20-40
Driver	Electrical	Fluid	Fluid	Electrical	Electrical	Thermal	Fluid	Fluid	Fluid	Fluid	Fluid	Electrical	Chemical
Driver – Magnitude	6-80 V	20 MPa	0.8 MPa	1-6 kV	0.1-10 V	25-250 °C	0.4 MPa	0.2-0.5 MPa	-80 kPa	-80 kPa	1.8 MPa	5-10 kV	—
Lifetime (Cycles)	~10⁴	>10⁶	10⁶	~10⁶	~10⁵**	>10⁶	>10⁵	~10⁶	>10⁴	—	>10⁴	>10⁵	>10⁹
Time Actuation Response	●	●	◐	●	●	◔	◑	◑	◑	●	◑	●	◑

*Skeletal muscles specific metrics include the weight of auxiliary components (onboard energy source and sensors). †This value is limited to the energy rate provided by the energy source. ‡Pneumatic. §Hydraulic. ¶Full-cycle analysis of actuator efficiency (includes energy recovery). ‖Actuators' energy conversion contractile efficiency (without energy recovery). **33% reduction in strain. ††Efficiency for a donut-HASEL.

53

Due to the muscle-like response of McKibbens, other fluid-driven soft actuators have been developed and investigated with the goal of better emulating the properties of biological muscles. Flexible Elastomer Actuators (FEAs) generate contractions up to 28%, blocked forces of 10 N, and specific power of 1 kW/kg [42]. FEA metrics depend on their configuration, and they can be programmed and designed to achieve specific metrics. Origami-based vacuum-actuators have also been developed for soft robotic applications. Fluid-driven origami-inspired artificial muscles (FOAMs) develop contractions of up to 100% and have a mechanical-to-mechanical energy conversion efficiency of 23 and 59% when pneumatically and hydraulically tested, respectively. However, similar to biological muscles, the large contractions by FOAMs significantly decrease with small load increments [189]. Although not as drastically in FOAMS, the force of most soft actuators (DEAs, CNTs, TPAs, PPAMs, FEAs, Cavatappi, and HASELs) typically depends on length and velocity [8, 127, 140, 189]. The related Origami-Based Vacuum Pneumatic Artificial muscles (OV-PAMs) solve the previous strain-stress ratio limitation of FOAMs by maintaining a strain close to 100% while generating maximum force. However, OV-PAMs are voluminous, limiting their implementation in small applications [184, 185]. Finally, cavatappi were conceived as a hybrid of twisted polymer actuators and McKibbens [140]. The metrics of cavatappi exceed those of biological muscles (Table 2.1). However, as is true for all fluidic soft actuators, cavatappi require a micro-pump along with a battery as energy sources, leading to an increase in total system weight, hindering but not preventing their implementation in portable applications.

Compared to biological muscles, conventional and soft actuators (Table 2.1) can actuate for a high number of cycles (life-span) without sacrificing performance, accuracy, and repeatability (CNTs are an exception). In contrast, biological muscles suffer from fatigue when they are cyclically actuated, leading to a drop in performance [26].

At first glance, various soft actuators achieve or even outperform metrics of biological
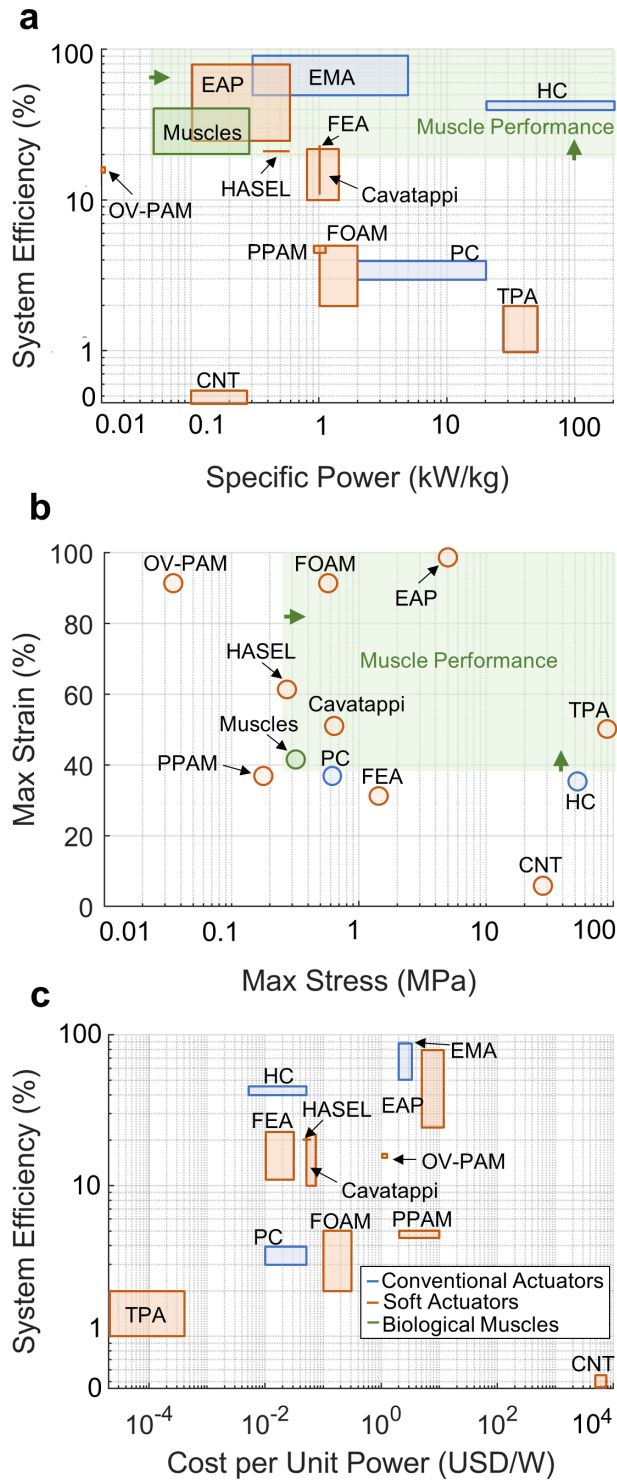
FIGURE 2.14: Comparison of selected metrics of conventional actuators, soft actuators, and biological muscles. (a) System efficiency versus specific power. (b) Maximum strain versus maximum stress. (c) Efficiency versus cost per unit power. In figures a and b, the green area indicates the performance region of biological muscles.

muscles (Table 2.1). However, unlike the soft actuators' metrics, the metrics for biological muscles also more or less account for the weight of auxiliary components like power source (ATP or onboard energy) and sensors (proprioceptors), which could lead to an improvement of the specific metrics of biological muscles compared to soft actuators. It is crucial to clarify that soft actuators mostly use off-board energy sources for actuation; thus, conducting an exhaustive comparison between soft actuators and biological muscles specific metrics is not realistic because the capacity to integrate onboard energy sources in soft actuators architecture is still very limited. Additionally, specific values for metrics that account for the weight of energy sources and sensors of soft actuators are largely unreported in the literature.

Figure 2.14 shows a graphical representation of some of the metrics presented in Table 2.1. The actuators are grouped into three categories; conventional, soft, and biological muscles. Performance varies widely within these categories; however, correlations are found when looking at the driving mechanisms. Thermally driven and ion transport actuators (TPAs and CNTs, respectively) have low efficiency and high maximum stress. Pneumatically driven actuators exhibit average maximum stress and strain, efficiency, and specific power. These actuators normally fall inside the muscle performance region (Fig. 2.14 (a) and (b)). Hydraulically and electrically driven actuators have higher maximum stress, efficiency, and specific power than pneumatically driven actuators, and they fall into a performance region located to the top-left from skeletal muscles. Finally, in terms of their efficiency versus cost-per-unit-power relationship, most actuators are found in the center region of the plot (Fig. 2.14 (c)) and can be considered inexpensive technologies. TPAs fall to the bottom-left of the plot as a result of low efficiency, and CNTs fall to the bottom-right due to their high extraction cost.

2.4.2 Control and Properties

The unique properties of biological muscles allow these living actuators to respond adaptively to perturbations by virtue of their embedded control, which off-loads computation from the brain via morphological computation, and onboard energy. Here, we investigate how soft actuation technologies emulate these properties. This section compares current soft actuation technologies to biological muscles in terms of control, self-sensing capabilities, modeling, tunable compliance and damping, variable recruitment, morphological computation, energy sources and temperature regulation, and length and velocity dependence.

2.4.2.1 Control Strategies

Unlike conventional robots, biological organisms have evolved to survive in environments characterized by rapid changes, high uncertainty, and limited information. Although conventional robots display highly repeatable and accurate actuation, a remaining challenge is to endow them with adaptive dynamics that would maintain stability and control in response to unexpected perturbations. Many roboticists have used advances in computation and data analysis to overcome this drawback in conventional actuators [52, 60–62, 107, 113, 183]; however, actuators that can adjust their dynamic behavior would aid this effort. A new trend is to use ideas from biology and self-organizing systems to inform the design of dynamically adaptive robots [212]. Although many challenges remain, bioinspired robotics will eventually enable researchers to engineer robots and actuators for the real world that will perform like biological organisms in adaptability, control, versatility, fast-response, and agility. Similar to biological muscles, actuator control can occur at three levels: 1) supervisory feedforward commands from an external control module

(brain in a biological system) to process sensed information, generate an output by actively adjusting the actuator dynamics, and even learn from experience [242, 260, 364]; 2) sensory feedback loops between proprioceptive length and force sensors in the actuator architecture; and 3) adaptive dynamic response provided by the passive tunable material properties (compliance and impedance) of the soft actuators themselves (morphological computation). The supervisory and embedded (feedback) control strategies will depend on the actuator's modeling, self-sensing capacities, tunability of the elements, variable recruitment, and morphological computation [115].

Self-sensing: Several soft actuators have self-sensing or partial sensing properties, including CNTs, TPAs, EAPs, FEAs, McKibbens, FOAMs, and HASELs. CNTs with graphite-carbon nanotube hybrid films [20] have used decoupling of electrothermal stimulus and strain sensation to provide real-time feedback [20, 117, 368, 370]. Another strategy is to combine CNT films sandwiched between two polydimethylsiloxane (PDMS) layers that function as a self-sensing soft actuator [368]. Twisted polymer actuators also integrate self-sensing abilities, including closed-loop control through self-sensing of joule-heated TPAs based on inductance [332]; adding conductive and stretchable nylon strings into TPAs to estimate strain from resistance [41, 310], or even integrating stretchable optomechanical film sensors into TPAs, which provides a simple strategy for dynamic strain sensing [373]. The predominant sensing mechanism of EAPs uses the actuator-sensor reversibility property; a sensor-actuator design is coupled in a parallel configuration to create self-sensing [149, 342].

Fluidic elastomer actuators (FEAs) also have the capacity for proprioception. FEAs with flexible or stretchable sensors within the soft bodies feature self-sensing with limited hindrance to motion. Different sensing technologies have been used, including resistive, magnetic, capacitive, optoelectronic, and even conductive working fluids [135, 340, 358, 367]. Although sensors have not been integrated into PPAMs, McKibbens have embedded

microfluidic sensing [257]. The McKibben was composed of three main components: an elastomer air chamber, embedded Kevlar threads, and a helical microchannel filled with a liquid conductor. During contraction, the microchannel can detect the shape change of the actuator by sensing the expansion of the air chamber. FOAMs were built with a nylon-based linear zigzag actuator (60-degree folds) with a reflective optical sensor (TCRT1000, Vishay Semiconductors) attached on its skeleton [189]. This optical sensor reads the distance between the two plates of one fold, which is used as a contraction sensor for the linear configuration. Finally, HASELs also serve as strain sensors and actuators simultaneously. The equivalence of HASELs to a resistor-capacitor circuit allows them to transiently measure the capacitance directly related to the actuation strain [8]. Most soft actuators are compatible with sensor integration. For example, cavatappi could take advantage of some of the sensing techniques used in other soft actuators, like stretchable optomechanical film sensors in TPAs or conductive working fluids in FEAs. Many soft actuators could sense by coactivating antagonist actuators similar to biological muscles [144]. In addition to strain sensing, self-sensing capabilities also include force sensing (similar to biological muscles), which could be achieved using material models. In terms of implementation, most of these sensing techniques have been characterized, modeled, and used in close-loop control strategies, facilitating the estimation of deflection and force [149, 189, 310, 332, 340]. This has helped to lay a foundation for control using the integrated sensing properties of soft actuators and provides insight for controlling untethered soft robots.

Modeling: In contrast to conventional actuators made from rigid components, soft actuators are fabricated from soft materials like polymers, whose properties are usually challenging to characterize and model. These soft materials can be sensitive to external environmental factors such as temperature, humidity, or UV light [19, 138, 363], which can encumber accurate models for actuation predictions. Additionally, most of the soft

actuators discussed here are viscoelastic [262, 304]. While the time-dependence of viscoelastic materials adds complexity to models, this viscoelastic behavior provides soft actuators with the potential benefits of tunable-element actuators and potentially adaptive dynamic response. This may enhance other advantageous properties such as tunable compliance and impedance, energy absorption (using passive mechanical dynamics), and morphological computation as in biological muscles. These features can significantly improve control and the capability of soft robots to adapt to unexpected perturbations [70, 265, 333]. Despite the modelling challenges discussed above (temperature, humidity, and UV light dependencies), initial quasi-static and dynamic material-based models have been achieved for DEAs [346, 372], CNTs [276], TPAs [119, 165, 179], PPAMs [74, 79], OV-PAMs [185], and FOAMs [121].

When modeling the motion of soft robots, two different strategies have been used, depending on the type of application: 1) articulated robots actuated with contractile soft actuators; and 2) continuum soft robots with multiple degrees of freedom (continuum soft actuators). Contractile actuators are normally deployed in articulated robots that use kinematic linkages (rigid bodies) to couple multiple joints together, similar to the skeletons of vertebrates. The actuation response of single DOF contractile soft actuators usually mimics biological skeletal muscles (EAPs, CNTs, TPAs, PPAMs, FOAMs, OV-PAMs, Cavatappi, and HASELs). The similarities of articulated applications of soft robots with those of conventional robots have led to modeling control schemas of low and mid-level operating spaces, using inverse kinematics and dynamic operations as the basis for classical rigid robotic models [17, 82, 125, 200, 277, 286, 337, 361].

Applications where the entire robot body is a soft deformable material capable of multiple degrees of freedom (FOAMs, HASELs, EAPs, and FEAs), like an octopus (invertebrates) present many challenges [99, 134, 282, 298]. For these cases, conventional robotic models are not suitable because of the continuum nature of these actuators, which makes it
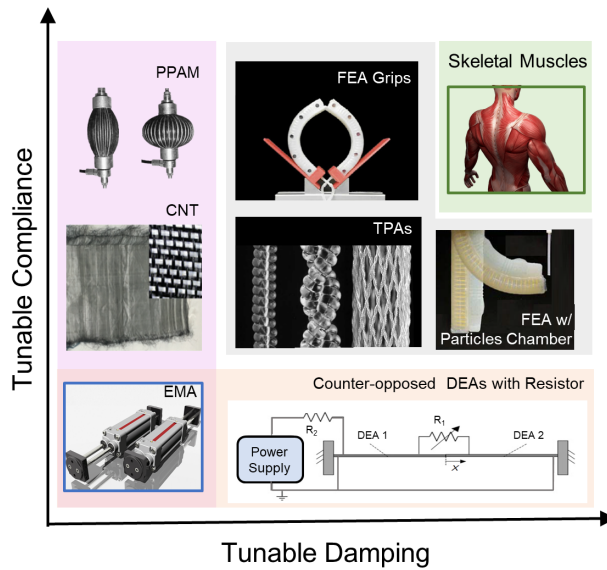
FIGURE 2.15: Progress and future directions in tunable compliance versus damping. Actuators as a function of their capacity to tune compliance and damping. (Left) Soft robots with tunable compliance that increases from bottom to top [79, 84]. (Middle) Soft actuators with tunable compliance and damping, from left to right and top to bottom [85, 128, 193]. (Bottom) Soft robots with little or no tunable compliance that increase their tunable damping capacities from left to right [259]. (Top-right-corner) High adaptive dynamic level of biological muscles and goal for soft actuators.

unclear how to represent the state variables, dimensions of design, and parameters at different body postures of the systems. Thus, continuum mechanical models are necessary. Although control models for these systems are very challenging to develop and implement, these actuators' advantages and muscle-like behavior are pushing researchers to find innovative bio-inspired continuum solutions to model and control these soft-bodied robots [58, 59, 82, 93, 94, 115, 166, 232, 233, 290].

Adaptive dynamic response: Although most materials used for soft actuators are inherently compliant, they also allow variations in compliance and, often, damping, meaning they can perform adaptive dynamic actuation [42, 209]. This property is a requirement in safe HMIs [42, 54, 71, 124, 209, 287, 329, 349] and is one of the principal motivations for creation of soft robots. The capacity of soft actuators to tune their compliance

and impedance allows for adapting their dynamics during actuation and yielding power and control to the human when necessary. Furthermore, and similar to biological muscles [241], they allow deviations from the equilibrium position depending on the applied external force, allowing modulation of load capacity.

Although conventional actuators can also achieve tunable compliance using rapid feedback control loops, this adds complexity to the system. Moreover, feedback control only works correctly if the actuator bandwidth is adequate to the applications' conditions [49, 89]. For this reason, compliant soft actuators, made from flexible materials such as polymers with similar elastic and rheological properties to soft matter found in nature, have been designed to make HMIs safer and improve control [205, 341].

The system's equilibrium position depends on the combination of the equilibrium positions of the constituent elements, so in some cases, it is possible to actuate the individual units while leaving the whole system at rest. This feature allows independent control of the compliance, damping, and equilibrium position of the system. The soft actuators presented in Section 2.2 have been implemented in this antagonistic-agonist configuration to modulate the joint compliance or just in applications where variable compliance was required. Variable compliance is normally a property of most soft actuators as they have in common that their actuation response is a result of changes in the compliance of their soft material or structure.

Dielectric elastomer actuators (DEA) have been laid out in a series of counter-opposed configurations to achieve variable compliance without shifting the equilibrium or zero force point, and even variable damping when using a variable capacitance connected between the counter-opposed DEAs to resist motion by dissipating electrical energy (see Fig. 2.15 bottom-right diagram); [259]). Additionally, DEAs have been deployed in dynamic hand splints for rehabilitation to help patients affected by motor disorders of the hand and have residual voluntary movements of fingers or wrist. DEAs have also been used

in active orthoses that allow for real-time control of the training exercise by modulating the mechanical compliance [54]. Although PPAMs are challenging to arrange in parallel and are less flexible than many other soft actuators, they have been used in a compliant antagonist-agonist actuator configuration for walking and running robots. The variable compliance provided by PPAMs in these applications contributes to absorbed and softened impacts during walking and effectively stores and releases energy during the phases of bending and stretching [74]. FEAs were fabricated with different modes of actuation using integrated adjustable compliance layers. Each layer was provided with a microheater and thermistors to modulate its temperature and stiffness, which allowed tunable compliance of the overall actuator [103]. Although not mentioned in their work, the adjustable temperature potentially allowed for changes in damping. Soft actuators configured in a helical shape such as TPAs and Cavatappi inherently provide tunable compliant features due to their variable spring design [128, 140, 196, 197, 202, 270, 322]. Twisted and coiled polymer actuators have been combined with silicone skin in a compliant haptic finger wearable device to provide lateral skin stretch sensations [64] or even used as twisted string actuators (TSA) to increase their compliance and maximum strain [41]. Finally, straight carbon nanotubes have been combined with dielectric elastomers made from polydimethylsiloxane and carbon grease to create compliant electrodes with large deformation under applied voltage [238].

The capacity to rapidly tune an actuator's dynamic response can also improve performance and efficiency in activities like walking [154, 168], running [147], and jumping [22]. The ability of muscles and tendons to act as springs enables storage and recovery of strain energy which saves metabolic energy. The benefits of this property in biological muscle have also led researchers to promote the addition of elastic elements in conventional robots to increase efficiency [288, 292]. This property could also be exploited in soft actuators [140, 223, 254, 321].

Actuators differ in terms of their tunable compliance and damping (see Fig. 2.15). Conventional actuators have null tunable compliance and damping compared to biological muscles with high tunable compliance and damping, representing the spectrum of adaptive dynamics. In Fig. 2.15, starting from the bottom-left, moving up leads to higher tunable compliance and moving right to higher tunable damping; the goal being to achieve the adaptive dynamics represented by biological muscles. Improving the muscle-like tuning of soft actuators will benefit bioinspired applications and robotics, including wearable haptics in gaming, health, virtual reality, prosthetics, and humanoid robots.

Morphological Computation: Biological muscles reduce the computational burden of the control system (brain) by using the adaptive dynamic response of the muscles themselves when external perturbations occur in an uncontrolled environment [242, 263–265]. This property has been defined as morphological computation and is an inherent property of biological muscles that simplifies control.

One of the fundamental control problems of rapid locomotion in conventional walking or running robots is that feedback control loops are too slow to adjust the system when quick perturbations occur. As morphological computation sidesteps this shortcoming, conventional actuators implemented this property by adding elastic elements. This addition contributed to exploiting interaction with the environment for rapid passive adaptive dynamics [263–265]. The morphological computation in these cases was the result of the complex interplay among agent morphology, material properties (in particular the added springs), control (amplitude, frequency), and environment (friction, shape of the ground, gravity).

To develop robotic technologies that can share the rapid adaptability benefits of biological muscles, morphological computation becomes another important property in novel

artificial muscle technologies. The main advantage is that complicated control architectures can be simplified using highly tunable element actuators (soft actuators), and interactions with objects or the environment derive from the passive tunability of the agent itself. Furthermore, to feature morphological computation in soft robotics, the soft actuation technologies must be purposely designed to meet specific requirements such as mechanical properties, morphological design, high integration of components (sensors and actuators), which push soft robotics technologies forward [369].

Morphological computation and tunability of soft or flexible materials has been used in robots to simplify control tasks that involve adapting to unstructured environments [85, 123, 133, 180, 331, 374]. An octopus-like robot capable of mimicking the real octopus arm behavior is one example of morphological computation in soft robotics [51, 69, 181]. These robots use a system of contractile shape memory alloy springs and motor-driven tendons that are capable of adaptation. The soft nature of the robot allows the arms to change their mechanical properties and exert forces on the environment. The soft octopus-like arm has been shown to implement motor control primitives (such as the ones found in the real octopus), which, together with the geometrical shape of the arm, demonstrated the possibility to perform effective and energetically efficient movements with a low computational burden.

Another example of morphological computation by soft robots involves soft lithographic microactuators. The microactuators combine conducting polymers to provide the actuation with spatially designed structures for a morphologically controlled, user-defined actuation. Soft lithography was employed to pattern and fabricate polydimethylsiloxane layers with a geometrical pattern for use as a construction element in the microactuators. These microactuators achieve multiple bending motions from a single fabrication process, depending on the morphological pattern defined in the final step [331].

This soft robot application shows how morphological computation can be used with soft actuators. Here, the mechanical properties of the materials and geometrical design are used to passively tune compliance and damping to simplify the system control behavior. Although morphological computation has been primarily investigated in soft continuum actuators using spring-shape memory alloys and soft lithography microactuators, there is no reason to think that similar spring-shape soft actuators presented in Section 2.2, such as CNTs, TPAs, and Cavatappi, or soft continuum actuators such as FEA, HASELs, and FOAMS could not feature morphological computation.

Muscle Synergy, Variable Recruitment, and Scalability: Pattern generators in the spinal cord can activate specific muscle groups synergistically to achieve desired movements and reduce control dimensionality [32, 63, 102, 190, 306, 320]. The concept of synergy has been successfully implemented in conventional robotic control models [14, 15, 155, 316]. These new control methods improve control of robots with high degrees of freedom. Although these control strategies require complex algorithms and computational cost, they are based on neural-engineering principles and show promise for use in soft robots. Artificial muscles share many biological muscle properties such as adaptive dynamic response, morphological computation, and element tunability, which will be advantageous when using muscle synergy-based control models. To perform variable recruitment, soft actuators require the capacity for fabrication at small scales (scalability), like biological muscles, allowing parallel arrangements.

CNTs, TPAs, thin McKibbens, FOAMS, cavatappi, and HASELs can be fabricated and maintain their performance metrics over a range of scales, and like muscle fibers, can be arranged in series and/or parallel [8, 128, 140, 167]. Series arrangements amplify strain and strain rate, whereas parallel arrangements increase contractile forces and allow for variable recruitment. Several design features of soft actuators can interfere with or prevent deployment in parallel arrangements, including large volumetric changes during

actuation (PPAMs) [79] or heat transfer in TPAs that requires isolation or wide spacing between actuators [170].

Variable recruitment has been studied extensively on McKibbens [46, 56, 81, 158, 171, 214, 215, 278]. As an attempt to mimic the selective recruitment of motor units in a human muscle, a variable recruitment control strategy was implemented using a parallel bundle of miniature McKibben actuators [81]. This bioinspired control strategy allowed muscle bundles to operate the fewest miniature McKibbes necessary to achieve the desired performance objective, improving the operating efficiency while also increasing force generation and displacement [81]. Additionally, a passive recruitment control approach using McKibben actuators was investigated [56]. This approach used a uniform applied pressure to all McKibbens while creating differential pressure responses and threshold pressures via tailored bladder elasticity parameters. They developed a model that uses elastic bladder stiffness to control an artificial muscle bundle with a single valve. This control strategy was compared to a bundle of McKibbens with both low and high threshold pressure units and a single fluidic artificial muscle of equivalent displacement and force capability. The results of this analysis indicate the efficacy of using this control method; it is advantageous in cases where a wide range of displacements and forces are necessary and can increase efficiency when the system primarily operates in a low-force regime but requires occasional bursts of high-force capability [56].

Although variable recruitment control strategies have mostly been investigated for PPAMs, there is no reason to think that other actuators that allow for parallel arrangements could implement similar variable recruitment techniques. Moreover, with PPAMs, the arrangements were voluminous, limiting the bioinspired applications at the human scale; however, this limitation could be mitigated by using other soft actuators.
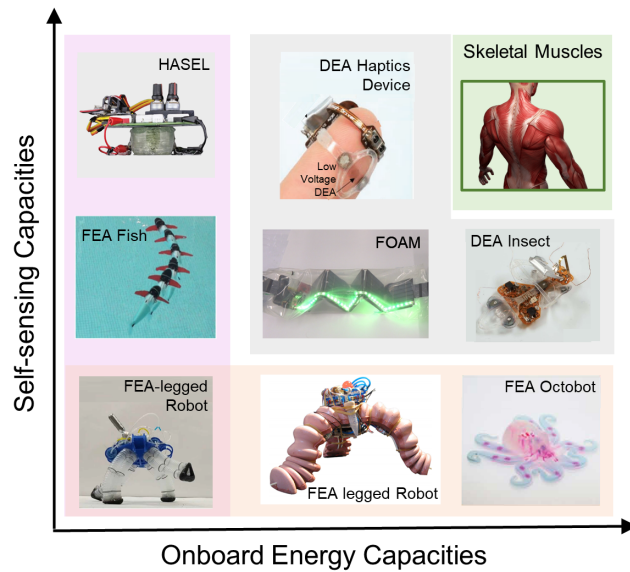
FIGURE 2.16: Progress and future directions in self-sensing versus onboard energy integration. Autonomos soft robots and actuators as a function of their level of self-sensing and onboard energy integration. (Left) A range of soft robots with levels of onboard energy integration and self-sensing capacities that increase from bottom to top [90, 210, 223]. (Middle) Soft robots that merge onboard energy and self-sensing, from left to right and top to bottom [90, 324, 345]. (Bottom) Soft robots with little or no self-sensing capacities with increasing onboard energy integration from left to right [159, 160, 189]. (Top-right-corner) High onboard energy integration and self-sensing of biological muscles and goal for soft actuators.

2.4.3 Energy Sources and Temperature Regulation

Biological muscles integrate onboard energy sources in ATP, creatine phosphate, and glycogen, allowing for short-duration actuation, but also use off-board energy sources outside the muscle for long-duration actuation. In a similar manner, when directly compared to biological muscles, artificial muscles could integrate onboard energy sources for short duration actuation. Although FEAs have onboard energy capabilities using catalyzed chemical decomposition of hydrogen peroxide [251, 345] and FOAMs can add solar panels and electronics to the skeleton [189], onboard energy has not been extensively implemented in soft actuators. In this section, we review the most promising methods

to integrate onboard energy in soft robots. In doing so, we distinguish the different actuators in terms of their energy input (activation mechanism) and focus on fluid-driven and electro-activated actuators. We also briefly review off-board energy sources of soft actuators for long-duration actuation. Finally, in this section, we also review one more energy aspect of biological muscles and soft actuators; temperature control a.k.a. thermoregulation. Temperature regulation plays an essential role in controlling soft actuators as their actuation response and performance is temperature-dependent, and temperature changes are unavoidable in unstructured environments.

Fluid-driven actuators such as FEAs, PPAMs, and Cavatappi are usually activated using external high-pressure tanks or portable pumps/compressors along with batteries [21, 23, 90, 140, 210, 271], while OV-PAMs and FOAMs require vacuum pumps for portable applications [185, 189]. In contrast, electro-activated soft actuators such as HASELs, TPAs, EAPs, and CNTs portably operate with just external batteries [223, 284]. These well investigated and widely used conventional energy sources are normally too large to be integrated into the actuator architecture. Onboarding energy in the actuator architecture would augment the degree of integration, decrease actuation time delay, and avoid cumbersome auxiliary components.

Although many chemical pressure generation methods are candidates for achieving onboard energy sourcing in fluid-driven soft actuators [9, 252], catalyzed chemical decomposition of hydrogen peroxide is the most promising method as it can quickly deploy a wide range of pressure (from 0 to 30 MPa) while keeping a high volumetric flow and specific energy density [9]. This method releases energy through exothermic chemical reactions in the presence of a catalyst. The decomposition of hydrogen peroxide produces an increase in pressure in the actuator, which allows for powering portable mobile soft robots [120, 172, 251, 345]. Stretchable microsupercapacitors have been used as onboard energy sources in electro-activated soft actuators. These are promising candidates due to high

power density, miniaturization, and feasibility of embedding in the actuator architecture [255]. Fig. 2.16 shows the progress of self-sensing versus onboard energy integration in the field of self-contained soft actuation. Here, the left column shows soft robots with low onboard energy integration and the bottom soft robots with low self-sensing capabilities. Self-sensing and onboard energy increases when moving toward the top-right corner of the graph.

Finally, developing soft actuators that can perform homeostasis similar to biological systems is crucial to improving functionality and efficiency in unstructured environments [208]. One key factor is thermoregulation. Generally, most soft materials (polymers) used for soft actuators are temperature sensitive, leading to changes in properties, performance, and time-variant dynamics which could reduce feedback control performance. Although changes in the actuation response due to temperature could be modeled, these models would be complex, resulting in cumbersome control strategies. A thermoregulation technique has been proposed using passive perspiration in 3D-printed hydrogel actuators [222]. The chemomechanical response of the hydrogel materials used for fabrication was such that, at temperatures below 30°C, the pores were sufficiently closed to allow for pressurization and actuation. In contrast, at temperatures above 30°C, the pores dilated to enable localized perspiration in the hydraulic actuator. These sweating actuators exhibit a 600% enhancement in cooling rate (i.e. 39.1°C/min) over similar non-sweating devices. Combining multiple finger actuators into a single device yielded soft robotic grippers capable of mechanically and thermally manipulating various heated objects. The measured thermoregulatory performance of these sweating actuators ($\sim$107 W/kg) dramatically exceeded the evaporative cooling capacity found in the best animal systems ($\sim$35 W/kg) at the cost of a temporary decrease in actuation efficiency. In general, minimal research has been conducted on temperature control of soft actuators (except for thermally activated actuators), and further research will be needed to inform

70

whether automatic perspiration mechanisms can be successfully used in other soft actuators. Similar to biological muscles, new materials used in soft actuators should have the capacity to sense and regulate their temperature.

2.4.4 Length and velocity dependence

From an actuation perspective, length- and velocity- dependence of biological muscles is considered as a limiting factor, as important metrics like stress, specific power, work, and efficiency vary with muscle length and velocity. [7, 18, 142]. Conventional actuators such as electric motors can deploy a constant maximum torque and/or stress during actuation independently of their joint angle or position, and are still capable of maintaining useful stress and power as a function of velocity [4, 96]. Similar to biological muscles, the force of soft actuators usually depends on length and velocity [8, 127, 140, 189]. There are some exceptions, such as OV-PAMs, which can hold constant force/torque independently of length [185].

2.5 Conclusions

Soft actuators and robots have been an important focus of study in the last decades to improve HMI, for example in individuals with gait disorders, limited mobility, amputated limbs, or even augmented performance. In this review, we developed an understanding of progress in soft actuation technologies compared to biological muscle performance, properties, and control. In doing so, we review advances in understanding of biological muscle properties that contribute to their high adaptability and compare them with some of the newest soft actuation technologies. The reviewed soft actuators with compliances ranging from ∼0.1 to 10 MPa^{-1} that perform contractile or bending actuation are the focus of our study as these are the most common actuation motions found in biological muscles. For

TABLE 2.2: Qualitative evaluation and comparison of muscle and soft actuator properties using Harvey balls. The red border in Harvey balls indicates that those properties have been initially implemented in control strategies. (Note that conventional actuators are excluded as they are not the focus of this comparison).

Muscle Properties	EAP	CNT	TPA	PPAM	FEA	FOAM	OV-PAM	Cavatappi	HASEL	Skeletal Muscles
Onboard Energy	—	—	—	—	●	◑	—	—	—	●
Temperature Control	—	—	●	—	◑	—	—	—	—	●
Self Sensing	●	●	●	●	●	◑	—	—	●	●
Tunable Compliance	◑	◕	●	◕	●	—	—	●	—	●
Tunable Damping	◕	—	◐	—	◕	—	—	◐	—	●
Morphological Computation	—	—	◕	—	◕	—	—	◕	—	●
Length/Vel. Force Dependence	◔	◔	◔	◔	—	○	●	◔	◔	◔
Variable Recruitment	◐	◔	◔	◔	—	●	◕	●	●	●

example, skeletal muscles develop contractile actuation while octopus tentacles develop bending actuation. Our comparative study shows that most soft actuators have performance metrics that are similar to those of biological muscles. Most soft actuators have tunable material properties (compliance and damping), integrate sensors in their architecture, and potentially feature variable recruitment. However, some muscle properties are still lacking in soft actuators. Remaining challenges include implementing morphological computation and muscle synergy in control strategies, as well as integrating onboard energy and thermoregulation in the actuator architecture.

Many previous reviews have focused on comparing the performance metrics of soft actuators and biological muscles [150, 195, 203, 220]. These works have shown that the current soft actuators' metrics differ from one technology to another, but, in general, are similar to those of biological muscles. The performance comparison in these works have also been used for selecting soft actuators for applications, where the goal is to find the actuator with the metrics that best fit a particular application. However, as shown here, metrics

(such as those in Table 2.1) are not the only requirements for soft actuators to mimic biological muscles. To perform safe HMI, soft actuators should also focus on featuring other muscle intrinsic properties (such as those in Table 2.2) that are fundamental for fast adaptation under external perturbations and robust control of the actuation system. Some of these properties are adaptive dynamic response, self-sensing, morphological computation, scalability, variable recruitment, onboard energy, and thermoregulation (Table 2.2) [87, 144, 206, 242, 243]. Furthermore, while some actuation technologies may have the capacity for a particular property (e.g. tunable compliance), not all technologies have yet exploited that property through their control strategies. Developing successful control strategies that can optimize actuation while integrating all the exclusive properties of soft actuators is a key factor for implementation, and the reason why this should be a large focus of future research. Those soft actuators that can better match biological muscle properties are closer to what should be considered a suitable candidate for muscle substitute or "artificial muscle".

Soft actuators and robots have been used in a wide variety of applications, only some of which would benefit from muscle-like actuation. Yet, the terms biomimetic actuators and artificial muscles have been extensively used in the soft robotics literature. Considering only applications for which a muscle-like response is desirable, particularly for many HMI and wearable applications, it is useful to clarify the meaning of these terms. On one hand, it seems that biomimetic actuators should feature metrics or properties that are intentionally designed to resemble biological muscles. On the other hand, it seems that artificial muscles could go one step beyond in terms of muscle mimicry by featuring some properties of biological muscles (e.g., tunable compliance) that simplify control and enhance adaptability. Artificial muscles should achieve specific metrics (Table 2.1) and properties (Table 2.2) that enable them to perform well as muscle substitutes. Artificial muscles have been previously defined as "open-loop stable systems that follow the

Hill force-velocity curve" [325]. Once again, in addition to their muscle-like actuation response, we reiterate that artificial muscles should focus on including those properties of biological muscles that simplify control strategies and improve adaptability. However, although Hill models successfully predict force in biological muscles under constant length (isometric) or constant load (isotonic) conditions, the force predictions typically have low accuracy at predicting muscle force during in vivo movements [86, 182]; thus, using the Hill force-velocity relationship as a criterion for artificial muscles might be misguided. Other features, such as adaptive dynamics, which is a crucial property of biological muscles [243] might be a better criterion for artificial muscles. This review identified several soft actuators that have the potential to sidestep most shortcomings of the current technologies and even outperform biological muscles (Tables 2.1 and 2.2, Fig. 2.3). We propose that these hypothetical "artificial supermuscles" would inherently feature the properties of biological muscles (Table 2.2) while also outperforming their metrics (Table 2.1), and bypassing their limitations (Section 2.3.5). Artificial supermuscles could motivate more sophisticated HMI or even allow for human-machine interaction and integration (HMII, see Fig. 2.1).

The changing view of muscles as tunable materials provides new directions for investigations geared toward emulating the intrinsic properties of biological muscles.

Conventional actuators have made notable advancements in self-contained and wearable robots. Some examples are all-terrain quadrupedal robots [3, 183, 355], humanoid robots [1, 25], and modular prosthetic limbs [267]. However, as the scale of these autonomous robots decreases, conventional actuators cannot be implemented, and highly integrated soft actuators are needed. A high degree of onboard energy sourcing, sensing, and integration in actuator architecture is crucial for simplifying mobile bio-inspired robots. Self-contained robots must be capable of carrying themselves (energy source, body/frame,

74

control system, manipulators, and drivetrain) while still achieving high performance metrics (Section 2.4.1). We suggest that specific performance metrics, such as those in Table 2.1, should include the weight of onboard energy sources and sensors, not just the weight of the actuator for fair comparison with muscles [50, 144].

Control of soft actuators, in particular, could benefit from emulating control of biological muscles, including self-sensing, adaptive dynamic response, morphological computation, and variable recruitment. These properties simplify control compared to conventional robotic systems [17, 82, 125, 337, 361]. However, some concerns remain regarding how to properly design feedback controllers without altering the natural compliance of the robot [286], and how to excite the robot's natural dynamics efficiently [124]. In addition, soft actuators' tunable compliance and damping should be characterized, modeled, and integrated into control strategies for applications. As most soft actuators are viscoelastic, predictive models will require characterizing the viscoelastic behavior of the soft materials, which is more complicated than for elastic materials. Neuro-inspired control models for soft robots appear to be ideal for integrating adaptive dynamics in control strategies, as initial efforts have already been successfully implemented in conventional [52, 60–62, 113] and soft actuators [27, 118, 275, 299, 307] and machine learning techniques have been used to continuously improve control [130, 162, 312].

In conclusion, future work in the field of soft robotics should focus not only on designing novel actuator technologies with specific performance metrics, but also on developing and deploying inherent properties of biological muscles such as adaptive dynamics. Only then can these actuators be successfully used as substitutes for biological muscles.

CHAPTER 3

MOISTURES SIGNIFICANT IMPACT ON TWISTED POLYMER ACTUATION

It was recently shown that inexpensive drawn polymer monofilaments, such as nylon fishing line, can be used to create thermally driven actuators. These actuators are called Twisted Polymer Actuators (TPAs). TPAs can produce linear actuation when they are both twisted and coiled. In this configuration, these actuators are called Twisted Coiled Polymer Actuators (TCPAs). These same drawn polymers can be used to create torsional actuation when the precursor monofilament is twisted but still remains straight, known as Straight Twisted Polymer Actuators (STPAs), which is also thought to be the elemental unit of TCPAs. The torsional thermal actuation of STPAs is primarily a result of the anisotropic thermal properties of the virgin material (axial thermal contraction and radial thermal expansion), which manifests as linear actuation in the coiled configuration (TCPA). This paper presents two moisture related matters: moisture content impact on the thermal actuation of TPAs and the capability of TPAs to actuate as a function of moisture absorption at room temperature. For the former, we first present moisture dependencies of the axial thermal contraction and axial modulus of the precursor (straight, untwisted) monofilament. This study is conducted because closed-form and finite element models often use the physical properties of the precursor monofilament as inputs to predict the thermal actuation of twisted polymer actuators. The results show that, both, axial thermal contraction and axial modulus, are strongly dependent on moisture content. Second, we present the experimental thermal actuation for STPAs and TCPAs at different moisture content percentages. We present torsional actuation responses for three different pitch angles STPAs (36, 25, and 15°) at two percentages added moisture by weight (0 and 4%). Similarly, we study the linear thermal actuation of TCPAs under

76

an isotonic tensile load at the above moisture percentages. The results show an increase in actuation for those samples at 4% moisture content of approximately 100% for STPAs at 75°C and a 50% for TCPAs samples at 100°C. Finally, we report for the first time, that twisted polymer actuators can be hygroscopically actuated. Here, we present torsional actuation responses under free torsion conditions for a 36° pitch angle STPA as well as axial contraction of a TCPA under an isotonic tensile load as a function of moisture absorption and show that moisture absorption can cause a similar actuation responses as seen when a thermal load is applied. Like the thermal actuation, we expect this hygroscopic actuation of TPAs is produced by a combination between the swelling that occurs on the precursor monofilament during moisture absorption and its anisotropic nature.

3.1 Introduction

Twisted polymer actuators (TPAs) are inexpensive drawn polymer monofilaments, such as fishing line, that can linearly actuate when they are configured under a coiled shape as a result of over-twisting the straight monofilament around its central axis [128]. These coil-shape actuators are known as Twisted Coiled Polymer Actuators (TCPAs) [296, 315], a.k.a. artificial muscles due to their potential to be implemented as such. However, these same twisted monofilaments can generate torsional actuation when they are set under a twisted configuration, but remain straight; these torsional actuators are known as Straight Twisted Polymer Actuators (STPAs) [28, 295]. The thermally driven actuation mechanism in STPAs is believed to be a result of the untwist that occurs about the monofilament's axis driven by the anisotropic thermal properties of the precursor monofilament—an untwisted monofilament with axially aligned internal fibers—which present axial thermal contraction and radial thermal expansion. In turn, the same untwist generated in the STPAs is responsible for the actuation in TCPAs, which manifests as a contraction of the helical configuration [28, 127, 296, 315].

77

In order to control and predict the linear and torsional actuation responses, many researchers are putting their effort on modeling these novel actuators. Some TPA models are based on the twisted or coiled monofilament properties (e.g. [165, 179, 191, 319, 366]), but such models do not allow for design of the initial twist. Other works use the properties of the precursor monofilament to predict the actuation response of STPAs and TCPAs. Shafer et al. [296] and Aziz et al. [28] developed models to predict the STPA actuation using the precursor monofilament's properties as inputs. Furthermore, Sharafi and Li [297] and Yang and Li [356] have published a multi-scale models that predict TCPA actuation using the fundamentals of the STPAs structure and in turn, can predict STPA/TCPA actuation behavior using the precursor monofilament's properties. The above models that use the precursor monofilament's properties allow for the design of the initial twist of the actuator and potentially the design or selection of properties which improve performance.

To accurately predict the thermal actuation response of TPAs using precursor properties, a full characterization of the precursor material is required. The properties of these precursor monofilaments have been investigated by Higueras-Ruiz under the linear elastic assumptions [136] and Swartz under the linear viscoelastic assumption [314]. The works presented by Higueras-Ruiz and Swartz used a preparation protocol that consists of storing the tested samples in desiccant for a total of three days and thermally precycling at 110°C for 30 minute before testing. This preparation protocol was done to keep all the tested samples under the same initial conditions and it was followed to obtain consistent mechanical/thermal property results. This protocol was followed because polymers are hygroscopic materials and they present significant dependencies of their mechanical and thermal properties as a function of moisture [19, 100, 253, 359, 375]. Pai et al. showed that nylon 6,6 could absorbed a maximum moisture content of 7.77% at a temperature of

10°C after 65 days, leading to a drop of mechanical properties (tensile strength and modulus) and heat resistance (softening temperature) [253]. In addition, they also showed that increases in temperature increases the moisture absorption behavior. This reported hygro-thermal behavior of nylon led us to realize that TPA's actuation could be affected by water and moisture, since they are thermally driven by: free convection using an oven [28, 127, 193], force convection using hot/cold air (heat gun) [225, 295, 315] or hot/cold water (water jet) [127, 128], and conduction by using conducting thread of nylon 6,6 or covering with conductive silver paint [221, 353, 360]. Some of these activation methods can lead to high rates of moisture absorption on the TPA's material, which in turn means a change in the actuation response due to the great changes that moisture content produces on mechanical and thermal properties of the precursor monofilament. Furthermore, the moisture absorption rate does not only depend on the heating method, but also on the relative humidity (%RH) of the environment where TPAs operate. Thus, the same TPA will develop a different actuation response in an arid environment, such as Arizona, than a humid environment, such as Florida.

This moisture dependence causes the modeling of TPAs to become arduous because the model's inputs are also moisture dependent, and requires characterizing the mechanical and thermal properties of the precursor monofilament as a function of moisture content as well as the precursor monofilament hygroscopic behavior as a function of temperature and relative humidity. In addition, during thermally driven actuation cycling, the TPA's moisture levels would also change, which will lead to a higher complexity when modeling these actuators.

The previously mentioned affinity of nylon with moisture has led our team to investigate the effect of moisture content on the thermal actuation response of twisted polymers. To do so, we first studied the moisture absorption/desiccation behavior of the precursor material at room temperature in order to quantify its hygroscopic behavior. Second, we

investigated two physical properties of the straight nylon monofilament: axial thermal contraction and axial mechanical modulus as a function of moisture content to observe its dependencies. Having observed that the two previous material properties were strongly dependent on moisture content, we investigated the torsional actuation of different pitch angle STPAs (36, 25, and 15°) at two different moisture levels (0 and 4%) under an isotonic torque. The actuation response reported on these tests showed an overall increase in torsional actuation of 2× for those samples that had a moisture added percentage by weight of 4%. Similarly, we tested the axial thermal actuation of TCPAs at the two moisture levels mentioned above, as a result, we observed an increase of approximately 1.5× for those samples with a 4% moisture content after 60°C. Additionally, while studying the hygroscopic behaviour of the precursor material, we observed that the straight monofilament swelled in the radial direction during moisture absorption. This observation made us think that twisted polymer actuators could have the potential to actuate during moisture absorption. Thereupon, we have reported and discussed the ability of TPAs to generate slow actuation as a response to moisture absorption under constant temperature conditions (room temperature).

3.2 Mechanics of Actuation

3.2.1 Micro-structure of the precursor monofilament

The source of the actuation mechanism of TPAs can be explained by looking at the micro-structure of the drawn polymer monofilaments used for fabrication. In this work, we used the Berkely Trilene® Big Game™ 80 lb precursor monofilament (0.89 mm diameter) for STPAs and 15 lb (0.38 mm diameter) for TCPAs fabrication. This material is the same product used by Shafer et al. [296] and Haines et al. [128] to fabricate TPAs. The micro-structure of precursor drawn monofilaments provides the fundamentals to understand

the different actuation mechanisms of twisted polymer actuators. Fig. 3.1 shows how the anisotropic behavior of the precursor monofilament is related to the micro-structure of the material. Choy et al. [68], Prevorsek et al. [268], Elad and Schultz [98], and Bukosek and Prevorsek [47] all published very similar models for the micro-structure of drawn polymer monofilaments. All these models conclude with a micro-structure that consists of three main domains of different properties: crystalline regions (a.k.a. crystallites) aligned with the draw direction, amorphous regions between crystallites (together amorphous and the crystallites are thought to form micro-fibrils), and bridges and/or inter-fibril tie molecules (a.k.a. internal fibers). The interfibrillar tie chain molecules are aligned with the draw direction, located between the micro-fibrillar regions, and have the role to connect adjacent micro-fibrils as shown in Fig. 3.1. The interfibrillar tie chain molecules provide the micro-structure of high strength and stiffness in the axial/drawn direction while the physical properties in the direction perpendicular to the drawn direction (radial direction) lack of such strength, resulting of a highly anisotropic material [261]. Furthermore, it is known that the oriented deformation from drawing leads to an increase in the number of formed tie molecules and in turn the anisotropic behavior of the polymer [268] and actuation of twisted polymer actuators (as it will be seen in Section 3.2.2 and 3.2.3).

3.2.2   Principle of thermal actuation

The thermal actuation phenomenon in TPAs is also a result of the anisotropic nature of the precursor monofilament. Specifically, the thermal actuation mechanism is thought to be caused by the thermal expansion in the direction perpendicular to the internal fibers (i.e. radial direction) and the thermal contraction along the internal fibers (i.e. axial direction). The asymmetric micro-structure shown in Fig. 3.1 was used by Bruno et al. [45] to explain the anisotropic thermal properties of drawn polymers. Specifically,
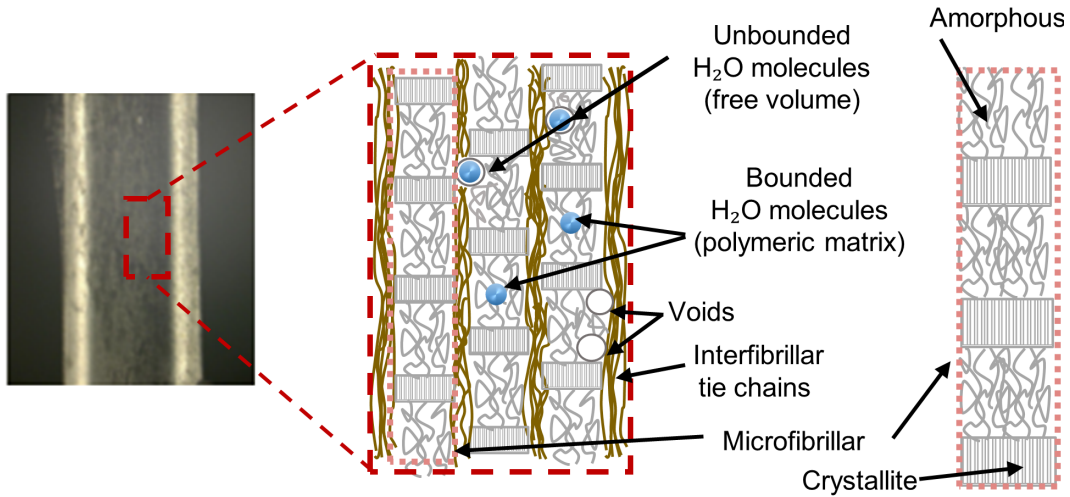
FIGURE 3.1: Prevorsek et al. micro-structure model for drawn polymers along with moisture absorption mechanisms.

they attribute the negative thermal expansion in the drawn direction (axial direction) to the tension produced by excited atomic vibrations in the interfibrillar molecules that are caused by thermal loads. Simultaneously, this effect contributes to the expansion perpendicular to the microfibrillar region because the connections between micro-fibrillar and interfibrillar are weaker in this direction. Thus, as shown in Fig. 3.2, the untwisted monofilaments expand radially and contract axially when heated. For a twisted monofilament with a helical orientation of its internal fibers, this negative thermal expansion is maintained along the now helically aligned internal fibers. So too is the positive thermal expansion perpendicular to the internal fiber direction. Thus, the new twisted orientation of the internal fibers causes shear deformation of the STPA when a thermal stimulus is applied. This shear deformation manifests as axial contraction of the coiled configuration (TCPA), where the untwist of the STPA generates a change in pitch on the TCPA due to its coiled geometry.

3.2.3   Principle of hygroscopic actuation and moisture absorption

To understand the hygroscopic actuation principle, we look at the moisture absorption mechanisms and the swelling effects that it has on the micro-structure of precursor monofilaments. Fig. 3.1 shows the two main moisture absorption mechanisms in polymers: the Fickian diffusion and relaxation processes. During Fickian diffusion the water molecules (blue circles in Fig. 3.1) move randomly and occupy the voids (moisture stays in free-volumes) leading to a null contribution to hygroscopic swelling [101]. During the relaxation process, the polar water molecules interact with the polymer network and form hydrogen bonds that are responsible for hygroscopic swelling [101, 280]. These bounded molecules of water in the polymeric matrix and the anisotropic mechanical properties (explained in Section 3.2.1) cause the precursor monofilament to expand more in the radial direction than the axial. Fig. 3.2 shows this anisotropic response for an untwisted monofilament (precursor monofilament). The new helically orientation of the internal fibers for a STPA translates the high radial and low axial expansion of the precursor monofilament into shear deformation. Finally, the same asymmetric dimensional growth that generates the shear deformation in STPAs is the responsible of the axial contraction (or change in pitch) of the twisted coiled configuration (TCPAs) as a result of its new coiled configuration. Additionally, this hygroscopic actuation is enhanced by the magnitude reduction of the mechanical properties of the precursor monofilament as a result of the plastification process that occurs in the material during moisture absorption. This leads to lower the internal-stresses in the material and facilitate the motion between the the internal layers of the material. More specifically, plasticization is a micro-structural process that occurs when the Van Der Waals bonds between polymer chains are interfered by water molecules in the free-volume. These interruptions increase the distance between polymer molecules which leads to a lowering of the interfacial strength of the polymer chains causing the polymer molecules to move more freely [350, 375]. Thus, we believe

Hygroscopic Actuation   Thermal Actuation

Bounded H_2O molecules cause high radial and low axial expansion by swelling

ΔM (%)

Untwisted Monofilament

ΔT

Heated drawn polymer monofilament expands radially and contract axially

Twist under tensile load. Thermally anneal

Bounded H_2O molecules cause untwist due to the new twisted fiber orientation

ΔM (%)

Straight-twisted polymer actuator (STPA)

ΔT

Torsion   Torsion

High stiffness internal fibers helically orientated cause shear deformation

Twist under tensile load until coiled to helix. Thermally anneal

Torsional response of STPA translates to contraction of TCPA due to the swelling in the material

ΔM (%)

Contraction

Twisted-coiled Polymer Actuator (TCPA)

ΔT

Contraction

The thermal torsional response of STPA translates to contraction of TCPA

FIGURE 3.2: Thermal and hygroscopic actuation mechanisms of STPAs and TCPAs.

the relaxation process resulting from moisture absorption is responsible for the swelling and, as a result, TPA hygroscopic actuation.

Finally, it is important to mention that hygroscopic and thermal actuation share the same actuation principle as seen in Fig. 3.2. Both amplify the anisotropy of the material through twisting and coiling. With both thermal and hygroscopic actuation, the change in volume (mostly radial growth) creates torsional (STPA) or linear (TCPA) actuation because of the geometry of the actuator.

3.3 Moisture absorption and desiccation behaviour

In this section, we present the method used to obtain the experimental moisture absorption and desiccation behavior of the precursor monofilament, experimental results, and discussion.

3.3.1 Experimental Set-up: Moisture absorption and desiccation behaviour

With the goal of obtaining the moisture absorption and desiccation characterization of the precursor monofilament used for the fabrication of TPAs, we began using a spool of precursor monofilament material that was previously annealed at 120°C for 20 minutes, to be consistent with the annealing process used in previous works [136, 295, 314, 315], and placed it on a bed of silica desiccant for several days. At this point, it is assumed that moisture content of the specimen is approximately zero. After annealing and desiccating, the spool was set in a 100% relative humidity (RH) controlled environment and kept at a constant temperature of 25°C, while measuring the mass every ten minutes (Fig. 3.3, Phase 1). To measure the mass, a Sartorius ENTRIS822i-1S precision balance with a resolution of 0.001 grams was used. The balance was combined with a desktop machine running a MATLAB script, taking measurements every ten minutes. After about five days, the rate of change of the sample's mass slowed significantly (see Fig. 3.4) and it was assumed that the sample was nearly fully saturated with moisture. Then, the spool of precursor material was set in a new dried controlled environment at a constant temperature of 25°C with silica desiccant to remove the moisture from the air and sample (Fig. 3.3, Phase 2). After five days the mass of the sample was changing very slowly and the trend did not show evidence that the material would recover to the initial mass (orange solid line in Fig. 3.4). In order to totally desiccate the sample and reach the initial mass, the temperature was raised to 70°C to enhance the moisture desiccation of

85
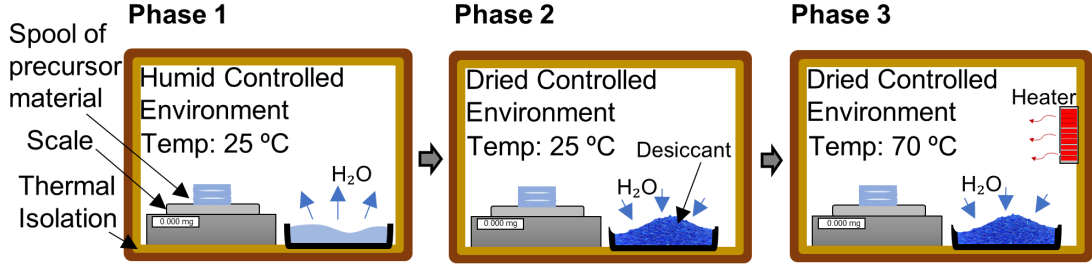
FIGURE 3.3: Experimental set-up for moisture absorption/desiccation. Moisture absorption at 25°C (Phase 1), desiccation at 25°C (Phase 2), and desiccation at 70°C (Phase 3).

the sample (Fig. 3.3, Phase 3). The sample's mass then returned to the initial mass of the dried sample after 10 hours, showing full recovery.

3.3.2   Results and Discussion: Moisture absorption and desiccation behaviour

In order to quantify the moisture absorption and desiccation behavior of the precursor material used in this work, we have characterized such behavior as a function of time. During the first five and a half days, a logarithmic moisture absorption rate of the precursor monofilament at room temperature is exhibited (Fig. 3.4). Here, fast moisture absorption takes place during the first day, in fact, the precursor monofilament exhibits strong hygroscopicity during the first hours when it is exposed to a humid environment, reaching 2.4% moisture content during the first ten hours of exposure (Fig. 3.4). This behavior is followed by

$$M(t) = 2.983 \ \ (1 - e^{-0.173t}) \qquad 0 \leq t < 10 \qquad (3.1)$$

where t is the time in hours and M is given in %.

After the first ten hours (fast absorption behavior), the moisture absorption rate slows down (relax) and the monofilament is relatively saturated with a moisture content of approximately 6.20% after five days. Such behavior is followed by

86

$$M(t) = 6.514 - 5.160e^{-0.024t} \qquad 10 \leq t \leq 130 \qquad (3.2)$$

where t is the time in hours and M is given in %.

Once the sample is saturated with moisture, it is set in a dry environment. Similarly, an exponential decrease is observed with a quick moisture desiccation during the first day and a tendency to reach an asymptote after five days. However, Fig. 3.4 shows that this desiccation process lacks reversibility at room temperature; the moisture content has a tendency to become constant at approximately 1.4% during desiccation. In order to reach the initial state of the precursor monofilament (M = 0%), the sample is set to a constant temperature of 70°C for ten hours. During this desiccation process, the sample exponentially dries and approaches the initial state after 10 hours. This last step in the desiccating process allows us to observe a strong temperature dependence of the moisture desiccation behavior of the precursor monofilament. For example, if using a TPA in a humid environment, the heat used to actuate the TPA is likely to also increase the moisture, while the converse is likely to occur in an arid environment, leading to less predictability in the response of the TPA. Moreover, these results suggest that desiccation procedure used by Swartz [315] may not have led to samples in the fully desiccated state. However, assuming that the temperature remained constant during desiccation, then the samples in this works all should have had a similar moisture content at the end of the so-called "desiccation" procedure.

Since TPAs are thermally driven actuators, these indications lead us to think that the temperature dependencies of moisture absorption and desiccation of polymers might have an impact on TPAs actuation.
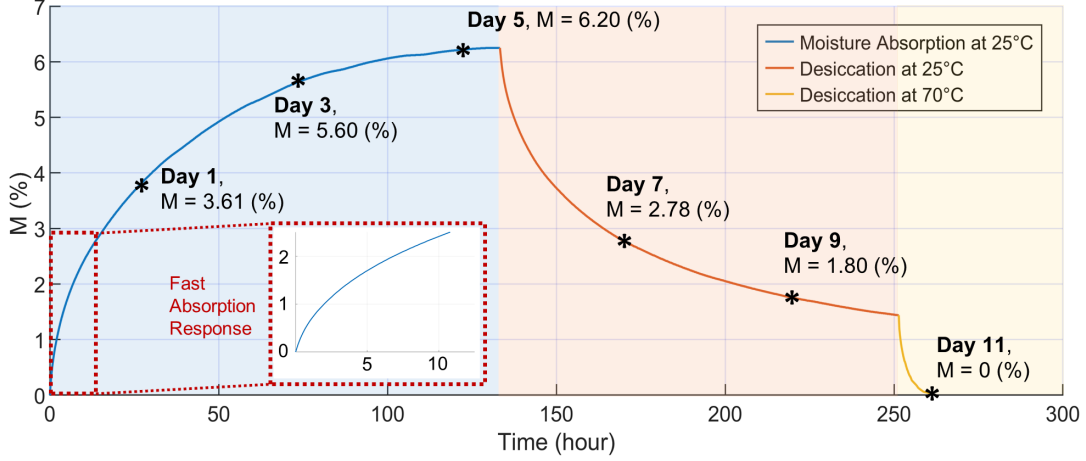
FIGURE 3.4: Moisture absorption behavior of a precursor monofilament at room temperature, followed by the desiccation behavior process of the precursor monofilament at room temperature and 70°C.

3.4 Moisture Effects on Thermal Actuation

3.4.1 Axial thermal contraction and elastic modulus

In this section, we present the experimental set-ups used to obtain axial thermal contraction, ε_{11}^T, and axial elastic modulus, E_1, data as well as the results and discussion of moisture content effects on such properties.

3.4.1.1 Experimental Set-up: Axial thermal contraction and elastic modulus

The axial thermal contraction, ε_{11}^T, of the precursor monofilament was measured using three systems: the Polytec OFV-5000 Vibrometer controller with the OFV 534 optics head to measure displacement, the FLIR A300-Series thermal camera with an IR 10 mm focal lens to measure temperature, and the Sparkfun Electronics 303 D heat gun to manually control changes in temperature, similar to other works [315]. Fig. 3.5(a) shows a 1.5 cm long sample vertically clamped by the top end to a fixed point and hanging freely at the bottom end with an approximately 1 gram mass to ensure that the sample

stays straight. The mechanical strain produced by the 1 gram mass was calculated to be approximately two orders of magnitude less than the axial thermal contraction and therefore considered negligible. The sample was manually heated using the Sparkfun Electronics303D heat gun with an attached 30 cm long insulated copper tube. To ensure a consistent temperature over time and space the tube was preheated for 20 minutes before running the test. A screen inserted inside the copper tube created a turbulent flow and thus a more uniform temperature profile. Aerodynamic forces resulting from the application of this hot air were calculated to be almost null (four orders of magnitude less than the axial load created by the hanging mass). The vibrometer was warmed up for 30 minutes to eliminate any drift effects on the displacement data. The thermal camera was placed perpendicular to the sample and out of the flow stream of the heat gun to avoid damage. The vibrometer was positioned directly below the sample with the laser reflecting off the bottom of the attached mass at the end of the sample. Here, the thermal camera was used to measure temperature, the vibrometer to measure axial displacement, and the heat gun to control the temperature input. For this test, the sample preparation consisted of three precursor monofilaments with different moisture concentrations of 0%, 3.61%, and 6.01%. The samples were initially stored in desiccant and annealed at 120°C for 20 minutes (same preparation protocol used by others [295, 315]). Then, they were stored in a 100% RH environment for several days until they reached the prescribed moisture content (0 days for 0%, 1 day for 3.61%, and 4 days for 6.01% based on mass). In order to calculate the heating rate, we did a thermal analysis by using the lumped capacitance method (after validating the Biot number). In this analysis, we obtained that, based on our experimental set-up and testing material, the heating rate required for the heat to be transferred from the hot air to the core of the monofilament is 10°C/s. In all our experimental set-ups where changes in temperature were involved, we set a heating rate of approximately 3.75°C/s to ensure that the heat transfer homogeneously occurs and that the actuation response is correctly recorded as a function of temperature.
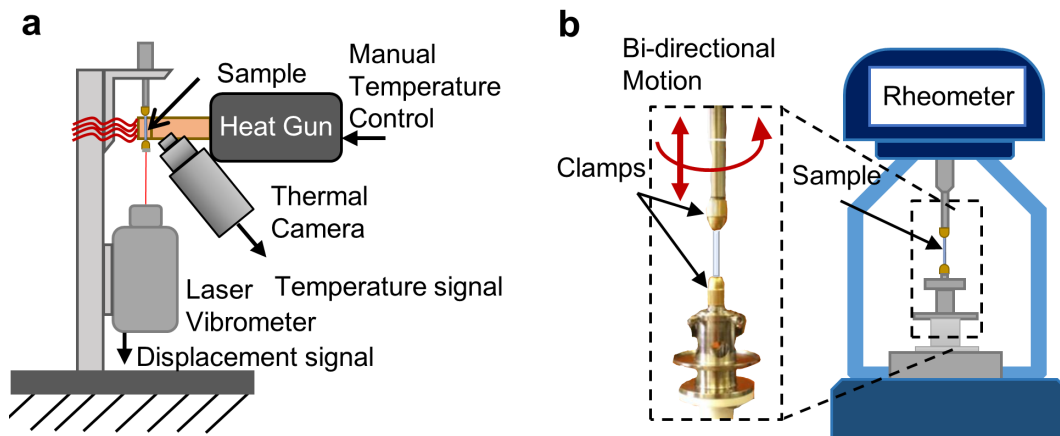
FIGURE 3.5: Axial thermal contraction and axial modulus experimental set-ups. (a) Experimental set-up for axial thermal contraction of a precursor monofilament; (b) Experimental set-up for the axial modulus of a precursor monofilament.

To obtain the elastic axial modulus, a TA Instruments Hybrid Discovery Rheometer 2 (HR-2) along with a torsional accessory were used to obtain stress-strain curves for three precursor monofilaments with different moisture content (see Fig. 3.5(b)). For each specimen, a total of five mechanical cycles (tension and compression) were conducted using a script in the TA instrument software to ensure convergence and avoid first cycle effects. The last converged cycle was used to calculate the axial modulus, E_1. Similarly to the axial thermal contraction test, samples with 0%, 3.61%, and 6.01% moisture content were prepared and tested. Every sample was fixed at the bottom end and clamped from the top end to a torsional collet, which in turn was attached to the HR-2 head. The HR-2 head applied a controlled change in axial strain of approximately 1% (this strain was found to not induce permanent deformation in the material), with a strain rate of 0.075%/s (this strain rate was found to induce minimal viscoelastic effects on the material) while measuring the mechanical stress on the sample. This test was conducted in an uncontrolled humidity environment. Therefore, the entire test was run in only two and a half minutes, limiting the amount of time that the sample was exposed to an uncontrolled environment.

90
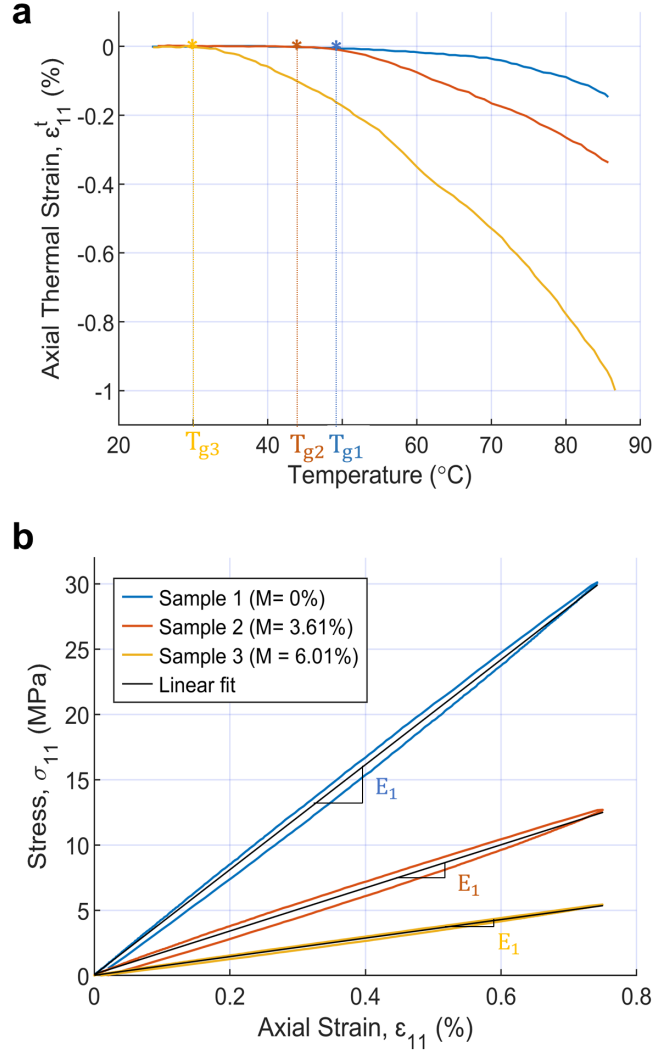
FIGURE 3.6: Axial thermal contraction and axial modulus for three samples at 0, 3.61, and 6.01 % moisture content. (a) Axial thermal contraction; (b) Axial modulus. The legend for both is in (b).

In this section, we present the axial thermal contraction and stress-strain curves of the precursor monofilament for the following moisture absorption concentrations: 0%, 3.61%, and 6.01%. Here, three thermal cycles were conducted where the first cycle behaved differently than the following two cycles which showed convergence. This "first cycle effect" matches that seen in the literature [192, 295]. The last converged cycle is used to plot axial thermal contraction, ε_{11}^T, over temperature (Fig. 3.6(a)). Fig. 3.6(a) shows a strong dependence of the axial thermal contraction, ε_{11}^T, as a function of moisture content.

Comparing sample 1 (0% moisture content) with sample 3 (6.01% moisture content), the latter shows an increase in axial thermal contraction six times higher at 85°C.

Fig. 3.6(a) also shows a drop of the glass transition temperature, T_g, as a function of moisture content. Here, the glass transition temperature is defined at the temperature where the monofilament starts contracting. This fact is important because the precursor monofilament shows a great increase in the axial thermal contraction magnitude after the glass transition temperature. This effect suggests that TPAs with high moisture content will develop higher actuation performance, since high moisture content precursor monofilaments are shown to generate higher thermal contractions in the axial directions and in turn, a greater anisotropy of the material.

The increase of the thermal monofilament's contraction at high moisture contents is a result of the drop in the glass transition temperature that occurs with the rise in moisture content as a result of the plasticising effect that moisture absorption has on nylon [169] and the softening that happens in polymers when heated above their glass transition temperature [11]. Thus, the drop in glass transition temperature promotes the axial contraction to occur sooner for humid samples than desiccated samples (Fig. 3.6(a)) and the material softening to increase the magnitude of the axial thermal contraction.

Fig. 3.6(b) shows stress-strain curves for various moisture content precursor monofilaments at room temperature and their linear fits. Here, the linear fits have been used to calculate the axial modulus:

- $E_1 = 4$ GPa at 0% added moisture by weight

- $E_1 = 1.6$ GPa at 3.61% added moisture by weight

- $E_1 = 0.7$ GPa at 6.01% added moisture by weight
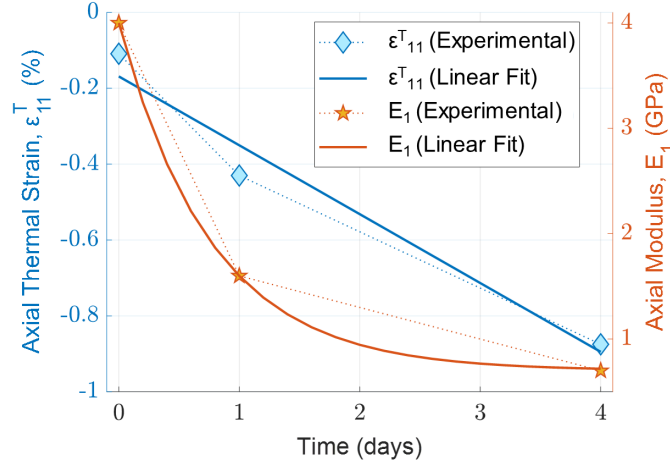
FIGURE 3.7: Predicted axial modulus at room temperature and axial thermal strain at 80°C as a function of time when set in a 100% relative humidity environment.

If we compare the axial modulus of sample 1 with the one of sample 3, we can see a drop in axial modulus of approximately six times. Higueras-Ruiz et al. reported an axial modulus of 3.8 GPa for a desiccated sample [136], similar to the 4 GPa axial modulus found in this study. Insufficient desiccation time/temperature could have led to some moisture content control error during preparation [136].

These drops in axial modulus could be explained by the plasticization effect that free water molecule diffusion can induce in polymers. Recall, plasticization is a micro-structural process that occurs when the Van Der Waals bonds between polymer chains are interfered by water molecules in the free-volume. These interruptions increase the distance between polymer molecules which leads to a lowering of the interfacial strength of the polymer chains causing the polymer molecules to move more freely [350]. As discussed for the axial thermal contraction results, the strong moisture dependence shown for the axial modulus could potentially affect the actuation responses of TPA, as well as their actuation predictions by models. In fact, high moisture content could lead to a contribution on the actuation response of TPAs because low axial modulus will reduce the internal stresses in the material.

Finally, Figs. 3.4 and 3.6 have been used to predict axial thermal contraction and axial modulus as a function of time for a dry sample placed within a 100% RH environment. Fig. 3.7 shows axial modulus at room temperature and axial thermal strain at 80°C for times equal to zero, one, and four days, which corresponds to a moisture content of 0, 3.61, and 6.01%, respectively. This shows an exponential drop of axial modulus as a function of time. This drop can be predicted using the exponential fit given by

$$E_1(t) = 0.7 + 3.3 \left(e^{-1.3t} \right) \tag{3.3}$$

where t is the time in days and E_1 is given in GPa. Fig. 3.7 also shows a decrease in axial thermal strain as a function of time. A linear fit is used to predict this decrease in axial thermal strain and it is given by

$$\varepsilon_{11}^T(t) = -(0.1816 + 0.1687t) \tag{3.4}$$

where t is the time in days and ε_{11}^T is given in %.

Both of these properties would be approximately $6\times$ higher at zero days than after four days.

3.4.2   Moisture content effects on STPAs under an isotonic torque

In this section, we present the torsional actuation response of three different pitch angle STPAs (36, 25, and 15°) at two different percentages added moisture by weight (0 and 4%) to show the moisture dependencies on STPAs thermal actuation.
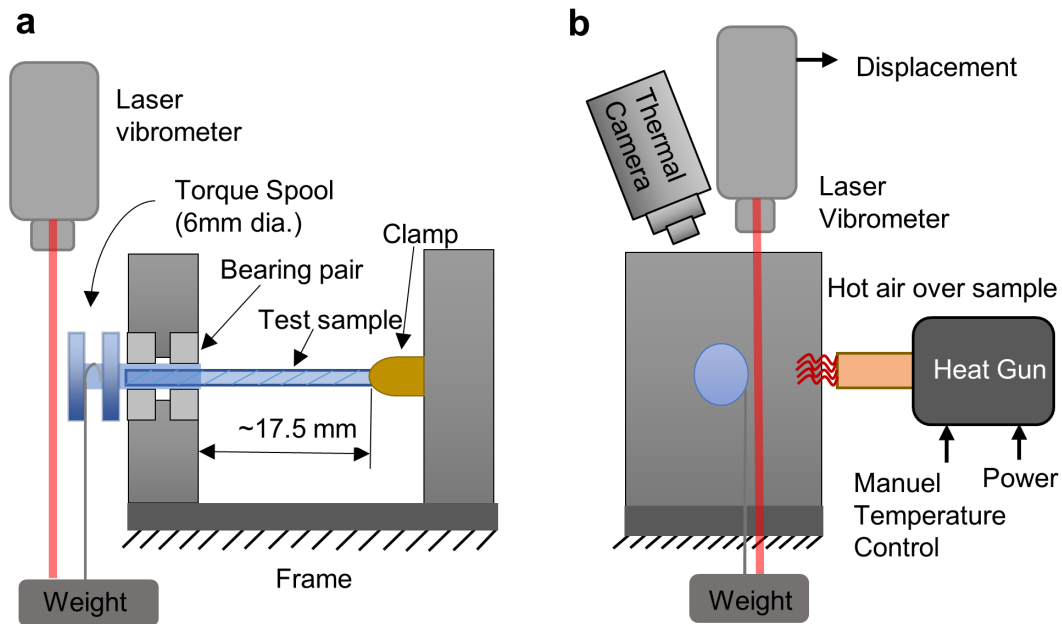
FIGURE 3.8: Torsion actuation set-up used to measure torsional displacement. (a) Side view with a 17.5 mm STPA set in place; (b) front view along with the IR camera, heat gun, and the vibrometer head.

3.4.2.1 Experimental Set-up: Moisture content effects on STPAS under an isotonic torque

A experimental set-up, similar to that used by Shafer et al. [295], was designed to measure torsional displacement under an isotonic torque (1 Nmm) using an aluminum frame, two ball bearings, a torque spool, a collet, and a weight, as shown in Fig. 3.8(a). The torsional actuator was fixed on the right by the collet. On the left, the actuator was glued into a torque spool, which was set in the bearing pair and free to rotate and move in the axial direction. A mass hung from the spool by a Kevlar chord generated a constant torque load on the STPA.

The position of the weight was measured using a Polytec OVF-5000/VF-534 vibrometer controller and sensor unit, along with DD-900 Digital Displacement Decoder unit. This vibrometer output was recorded by a National Instruments PXI-6361 multifunction data

acquisition card, which was manually synchronized with average temperature measurements recorded by the the FLIR A300-Series thermal camera with an IR 10 mm focal lens. Changes in temperature were applied manually with a Sparkfun Electronics 303D heat gun controller.

After setting a approximately 17.5 mm sample in place (Fig. 3.8(a)) the heat gun was used to apply an initial thermal load to approximately 90°C (thermal precycle) along with three more thermal cycles from room temperature to approximately 80°C, while measuring the weight's displacement with the vibromenter under the settings of 0.2 mm/V and a slow tracking filter. Thermal ramps with a heating rate of 3.75°C/s were conducted (after applying the lumped capacitance method thermal analysis explained in Section 3.4.1.1) and the last converged cycle was used to present torsional actuation as a function of temperature.

3.4.2.2 Results and Discussion: Moisture content effects on STPAs under an isotonic torque

To show the moisture content dependencies on the thermal actuation of STPAs, we tested the torsional actuation response of different pitch angle STPAs (36, 25, and 15°) at 0 and 4% added moisture by weight. Fig. 3.9 shows the torsional actuation of three STPAs for each pitch angle/moisture content condition, with the exception of the 15° pitch angle STPAs where only two samples are shown (Fig. 3.9(c)). In these tests, a first thermal cycle was conducted where the monofilament was heated from room temperature to a temperature of approximately 90°C. This first cycle was conducted to eliminate first cycle effects that have been previously shown in other works [295, 315] where the first thermal cycle shows a response bigger in magnitude than the consecutive cycles. After the first cycle, three more thermal cycles were conducted with a change in temperature from room temperature to a temperature slightly bellow 80°C. The torsional actuation

response of the three following cycles converged, and this data was used to plot Fig. 3.9. Figs. 3.9(a)–(c) show the torsional thermal actuation of STPA pitch angles of 36, 25, and 15°, respectively, for desiccated STPAs (M = 0%) and 4% moisture added by weight. The torsional actuation generated by the 4% moisture content STPAs was approximately twice as much than that one generated by the desiccated STPA samples when evaluated at a temperature of 75°C. This increase in torsional actuation is observed for each pitch angle STPA presented in Fig. 3.9, thus a first order approximation could suggest that thermal actuation is linearly proportional to moisture level.

3.4.3 Moisture content effects on TCPAs under an isotonic tensile load

In this section, we present the axial contraction actuation response of a TCPA made of a precursor monofilament of 0.38 mm diameter at two different percentages added moisture by weight (0 and 4%) to show the moisture dependencies on TCPAs thermal actuation.

3.4.3.1 Experimental Set-up: Moisture content effects on TCPAs under an isotonic tensile load

To measure linear actuation of a TCPA as a function of temperature under a load of 300 grams, similar to the experimental methodology used for axial thermal contraction in Section 3.4.1.1, the vibrometer, heat gun, and thermal camera were used. Fig. 3.10 shows a very similar set-up as seen in Fig. 3.5 but with a TCPA connected in place instead of a precursor monofilament. In addition, during the TCPA actuation tests, the samples were also constrained from rotation at the end of the sample by adding a small rod to the hanging weight which contacted the vertical beam, adding only negligible amounts of friction to the actuation. The heating rate applied during the test was 3.75°C/s. This
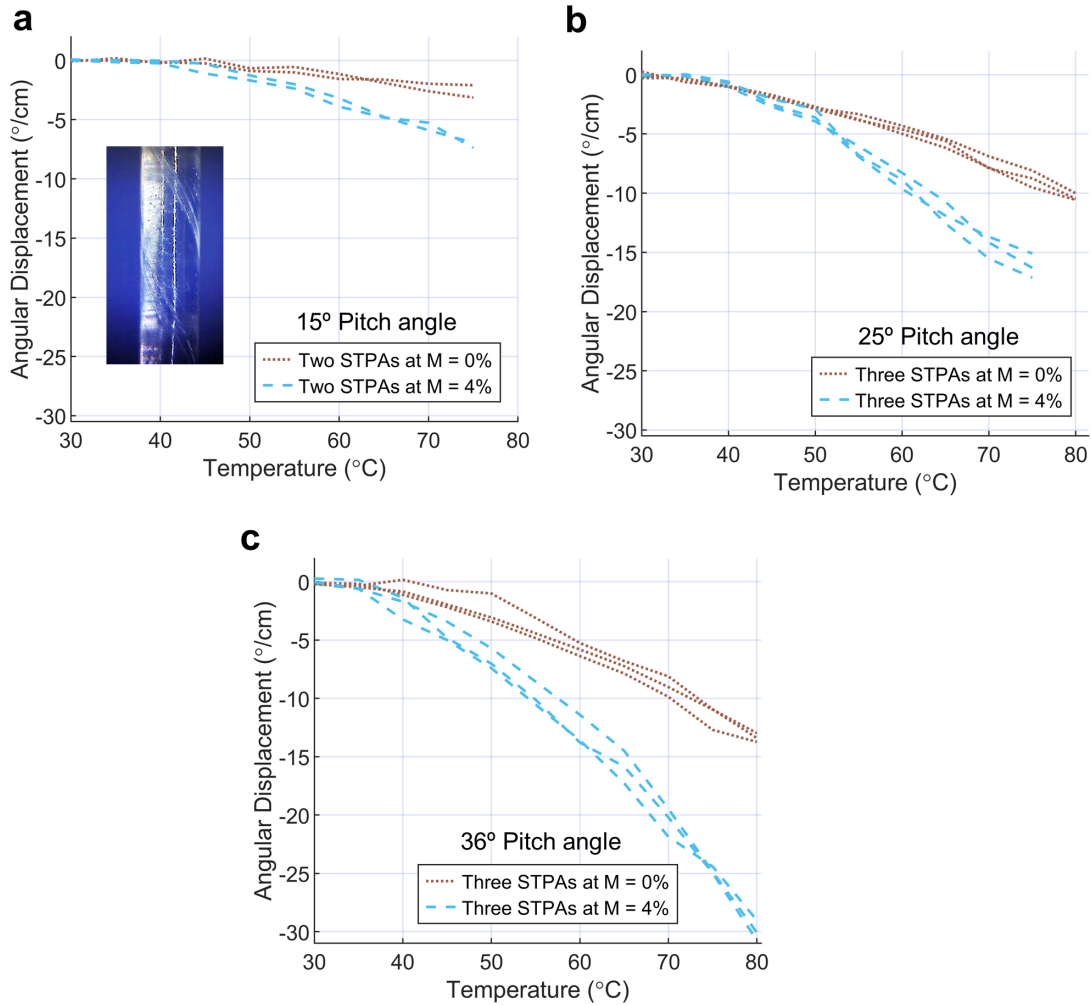
FIGURE 3.9: Torsional thermal actuation under an isotonic torsional load of 1 Nmm at 0 and 4 % added moisture by weight. (a) Torsional thermal actuation for a 15° pitch angle STPA; (b) Torsional thermal actuation for a 25° pitch angle STPA; (c) Torsional thermal actuation for a 36° pitch angle STPA.

was the same rate used for the STPAs, since the diameters of the two materials were quite similar (0.89 mm for the STPA and 0.91 mm for the TCPA).

3.4.3.2 Results and Discussion: Moisture content effects on TCPAs under an isotonic tensile load

A TCPA fabricated from a precursor monofilament of 0.38 mm diameter was used to generate axial actuation under a tensile load of 3N at 0 and 4% added moisture by
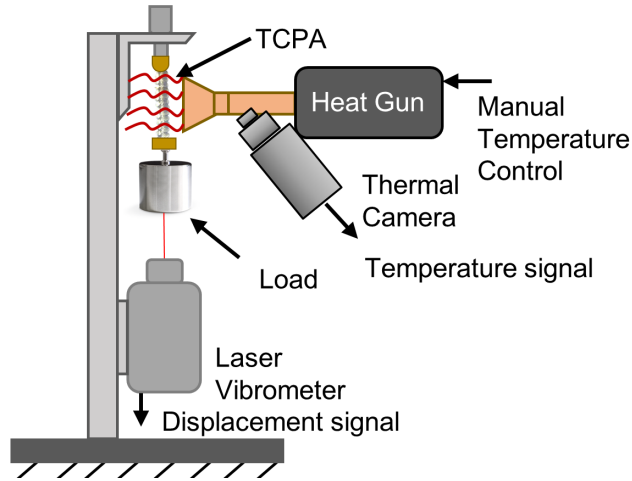
FIGURE 3.10: Experimental set-up for axial thermal actuation of a TCPA.
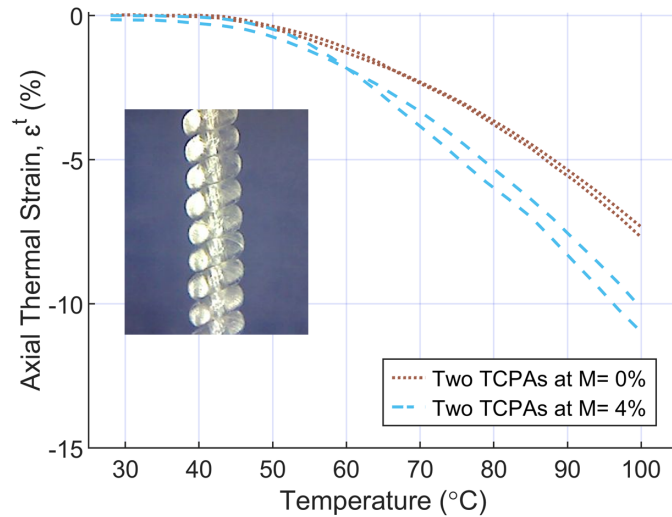
FIGURE 3.11: Axial thermal actuation of a TCPA at 0 and 4% added moisture by weight.

weight. Fig. 3.11 shows the axial actuation of two TCPAs at 0% moisture content and two TCPAs at 4%. As before, a first thermal cycle was conducted where the TCPA was heated from room temperature to a temperature of approximately 110°C to eliminate any first cycle effect. After the first cycle, three more thermal cycles were conducted with a change in temperature from room temperature to a temperature slightly bellow 100°C. The axial actuation response of the three following cycles showed convergence, and this data was used to plot Fig. 3.11. Fig. 3.11 shows an increase in thermal actuation of

99

approximately 50% for the M = 4% samples as compared to the desiccated TCPAs at a temperature of 100°C.

It should be noted that the multiple thermal cycles in a non-humidity controlled environment likely dried out the sample some during the tests. Therefore, addition actuation with both STPAs and TCPAs may occur if the moisture content was controlled to remain at 4% for the duration of the test. However, the fast heating rate used in these tests makes us to believe that any resulting errors are minimal.

3.5   Hygroscopic actuation

In this section, we present the set-ups used to collect hygroscopic actuation data, experimental hygroscopic actuation responses of a STPA and TCPA, and discuss the mechanism that drives such actuation.

3.5.1   Experimental Set-up: Hygroscopic actuation

The methodology used to record the experimental hygroscopic actuation of a straight twisted polymer actuator (STPA) under free torsion conditions consisted of a controlled environmental chamber with a camera installed on top used to film the change in twist produced during moisture absorption. A water reservoir was set into the environmental chamber to create a 100% RH environment, along with a vertically aligned STPA (Fig. 3.12(a)). The STPA was constrained in rotation at the bottom using a collet fixed to the ground, and set free to rotate at the top with an attached flag that was used to monitor the actuation response (Fig. 3.12(b)). Before collecting the hygroscopic actuation data as a function of time, the water reservoir was set inside the chamber two hours previous to the test to ensure 100% RH, then the STPA was placed in the chamber for 20 hours

100
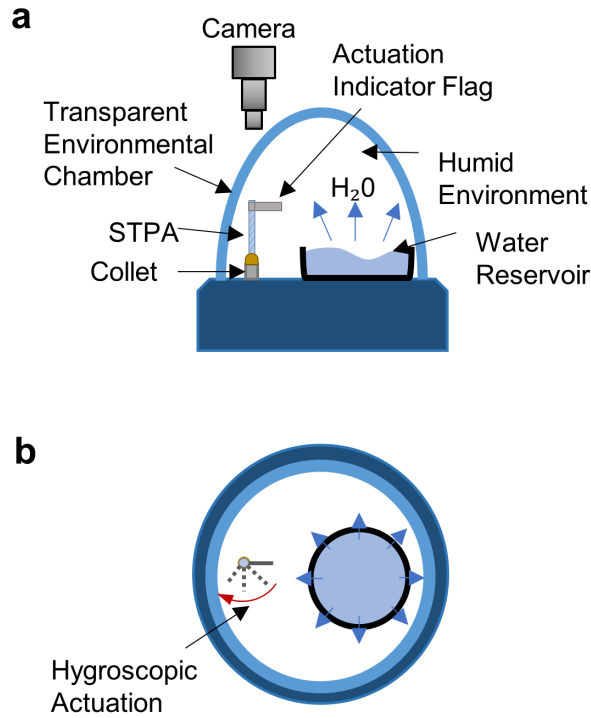
FIGURE 3.12: Experimental set-up for free torsion hygroscopic actuation. (a) Front view; (b) Top view.

while the camera captured pictures of the sample every ten minutes. The images were processed as a function of time to obtain angular displacement-time actuation data.

In order to select the STPA pitch angle to be tested, we planned to use the maximum performance pitch angle for STPAs under free torsion conditions calculation presented by Swartz et al. using their closed-form model. This pitch angle was found to be 63.2° to the axial axis [315]. However, a pitch angle of 36° was used because all attempts to insert any more initial twist resulted in coiling or failure during fabrication. Therefore 36° may be considered the largest practical pitch angle, which should lead to maximization of actuation in a STPA.

A similar test set-up as the one above was used to collect axial contraction of a TCPA as a function of time (see Fig. 3.13). For this experiment, the camera was installed in front of the TCPA and axial actuation was recorded as a function of time. As shown in
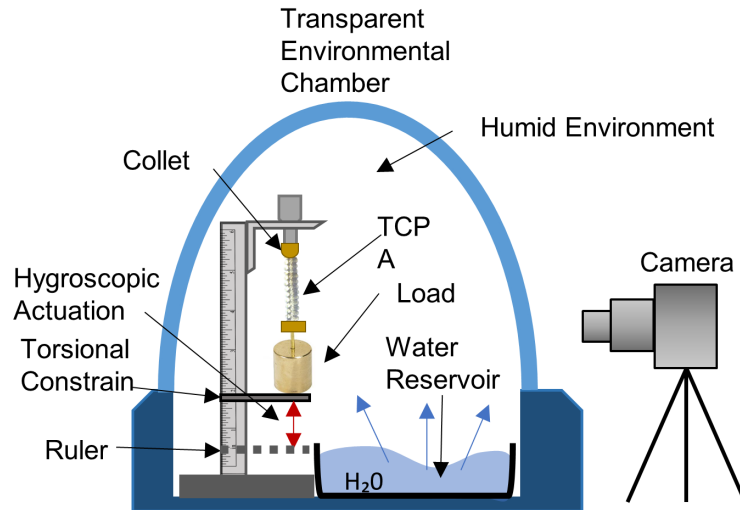
FIGURE 3.13: Experimental set-up for axial hygroscopic contraction of a TCPA under an isotonic load.

Fig. 3.13, a 65 mm TCPA was set in a 100% RH environment under an isotonic load for 22.5 hours. The sample was attached vertically at the top and constrained in axial and torsional displacement by a collect. The bottom end was loaded with a mass of 300 grams (26 MPa) in order to create an initial pre-strain condition and allow it to move in the axial direction (free to contract) but constrained in rotation by adding a small rod to the hanging weight which contacted the vertical beam, adding only negligible amounts of friction to the actuation (see Fig. 3.13). Both, STPA and TCPA's hygroscopic actuation data was processed to report the hygroscopic actuation responses as a function of time and moisture content.

3.5.2 Results and Discussion: Hygroscopic actuation

The actuation developed by a STPA with a 36° pitch angle during moisture absorption was observed during this test to be of the same magnitude as the actuation response from temperature changes. As mentioned in Section 3.5, a 2 cm sample was set in a 100% RH environment for a total of 20 hours. Fig. 3.14(a) shows a linear relationship between
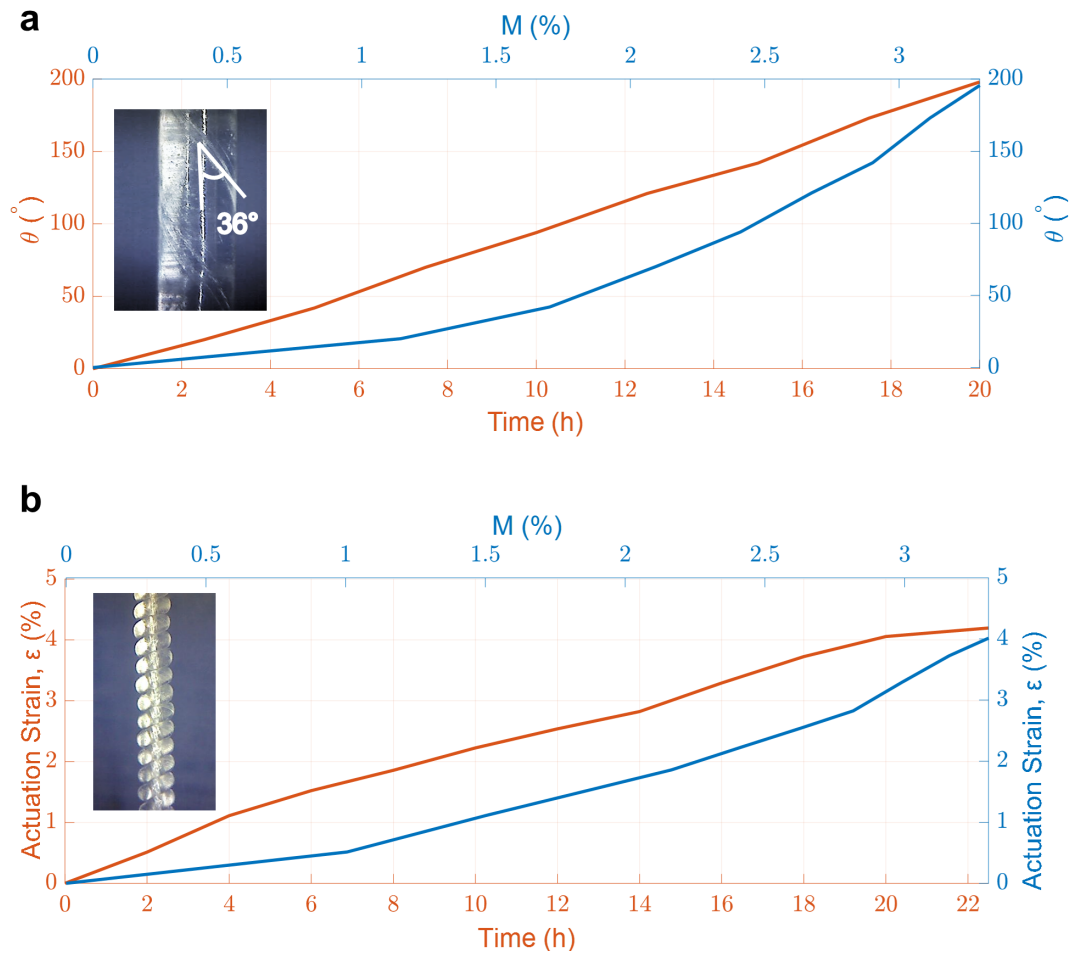
FIGURE 3.14: Hygroscopic actuation on twisted polymer actuators. (a) Hygroscopic actuation response of a 36° pitch angle STPA as a function of time (orange, left) and moisture content (blue, right); (b) Hygroscopic actuation response of a TCPA as a function of time (orange, left) and moisture content (blue, right).

angular displacement, θ, and time during this test. Here, an angular displacement of almost 200° (0.28 rev/cm) was generated during moisture absorption for 20 hours. Using the previous moisture absorption behavior plot (Fig. 3.4), the angular displacement is also plotted as a function of moisture content in Fig. 3.14(a). Angular displacement as a function of moisture content seems to follow an exponential relationship similar to the moisture absorption functions observed in Fig. 3.4.

Next, we consider the hygroscopic actuation responses for a TCPA. Fig. 3.14(b) shows a similar linear response between time and axial actuation strain, ε. Fig. 3.14(b) shows a

103

total axial contraction of 4% after 22.5 hours. In other words, the actuator was capable of developing a specific work of 0.02 kJ/kg after almost a day of being exposed in a 100% RH environment. Similarly, the axial actuation is plotted in Fig. 3.14(b) as a function of moisture content to show the hygroscopic actuation response of the tested TCPA.

After the moisture absorption actuation test, both samples were placed in a dry environment with desiccant and recorded for 20 hours at room temperature. During this time, the STPA and TCPA did not show any sign of actuation and recovery was not observed. As previously mentioned in Section 3.2.3, the hygroscopic actuation in twisted polymer actuators is a combination between the anisotropic mechanical properties of the precursor monofilament and swelling due to moisture absorption. The axial modulus of the precursor monofilament has been reported to be an order of magnitude higher than the radial modulus at room temperature [136], which means that under the same amount of hygroscopic swelling, the precursor monofilament in the radial direction experiences a greater growth than the one in the axial direction.

In order to understand what moisture absorption mechanisms produce swelling in the sample and, consequently, hygroscopic actuation, we look at the absorption moisture behavior shown in Fig. 3.4. Here, we observe a rapid initial uptake of moisture during the first day of 3.61% to a quasi-equilibrium moisture state, followed by the tendency towards total equilibrium after five days. Similar moisture absorption behaviors have been reported and modeled by Berens and Hopfenberg for polymers [37]. These authors claimed a "two-stage" absorption behavior also known as Non-Fickian process. This diffusion process can be explained by a coupling of a Fickian diffusion and relaxation process. The Fickian diffusion process is characterized by a quick initial uptake where moisture diffuses into the polymer through atomic motion occupying voids in the material (free volume) [44, 266] followed by a relaxation process (hydrogen bonding), a slower absorption process, until it reaches the total moisture saturation [37].

Fig. 3.1 (Section 3.2) shows the aforementioned Fickian diffusion and relaxation processes. During Fickian diffusion the water molecules (circles in Figure 3.1) move randomly and occupy the voids (moisture stays in free-volumes) leading a null contribution to hygroscopic swelling. This is the rapid moisture absorption mechanism shown in Fig. 3.4. During the relaxation process, the polar water molecules interact with the polymer network and form hydrogen bonds that are responsible for hygroscopic swelling [101, 280], (the slow moisture absorption mechanism seen in Figure 3.4). These bounded molecules of water in the polymeric matrix and the anisotropic mechanical properties cause the precursor monofilament to expand more in the radial direction than the axial which manifests as shear deformation for a STPA under free torsional conditions and as linear strain in a TCPA. Consequently, the relaxation process i.e. hydrogen bonding of moisture absorption is thought to be the responsible of hygroscopic actuation.

The previous stated hygroscopic actuation mechanism is also supported by Fig. 3.14, which shows small actuation responses during the quick initial moisture uptake, followed by an increase in actuation. At first, the moisture absorption process is thought to be driven by the Fickian diffusion (unbounded water molecules into free-volume) followed by the relaxation process (bounded water molecules into the polymeric matrix) that creates the moisture-induced swelling [101] and the resulting torsional and linear actuation.

Finally, this actuation mechanism can also explain why the tested TPAs did not show recovery during 20 hours set in a dried environment (testing chamber with desiccant), since the desiccant may primarily absorb moisture located in the voids (Fig. 3.4) but none of the water molecules positioned in the polymeric matrix due to hydrogen bonding. Full recovery of actuation due to hygroscopic actuation may occur if desiccanted at elevated temperatures, since, as shown in Fig. 3.4, desiccation at 70°C for 10 hours makes the water molecules to exit the polymeric matrix.

105

3.6   Conclusions

This paper presents two main subject matters. The first one is the ability of TPAs to actuate while they absorb moisture from the environment and the second one is the significant impact of moisture content on the thermally driven actuation of TPAs. For the former, we show that STPAs and TCPAs developed hygroscopic actuation during a period of approximately 20 hours when a desiccated sample is exposed to humid air. This actuation response is found to be fairly linear as a function of time. This linear relationship between actuation and time enhances its potential for use as long term actuators or sensors, where the driving force of actuation/sensing is the change in moisture in the TPA since the linear relationship makes this actuation mechanism easy to predict and control. For the latter, it is demonstrated that the moisture content in TPAs has a significant impact on the thermal actuation. In other words, TPAs will not develop the same actuation responses in humid areas, such as Miami where the annual RH average is 72% than the actuation responses in arid areas, such as Phoenix where the annual RH average is 36% [5].

In order to predict thermal STPAs and TCPAs actuation response with finite element or closed-form models, a full characterization and modelling of the mechanical and thermal properties is required as a function of moisture and temperature. This information will serve as inputs for the actuation prediction models. Models for the mechanical properties of polymers as a function of moisture content at room temperature using a moisture-time superposition principle has been already presented and validated [100, 375]. Although, these works are a good starting point to be implemented, the mechanical and thermal properties as a function of both, moisture and temperature need to be experimentally characterized.

In future work, we would like to propose the design of TPA hygroscopic actuation models by using moisture expansion models of the precursor untwisted monofilament and TPAs close-form kinematic models. Similar to thermal expansion coefficients, researchers have studied the characterization of moisture-induced swelling of polymers by using a coefficient of moisture expansion (CME) [83, 101]. This requires experimental identification of the CME, and from this work, we know that the CME will depend on temperature, time, and relative humidity, which might be complex. Once identified, this coefficient can be used in already presented closed-form models [28, 296, 297, 356] to predict the actuation response of TPAs as a function of moisture content.

Additionally, a similar approach can be done to predict the behavior of TPAs when both moisture and temperature change. In this case, models will need to account for the hygro-thermal behavior of nylon since temperature has been shown to be a booster of moisture absorption [253]. Fast rates of moisture absorption will lead to variations on the moisture content and, in turn, to variations on the material properties. One potentially simplifying feature of this complex modeling task may be the fact that thermal changes tend to be much faster than moisture changes. In particular, TPAs hygroscopic actuation contributions will not be notable in short-term actuation cycles but temperature actuation would. However, in long-term actuation cycles or a long continuous sequence of short-term actuation cycles, hygroscopic actuation may be important.

Finally, in terms of engineering design, we would like to propose the use of this thermally driven actuators with a hot/cold water jet force convection activation method because will lead to the elimination of moisture content dependencies, since the material will be fully saturated under these conditions and, more importantly, the total developed actuation will be greater leading to a higher performance of twisted polymer actuators.

CHAPTER 4

CAVATAPPI ARTIFICIAL MUSCLES FROM DRAWING, TWISTING, AND COILING POLYMER TUBES

Compliant, biomimetic actuation technologies that are both efficient and powerful are necessary for robotic systems that may one day interact, augment, and potentially integrate with humans. To this end, we introduce a fluid-driven muscle-like actuator fabricated from inexpensive polymer tubes. The actuation results from a specific processing of the tubes. First, the tubes are drawn, which enhances the anisotropy in their microstructure. Then, the tubes are twisted, and these twisted tubes can be used as a torsional actuator. Last, the twisted tubes are helically coiled into linear actuators. We call these linear actuators cavatappi artificial muscles based on their resemblance to the Italian pasta. After drawing and twisting, hydraulic or pneumatic pressure applied inside the tube results in localized untwisting of the helical microstructure. This untwisting manifests as a contraction of the helical pitch for the coiled configuration. Given the hydraulic or pneumatic activation source, these devices have the potential to substantially outperform similar thermally activated actuation technologies regarding actuation bandwidth, efficiency, modeling and controllability, and practical implementation. In this work, we show that cavatappi contracts more than 50% of its initial length and exhibits mechanical contractile efficiencies near 45%. We also demonstrate that cavatappi artificial muscles can exhibit a maximum specific work and power of 0.38 kilojoules per kilogram and 1.42 kilowatts per kilogram, respectively. Continued development of this technology will likely lead to even higher performance in the future.

4.1 Introduction

Traditional electric and fluidic actuators operate effectively in many tasks, yet their complexity and rigid configuration often limit their deployment in areas such as biomimetic robotics and compliant structures and limit the design space of their host system. This has driven research into alternative solid-state, flexible actuators, but the challenge has been producing high specific power metrics while maintaining the efficiency, form factor, and predictable performance necessary for adoption. The key metrics often used for soft actuator selection in applications are average and peak specific power, specific work, maximum actuation strain and stress, lifetime, and actuator efficiency. Many of these metrics are governed by the input driver of the actuator, for example, electrically or fluidically driven actuators tend to be much more efficient than thermally driven actuators.

To help compare different soft actuator technologies, Table 4.1 summarizes key metrics of several soft-actuators and human muscle, which many of these actuators aim to mimic, and provides total system efficiency metrics that consider the electric energy to mechanical work conversion (chemical free energy to mechanical work for human muscles). Included in this table are thermally activated twisted polymer actuators (TPAs), which are made from inexpensive fibers, such as fishing line. TPAs have been shown to develop a specific work of 2.48 kJ/kg and an average specific power of 27.1 kW/kg [128]; however, their thermal activation limits response time, controllability, and efficiency. The electric-mechanical energy conversion efficiency for TPAs is thought to be similar to that presented for shape-memory alloys, which is about 1 to 2% [128]. McKibben actuators are pneumatically or hydraulically driven artificial muscles (PAMs or HAMs) widely used in robotics [250, 326]. They change length by inflating a bladder that is surrounded by a counter double-helix–braided sheath. The macroscopically developed anisotropy allows the device to contract in length and expand radially [65]. Pleated pneumatic artificial

109

muscles (PPAMs) are a recently improved incarnation of the conventional McKibben actuator that can develop a specific work of 1.1 kJ/kg, an average specific power of 1 kW/kg, and contractions of 38% [75, 336]. Small McKibbens can be fabricated with dimensions on the order of a few millimeters in diameter [178], yet at both large and small scales, their multicomponent nature causes frictional losses and hysteresis, which has frustrated the development of accurate models that would allow precise control algorithms [129]), although this has been reduced in PPAMS. But for all McKibbens, during actuation, their diameter increases as a result of the inflation that drives their actuation. These radial changes make parallel operation volumetrically inefficient.

To improve some of the McKibbens drawbacks, new actuator designs have been presented such as pouch motors, fluid-driven origamiinspired artificial muscles (FOAMs), and origami-based vacuum pneumatic artificial muscles (OV-PAMs). Pouch motors are fabricated from bonded films that form an inflatable planar pouch that can be connected in series, forming paired pouch motors. This configuration can develop contractions of 31% with payloads of 10 kg when the pouches are pressurized [239, 248]. Although paired pouch motors are mentioned here and can be used in soft robotics, these do not appear in Table 4.1 because nondimensional or specific metrics have not been directly reported in the literature. Both FOAMs and OV-PAMs are origami-based vacuum-actuated actuators. The former uses a skeleton with a repeated zigzag pattern in a sealed bag. When negative pressure is applied to the actuator, the air within exits the bag, and the zigzag pattern leads to the contractile deformation of the actuator. These actuators develop contractions of up to ∼90% and a mechanical-to-mechanical energy conversion contractile efficiency of 23 and 59% when pneumatically and hydraulically tested, respectively. However, the great generated contractions by FOAMs substantially decrease with small actuation load increments [189]. The related OV-PAMs consist of a sealed film chamber made from polyvinyl chloride (PVC) connecting a top and a bottom plate with evenly

TABLE 4.1: Comparison of metric for various soft actuators. Dash entries indicate data not found.

Metric	Cavatappi [38, 327, 328, 351]	TPA [128]	PPAM [75, 215, 336]	HASEL [8, 167]	OV-PAM [184, 185]	FOAM [189]	Human Muscle [203, 313]
Avg/Peak Specific Power* (kW/kg)	0.8 / 1.42	27 / 50	1 / −	0.36 / 0.59	- / 0.02	$\sim$1 / $\sim$2	0.05 / 0.28
Specific Work (kJ/kg)	$0.11 - 0.38$	2.48	1.1	0.07	0.19	$\sim$0.25	0.04
Maximum Actuation Strain (%)	$\sim$50	49	38	$\sim$60	>90	90	>40
Maximum Actuation Stress (MPa)	$\sim$0.70	$\sim$100	0.67	0.3	0.04	$\sim$0.6	0.35
Lifetime (cycles)	$>10^{4\dagger}$	$>10^6$	$>10^5$	$>10^5$	–	$>10^4$	$>10^9$
Actuator Efficiency (%)	$\sim9^{\dagger\S}$ & $\sim45^{\dagger\P}$	–	$\sim57^{\dagger\P}$	–	$\sim99^{\dagger\S}$	$23^{\dagger\S}$ & $59^{\dagger\P}$	–
Total System Efficiency (%)	$10 - 22^{\dagger\P}$	$\sim$1	$\sim5^{\dagger\P}$	$21^{\dagger\|}$	$16^{\dagger\S}$	$2 - 5^{\dagger\S}$	$\sim$20

*This value is limited to the energy rate provided by the energy source. †This was the maximum number of cycles tested, not an upper limit on lifetime. Cavatappi showed no signs of degradation. ‡Actuators' energy conversion contractile efficiency (without energy recovery). §Pneumatic. ¶Hydraulic. ‖Full-cycle analysis of actuator efficiency (includes energy recovery).

spaced transverse reinforcements. The previously mentioned actuation strain-stress ratio limitation of FOAMs is solved with OV-PAMS because they can keep an actuation strain close to 100% while generating their maximum actuation force. However, OV-PAMs are voluminous, which could limit their implementation in small robotic applications [184, 185].

The previously mentioned actuators are all thermally or fluidically driven; hydraulically amplified self-healing electrostatic actuators (HASELs) are electrohydraulic activated. These muscle-mimetic actuators are fabricated from an elastomeric shell partially covered by a pair of opposing electrodes and filled with a dielectric liquid. Upon voltage application, the induced electric field generates an electrostatic Maxwell stress that pressurizes and displaces the liquid dielectric leading to the actuator's contraction. HASELs can generate actuation strains of about 60% (calculated as the actuator contraction displacement divided by the actuator initial length) and full-cycle electric-mechanical efficiency

of 21% (see Table 4.1). However, these actuators require high voltage (> 5 kV) and have thus required voluminous power electronics in testing [8, 167].

Here, we present an actuation mechanism that is a hybrid of TPAs and McKibben actuators, which we have named cavatappi, after the Italian pasta with similar shape (see Fig. 4.1(a)). Cavatappi exploits the material's anisotropic microstructure to develop actuation like TPAs, yet they are pneumatically/hydraulically driven like McKibben actuators. The anisotropic microstructure is developed through drawing of inexpensive polymer tubes. After drawing, the tubes are twisted and coiled like TPAs. Therefore, cavatappi have the simplicity and size of TPAs with the actuation response and mechanical efficiencies of McKibben actuators. Table 4.1 shows actuation characterization of single-component cavatappi artificial muscles as compared with the other soft actuators. Although sacrificing some performance of TPAs, cavatappi drastically increase others and in doing so, better meet or exceed the performance of skeletal human muscle in many key metrics. With specific peak power metrics of 1.4 kW/kg, cavatappi exceeds the capacity of human muscle while maintaining a mechanical conversion efficiency of 45%. With actuation strains of up to 50% and minimal diametral changes during actuation, these devices can be placed in parallel to increase actuation force akin to biological muscle fibers. Because of their cost, performance, ease of fabrication, and compliant form, cavatappi fit the needs of many current and future robotic actuation applications.

4.1.1 Design and development of cavatappi

The design and development of cavatappi was originally inspired by the mechanics of TPAs, particularly the idea of exploiting the material's anisotropy to generate actuation [128]. TPAs are thermally driven linear or torsional actuators, whose actuation response is a result of the anisotropic thermal properties of the precursor (untwisted) material, which experiences axial thermal contraction and radial thermal expansion. They are
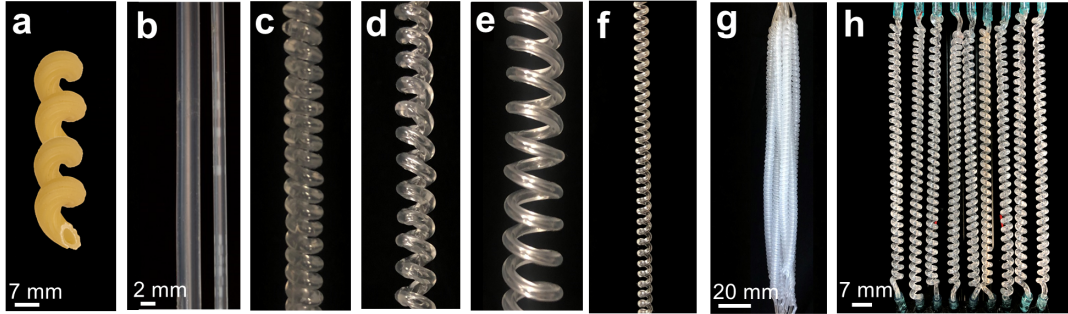
FIGURE 4.1: Cavatappi pasta, cavatappi artificial muscles, and precursor tubes. (a) Cavatappi pasta is shaped as a helical tube yet lacks the anisotropic material properties necessary to be deployed as an effective actuator. (b) Precursor undrawn tube (left, 3.18 mm OD and 1.58 mm ID) and precursor drawn tube (right, 1.8 mm OD and 0.85 mm ID). (c) Cavatappi made from a 1.8-mm-OD/0.85-mm-ID tube. (d) Cavatappi in (b) that has been prestretched and annealed after fabrication to increase the helix pitch. (e) Cavatappi made from the drawn precursor tube shown in (b) and coil ID of 7 mm. (f) Mini-cavatappi made from a 0.7-mm-OD/0.25-mm-ID tube. (g) Bundle of cavatappi artificial muscles that simulate a human skeletal muscle bundle. (h) Linear-parallel configuration of nine cavatappi from (c). The scale bar in (b) is used for (b) to (f), and the scale bars for (a), (g), and (h) are shown in the figures. All tube diameters listed here are the drawn diameters.

inexpensive, often fabricated from fishing line, and have been demonstrated in areas such as robotics [309, 353, 360], medical devices [202], and active textiles [128, 143]. In the past few years, our team has focused its effort on understanding the actuation mechanism of TPAs and how TPAs' actuation can be modeled using the material properties of the precursor fibers [137, 296, 315]. As part of this work, we found the standard TPA materials to be highly viscoelastic [136, 295, 314] and hygroscopic, which causes their response/performance to depend on moisture content [138]. Moreover, the viscoelastic and hygroscopic properties of TPAs are strongly affected by temperature changes, and temperature changes are required for actuation. This makes TPAs challenging to model and therefore control [28, 137, 165, 296, 297, 315]. Last, thermal activation is generally an inefficient and time-consuming (particularly during cooling) driver.

The extreme performance and shortcomings of TPAs led our team to explore alternative actuation modalities that might mitigate inherent drawbacks yet take advantage of their

strengths by mimicking their actuation mechanism. We surmised that internal pressure in a tube could be used to develop similar anisotropic expansion seen during TPA heating and initially tested straight extruded/drawn tubes of polymers. Pressure testing showed that soft PVC tubing (Fig. 4.1(b), left) was able to generate radial expansion similar to TPAs, yet the tubing developed axial expansion, which we knew from our TPA modeling would reduce actuation performance when twisted. Given the PVC microstructure, we set out to mitigate this axial expansion by enhancing anisotropy by cold drawing (Fig. 4.1(b), right) [24, 261, 268]. Fig. 4.1(b) shows the precursor tube [left, 3.18 mm outer dimater (OD) and 1.58 mm inside diameter (ID)] and the same tube (right, 1.8 mm OD and 0.85 mm ID) after the cold drawing necessary to increase axial stiffness relative to radial stiffness. Note the substantial change in diameter that occurs during the drawing process. We found that internal pressurization after drawing induced positive radial strains and negative axial strains that mimicked those of heated TPA precursor fibers. Next, we twisted these drawn tubes, which we knew from our work with TPA would reorient the highstiffness molecular chains into a helical configuration around the central tube axis while maintaining the tube's ability to radially expand. Such a straight-twisted tube configuration would generate an untwisting when pressurized (torsional actuation). The twisted tubes were then helically coiled (Fig. 4.1(c) to (h)) so that the localized untwisting would manifest as linear actuation by reducing the coil's pitch. In this sense, the torsional actuators can be considered elemental units of the cavatappi (movie A1 ▶). Testing showed that the coiled configuration was able to lift weights, demonstrating the actuation phenomenon (see movie A2 ▶).

Once actuation was proven, other configurations of cavatappi were explored, see Fig. 4.1 (c) to (h), which includes prestretched cavatappi (Fig. 4.1, (d) to (e)), cavatappi with various coil diameters (Fig. 4.1(e)), minicavatappi made from smaller PVC tubing (Fig. 4.1(f)), and grouped cavatappi as bundled (Fig. 4.1(g)) or in parallel (Fig. 4.1, (g) and

114

(h)). Here, we use the reinforced cavatappi artificial muscles with the configuration and dimensions shown in Fig. 4.1(c) and detailed in the Supplementary Materials (specifically, Fig. A.2) to characterize the actuation responses and performance properties of cavatappi artificial muscles, including actuation under various loads as a function of pressure and time, specific work, specific power, lifetime, creep, and actuator contractile efficiency. We also present some applications of cavatappi that demonstrate the use of prestretched cavatappi (similar to that in Fig. 4.1(d)) to increase the maximum actuation stroke, pairs or bundles (similar to that in Fig. 4.1, (g) and (h)) of cavatappi to increase the actuation contraction force, and mini-cavatappi (similar to that in Fig. 4.1(f)) for smaller-scale robots.

4.2 Results

4.2.1 Mechanism of actuation

Cavatappi artificial muscles are fabricated from extruded polymer "precursor tubes" (Fig. 4.3, Fab. stage 1). During the extrusion process, the original material deforms into tubular structures, and anisotropy between the axial and hoop directions is induced. This extrusion process creates axially orientated tie molecules responsible for high axial strength [261]. However, this anisotropy can be increased when the precursor tube is cold drawn, (Fig. 4.3, Fab. stage 2), by increasing the number of formed tie molecules [24, 268].

To demonstrate the change in the anisotropic properties produced by drawing precursor tubes, we pressurized undrawn and drawn samples while measuring axial and radial strains (Fig. 4.2(a)). For the undrawn precursor tube, both axial and radial expansions show growth as a function of pressure, with axial changes of about 40% of the radial. After drawing this tube, the magnitude of radial expansion remains relatively unchanged
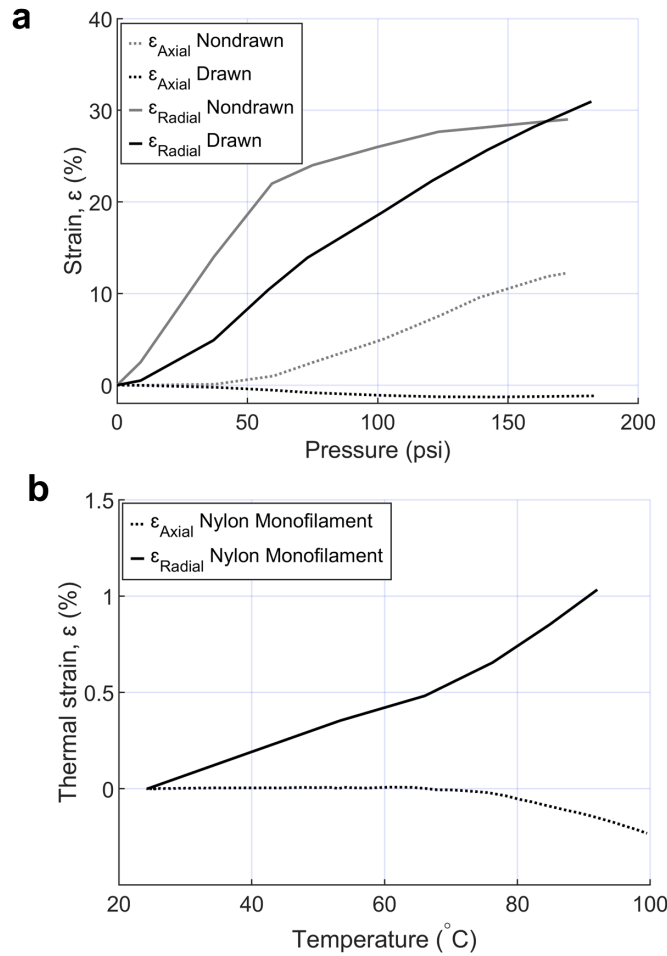
FIGURE 4.2: Comparison of the axial and radial deformation for drawn and undrawn precursor tubes, as well as a nylon monofilament used for TPAs. (a) Axial and radial expansion of a drawn and undrawn precursor tubes as a function of pressure. Radial expansion response changes slightly after drawing, but axial direction switches from expansion to contraction. This response is similar to the axial and radial thermal expansion of a precursor nylon monofilament (b) used to make TPA. Note that drawn tubes in (a) show similar response to pressure as nylon monofilaments do to temperature in (b) where in the radial direction it expands, whereas in the axial direction it contracts. [Credit: Originally presented by Swartz et al. [315], IOP Publishing. Reproduced with permission. All rights reserved.]

but develops a more linear relationship with pressure. The axial response to pressure after drawing transitions from expansion to contraction, leading to a higher degree of anisotropy. The anisotropy of the material can be measured as the ratio of radial to axial strain or the difference between the radial and axial strain in response to pressure. The ratio highlights the sign changes of the expansions, and the difference is key in modeling

116

of TPAs [296, 315]. At 175 psi, the undrawn tubes have an anisotropy ratio of about 2.4 and an anisotropy difference of about 12%. After drawing, the anisotropy ratio becomes about 31, and the difference becomes about 32%, highlighting the importance of drawing the tubes before fabrication of cavatappi artificial muscles. The positive radial strain and negative axial strains observed in the drawn tubes mirror the thermal response of TPA precursor fibers shown in Fig. 4.2(b), which were reported by Swartz et al. [315]. In this figure, we observe a similar negative anisotropy ratio and a large anisotropy difference, which is known to be the source of actuation in TPAs [128].

After drawing, the tubes can then be twisted to reorient the high-stiffness molecular chains into a helical configuration (Fig. 4.3, Fab. stage 3) so that internal pressurization generates an untwisting of the tube (Fig. 4.3, Act. stage 3, and movie A1 ▶). We think of sections of the twisted tubes as "elemental units" of the cavatappi because the localized shear deformation (untwist) is the fundamental actuation mechanism of the cavatappi muscle. The orientation of the twisted outer fiber is shown by the pitch angle, α, which is the angle between the original draw direction and the plane perpendicular to the longitudinal axis of the tube. If the tube is thin enough, then this pitch angle would be roughly constant through the tube wall thickness, but for thicker tubes, the pitch angle will vary radially, similar to TPAs. If the elemental unit is thermally annealed to release internal stresses, then the twisted configuration can be set. The actuation response of the elemental unit was tested under free torsion conditions, and the results are presented in section A.4.

After twisting, a drawn tube can also be coiled (Fig. 4.3, Fab. stage 4) to create the final cavatappi artificial muscle. When this helical configuration is thermally annealed, the internal stresses are released, and this new shape holds after the loads that are used to maintain the configuration during the coiling process are removed. As a final step, as shown in Fig. 4.1(d), the cavatappi may be prestretched to increase pitch before

117
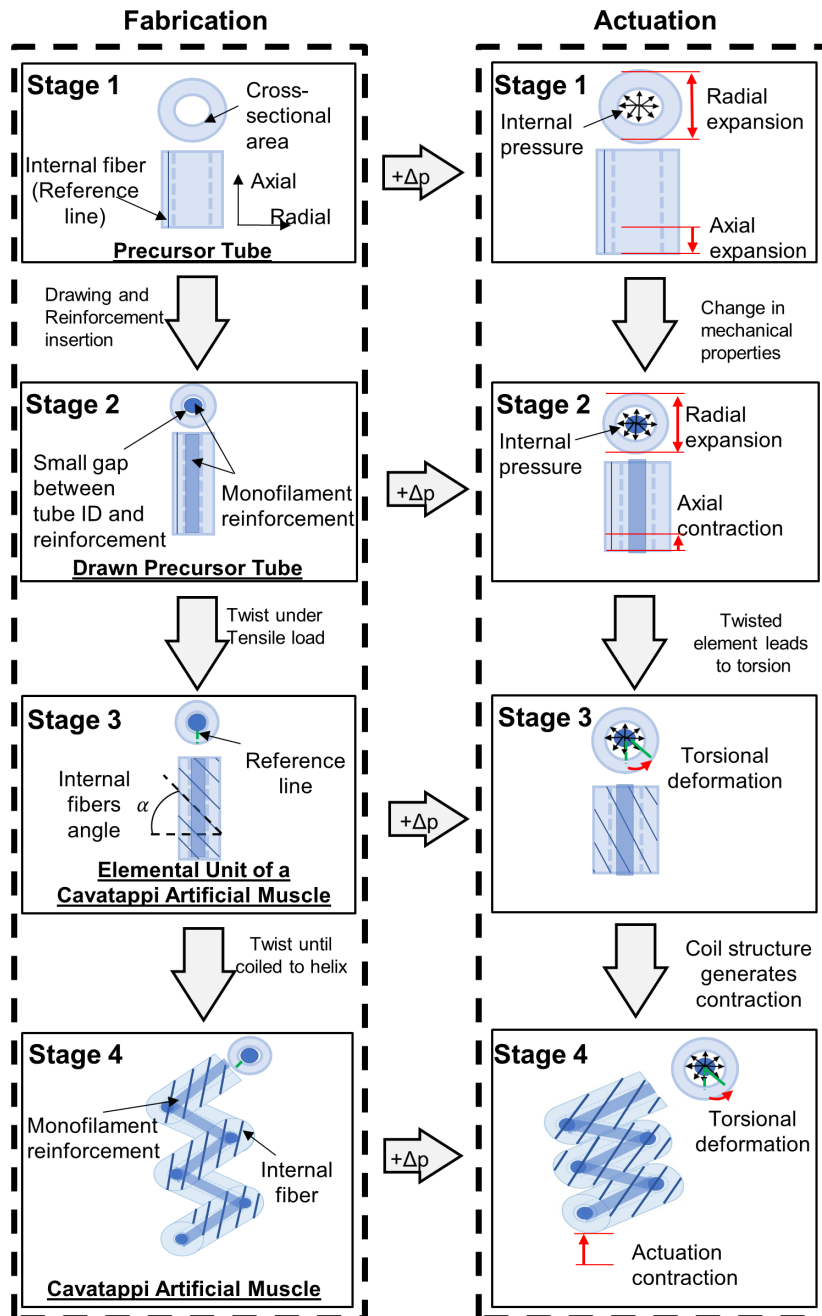
FIGURE 4.3: Stages of fabrication of a cavatappi artificial muscle along with their actuation response at each stage. A blue reference line on the tube wall is used to track the actuation.

annealing. In these coiled configurations, when internal pressure is applied, the untwist in the elemental presents as helical contraction in the overall artificial muscle coil pitch (Fig. 4.3, Act. stage 4). We should note that the reinforcing monofilament of nylon 66 (used for increasing actuator stiffness and lifetime) is kept inside the tubular structure through the entire fabrication process and is thus also twisted and coiled. However, the monofilament used for reinforcement does no work during actuation, and any external loads on the cavatappi are not attached to the reinforcing filament. Thus, the reinforcement is solely there to increase the structural stability of the cavatappi.

4.2.2 Cavatappi artificial muscle: Actuation characterization

With the actuation phenomenon established, the motion of elemental segments discussed in section A.4, and the dimensions and materials of the tested actuators presented in Materials and Methods, we present the cavatappi actuation response. Our testing to date has included actuations under various loads as a function of pressure and time; the latter illuminates viscoelastic effects. We have also developed tests to characterize specific work, specific power, lifetime, creep, and actuator contractile efficiency.

4.2.2.1 Force-strain-pressure and time response characterization

To develop an understanding of the actuation response under load, we conducted a series of isotonic actuation tests where pressure was cyclically ramped and tests where a step change of pressure was applied. The ramp test provided insights into how contraction depended on pressure, whereas the step change test informs bandwidth, specific power, and hints at how future dynamic models might be applied to these devices.

The isotonic actuation response of cavatappi to a ramped pressure input is shown in Fig. 4.4(a). Here, we present the mean actuation results as a function of pressure, along with

119
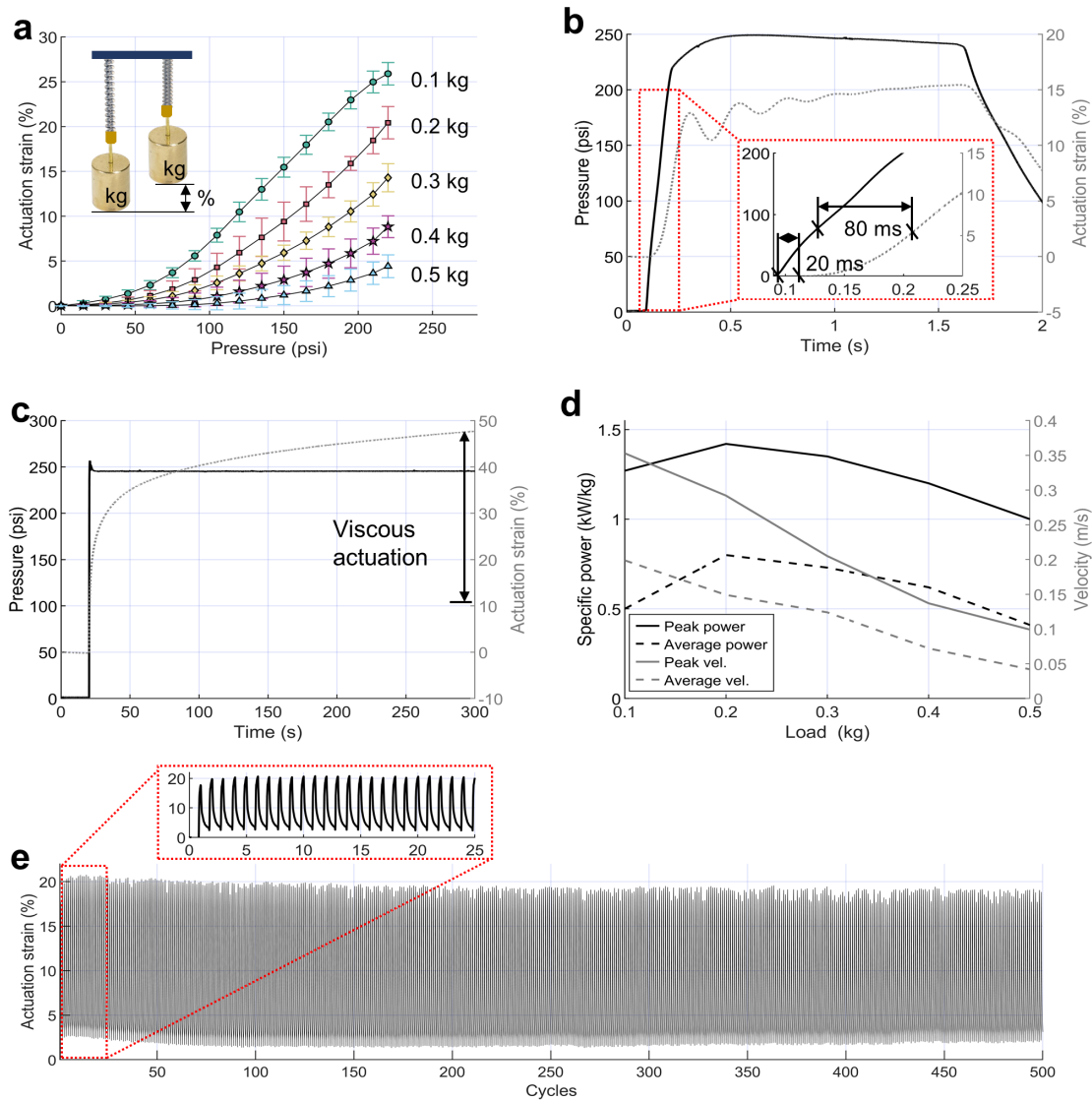
FIGURE 4.4: Cavatappi artificial muscle actuation results. (a) Actuation strain as a function of pressure for 0.1-, 0.2-, 0.3-, 0.4-, and 0.5-kg applied tensile loads using a ramped pressure along with the 95% confidence intervals from data taken from trials on three different samples. (b) Pressure and actuation strain as a function of time under 0.4-kg tensile load. Inset is a zoomed image region of the first 0.25 s highlighting the response time and time lag. (c) Pressure and actuation strain as a function of time under 0.4-kg tensile load for a long period actuation cycle used to show actuation viscoelastic effects. (d) Peak and average specific power and velocity for 0.1-, 0.2-, 0.3-, 0.4-, and 0.5-kg tensile loads. (e) First 500 and 25 cycles of a 10,000-cycle lifetime test used to show first cycle effects and actuation creep. A cycle frequency of 1 Hz was limited by the regulator used for testing, not the bandwidth of the actuator itself.

120

the 95% confidence intervals from data taken from trials on three different samples. For every test, four actuation cycles were executed. Each cycle included a 1.5-s ramp to 240 psi and a 2.5-s ramp back to atmospheric pressure. The data from the last cycle were used to calculate the average results plotted in Fig. 4.4(a), as initial cycles exhibit some nonrecoverable deformation as the actuator is "worked in" (similar to the Mullins effect seen in many polymers).

The actuation strain shown in Fig. 4.4(a) generally increases as a power of pressure. This behavior is shown for all loads, except for the 0.1-kg mass where the nonlinear behavior stops after 75 psi and appears more linear. In addition, this linear behavior stops for this mass at about 200 psi, where after the second derivative of strain in pressure becomes negative. We believe that this is because the coiled shape is completely saturated (there is little to no space between the coils of the helix) under these conditions.

Fig. 4.4(b) shows the actuation of a cavatappi in response to a pressure step when loaded with a 400-g weight. Here, when plotted in the time domain, we can see an actuation contraction generated during the first 0.25 s followed by an underdamped vibration. This ringing is expected from the elastic material properties, coiled shape of the muscle, and the dynamic loading of the actuator whose stiffness and equilibrium position are affected by the internal pressure.

Initially though, the actuation response of Fig. 4.4(b) consists of a dwell time of 20 ms where pressure is increasing and actuation is not initiated. This is followed by the pressure-to-actuation time lag, which is the time delay between input pressure and output actuation. This time lag of about 80 ms may be a result of viscoelasticity of the material or restriction to the fluid's flow through the small diameter tubes due to viscous shear, although further testing would be needed to verify this. This viscoelasticity is apparent in the actuation data of Fig. 4.4(b) between 0.25 and 1.6 s, where there is a steady increase in actuation, superimposed on the aforementioned ringing, under constant internal pressure.

121

We hypothesize that during this time, the actuator diameter is steadily growing, causing not only (i) an increase in untwist of the tube but also (ii) an increase in effective spring stiffness due to changes in the polar moment of inertia of the tube cross section.

In addition, Fig. 4.4(a) does not show the maximum actuation strain generated during the conducted pressure ramp (Fig. 4.4(b)) because the actuation strain used to plot Fig. 4.4(a) is the data collected during the first 0.25 s, measured after the 20 ms it takes for the material to respond; however, the muscle keeps contracting after this time. By comparing Fig. 4.4(a) with Fig. 4.4(b), we see that the total actuation strain under a load of 0.4 kg is 16% after an actuation cycle of 1.5 s. This extra actuation strain seen in Fig. 4.4(b) compared with Fig. 4.4(a) is a result of various factors, such as the time lag and viscoelastic effects already mentioned and the inertial masses during actuation testing. Movie A2 ▶ shows the actuation responses under a load of 0.2 and 0.4 kg, respectively, where the dynamic actuation strain can be observed. Maintaining a steady high pressure on the cavatappi would produce actuation strains exceeding the results presented in either Fig. 4.4(a) or Fig. 4.4(b) as the tubes expand further.

4.2.2.2 Longer period actuation

With the knowledge of the PVC viscoelastic material response, a load of 0.4 kg was attached to a cavatappi after which a 240-psi pressure step was maintained for 5 min to observe longer-term actuation capacity. Here, the actuation response during the first 0.25 s is 11%, which aligns with the actuation response in Fig. 4.4(b). However, as time passes, the actuation strain increases substantially, but the rate of change tends toward zero. This is further evidence of the viscoelastic behavior of the material, which appears to be a first-order dynamic response to the step input. Fig. 4.4(c) shows that after 5 min, the muscle develops 46% contraction, more than three times that after 0.25 s. This represents

an increase in the work done by the actuator, which may have important applications where high strain is required, although the increased time reduces the actuator power.

4.2.2.3 Specific work and power

The time domain results of Fig, 4.4(b) and (c) were used to calculate the specific work for these short- and long-term actuation modes to develop metrics to compare with other soft robotic actuator technologies (Table 4.1). The calculations are detailed in the Supplementary Materials (A.3) but involve finding power and then integrating to get work. The short-term actuation response (0.25 s) developed a specific work of about 0.105 kJ/kg, whereas that of the long actuation response (5 min) was 0.38 kJ/kg.

Following the same methodology as the strain-time, another test was performed wherein velocity rather than position was measured to characterize the actuator's power. Fig. 4.4(d) shows the peak and average velocities measured in these tests, as well as the calculated specific power results for various loads applied to the cavatappi. The applied internal pressure for these tests was 300 psi. The test with a 0.2-kg weight provided the highest peak and average power results of 1.42 kW/kg and 0.8 kW/kg, respectively, and therefore likely represents the mechanical matched-impedance at this input frequency. We should note that the pressure step occurred more than about 70 ms due to limitations in the regulator. The results in Fig. 4.4(b) show that about an 80-ms delay is expected between pressure application and actuation response. Hence, we believe that the specific power of cavatappi may be closer to two times the values presented above (2.84 and 1.6 kW/kg, respectively) but improved experimental set ups would be required to validate the exact increase in the power. More details on the power calculation methods can be found in the Supplementary Materials.

123

4.2.2.4   Actuator lifetime

To assess actuator longevity, we conducted a 10,000 actuation cycle life test (500 of which are shown in Fig. 4.4(e)) of the cavatappi using a 0.2-kg load. The test concluded without failure or any sign of degradation, and the duration of the test was only limited by the size of the pressurized gas bottle used to actuate the cavatappi. Details related to this lifetime test can be found in the Supplementary Materials. Notice that the first 25 cycles in Fig. 4.4(e) also provide information on the viscous effects during the actuation recovery process of an actuation cycle. The recovery time seems to be about $2.5\times$ the time it takes the actuator to contract. Such time recovery may be improved by using the prestretched configuration of cavatappi because this configuration does not depend on a bias load for recovery.

4.2.3   Application demonstrations

To illustrate the operability, applicability, fast actuation, energy storage, and precision control of cavatappi artificial muscles, we developed a number of demonstrations (see Figs. 4.5 and 4.6). In Fig. 4.5(a), a single cavatappi artificial muscle is used to lift a 0.2-kg mass, and in Fig. 4.5(b), cavatappi flexor and extensor muscles are used to actuate a robotic digit. Both Figs. 4.5(a) and (b) are time frames that have been extracted from movies A2 ▶ and A5 ▶, respectively, which highlight the speed of actuation. The basic actuation demonstration in Fig. 4.5(a) used a single cavatappi artificial muscle that was cyclically actuated with 240-psi air under a tensile load of 0.2 kg. A fast-opening valve was manually triggered such that an entire contraction and expansion cycle required only 0.24 s ($\sim$4 Hz). Under these actuation conditions, the muscle generated an axial contraction of 30%. Fig. 4.5(a) also shows that at a pressure of 240 psi, the maximum actuation

response was limited by the saturation of the cavatappi coils, and thus, higher pressures would do little to change the performance.
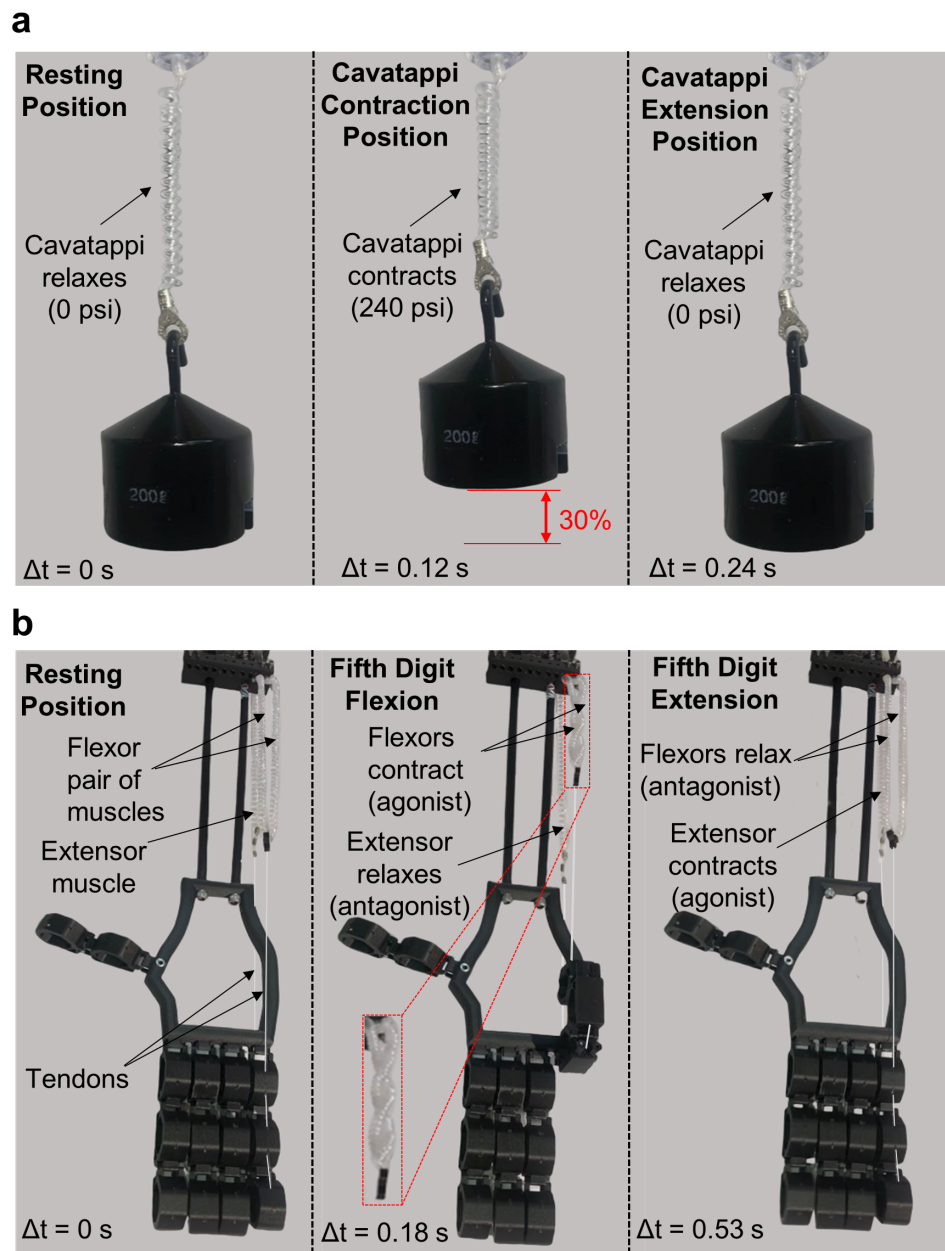
FIGURE 4.5: Demonstration of the contraction response and biomimetic application of cavatappi artificial muscles. (a) Actuation strain cycle response for a 0.2-kg tensile load with a maximum internal pressure input of 240 psi. (b) Fifth digit actuation of a robotic hand using two cavatappi artificial muscles as the flexor muscles and one as the extensor muscle.

Whereas the muscle shown in Fig. 4.5(a) was fabricated without an initial prestretch, movie A2 ▶ also shows a second similar muscle fabricated with prestretched and actuated under the same axial load of 0.2 kg. During fabrication, this muscle was stretched by 130% and thermally annealed at 190°F for 30 min, before cooling under room temperature conditions to maintain the stretched configuration after removal of the mechanical restraints. That cavatappi contracted 40% during actuation, an increase of 10% more than the unstretched muscle. The extra 10% actuation response shown in movie A2 ▶ is attributed to the prestretched configuration, which delays muscle saturation. Movie A2 ▶ also shows the same prestretched cavatappi artificial muscle but under an axial load of 0.4 kg. Under this condition, the sample contracts 16% with a pressure of 240 psi; a similar result was found using unstretched muscle because under this higher applied load, neither muscle contracts enough to saturate.

Following others [224, 360], we three-dimensionally printed a robotic hand with dimensions similar to those of an adult human to show the biomimetic potential of cavatappi (Fig. 4.5(b)). The cavatappi were placed on this model to allow for flexion and extension of only the fifth digit. Cavatappi could have also been placed on the other digits to develop a fully functional robotic hand, but they were excluded in this work for image clarity. Like human hands, each finger was composed of three segments. The pinky (or fifth digit) shown in Fig. 4.5(b) was actuated by the contraction of two parallel cavatappi artificial muscles placed in the interior forearm, mimicking those muscles in a human arm, with restorative forces induced by a single antagonistic cavatappi on the posterior of the arm. Both flexors and extensor muscles were prestretched cavatappi. The linear actuation was transmitted to the tip of the finger by a 0.2-mm-diameter monofilament nylon tendon.

In the resting position, the flexor and extensor muscles were set into an extended position of the fifth digit (Fig. 4.5(b), Resting Position), and all had an internal pressure of 0 psi.

126
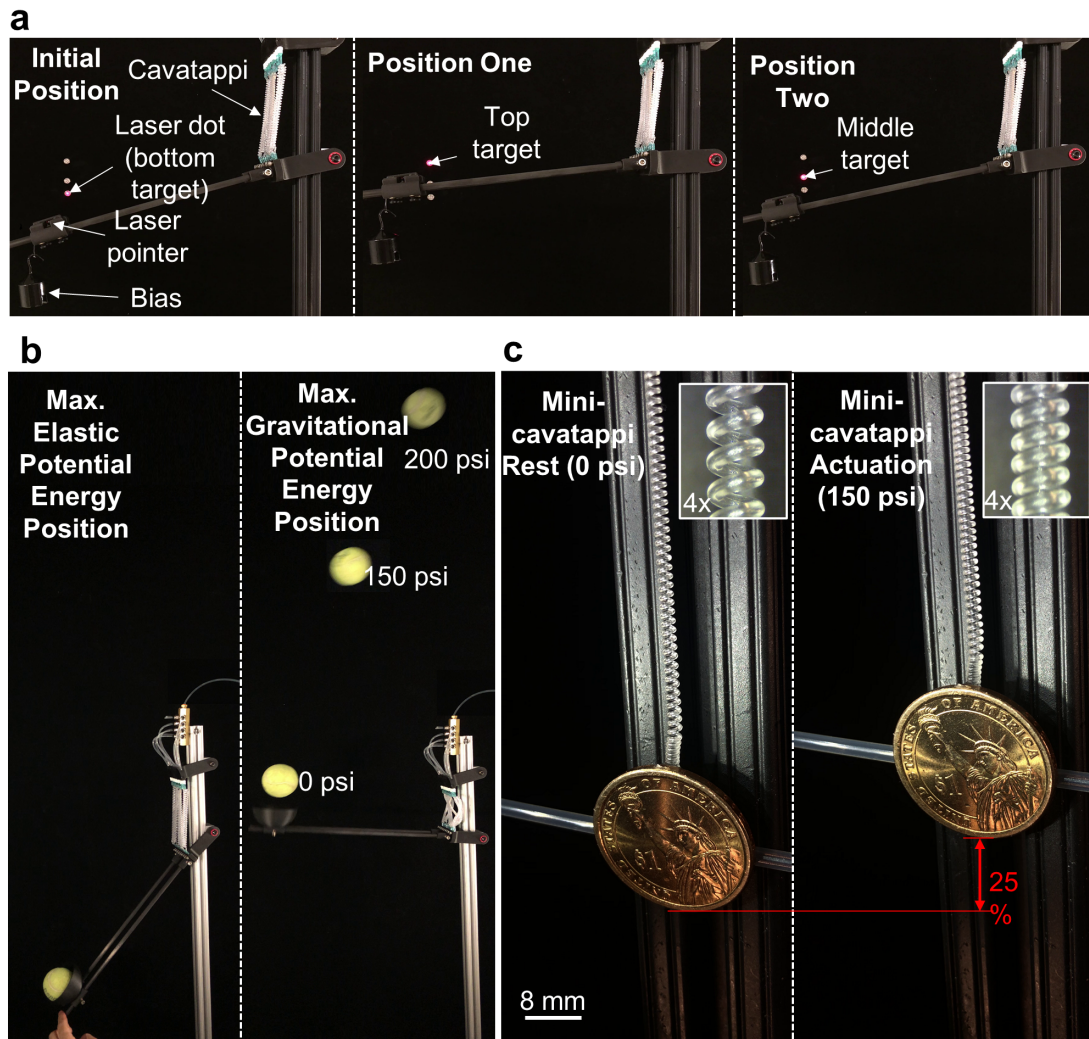
FIGURE 4.6: Applications of cavatappi artificial muscles to show the precise actuation, elastic energy storage, and scalability properties. (a) High precision actuation strain for a linear-parallel configuration of nine cavatappi used to aim at three different targets with a laser pointer attached to the actuated arm. (b) Same application shown in (a) used to highlight the potential elastic energy storage capacity of cavatappi. (c) Actuation response developed by the mini-cavatappi shown in Fig. 4.1(f) under a load of 8.1 g (dollar coin).

To actuate, pressure was cycled between 0 and 240 psi by opening and closing a pneumatic valve. During the finger flexion, the flexors rapidly contracted in 0.18 s. This contraction also led to an extension in the extensor muscle (Fig. 4.5(b), Flexion). As shown in the inset of Fig. 4.5(b), during flexion, the flexors not only contract but also helically wrap around each other as a result of the untwist that occurs on the sample, leading to an

increase in the finger flexion. The secondary helical twisting of the actuator around each other provided additional path length and contraction as a result, beyond what would be expected from a single cavatappi. After the flexion, the flexors were depressurized, and the extensor was pressurized. This induced extension of the finger (Fig. 4.5(b), Extension), at which point, both muscles were depressurized. Fig. 4.5(b) also shows the actuation time for a cycle (finger flexion and extension) to be about half of a second (~ 2 Hz).

To emphasize high precision actuation and potential elastic energy storage capacity (strain energy), Fig. 4.6(a) and (b) shows actuation of a mechanical arm via a linear-parallel configuration of nine cavatappi (the same cavatappi shown in Fig. 4.1(c) with the configuration shown in Fig. 4.1(h)). In Fig. 4.6(a) (movie A7 ▶), a laser pointer is attached to the end of the arm. The laser pointer illuminates a red dot on the black background in Fig. 4.6(a), where three different targets were set (bottom, middle, and top targets as shown in Fig. 4.6(a)). As previously mentioned, the mechanical arm was actuated using a linear-parallel configuration of nine cavatappi; to generate initial stretching of the muscle, a bias mass of 0.2 kg was hung from the platform where the laser was sitting, although prestretched muscles could have been used. At the initial position, the muscles were slightly pressurized (50 psi) to aim the laser at the bottom target. After 3 s, the internal pressure was increased to 200 psi, moving the arm to illuminate the top target (position 1 in Fig. 4.6(a)), after which the arm was controlled to illuminate the middle target.

The strain energy stored in an ideal helical spring is $\frac{1}{2}kx^2$, where k is the spring constant and x is the deflation of the spring from its equilibrium position. The helical shape of cavatappi invites the application of this standard model, albeit with variable stiffness and equilibrium positions in response to pressure. Hence, it is clear that cavatappi have an inherent energy storage capacity that, like human muscle, can be used to increase

the actuation cycle efficiency in applications such as robotic running (35). This effect is highlighted in Fig. 4.6(b) (movie A6 ▶), wherein the arm of Fig. 4.6(a) is adapted to hold a standard tennis ball. In this test, the linear-parallel cavatappi configuration was initially stretched to store strain energy and subsequently released to launch a tennis ball. This experiment was repeated at pressures of 0, 150, and 200 psi to vary both the actuator stiffness and equilibrium position and thus store varying energy for a given arm angle. The maximum gravitational potential energy position illustrates the maximum height that the tennis ball reached under the above specified pressures. Here, it observed an increase in gravitational potential energy as the pressure increases; at a pressure of 200 psi, the tennis ball exited the frame of the recorded video; thus, it is shown before departure in Fig. 4.6(b).

One more interesting feature of cavatappi artificial muscles are the potential to be scaled down. The limits on miniaturization of these devices are primarily related to the manufacturing limits of the precursor tube. One might initially think that miniaturization of the tube would decrease the flow, which is needed to inflate the actuators because of viscous losses, but the required inflation flow rate in these actuators scales by the square of the internal diameter. The average velocity in a laminar flow scales in the same way for a given applied pressure gradient. We therefore do not expect substantial bandwidth limits associated with viscous losses when miniaturized. To highlight the capacity for miniaturization, we reduced the size of the principal cavatappi studied in this work (Fig. 4.1(c)) by 2.5× through the use of a tube with 250 μm ID and 700 μm OD (Fig. 4.1(f)). Figure 4.6(c) and movie A4 ▶ show the actuation response of this mini-cavatappi under the tensile load generated by a coin that was glued to the end of the muscle. Under this load, the mini-cavatappi contracted 25% when a pressure of 150 psi was internally applied. Fig. 4.6(c) also shows a 4× zoomed image of the coiled section, which highlights the change in pitch of the helical structure during actuation.

4.2.4 Preliminary modeling of cavatappi artificial muscles

Our initial modeling efforts focus on the variation in the cavatappi stiffness and free length in response to internal pressure changes. We know from classical mechanics theory that the torsional stiffness of a hollow tube can be related to the internal and external diameters via

$$k_t = \frac{\pi G}{32l}(OD^4 - ID^4) \tag{4.1}$$

Here, G is the material's shear modulus, l is the length of the tube, and OD and ID are the outer and inner diameters of the tube, respectively. Note that Eq. 4.1 neglects viscous effects. Although we have shown viscoelastic effects to be present in cavatappi, for high bandwidth actuation, these effects would be relatively small. In addition, the internal material damping, apparent in the exponential decay of the ringing response in Fig. 4.4(b), is relatively small.

If we assume that the wall thickness does not change substantially during internal pressurization (only because of Poisson's effect) and add a change in diameter, Δd, to both the OD and ID terms, then we get a fourth-order polynomial for stiffness k as a function of Δd. Under certain conditions, e.g., when $0 < \Delta d/OD < 1$ and $ID \sim OD/2$, which reasonably approximates the conditions for the experiments in this work, the fourth-order polynomial for k can be approximated as linear. Given this result, we can see that the torsional stiffness of an inflating tube like a cavatappi scales approximately with the relationship $k_t = k_{t0} + c_t \Delta d$, where k_{t0} is the original torsional stiffness and c_t is a constant of proportionality. Figure 4.2(a) shows a relatively linear relationship between pressure and diameter, and therefore, the stiffness can also be considered linear in pressure. The torsional stiffness of such a straight tube is directly related to the linear stiffness of a coiled helical spring, and hence, the cavatappi spring stiffness could be modeled as two

springs in parallel, one with some initial stiffness (k_0) and one with a stiffness linearly dependent on pressure (k_p).

In addition to stiffness changes, the free length of the cavatappi changes during pressurization. A prestretched cavatappi with no hanging weight contracts to a new free position when pressurized. This change in length is a result of the local untwisting of the elemental sections. We have shown in our work on TPAs that for a given radial layer, the amount of untwist, and therefore free contraction, is linearly related to the radial strain [315]. To first order, this radial strain is related linearly to internal pressure. It is therefore reasonable to assume that the free retraction length (δx_f) of these actuators is linearly related to internal pressure, a fact verified for pressures above $\sim$60 psi in Fig. 4.4(a) for the lightest load applied (0.1 kg). However, this figure also shows that more advanced nonlinear modeling would be needed for less pressure or higher loads.

$$F_c = (k_0 + k_p)(x + \delta x_f) \tag{4.2}$$

Here, k_0 is the initial cavatappi spring stiffness, k_p is the stiffness changes due to pressurization, δx_f is the free retraction length for the applied pressure, and x is the displacement of the end of the actuator from its initial position. As previously mentioned, it is likely that both k_p and δx_f are linearly related to pressure and could therefore be easily modeled for a given actuator. Even if nonlinearities are present, they could also be modeled or empirically derived to apply the actuator model in Eq. 4.2. Future work will be needed to include viscoelastic effects on stiffness and free retraction lengths, as well as a modeling effort to understand how internal damping is affected by internal pressure and the resulting tube diametral changes. We saw in Fig. 4.4(b) and (c) that the work and power capacities of these devices are input frequency–dependent, so we expect that damping terms may be needed in Eq. 4.2 to accurately predict this time dependence. In addition,

131

the internal material damping apparent in the exponential decay of the ringing response in Fig. 4.4(b) shows that advanced modeling will need to include damping.

4.3   Discussion

Here, we have introduced a low-cost, lightweight, fluidic artificial muscle whose actuation relies upon (i) the anisotropic physical properties introduced into the virgin material through extrusion and enhanced by a cold drawing process, (ii) the reorientation of those properties through a twisting or twisting and coiling process, and (iii) the deformation of the reconfigured material through the application of an internal pressure. The flexibility of cavatappi will allow them to be used on applications over corners/joints such as a knee, elbow, or ankle, because they can be placed under a curved deformation and still actuate. Their simplicity also presents an advantage in applications. Because cavatappi are fabricated from soft PVC tubing, the same tube length could consist of sections where the drawn precursor tube is coiled-twisted, straight-twisted, or simply kept as the original straight drawn configuration. Hence, a single tube length with a coiled section in the middle could serve as (i) the plumbing from the pressure source, (ii) the actuator, and (iii) the tendon running to the point of force application. Such an implementation would decrease the overhead mass and complexity from fittings, increase reliability by eliminating leaks, and decrease maintenance.

The data collected and testing presented herein for cavatappi can be used to develop performance metrics that can be compared with similar actuator technologies. The data in Table 4.1 compare cavatappi with other soft robotic technologies. In addition to Table 4.1, Fig. 4.7 also provides quick comparisons between cavatappi artificial muscles and PPAMs, TPAs, and human skeletal muscles for a variety of performance metrics often reported for artificial muscles: average specific power and specific work, response time,

132

maximum stress and strain, and total contractile efficiency. Once again, we consider cavatappi to be, to an extent, a hybrid configuration between TPAs and PPAMs; thus, Fig. 4.7 compares these and human skeletal muscles. We should note that the response times presented in the spider graph are somewhat subjective estimates of the authors based on the actuation driver. The exact response time depends on the details of the driver (for example, a much faster actuation response can be obtained in thermally activated TPAs when is applied via conduction, as compared with convection), so only categories of response times are presented.

Both Fig. 4.7 and Table 4.1 show that TPAs present high specific work and power as well as high maximum stress and strain, which has led to notable research interest, yet their thermal activation limits their total efficiency and response time. PPAMs show similar maximum actuation stress and strain properties as human muscles but outperform human muscles in specific power, work, and response time. Because they are also pressure driven, similar actuation properties are found for cavatappi artificial muscles as those for PPAMs; however, cavatappi artificial muscles are shown to exceed PPAMs maximum actuation strain and the total system efficiency. Furthermore, when compared with PPAMs, cavatappi artificial muscles are inexpensive ($0.9/m of cavatappi muscle), and because cavatappi fabrication processing embeds similar microstructural anisotropy developed through macroscale features in PPAMs, they are far simpler to fabricate yet develop similar specific power and work metrics. Moreover, PPAMs expand drastically in the radial direction during actuation. Cavatappi bypass this pitfall, relying upon an internal microstructure for anisotropy and developing relatively little helix diametral deformation during actuation (see Fig. 4.5, (a) and (b)).

As we see in Fig. 4.7, cavatappi artificial muscles are capable of mimicking some human muscle properties and outperforming others, such as fast contraction activation, specific power and work, and maximum force and contraction. Furthermore, like human skeletal

133
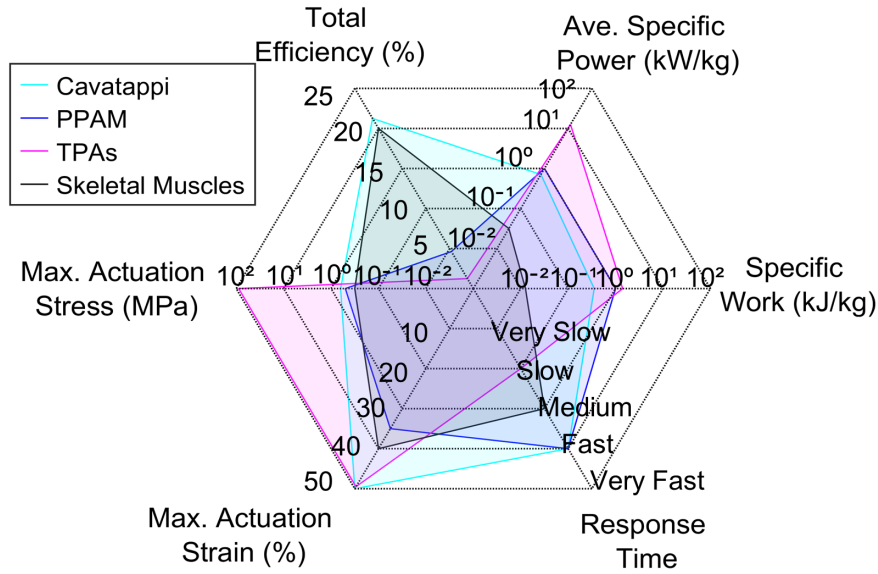
FIGURE 4.7: Artificial muscles performance comparison along with those of skeletal muscles [65, 74, 128, 249, 326, 336, 353]

muscles, cavatappi artificial muscles have the potential for stacking in parallel to increase force generation (see movies A5 ▶ to A7 ▶). We have demonstrated parallel operation here: Nine cavatappi artificial muscles of the same length were connected in parallel to increase the generated torque by nine times on the arm in Fig. 4.6(b). Extending this concept, cavatappi could be bundled similarly to that of biological muscle bundles, as shown in Fig. 4.1(g).

The maximum actuation strain of cavatappi is somewhat limited by the bursting pressure, which we think is related to the ultimate strength of the drawn PVC material in the direction perpendicular (transverse) to the tie-chain molecules running in the helical direction around our actuators. The observed failure mode is one in which bursting occurs in tiers parallel to the draw direction. Increasing wall thickness increase would increase burst pressure but at the expense of diametral expansion and proportionally higher pressure for a given amount of actuation. Similarly, increasing the amorphous region tensile limit would likely lead to increased burst pressure, but work in this area

would need to ensure that the modulus in the hoop direction was not also increased, as doing so would adversely affect actuation.

We have used soft PVC to fabricate these actuators, but there may be polymers with the right combination of anisotropy and radial compliance after cold drawing needed for cavatappi-type actuation, and there may be polymers that allow for a larger maximum pressure or actuate more efficiently. We tested some nylon and polyurethane tubes, but we found that nylon had a hoop stiffness too high to actuate at the pressures that we were able to apply and that polyurethane was so weak radially that it failed at relatively low internal pressures. Although this limited material study used PVC, we have no reason to believe that this is the only material that can serve as cavatappi. On the contrary, we believe that cavatappi can be optimized by designing and/or selecting precursor materials that maximize anisotropic properties and allow those properties to reorient with twisting/coiling.

Reducing pressure required for a given amount of actuator strain should be a primary future goal of this technology, but it is fundamentally a question of actuator efficiency. To reduce the amount of required pressure for a given actuation strain, the actuator efficiency would need to be increased because pressure is directly related to the input work. We have demonstrated an actuator contractile efficiency of about 45%, which is similar to related technologies. If a material could be found that has a lower transverse modulus, then high pressure could be traded for larger requirements on pumped internal volume while maintaining this high actuator efficiency. Doing so though would necessarily increase the rate of tube expansion and therefore more quickly saturate the muscle, thus potentially reducing the actuator stroke and specific work capacity. The wall thickness to inner diameter ratio could potentially be reduced to increase the diametral deformation in response to internal pressure and thereby increase efficiency, but it is critical that the ratio is not reduced so far that the tubes can kink during twisting, which would, in turn,

prevent the actuator fluid flow through the entire actuator length. This "kink" stability is a critical design objective of future optimization, although the reinforcing monofilaments would help to prevent this failure mode. The tubes used in this work have used a predrawn OD/ID ratio of 2.1/2.8, which has resulted in tubes that have yet to fail to actuate due to kinking.

More extensive material modeling of cavatappi would highlight some of these trade-offs and how material properties directly affect actuation performance. Expanding and validating the model of cavatappi artificial muscle presented in this work will be the subject of future work; however, compared with TPAs, it will be substantially simpler because only the mechanical properties of the precursor tube are needed, and there is a reduced need to collect mechanical properties as a function of temperature. Furthermore, the soft PVC used for our cavatappi presents small moisture absorption [344]; thus, moisture dependencies would not need to be included in actuation models, unlike nylon TPAs, which require material models that include thermal and hydroscopic effects [138]. The modeling of PVC cavatappi artificial muscles will need to follow a linear viscoelastic characterization due to the viscoelastic effects that are reported in this work. Last, we expect that future work will include the use of cavatappi artificial muscles in many applications due to their simplicity, low-cost, lightweight, flexibility, efficiency, and strain energy recovery properties, among other benefits.

4.4 Materials and Methods

The material used throughout this work is Soft ND-100-65 Tygon PVC tubing. As described in section A.1, cold drawing, twisting, and coiling of this PVC tubing make the cavatappi artificial muscle. The results presented in this work use the cavatappi in Fig. 4.1(c) with linear density of 0.014 g/mm and dimensions in Fig. A.2 (except the

mini-cavatappi was used in Fig. 4.6(c) and movie A4 ▶). This cavatappi was reinforced with an internal nylon monofilament inserted into the hollowed tube during fabrication (see section A.1). The reinforcement was found to reduce a pinching-type failure mode observed in life-cycle testing. In addition, it was found that over thousands of cycles, actuation creep was observed for cavatappi without a reinforcement. The reinforcing monofilament provided a restoring force after pressure was removed, which helped to reduce actuation creep. For all actuation tests and metrics calculations performed in this work, we used a Polytec OFV-5000 Vibrometer controller with the OFV-534 optics head. To apply and measure pressure in these tests, we used a RG1262-1500 pressure regulator along with QB1T closedloop servo system and a DS-series pressure transducer from ProportionAir. The voltage outputs of these systems are linearly related to a change of position of the object on which it focuses (vibrometer) and change in pressure (pressure transducer) (Fig. A.3). This voltage was recorded by a National Instruments PXIe-6361 multifunction data acquisition card and subsequently analyzed to develop the data presented in this work. More details on testing methods and calculations of metrics in Table 4.1 and Fig. 4.7 are found in the Supplementary Materials.

CHAPTER 5

MATERIAL-BASED MODELING OF CAVATAPPI ARTIFICIAL MUSCLES

Soft actuators show much promise for use in bioinspired and biomimetic robotics as they share many similarities with actuation systems found in nature. Twisted and coiled actuators are soft actuators that have been shown to outperform many metrics of biological muscles, leading researchers to derive actuation models for future control and implementation. Although models have been proposed for twisted and coiled carbon nanotubes and polymer fibers, cavatappi artificial muscles—a novel twisted and coiled fluidic soft actuator—have not been modeled yet. This work establishes a framework for modeling cavatappi using the thick-wall pressure vessel stress analysis and the spring theory. The presented model uses the mechanical properties of the precursor drawn material used for fabrication, initial twist (internal fiber angle), muscle geometry, and internal pressure to predict the artificial muscles contraction under different external loads. The model predictions agree with the experimental results for cavatappi of different internal fiber angles and load conditions. Given their potential implementation in bioinspired applications, our model can help better design, optimize, and control the actuation response of cavatappi.

5.1 Introduction

The need for safe human-machine interactions (HMIs) [111, 182, 194, 272] in applications such as smart exoskeletons and prosthesis [57, 334], wearables [10], surgical tools [48], and even humanoids [25, 52] has led many in search for new soft actuation technologies. Unlike traditional actuators, soft actuators have the potential to mimic the

adaptive dynamic behavior of biological muscles, which could enable an affordable solution for HMIs [139]. As a result, many new soft actuation technologies are developed every year [8, 34, 128, 140, 185, 189, 345]. Although they share the common goal of achieving compliant actuation systems capable of adapting to unstructured environments safely, their activation, materials, morphology, and performance can substantially vary from one to another. However, a subgroup of these actuators employ twisting and coiling precursor structures and therefore share similar fabrication procedures, actuation principle, and helical shape. These soft actuators are twisted/coiled carbon nanotubes (CNTs), twisted/coiled polymer actuators (TCPAs), and cavatappi artificial muscles.

Initially, high-force/low-stroke straight CNTs actuators were twisted and/or coiled to create torsional and/or linear actuators [105, 196, 197]. By twisting and coiling, linear CNT actuators increased their actuation contraction 10 times the contraction found in the straight configuration while maintaining high actuation forces. CNTs use ion transport in the material matrix to generate asymmetric swelling (radial expansion and axial contraction) of the precursor straight CNTs, leading to torsion or contraction when only twisted or twisted and coiled, respectively. Similar actuation responses were obtained in twisted/coiled CNTs using different activation methods, including electrical, chemical, and photonic excitations [197].

Next, inexpensive drawn fibers such as fishing lines and sewing threads used the same fabrication concept to create twisted and coiled polymer actuators (TCPAs). Similar to CNT actuators, the source of actuation is due to the axial contraction and radial expansion of the straight precursor fibers resulting from the anisotropic nature of the material. However, for TCPAs the asymmetric growth in the drawn fibers is driven by changes in temperature in the polymer [127, 128].

Although CNTs and TCPAs can considerably outperform many metrics of biological muscles such as specific peak and average power, specific work, and actuation stress,

Introduction

Section 1

- Introduction to twisted & coiled soft actuators: CNTs, TCPAs, and cavatappi artificial muscles.
- Cavatappi artificial muscles actuation mechanism
- Scope of the study

Material Properties

Section 2

- Linear elastic material properties characterization of the drawn precursor tube used for cavatappi artificial muscles fabrication: E_1, E_2, G_{12}, G_{23}, ν_{12}, and ν_{23}

Section S1 & S2

- Sample preparation for experimental testing characterization
- Experimental testing methods

Model Framework

Section 3

- Elemental unit:
- Transversely isotropic rotated compliance matrix.
- Formulate stress tensor, using Lamé's equations & shear stress from isotorque (cavatappi torsional actuator) or isotonic load (cavatappi artificial muscle)
- Solve for shear strain
- Convert shear strain in axial contraction (cavatappi artificial muscle)

Results

Section 4

- Experimental and model results:
Cavatappi torsional actuator
- Free torsion conditions
- Isotorque conditions
Cavatappi artificial muscle
- Isotonic conditions

Section S1 & S3

- Cavatappi torsional actuator and artificial muscle fabrication
- Experimental testing methods

Conclusions & Discussion

Section 5

- Discussion on the experimental and model results
- Fiber angle study and optimization
- Future directions in viscoelastic material properties characterization, modelling, and control strategies

FIGURE 5.1: Paper structure at a glance.
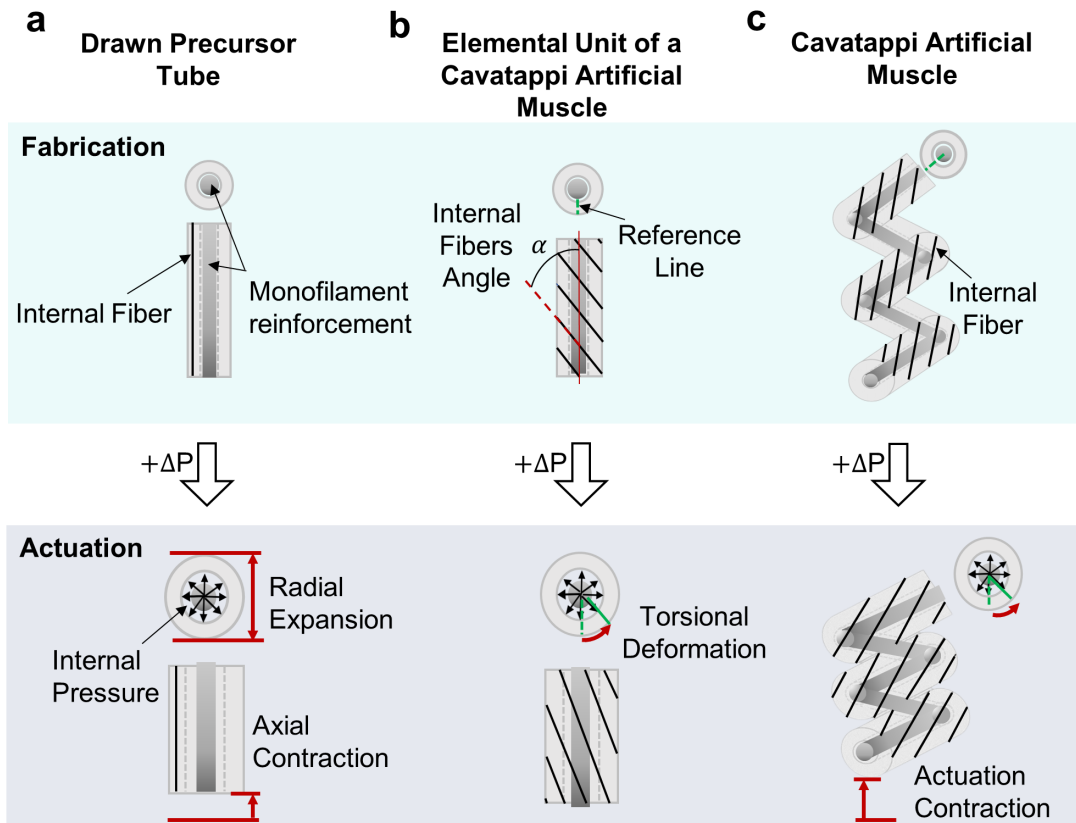
FIGURE 5.2: Different states of fabrication and actuation of cavatappi artificial muscles. (a) Straight untwisted drawn precursor polymer tube. (b) Cavatappi elemental unit, which acts as a cavatappi torsional actuator. (c) Cavatappi artificial muscles; axial actuator.

they fall short when performing other metrics such as time response or efficiency. To sidestep the drawbacks of CNTs and TCPAs, the previously mentioned fabrication process (twisting and coiling) and actuation principle was used in thin, soft PVC tubes to create fluid-driven soft actuators named cavatappi artificial muscles [140]. By sacrificing some of the high-performance metrics of CNTs and TPAs (specific work and power and actuation stress), cavatappi were able to improve response time and efficiency and better match many metrics of biological muscles, which could potentially contribute to an improvement in HMI applications.

Cavatappi artificial muscles are fabricated from extruded and cold-drawn polymer tubes. Both material processes, extruding and cold-drawing, create axially orientated tie-chain

molecules responsible for high axial strength. At the same time, the mechanical properties in the radial (hoop) direction remain mostly unchanged, leading to an increase of anisotropy in the straight tubes [261, 268]. While the extrusion process is required for the fabrication of the tubular structure, cold-drawing is a post-process conducted to enhance the anisotropy of the straight precursor tubes (Fig. 5.2(a), Fabrication). Upon internal pressurization, the drawn precursor tube develops axial contraction and radial expansion (Fig. 5.2(a), Actuation). The drawn tubes can then be twisted to reorient the high-stiffness molecular chains into a helical configuration (Fig. 5.2(b), Fabrication) so that internal pressurization generates shear deformation on the straight/twisted tube (Fig. 5.2(b), Actuation). Here, the twisted tubes are thought to be "elemental units" of the twisted/coiled actuator because the localized shear deformation (untwist) is the contraction generator in the cavatappi artificial muscle.

The orientation of the twisted outer fiber is shown by the fiber angle, α, in Fig. 5.2(b) which is the angle between the original draw direction and the new oriented internal fiber. If this straight/twisted tube is thermally annealed at 90°C to remove internal stresses and reset the actuator's unstressed static equilibrium position, then the twisted configuration can be used as a torsional actuator under the name of cavatappi torsional actuator. After twisting, a drawn tube can also be coiled (Fig. 5.2(c), Fabrication) to create a cavatappi artificial muscle. When this helical configuration is thermally annealed as specified before, the internal stresses are released, and this new shape holds after the loads that are used to maintain the configuration during the coiling process are removed. In these coiled configurations, when internal pressure is applied, the untwist in the elemental units presents as a helical contraction in the overall artificial muscle coil pitch (Fig. 5.2(c), Actuation).

A reinforcing monofilament made of nylon 66 (used to increase actuator lifetime and reduce actuation creep) is kept inside the tubular structure through the entire fabrication

142

process and is thus twisted and coiled. This monofilament does no work during actuation, as external loads on the cavatappi are not attached to the reinforcing monofilament. Thus, the reinforcement is solely there to increase the structural stability of the cavatappi. Although the actuation mechanism of cavatappi artificial muscles seems to follow a similar pattern to the ones found in CNTs and TCPAs, contrary to those cavatappi are relatively new, and currently there are no models to predcit the actuation behaviour of cavatappi. To this end, we focus on modeling the actuation response of cavatappi artificial muscles, in order to provide a better understanding of their actuation mechanism and contribute to future control strategies, so that eventually they can be implemented in HMI applications efficiently and safely.

This work introduces a material-based model for cavatappi artificial muscles (see Fig. 5.1). Modeling cavatappi artificial muscles using precursor material-based models is convenient for their design and optimization and necessary for control as accurate initial actuation predictions output are required, which, in turn, will allow for their use in bioinspired and biomimetic applications. Previous models for CNTs and TCPAs help inform about modeling approaches for cavatappi artificial muscles as they all share similarities in fabrication, actuation mechanism, and morphology. Most of the precursor material-based models for CNTs and TCPAs have in common that they combine the mechanical spring theory and continuum mechanics to predict their actuation [73, 116, 137, 165, 175, 309, 352, 356].

In this work, we present an analytical model for cavatappi artificial muscles that predicts actuation strain under isotonic loads using the material properties of the precursor drawn tubes and initial twist as constant model inputs and internal pressure and lifting loads as variable inputs. In doing so, we start our modeling by assuming the material is transversely isotropic, then forming the rotated compliance matrix of the elemental unit using the elastic material properties of the drawn precursor tube (also obtained in this work) and the initial twist of the internal fibers (fiber angle, α). Here, the compliance

143

matrix is used to relate stresses and strains of the elemental unit. Next, we formulate the stress distribution in the elemental unit as a result of internal pressurization using Lamé's equations (thick-walled vessel stress analysis), which in turn, allows us to predict the torsional actuation of the elemental unit when using the compliance matrix. To relate torsion at the elemental unit with the contraction of the helically shaped cavatappi, we apply the elementary spring theory to solve for the applied shear stress by the isotonic axial load on the cavatappi artificial muscle (similar to those models presented for CNTs and TCPAs).

Finally, we assess the presented model predictions using experimental results of cavatappi torsional actuators under free torsion and constant torque and cavatappi artificial muscles under different isotonic loads. The presented precursor material-based model agrees with the experimental data under all the different testing conditions for cavatappi torsional actuators and artificial muscles.

5.2   Precursor Material Properties

This work compares the model predictions with experimental results of cavatappi torsional actuators and artificial muscles. Our model requires the precursor material properties of the drawn tube as inputs. Therefore, in this section, we present the elastic mechanical properties characterization of drawn (3:1 draw ratio) soft ND-100-65 Tygon PVC tubing used in this work (Fig. 5.2(a), Fabrication), while the sample preparation and testing methods are presented in Section B.1 and B.2 in the Supplementary Materials, respectively.

As previously mentioned, the drawn precursor tube is assumed to be transversely isotropic, which is a fair assumption after inducing permanent axial deformation while cold drawing the tubes. Fig 5.3(a) shows the directions. Before twist, the 1-direction is axial and

along the direction of the polymer chains. After twist, the 1-direction rotated with the polymer chains. The material is isotropic in the 2-3 plane as these directions are both perpendicular to the polymer chains and radial before twisting. Given these directions and assuming linear elasticity, the required mechanical properties to predict the actuation response of cavatappi artificial muscles are:

- Axial modulus, E_1

- Radial modulus, E_2

- Shear moduli: G_{12} and G_{23}

- Poisson's ratios: ν_{12} and ν_{23}

To ensure minimal viscous effects during the linear elastic material characterization approximation, as well as the experimental actuation results acquisition, the experimental tests presented in this work has been conducted in the time range of few seconds (~ 3 seconds for cycle). These short time-scales should avoid material relaxation, and in turn, large viscous effects. The measured properties are expected to be suitable input parameters to predict actuation responses for short-term actuation cycles—actuation cycles contained in the previously mentioned time range. In contrast, those actuation cycles in a longer time range where viscous effects are notable will require a viscoelastic characterization of the precursor material (long-term actuation cycles) to predict the actuation response cavatappi successfully. Although characterizing the viscoelastic behavior of the precursor tubes is critical for accurate predictions of long-term actuation cycles, this work focuses its effort on modeling the short-term actuation response of cavatappi artificial muscles because it is a fundamental step for future control. However, the model presented will also allow viscoelastic properties to be used as inputs to predict actuation under long-term conditions. Furthermore, for each experimental test presented in this

145
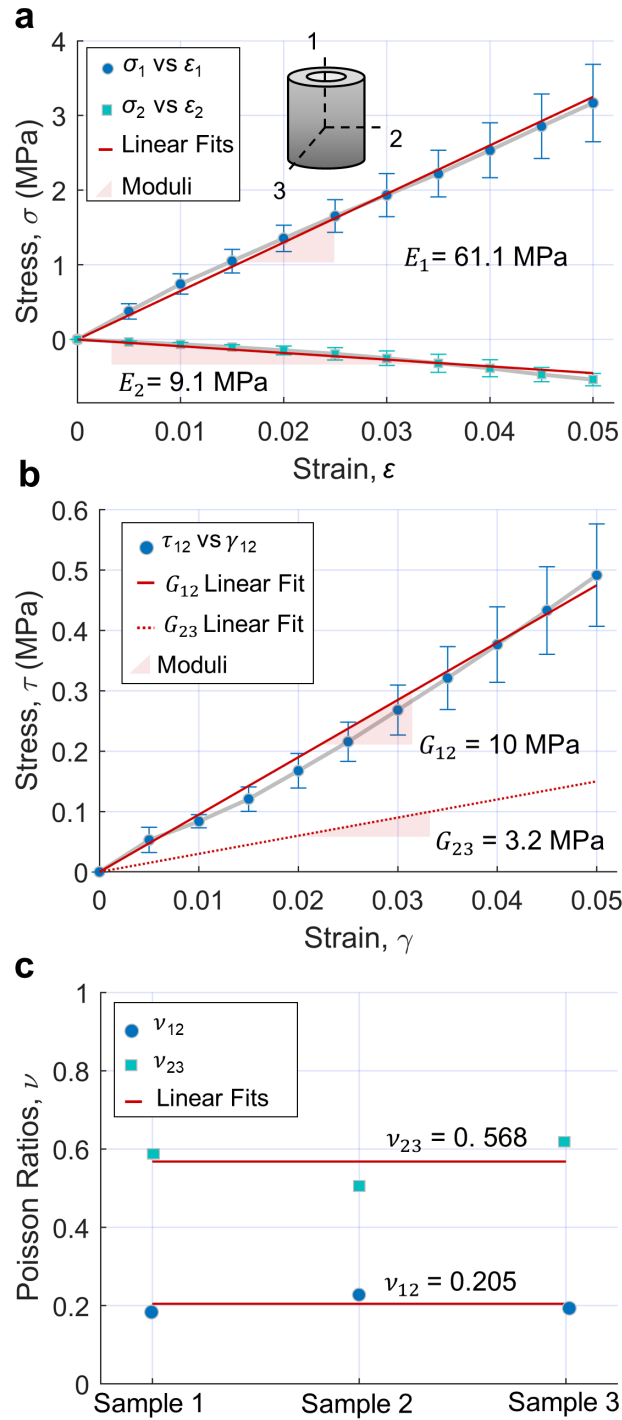
FIGURE 5.3: Experimental results and linear fits for the precursor tube mechanical properties. (a) Axial and radial stress-strain results with the calculated moduli (E_1 and E_2). (b) Shear stress-strain results in the 1-2 direction with the calculated shear modulus, G_{12}, and an approximation of G_{23} based on a transversely isotropic assumption (see Eq. 5.1). (c) Poisson's ratio in the 1-2 and 2-3 directions for three samples along with their averages. Note that the principal coordinate system for a precursor tube is shown in a.

146

work, the samples were precycled with three loading/unloading initial cycles under the same testing conditions to eliminate first-cycle effects (Mullin's Effect) resulting from polymer chains reorientations and ruptures. [192].

Fig. 5.3 presents the approximated linear elastic material properties for E_1, E_2, G_{12}, G_{23}, ν_{12}, and ν_{23} (note that G_{23} is calculated using transversely isotropic material relations and not experimentally obtained, as it will be explain later). Fig. 5.3(a) presents the results for axial and radial stress-strain (σ vs. ε) tests along with the 95% confidence intervals of data taken from trials on three different samples during loading. Here, we use a linear fit to approximate axial, E_1, and radial, E_2, moduli as 61.1 and 9.1 MPa, respectively. Similarly, Fig. 5.3(b) presents the results of shear stress-strain (τ_{12} vs γ_{12}) tests along with the 95% confidence intervals of data taken from trials on three different samples during loading. The shear modulus in the 1-2 dir., G_{12}, was found to be 10.2 MPa by using a linear approximation. Furthermore, Fig. 5.3(b) also presents the shear modulus in the 2-3 dir. (plane of isotropy), G_{23}, from the elasticity theory and expressed as

$$G_{23} = \frac{E_2}{2(1 + \nu_{23})}, \tag{5.1}$$

where E_2 and ν_{23} are the modulus and Poisson's ratio in the plane of symmetry. Although in Figs. 5.3(a) and (b), linear approximations are fitted to the experimental results to approximate the elastic moduli during loading, small hysteresis resulting from viscous effects in the material are observed in the loading-and-unloading tests (not shown in Fig. 5.3). However, the viscous effects here are found to be minimal due to the short-term testing cycles and can be neglected when predicting the actuation response under this condition. Finally, Fig. 5.3(c) presents the values for Poisson's ratios in the 1-2 dir., ν_{12}, and 2-3 dir., ν_{23}, for three test samples. Approximated values for ν_{12} and ν_{23} were calculated using averages. As a result, ν_{12} was found to be 0.205 and ν_{23} equal to 0.568.

Stage 1. Model Inputs

- Geometry of the cavatappi artificial muscle and outer fiber angle, α

- Linear elastic mechanical properties of the straight drawn precursor material

  Axial modulus, E_1
  Radial modulus, E_2
  Shear moduli, G_{12} and G_{23}
  Poisson's rations, ν_{12} and ν_{23}

- Internal pressure
- Isotonic load (cavatappi artificial muscles) or isotorque load (cavatappi torsional actuator)

Stage 2. Elemental Unit

- Forming the transversely isotropic rotated compliance matrix, $[\bar{S}]$

$$[\bar{S}] = [T_\sigma]^T \, [S] \, [T_\sigma]$$

- Formulate the stress tensor, $[\sigma]_{z\theta r}$, using Lamé's Equations

&

Cavatappi Torsional Actuator

- Shear stress due to pure torque, $\tau_{z\theta(tor)}$

or

Cavatappi Artificial Muscle

- Shear stress due to pure torque w/ curvature effects & direct shear, $\tau_{z\theta(tor \, \& \, cur.eff.)} + \tau_{z\theta(dir)}$

$$[\varepsilon]_{z\theta r} = [\bar{S}][\sigma]_{z\theta r}$$

Stage 3. Cavatappi Torsional Actuator & Artificial Muscle Actuation

Cavatappi Torsional Actuator

- Shear strain, $\gamma_{z\theta}$, used to calculate torsion (untwist), due to pure torque, $\phi_{z\theta}$

Cavatappi Artificial Muscle

- Shear strain, $\gamma_{z\theta}$, used to calculate axial contraction, ε_a, using the spring theory

FIGURE 5.4: Model flowchart.

148

5.3 Modeling Cavatappi Torsional Actuators and Artificial Muscles. Framework

After characterizing the elastic mechanical properties of the precursor tubes used to fabricate cavatappi artificial muscles, we next present an analytical model to predict torsional and linear actuation of cavatappi torsional actuators and artificial muscles under external loads. Fig. 5.4 shows the flowchart of this model.

First, the obtained mechanical properties, geometric parameters, internal pressure, and external loads are used as inputs in the model (stage 1). Here, the mechanical properties and geometry are considered constant parameters, while internal pressure and the axial load on the cavatappi artificial muscles or torsional load on the cavatappi torsional actuator are variables. Next, stage 2 uses the model inputs, to calculate the shear strain, $\gamma_{z\theta}$, in the elemental unit using a twisted cylindrical laminate analysis to form the transversely isotropic rotated compliance matrix, $[\bar{S}]$, (rotation of the mechanical properties) and formulating the stress tensor, $[\sigma]_{z\theta r}$. The stress tensor is found using the internal pressure along with the Lamé's equations (thick-walled vessel stress analysis) and external loads applied force or torque. When calculating the shear stress, $\tau_{z\theta}$, resulting from the external axial or torsional load, we differentiate two cases, cavatappi torsional actuator, and artificial muscles. In the first case, the shear stress is exclusively produced by the pure torque applied to the torsional actuator $(\tau_{z\theta(\text{tor})})$, while in the second case, the shear stress due to the axial load applied on the cavatappi artificial muscle is calculated using the spring theory. For this last case, the shear stress generated by the axial load must take into account curvature effects $(\tau_{z\theta(\text{tor \& cur.eff.})})$, in addition to the direct shear $(\tau_{z\theta(\text{dir})})$. This is done using the elementary spring theory, which provides a relationship to obtain the total shear stress in the elemental unit generated by the isotonic load.

Combining the stress analysis with the rotated compliance matrix, the elemental unit's shear strain (untwist) can be predicted for the previous two cases. Finally, at stage 3, the elementary spring theory is used one last time to relate the shear strain developed in the elemental unit to the axial contraction in the cavatappi artificial muscle, while for a cavatappi torsional actuator, the shear strain obtained from combining $[\bar{S}]$ and $[\sigma]_{z\theta r}$ can be easily related to untwist using the length and the outer radius of the actuator. Note that the model lay-out in Fig. 5.4 can be used to predict the actuation response for variable external loading when using a feedback control system capable of informing the model about external load changes. The performance of such a control system will depend on the controller bandwidth. The higher the bandwidth, the faster the stress tensor will be updated, leading to faster actuation predictions, resulting in higher control capacity.

To explain every module presented in Fig. 5.4 in detail, this section consists of the following sections: elemental unit properties rotation, thick-walled vessel stress analysis, shear stress calculation for a cavatappi torsional actuator and artificial muscle, and contraction actuation on the cavatappi artificial muscle using the spring theory.

5.3.1 Elemental Unit Mechanical Properties Rotation

As mentioned in Section 5.2, transverse isotropy and linear elasticity is assumed for the precursor tube. We establish that the properties in the 2 and 3 directions are the same and different from those in the 1 direction (see Fig. 5.3(a)). As previously mentioned, this assumption relies on the fabrication and processing of the straight polymer tubes used in this work. With these assumptions and using Voigt notation, we form the compliance matrix of straight drawn precursor tubes as

$$[S] = \begin{bmatrix} \dfrac{1}{E_1} & \dfrac{-\nu_{12}}{E_1} & \dfrac{-\nu_{12}}{E_1} & 0 & 0 & 0 \\[2mm] \dfrac{-\nu_{12}}{E_1} & \dfrac{1}{E_2} & \dfrac{-\nu_{23}}{E_2} & 0 & 0 & 0 \\[2mm] \dfrac{-\nu_{12}}{E_1} & \dfrac{-\nu_{23}}{E_2} & \dfrac{1}{E_2} & 0 & 0 & 0 \\[2mm] 0 & 0 & 0 & \dfrac{1}{G_{23}} & 0 & 0 \\[2mm] 0 & 0 & 0 & 0 & \dfrac{1}{G_{12}} & 0 \\[2mm] 0 & 0 & 0 & 0 & 0 & \dfrac{1}{G_{12}} \end{bmatrix},$$

(5.2)

For the twisted cavatappi elemental unit, the compliance matrix must be rotated by the same angle that the internal fibers are rotated, α. This is the angle of the internal fibers at the outer surface of the twisted tube to the 1-3 or 1-2 planes (see Fig. 5.6 or Fig. 5.4), and is dictated by the amount of inserted twists in the precursor drawn tube during fabrication. While the tubes are thick walled, we do not account for how this angle changes throughout the thickness, as accounting for that change in angle would add significant complication to the model [137, 315] and likely little improvement on predictions (see Section 5.4. The rotation is conducted using the following transformation matrix,

$$[T_\sigma] = \begin{bmatrix} c^2 & s^2 & 0 & 0 & 0 & 2cs \\ s^2 & c^2 & 0 & 0 & 0 & -2cs \\ 0 & 0 & 1 & 0 & 0 & 0 \\ 0 & 0 & 0 & c & -s & 0 \\ 0 & 0 & 0 & s & c & 0 \\ -sc & sc & 0 & 0 & 0 & c^2 - s^2 \end{bmatrix}, \tag{5.3}$$

where c and s is $cos(\alpha)$ and $sin(\alpha)$, respectively. Finally, the compliance matrix is rotated using

$$[\bar{S}] = [T_\sigma]^T [S][T_\sigma], \tag{5.4}$$

and the strain tensor can be obtained from

$$[\varepsilon]_{z\theta r} = [\bar{S}][\sigma]_{z\theta r}. \tag{5.5}$$

Eq. 5.5 relates the strain and stress tensor in the zθr coordinate system (see Fig. 5.4 stage 2) using the rotated compliance matrix. This equation will allow calculating the shear strain in the elemental unit that will later be used to predict the actuation contraction of cavatappi artificial muscles, but first, we will need to solve for the stress tensor in the elemental unit (see Sections 5.3.2 and 5.3.3) to serve as inputs to Eq. 5.5.

5.3.2 Thick-walled Vessel Stress Analysis

The internal pressurization in the elemental unit is one of the sources that contribute to the stress tensor $[\sigma]_{z\theta r}$ in Eq. 5.5. The vessel stress analysis may apply when evaluating
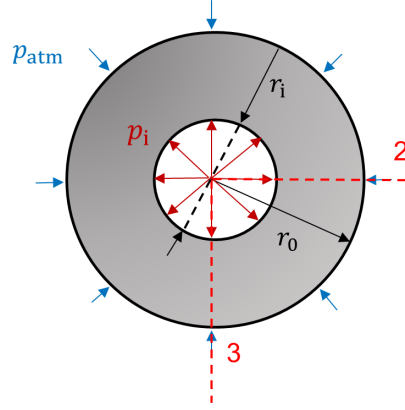
FIGURE 5.5: Cross section view of a cavatappi elemental unit with applied pressures.

internally pressurized tubular structures like the one presented in this work. Here, we must differentiate between thin and thick-walled vessel stress analysis. In this work, we used the second case, as the wall thickness of the cavatappi elemental unit exceeds the inner radius by more than 10% (it is $\sim 50\%$), which is the requirement for the thin-walled vessel assumption. As a result, the stress distribution of the elemental unit is classified as thick-walled, and the variation of stress with radius cannot be disregarded.

For a thick-walled long tube case subjected to uniform internal and external pressure (see Fig. 5.5), the deformation is the same in the z-direction. Assuming that the ends of the tube are unconstrained and that the length of the elemental unit is much longer than the outer diameter of the tube, the stress distribution for radial, σ_r, tangential, σ_θ, and axial, σ_z stresses can be calculated as

$$\sigma_r = \frac{r_i^2 p_i - r_0^2 p_{atm}}{r_0^2 - r_i^2} - \frac{(p_i - p_{atm})r_i^2 r_0^2}{(r_0^2 - r_i^2)r^2}, \tag{5.6}$$

$$\sigma_\theta = \frac{r_i^2 p_i - r_0^2 p_{atm}}{r_0^2 - r_i^2} + \frac{(p_i - p_{atm})r_i^2 r_0^2}{(r_0^2 - r_i^2)r^2}, \tag{5.7}$$

153

$$\sigma_z = \frac{r_i^2 p_i - r_0^2 p_{atm}}{r_0^2 - r_i^2}. \tag{5.8}$$

Eqs. 5.6, 5.7, and 5.8, a.k.a. Lamé's equations, are used to calculate the stresses in the cavatappi elemental unit which are also inputs in Eq. 5.5. Additionally, the radial displacement of any radial position through the wall thickness can be also derived using

$$u = \frac{1 - \nu_{23}}{E_2} \frac{(r_i^2 p_i - r_0^2 p_{atm})r}{r_0^2 - r_i^2} + \frac{1 + \nu_{23}}{E_2} \frac{(p_i - p_{atm})r_i^2 r_0^2}{(r_0^2 - r_i^2)r}. \tag{5.9}$$

Eq. 5.9 is used in the model to calculate radial growth of the elemental unit as a function of pressure during actuation. Note that Eqs. 5.6, 5.7, 5.8, and 5.9 can be considerably simplified if gauge pressure is used as p_i and p_0 is equal to zero. Because of the large radial displacements expected under the actuation applied pressures, we accounted for geometric changes by using $r_i = r_i + u(r = r_i)$ and $r_0 = r_0 + u(r = r_0)$ in Eqs. 5.6, 5.7, 5.8 to find the stresses from the applied pressure. Later, we will also use the updated geometry to find the cross-sectional area, A, and polar moment of inertia, J.

5.3.3 Shear stress, $\tau_{z\theta}$

The thick-walled vessel stress analysis (Section 5.3.2) allows to calculate σ_r, σ_θ, and σ_z resulting from internal pressurization in the elemental unit. However, to complete the stress tensor, $[\sigma]_{z\theta r}$, in Eq. 5.5, we still require to calculate the shear stress, $\tau_{z\theta}$ in the elemental unit. As previously mentioned, to calculate $\tau_{z\theta}$, we distinguish two cases, (i) shear stress in the cavatappi elemental unit when operating as a torsional actuator (twisted straight tube, a.k.a. cavatappi torsional actuator) and (ii) shear stress in the cavatappi elemental unit when operating as an axial actuator (twisted and coiled tube, a.k.a. cavatappi artificial muscle). In the first case, the elemental unit is under a pure

154

torsional load, while the second case is under a lifting load (axial load). Under the lifting load, in addition to the torsional load, direct shear and curvature effects must be taken into consideration. As the model presented in this work can predict both torsional (cavatappi torsional actuator) and linear (cavatappi artificial muscle) actuation, in this section, we present methods to calculate the shear stress for both cases.

5.3.3.1 Shear stress, $\tau_{z\theta}$. Cavatappi Torsional Actuator

For a torsional actuator loaded under an isotorque, T_{iso}, the shear stress is calculated using

$$\tau_{z\theta(tor)} = \frac{T_{iso}r}{J},\tag{5.10}$$

where r is the radial position and J is the polar moment of inertia at a given internal pressure. While the applied torque is a constant, the shear stress changes as a function of internal pressure due to the radial growth that varies the r and J parameters. Such increments are calculated using the radial displacements as a function of pressure, u, from Eq. 5.9, and updated into Eq. 5.10. As a result, the shear stress under pure torsion is obtained at any pressure state.

5.3.3.2 Shear stress, $\tau_{z\theta}$. Cavatappi Artificial Muscle

As previously mentioned, the calculation for shear stress, $\tau_{z\theta}$ in Eq. 5.10 is not valid to calculate the shear stress on the elemental unit of the cavatappi artificial muscles as different loading conditions are applied. Here, torque shear stress along with curvature effects and direct shear stresses must be taken into account. In doing so, the spring actuator shape is considered a straight bar under torsion for small helix angles (this

155

assumption is valid for nearly all practical springs). Under this assumption, we use an approximate theory for small index considering curvature effects presented by Wahl [338]. This approximate solution is accurate for practical uses within about 2 percent errors when compared to the exact solution, and experimental testing [338].

Wahl formulates the shear stress distribution of the cross-section area of the elemental unit using the approximate spring theory as

$$\tau_{z\theta(\text{tor \& cur.eff.})} = \frac{FR^2x}{J\left(R - \dfrac{2r^2}{16R} - x\right)}, \tag{5.11}$$

where F is the axial load (lifting mass), R is the mean radius of the coil, r is the radial position of the precursor tube, and x is a radial coordinate that varies from $r_0 - 4r_0^2/16R$ to $-r_0 - 4r_0^2/16R$. Eq. 5.11 is used to solve the shear stress, $\tau_{z\theta(\text{tor \& cur.eff.})}$, generated by the localized torque under the axial load on the cavatappi artificial muscle taking into account the curvature effects of the spring. However, in order to calculate the total shear stress, $\tau_{z\theta(\text{total})}$, on the elemental unit, we must add the direct shear stress, $\tau_{z\theta(\text{dir})}$, obtained as

$$\tau_{z\theta(\text{dir})} = F/A, \tag{5.12}$$

where F is the axial load (lifting mass) and A the updated cross section are of the tube,

$$\tau_{z\theta(\text{total})} = \tau_{z\theta(\text{tor+cur.eff.})} + \tau_{z\theta(\text{dir})}. \tag{5.13}$$
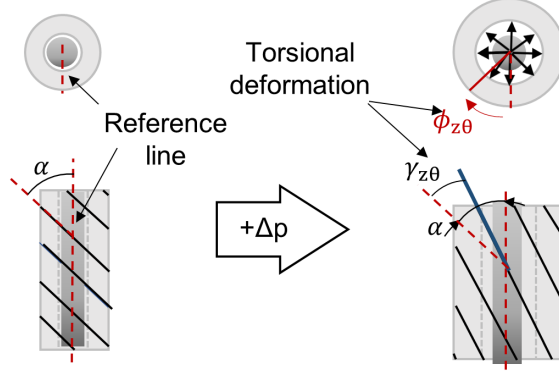
FIGURE 5.6: Torsional actuation of the elemental unit.

5.3.4 Contraction Actuation on the Cavatappi Artificial Muscle

Once the stresses on the elemental unit are found (Sections 5.3.2 and 5.3.3) and the rotated compliance matrix, $[\bar{S}]$, is solved, we can use the last row from Eq. 5.5,

$$\gamma_{z\theta} = \bar{S}_{16}\sigma_z + \bar{S}_{26}\sigma_r + \bar{S}_{36}\sigma_\theta + \bar{S}_{55}\tau_{z\theta}, \tag{5.14}$$

to calculate the shear strain, $\gamma_{z\theta}$. Fig. 5.6 show the shear deformation and untwist produced in the elemental unit when internal pressure, p_i, is applied.

Once the shear strain is calculated, it can be directly related to the axial contraction of the cavatappi using the general equation for spring's deflection presented by Wahl. Here, Wahl uses the point of maximum shear stress in the cross-section area to predict springs' deflections as it is shown to be the driving radial position of springs' contractions used in the practical design of springs. Furthermore, this approximation has been validated using finite element methods [67, 231, 308] and widely used in the modeling of TCPAs [6, 165, 175, 356]. For a cavatappi artificial muscle under an axial load, the maximum shear stress occurs at $r = r_0$ and $x = -(r_0(p_i)) - 4(r_0(p_i))^2/16R$, while for a cavatappi torsional actuators the maximum shear stress is at $r = r_0$. To calculate the defection,

157

we assume again that the spring may be considered as a straight bar of length equal to $2\pi n_{\mathrm{c}} R$ where n_{c} is the number of active coils. The angular deflection, β, is formulated as

$$\beta = \int_0^{2\pi n_{\mathrm{c}} R} \frac{\gamma_{\mathrm{z\theta}}}{r_0} dx = \frac{2\pi n_{\mathrm{c}} R \gamma_{\mathrm{z\theta}}}{r_0},$$ (5.15)

Finally, we multiply the angular deflection by the effective moment arm of the axial load, F, (mean radius, R) and divide by the initial cavatappi length, H. This leads to the actuation strain, which is found as

$$\varepsilon_{\mathrm{a}} = \frac{2\pi n_{\mathrm{c}} R^2 \gamma_{\mathrm{z\theta}}}{r_0 H}.$$ (5.16)

5.4 Results

With the actuation mechanism explained, the elastic material properties of the precursor drawn tube collected, and the actuation model derived, we present an initial experimental validation of the model. Here, cavatappi torsional actuators and artificial muscles are tested under different conditions. First, we focus on assessing the torsional actuator model under two actuation scenarios: free torsion and isotorque loading conditions. For the free torsion tests, we evaluate the model for two different internal fiber angles. Second, we test the actuation contraction of cavatappi artificial muscles under three different loads, 2, 3, and 4 N. The methods used to fabricate cavatappi and collect the experimental testing data are presented in Section B.1 and B.3, respectively.
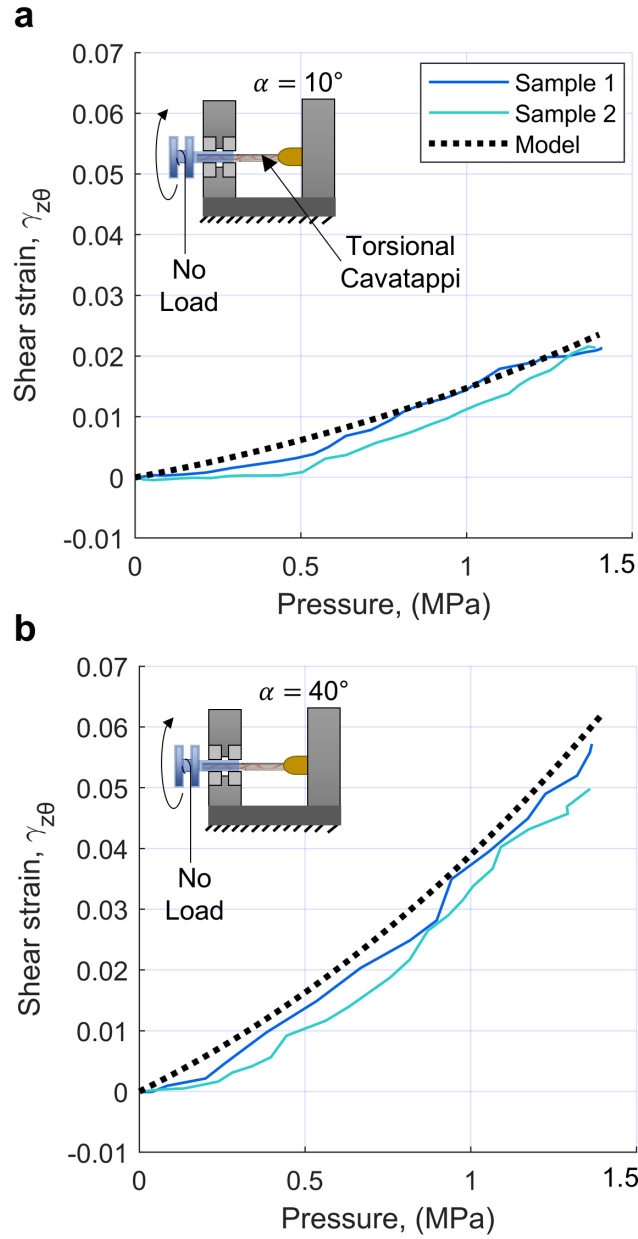
FIGURE 5.7: Actuation results of torsional cavatappi along with model predictions under free torsion conditions. (a) Torsional cavatappi actuator with a fiber angle, α, of 10°. (b) Torsional cavatappi actuator with a fiber angle, α, of 40°.

5.4.1 Cavatappi Torsional Actuator

As previously mentioned, the model presented in this work allows predicting the actuation response of cavatappi torsional actuators (torsion) when using the shear stress in the
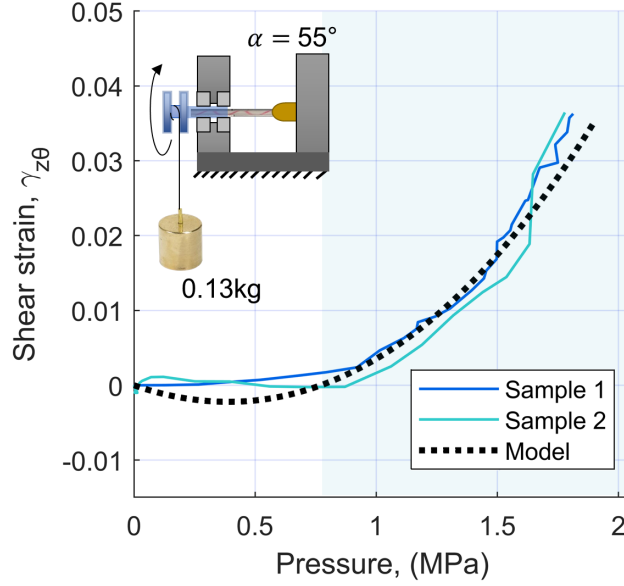
FIGURE 5.8: Actuation results of 55° torsional cavatappi along with model predictions under an isotorque load of 4 Nmm.

elemental unit under exclusive pure torsion conditions or artificial muscles (contraction) when accounting for pure torsion with curvature effects and direct shear stress. Additionally, the model also allows predictions for cavatappi with different internal fabrication fiber twists (fiber angle), as we use the material properties of the precursor drawn tube as inputs. This can inform of the fiber angle capable of developing the maximum actuation (see Section 5.5).

We initially test torsional cavatappi actuators with different fiber angles under free torsion conditions to assess the model. The first is a small fiber angle ($\alpha = 10°$) torsional actuator, and the second is a large fiber angle ($\alpha = 40°$) actuator. Fig. 5.7 shows the experimental results of two samples from the small and large torsional cavatappi actuators along with the model predictions under free torsion (no torsional load applied, $T_{\mathrm{iso}} = 0$ in Eq. 5.10). The experimental results from the two samples in Fig. 5.7(a) and (b) present a similar actuation behavior as a function of pressure (gauge pressure). Fig. 5.7(a) compare the model with the experimental results for torsional cavatappi actuators with $\alpha = 10°$. Here, during the initial pressurization of the sample ($p < 0.5$ MPa), the initial

actuation response is minimal, but as the internal pressure increases ($p > 0.5$ MPa), the actuation ramps up in a linear fashion. Although the actuation deadpan showed by the experimental results in Fig. 5.7 is minimal, actuation tests with external loads will show a larger deadpan. The model slightly over-predicts the torsional actuation response initially, but after 0.5 MPa, it generates accurate predictions with a maximum error of less than $\sim$5%. In contrast to the small fiber angle torsional cavatappi, the large fiber angle samples' results show less of the initial actuation behavior (smaller not shaded region), where minimal untwist is presented ($p < 0.2$ MPa). The experimental actuation response, as well as the model predictions, present a small non-linear behavior, but overall, the model captures the actuation response presented here (Fig. 5.7(b)). In addition to the initial validation on variable fiber angles cavatappi torsional actuators, Fig 5.7 also shows that when comparing the large with the small fiber angle actuator, the actuation response of the former is approximately $3\times$ larger.

After assessing the model for torsional cavatappi actuators under no applied torsion, we tested torsional cavatappi fabricated with a fiber angle of approximately 55° under an isotorque of approximately 4 Nmm. Fig. 5.8 shows the actuation response for a two torsional cavatappi along with the predictions of the model (Section 5.3.3.1). In contrast to the free torsion case, the experimental results show a larger actuation deadpan, where the actuation response is null or even negative (not shaded region), meaning that the torsional actuator does not untwist or twist in the applied isotorque direction. This undesired negative actuation response occurs because the initial untwist of the actuator due to internal pressurization does not overcome the applied external shear stress. In the second region (shaded region), after 0.75 MPa, the actuation response rapidly increases as the untwist generated by the internal pressure overcomes the external shear stress applied on the torsional cavatappi. The model well captures these two actuation regions. In the not shaded region, the model tends to under-predict the actuation response; however,

161

after $p = 0.75$ MPa, the model data matches well the experimental results.

5.4.2 Cavatappi Artificial Muscle

After obtaining model predictions for the cavatappi torsional actuator case under different loading conditions and fiber angles (Section 5.4.1), we assess the model for cavatappi artificial muscles using the model variant derived in Section 5.3.3.2 and 5.3.4. In this section, we present experimental contraction results of cavatappi artificial muscles with a fiber angle, α, of approximately 55° under three different isotonic loads, 2, 3, and 4 N. For each load condition, a total of two samples are tested to ensure that the actuation results are repeatable.

Similar to the results presented for the torsional cavatappi actuators, the actuation responses can be separated into two regions, not shaded (deadpan) and shaded. In the not shaded region, the actuation response is null or minimal, and, in the shaded region, the actuation increases rapidly (Fig. 5.9). Additionally, the actuation regions are load-dependent, as Fig. 5.9 shows how they vary from one load to other. Fig. 5.9(a) shows model predictions along with the experimental results under loading conditions of 2 N. Here, the model slightly over-predicts the experimental results between 0.5 and 1.25 MPa; however, as the pressure keeps increasing, the model error decreases. Fig. 5.9(b) shows successful predictions for the model under an axial load of 3 N. Finally, Fig. 5.9(c) shows under-predictions in the not shaded region of a cavatappi artificial muscle under a load of 4 N. Overall, the model present actuation model data with an average error of < 8 %.
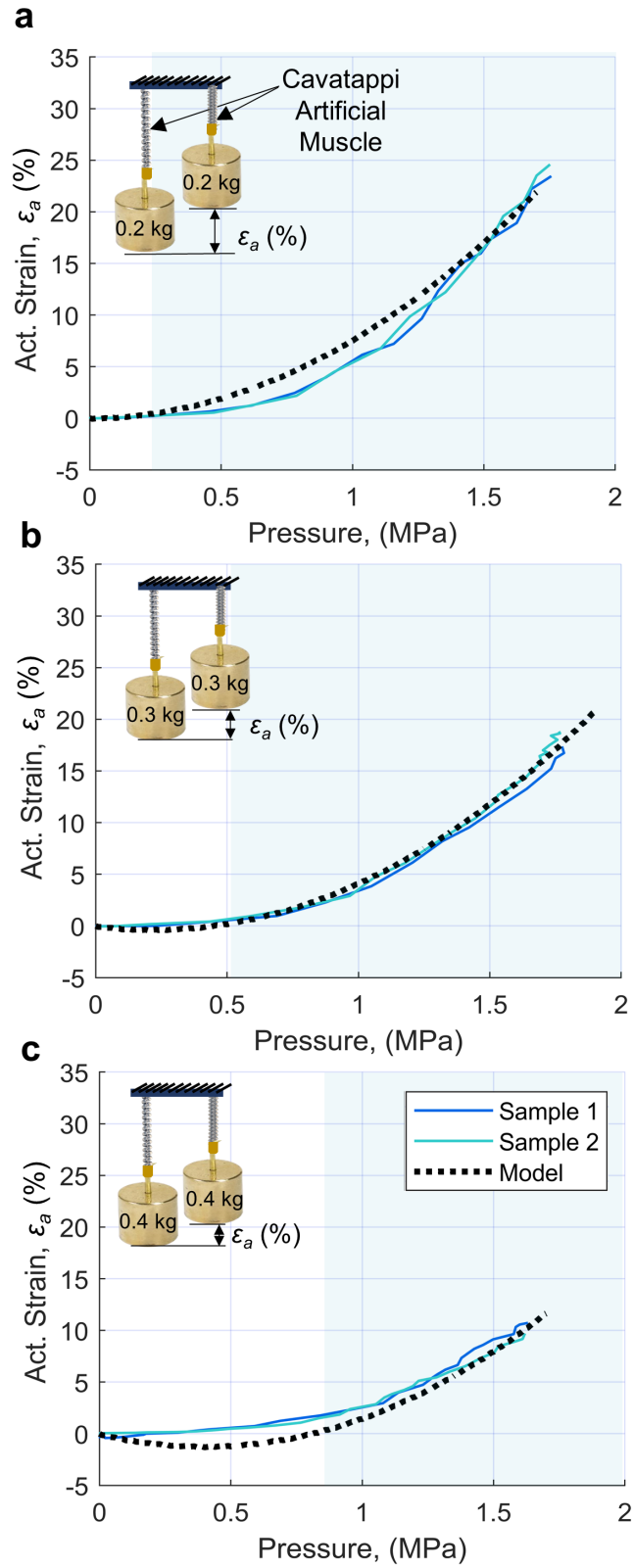
FIGURE 5.9: Cavatappi artificial muscles actuation response under an isotonic load of (a) 2 N, (b) 3 N, and (c) 4 N, along with model predictions.

5.5 Discussion

The work in this paper provides a precursor material-based modeling effort that can be used as an initial step to control and optimize cavatappi artificial muscles. The experimental results and model predictions show two actuation regions. The initial region is named deadpan, where the actuation response is minimal, null, or even negative, and a second region where the actuation increases rapidly as a function of pressure. The initial actuation response in the deadpan region results from the external loads (isotorque or isotonic) and low internal pressure. Under these conditions, the cavatappi internal pressure does not generate sufficient stress capable of overcoming the initial shear stress applied by the external load that increases as a result of geometric changes (radial growth and cross section area variations), leading to this undesired actuation region. As the pressure increases, the stress tensor in the elemental unit develops enough positive shear stress to overcome the negative one generated by the external load, which leads to an increase in actuation outlined by the shaded region. The not shaded region will increase or decrease as a function of the actuation load; thus, this region will be prominent for high loads, and low loads will be small. Although this actuation region might be undesired for bio-robotic applications, they can be predicted as a function of the external load using the presented model; as a result, in order to optimize the actuation response, cavatappi can be constantly pressurized to the internal pressure at the end of the linear deadpan region.

Our initial material characterization effort of the drawn precursor tube used in this work has allowed for the model assessment under the assumption of elasticity. To meet this assumption, all experimental testing for this work was conducted in the time range of few seconds (short-term actuation). Although this short-term actuation condition was applied to all testing, minor viscous effects were present in most of our experimental

results. As a result, we believe that the elasticity assumption will not hold for long-term actuation cycles, and further characterization will be required to capture the time-dependent actuation response. Additionally, it is expected that the material properties for soft PVC used for cavatappi artificial muscles would also be highly sensitive to changes in temperature, and temperature changes usually occur in any robotic environment. As a result, thermoviscoelastic models will be needed to predict the actuation response of cavatappi in an uncontrolled environment.

Nonetheless, the model in this work will allow the future thermoviscoelastic properties to be used as inputs in the compliance matrix (Eq. 5.3.1) to incorporate the time and temperature variables. Furthermore, we have used our model to conduct a sensitive study on the material properties inputs to evaluate those properties that have the highest impact on the cavatappi actuation response. When compared to other properties, we observed the radial modulus, E_2, to notably be the most sensitive input in the model. Changing the radial modulus by 20% its initial value, the actuation results varied by $\sim$15% at an internal pressure of 1.5 MPa. As a result, since E_2 presents the most significant impact on cavatappi actuation, we think that its viscoelastic characterization might be sufficient to capture the viscous effects shown in cavatappi actuation; however, future research should validate this hypothesis.

In this work, the fiber angle, α, used for cavatappi artificial muscles fabrication was 55°. This angle was initially selected because it is the critical angle at which the twisted tube buckles in torsion and starts coiling during fabrication. However, we have used the model presented in this work to understand the fiber angle impact on cavatappi actuation and gain insight about the highest performance fiber angle (optimal fiber angle, α_{opt}). Fig. 5.10(a) shows the actuation predicted by the model under an axial load of 3 N, as a function of internal pressure and α. Fig. 5.10(c) shows the isobar resulting from a perpendicular cut of Fig. 5.10(a) at a pressure of 1 MPa (green dotted line). Additionally,
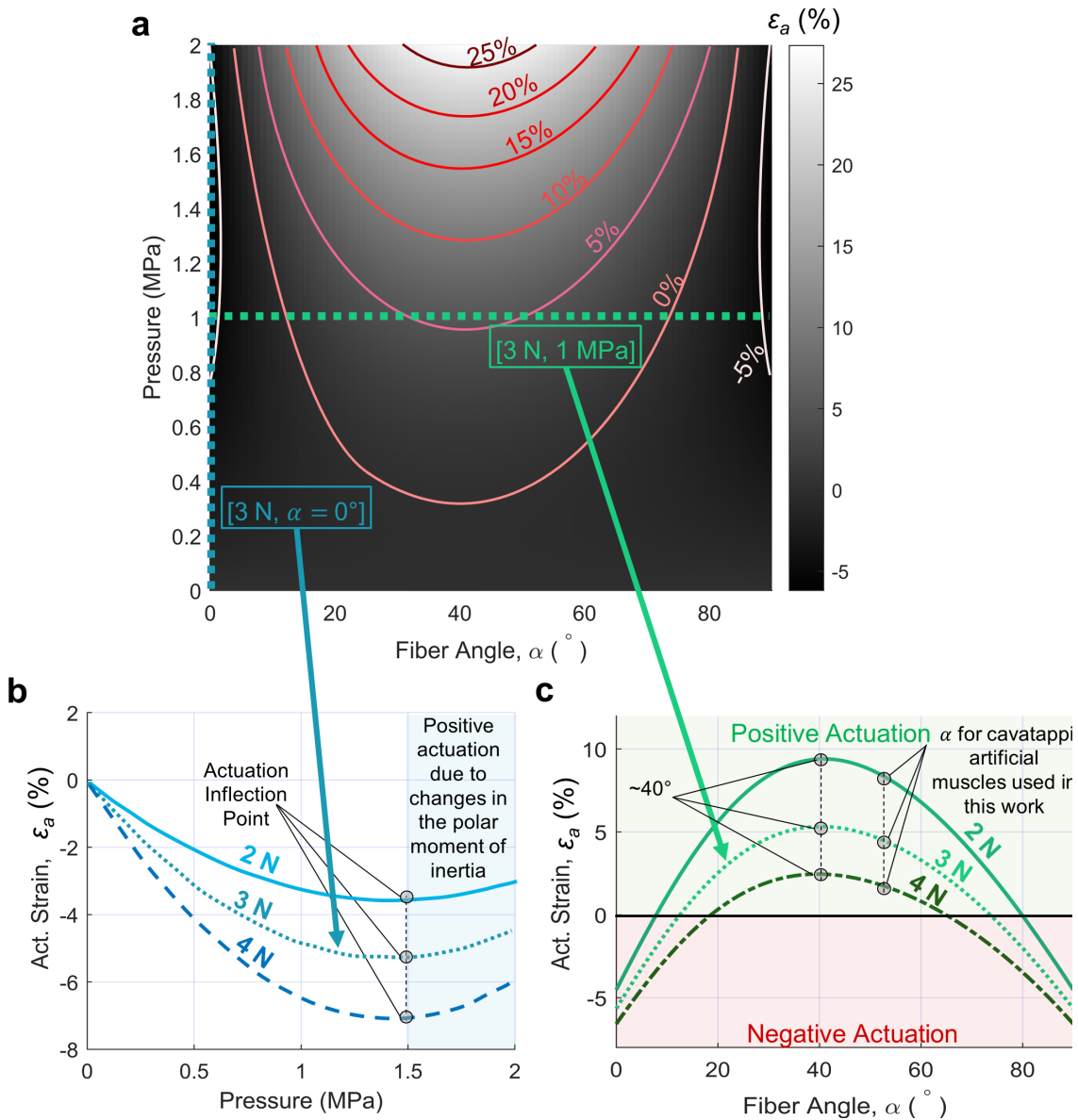
FIGURE 5.10: Fiber angle dependence on actuation and pressure. (a) Actuation predictions by the model as a function of internal pressure and α under an axial load of 3 N. (b) Actuation predictions for a cavatappi artificial muscles with a $0°$ fiber angle as a function of pressure for three axial loads, 2, 3, and 4 N. (c) Actuation predictions for a cavatappi artificial muscles at 1 MPa as a function of the fiber angle for three axial loads, 2, 3, and 4 N.

Fig. 5.10(c) also shows the isobaric lines for actuation under 2 and 4 N loads. As a result, both, Fig. 5.10(a) and (c) show an α_{opt} to be approximately $40°$.

Although fabricating cavatappi artificial muscles to this level of accuracy might be difficult, and the fiber angle during actuation can vary approximately $\pm 3°$, Fig. 5.10 shows that for any cavatappi with a α between 35 to 45° will present a maximum variability in actuation is $< 2.5\%$. As long as, the fiber angle is maintained inside this region, the actuation error due to the fiber angle inaccuracies or variations during actuation will be minimal. In contrast, for the fiber angle used in this work ($\alpha = 55°$), the change in fiber angle can cause maximum errors of approximately 8% in the actuation response. In conclusion, we propose that future cavatappi artificial muscles be designed with a fiber angle of $\sim 40°$ to obtain maximum actuation performance and minimal error.

Finally, Fig. 5.10(b) shows the actuation predictions for a cavatappi artificial muscles with a 0° fiber angle (coiled untwisted tube) as a function of pressure for three axial loads, 2, 3 (blue dotted line in Fig. 5.10(a)), and 4 N. Here, for the three different loads there is a change in the actuation slope from negative to positive at approximately 1.5 MPa. This increase in positive actuation results from the radial growth due to internal pressurization, leading to an increase in the polar moment of inertia and cross-section area. Although the increase in polar moment of inertia and cross-section area contributes to the positive actuation of cavatappi artificial muscles, this contribution is minimal compared to the contribution from the untwist of the elemental unit.

When exposed to water, the soft PVC used in cavatappi artificial muscles present minimal moisture absorption (< 0.12 % at 23°C for 24 hours). Highly hygroscopic polymers can present significant variations in the material properties for different moisture content, which in turn causes changes in the actuation magnitude. Twisted and coiled polymer actuators fabricated using drawn monofilaments of nylon 66 have been shown to increase their actuation response 50% for samples with an added-weight moisture content of 4% [138]. However, polymer-based soft actuators are not the only ones that can suffer from

such moisture dependencies; twisted and coiled CNTs also are moisture content dependent [173]. Although this property can be used in moisture-powered applications, it usually leads to inaccuracy in model predictions when exposed to an uncontrolled humidity environment. The almost null hygroscopicity in the precursor material used for cavatappi artificial muscles, along with the agreement between model and experimental results presented in this work, could lead to the conclusion that cavatappi artificial muscles are moisture independent and their actuation response can be accurately predicted when operating under an environment with different humidity levels.

To study the use of cavatappi artificial muscles in HMI applications and their biomimetics, we use the presented model to design an actuation system for an assisting ankle exoskeleton. Here, a bundle of cavatappi artificial muscles is selected to provide a variable assisting torque on the ankle during the walking cycle. We use a moment-arm of 5 cm similar to previously published devices [114, 131, 188], and the average distance between ankle and knee for an adult [302, 376] to select a suitable cavatappi bundle length of 12.5 cm. The cavatappi bundle is considered to be fixed at a height below the knee at the top end while attached to a pulley at the ankle's height at the bottom end; thus, the force generated on the cavatappi bundle during activation is converted into assisting torque around the ankle joint.

Using previous research for this case of study, ankle assistance is provided to an individual at different stages during the walking cycle [40, 114, 131, 188]. Initially, at the stance phase, the foot rests with an angle of 0° respect to the ground and the assisting torque needed is zero (Fig. 5.11, stage 1). The null assisting torque at this stage results from the zero torque generated by the reaction force on the ground (green arrow); thus, assistance at this stage is not required. As the foot starts rotating around the ankle joint a maximum assisting torque of 49 Nm (1000 N cavatappi force) is required at approximately 10° (approximately 10 mm of actuation displacement) (Fig. 5.11, stage 2). After stage 2, the
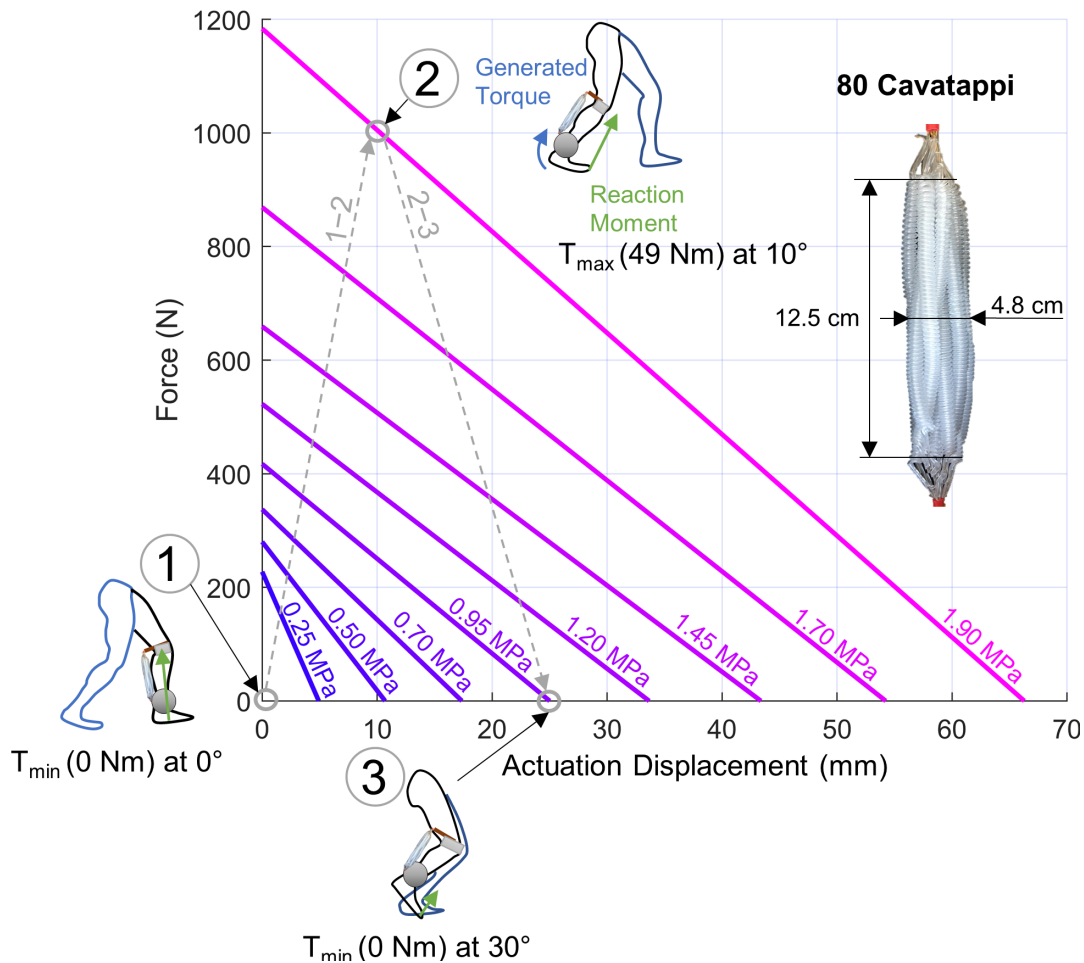
FIGURE 5.11: Isobaric force vs. actuation displacement curves for a bundle of 80 cavatappi used to design the actuation system of an ankle exoskeleton assisting device.

foot starts the swing phase, where an angle of 30° and zero assisting torque is required (Fig. 5.11, stage 3). Fig. 5.11 uses the model presented in this work to provide the force-actuation displacement relationship for a bundle of 80 cavatappi units at different pressures. Here, we have highlighted the three mentioned stages of actuation during a walking cycle. Initially, no pressure is applied in the cavatappi bundle during stage 1 to obtain zero torque and actuation displacement conditions. As the individual starts walking, the ankle angle increases reaching to a maximum assisting torque requirement of 49 Nm (1000 N cavatappi force) at approximately 10°. Such torque is delivered on the ankle by increasing the cavatappi bundle activation pressure to 1.9 MPa. Finally,

the pressure is dropped to 0.95 MPa to meet the zero torque and 30° actuation condition (bundle actuation displacement of 25 mm). As previously mentioned, a total of 80 cavatappi units with 40° internal fiber angle are configured in parallel for this case of study. The number of cavatappi in the bundle was calculated using the torque-actuation displacement of stage 2 as key design specification. This stage presents the maximum force required for the cavatappi bundle. As a result, a bundle of 80 cavatappi (bundle diameter of approximately 4.8 cm) can suitably perform ankle assistance during walking without reaching the bursting pressure of cavatappi artificial muscles [140]. Finally, the slope provided by the force-actuation displacement presented in Fig. 5.11 should not be seen as the stiffness of the actuator as the actuation displacement is the change in free length of the cavatappi as a result of pressurization.

Overall, the model presented in this work can predict the actuation response of cavatappi under different loads for short-term actuation cycles. The actuation response of cavatappi artificial muscles results from a change in the twist and radial growth resulting from internal pressurization, which can be seen as a change in the compliance of the spring that is the cavatappi artificial muscle. Although further research should be conducted on capturing the thermo-viscoleastic response of these muscles, this model could contribute to initial cavatappi control strategies. As previously stated, our model predicts actuation strain as a function of two variable inputs, internal pressure and isotonic loads; thus, for developing feasible feedback control systems, a conventional force sensor should be added to the actuator. However, this rigid addition could compromise the benefits linked to their soft actuation behavior and add complexity to the system. Typically, soft robotic systems require both soft actuators and soft sensors to perform complex operations in a controlled fashion. We propose that future research should study the potential capacity for proprioception of cavatappi artificial muscles by using similar length self-sensing

approaches used in flexible elastomeric soft actuators [135, 340, 358, 367]. More specifically, we propose using conductive fluids as the working fluid to perform both sensing and actuation. The conductive working fluid could drive actuator deformation while simultaneously acting as a strain-sensing component for detecting actuator deformation when using the change in resistance to infer actuation strain [135].

Adding sensing capacities to cavatappi, the actuation system would be considerably simplified, and the model could be rewritten to output force as rather than actuation strain a function of pressure following the same procedure out lined in this work, leading to a highly integrated control actuation system. Going one step further into the controlling aspects of cavatappi artificial muscles, we propose that future work looks into actuation mechanisms that could tune the damping term of these artificial muscles. Adding active tunable compliance and damping mechanisms to these actuators could potentially help to create highly adaptable actuation systems, similar to those found in nature, such as biological muscles [139].

Biocompatible proprioceptive soft actuators capable of featuring those properties found in biological actuators are ideal for low-cost biomimetic components such as exoskeletons, prosthetics, or muscle substitutes. However, it is fundamental to understand their actuation mechanism and behavior to allow the optimal design and control strategy for implementation. To this end, our model put cavatappi artificial muscles one step forward on their future implementation by providing a better understanding of the actuation mechanism and actuation predictions.

CHAPTER 6

CONCLUDING REMARKS

Conventional actuation systems, which are briefly introduced in Chapter 2, rely on rigid configurations and lack tunable compliance and impedance and, consequently, limit their efficient and straightforward deployment in areas such as biomimetic and bio-inspired applications.

To this end, this work develops an understanding on what are those performance metrics and properties from biological muscles that allow them to rapidly adapt under unpredicted external perturbations (Chapter 2). Once these properties were found, this work compared these metrics and properties to the most recent soft actuation technologies and presented the current accomplishments, the remaining challenges, and future directions of each soft actuation technology. As a result, this study helped better benchmark the widely used term in the soft robotic field of "artificial muscle". Then, Chapter 3 introduces two moisture-related matters regarding twisted polymer actuators: moisture content impact on the thermal actuation of TPAs and the capability of TPAs to actuate as a function of moisture absorption at room temperature. Chapter 4 introduces a fluid-driven muscle-like actuator fabricated from inexpensive polymer tubes named cavatappi artificial muscles. Here, the tubes are drawn, which enhances the anisotropy in their microstructure, next, twisted, to generate torsional actuation, and, finally, helically coiled into linear actuators. These new devices contribute to creating an entirely new field of actuator research, and, although they are presented in their early stage in this Ph.D. work, they are expected to develop a new research path in the soft actuation field. Last, Chapter 5 presents a material-based model capable of predicting the actuation response of cavatappi artificial muscles using the mechanical properties of the precursor material

used for fabrication. A summary of the significant contributions of this dissertation is presented next:

- I developed an understanding of progress in soft actuation technologies compared to biological muscle performance, properties, and control. In doing so, I review advances in understanding biological muscle properties that contribute to their high adaptability and compare them with some of the newest soft actuation technologies. Here, it is shown that most soft actuators have performance metrics similar to those of biological muscles. Most soft actuators have tunable material properties (compliance and damping), integrate sensors in their architecture, and potentially feature variable recruitment. However, some muscle properties are still lacking in soft actuators. The remaining challenges include implementing morphological computation and muscle synergy in control strategies and integrating onboard energy and thermoregulation in the actuator architecture. Artificial muscles should achieve specific metrics and properties that enable them to perform well as muscle substitutes. The changing view of muscles as tunable materials has provided new directions for investigations geared toward emulating the intrinsic properties of biological muscles, leading to the conclusion that novel soft actuators should focus on developing and deploying inherent properties of biological muscles such as adaptive dynamics. Only then can these actuators be successfully used as substitutes for biological muscles [139].

- I present two main subject matters on TPAs' moisture effects. The first one is the ability of TPAs to actuate while they absorb moisture from the environment, and the second one is the significant impact of moisture content on the thermally driven actuation of TPAs. For the former, we show that STPAs and TCPAs developed hygroscopic actuation during approximately 20 hours when a desiccated sample is exposed to humid air. This actuation response is found to be reasonably linear as

173

a function of time. This linear relationship between actuation and time enhances its potential for use as moisture-activated long-term actuators or sensors since the linear relationship makes this actuation mechanism easy to predict and control. For the latter, it is demonstrated that the moisture content in TPAs has a significant impact on thermal actuation. In other words, TPAs will not develop the same actuation responses in humid areas, such as Miami, where the annual RH average is 72% than the actuation responses in arid areas, such as Phoenix, where the annual RH average is 36% [138].

- I introduced a low-cost, lightweight, fluidic artificial muscle whose actuation relies upon (i) the anisotropic physical properties introduced into the virgin material through extrusion and enhanced by a cold drawing process, (ii) the reorientation of those properties through a twisting or twisting and coiling process, and (iii) the deformation of the reconfigured material through the application of internal pressure. Cavatappi artificial muscles can mimic some human muscle metrics and outperform others, such as fast contraction activation, specific power and work, and maximum force and contraction. Furthermore, like human skeletal muscles, cavatappi artificial muscles have the potential for stacking in parallel to increase force generation. I have demonstrated parallel operation with nine cavatappi artificial muscles of the same length to increase the generated torque by nine times on the arm [140].

- For this work's actuation model assessment, I characterized the linear elastic mechanical properties of the drawn precursor tube used for cavatappi artificial muscles fabrication. In doing so, experimental testing set-ups for the material characterization were provided for all the required mechanical properties and used to collect them in the time range of few seconds (short-term actuation) to avoid viscous effect in the material [141].

- I provided a precursor material-based model that can be used as an initial step to control and optimize cavatappi artificial muscles. Here, I establish a framework for modeling cavatappi using the thick-wall pressure vessel stress analysis and the spring theory. The presented model uses the mechanical properties of the precursor drawn material used for fabrication, initial twist (internal fiber angle), muscle geometry, and internal pressure to predict the artificial muscles contraction under different external loads. The model predictions agree with the experimental results for cavatappi of different internal fiber angles and load conditions. Given their potential implementation in bioinspired applications, this model can help better design, optimize, and control the actuation response of cavatappi [141].

6.1 Future work

The work in this dissertation suggests several directions for further study. We describe some potential future research ideas as follows:

- Further research will be necessary for material selection for cavatappi artificial muscles. Although Soft ND-100-65 Tygon PVC tubing has been demonstrated to successfully meet all the material properties requirements needed to be used as suitable soft actuators, future work should investigate if other drawn polymer tubes can outperform the current cavatappi artificial muscles. Future research could also contribute to avoiding the current mode of failure, where cavatappi fails at the bursting pressure related to the ultimate strength in the direction perpendicular to the internal fibers at the artificial muscle tail. In doing so, subsequent studies can focus on modifying the material properties (ultimate stress) in the perpendicular direction of the internal fibers (tie-chain molecules) or designing new connections between cavatappi and end-effector (the connecting point between load and actuator) to avoid

175

that transition between the coiled and the straight-twisted tube geometry where cavatappi tend to fail.

- The current initial material characterization effort of the drawn precursor tube used in this work has allowed for the model assessment under the assumption of elasticity. To meet this assumption, all experimental testing for this work was conducted in the time range of few seconds (short-term actuation). Although this short-term actuation condition was applied to all testing, minor viscous effects were present in most of our experimental results. As a result, we believe that the elasticity assumption will not hold for long-term actuation cycles, and further characterization will be required to capture the time-dependent actuation response. Additionally, it is expected that the material properties for soft PVC used for cavatappi artificial muscles would also be susceptible to changes in temperature, and temperature changes usually occur in any robotic environment. As a result, thermo-viscoelastic models will be needed to predict the actuation response of cavatappi in an uncontrolled environment.

- Testing those properties of biological muscles (such as tunable compliance and impedance, morphological computation, muscle synergy, self-sensing, etc.) in cavatappi artificial muscles will be fundamental in the future to better understand if cavatappi will be able to perform as muscle substitutes. Although the change in compliance by internal pressurization has already been demonstrated in this work, I propose that future research investigate the use of different activation mechanisms to tune the damping coefficient of these soft actuators. For example, it is well-known that temperature changes can modify the viscoelastic behavior of most polymers; as a result, I propose to use thermal activation to unlock the full capacity of the adaptive dynamics of cavatappi artificial muscles. Besides the modeling difficulties
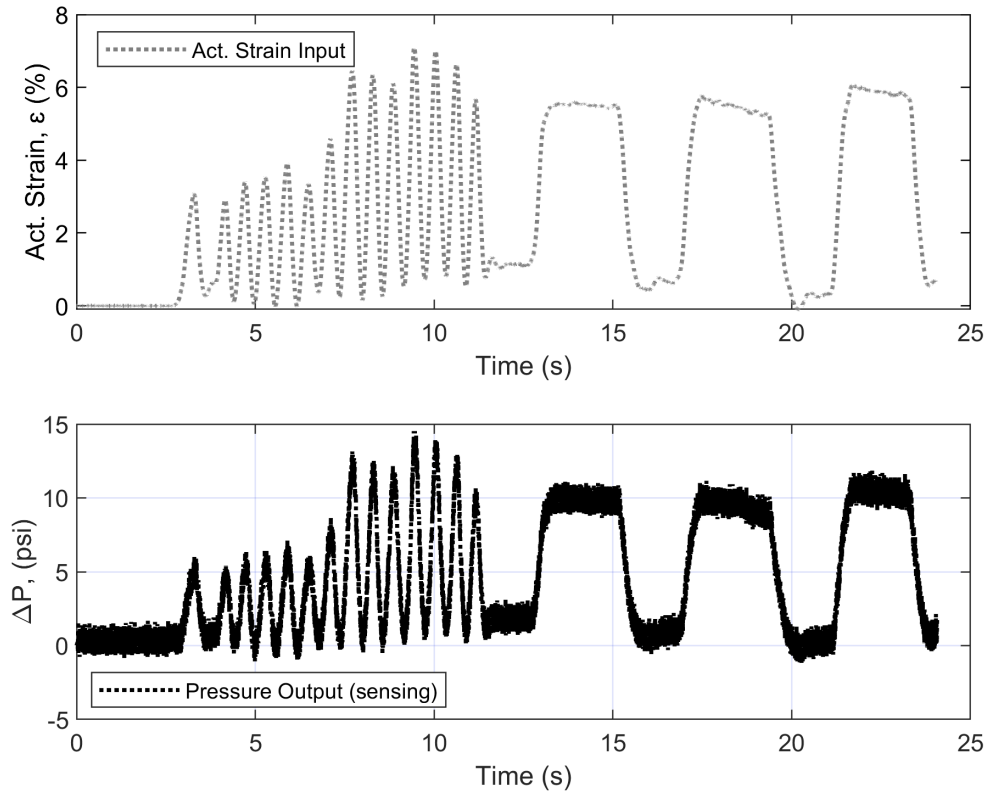
FIGURE 6.1: Cavatappi artificial muscles partial sensing capacity.

that such an approach will carry, this could put cavatappi artificial muscles one step closer to emulate biological muscles fully.

- As typically, soft robotic systems require soft actuators and soft sensors to perform complex operations in a controlled fashion. I propose that future research study the potential capacity for proprioception of cavatappi artificial muscles by using similar length self-sensing approaches used in flexible elastomeric soft actuators. More specifically, we propose using conductive fluids as the working fluid to perform both sensing and actuation. The conductive working fluid could drive actuator deformation while simultaneously acting as a strain-sensing component for detecting actuator deformation when using the change in resistance to infer actuation strain. Furthermore, this work presents initial work regarding this matter, demonstrating the capacity to partially sense position. Fig. 6.1 shows how changes in position

177

(actuation strain) can be related to changes in the internal pressure fluid in the cavatappi. Such partial-sensing capacity can be used in applications where agonist and antagonist pairs of artificial muscles are necessary.

- The actuation system would be considerably simplified by adding sensing capacities to cavatappi. The presented model could be rewritten to output force rather than actuation strain, a function of pressure following the same procedure outlined in this work, leading to a highly integrated control actuation system. Furthermore, future work should look into control strategies that can efficiently integrate and implement self-sensing, tunable compliance and damping, morphological computation, muscle synergy, and other properties of biological muscles that make them highly adaptable structures under unpredictable perturbations.

- Looking into longer term future work, the auxiliary components used for cavatappi artificial muscles such as power sources (micro-pumps or pressurized tanks), hydraulic components (electro-valves and pressure regulators), and hydraulic lines, should be further investigated because high pressure current technologies are voluminous, heavy, and expensive, which limits cavatappi artificial muscles implementation in portable systems. One solution could be found using different activation methods. For example, using the dielectric elastomer actuation principle, where Maxwell stresses can be generated in the elemental unit of cavatappi artificial muscle could lead to the same actuation results produced by internal pressure in the current configuration while avoiding the use of hefty hydraulic components.

The main contributions of this dissertation and the above-mentioned future directions will substantially impact the next future generation of soft actuators in robotics.

APPENDIX A

CAVATAPPI ARTIFICIAL MUSCLES FROM DRAWING, TWISTING, AND COILING POLYMER TUBES. SUPPLEMENTARY MATERIALS

science.org/doi/10.1126/scirobotics.abd5383

Materials and Methods

Fig. A1. Fabrication and processing of a cavatappi artificial muscle and its elemental unit.

Fig. A2. Side, cross-sectional, and top views of a cavatappi along with its dimensions.

Fig. A3. Experimental setups used to measure axial strain of the precursor tube, radial strain for the precursor tube, the torsional actuation of an elemental unit of a cavatappi, and the axial actuation of a cavatappi artificial muscle.

Fig. A4. Pressure-volume curve used to calculate the energy in during an actuation contraction and force-displacement used to calculate the work generated during an actuation contraction.

Fig. A5. Actuation under a load of 1.1 kg to show the maximum stress and under a load of 0.1 kg to show maximum strain.

Fig. A6. The torsional actuation of a cavatappi artificial muscle elemental unit.

Table A1. Values obtained from Fig. A.4.

Movie A1. Mechanism of cavatappi actuation ▶.

Movie A2. Cavatappi actuation ▶.

Movie A3. Prestretched cavatappi actuation under no load ▶.

Movie A4. Mini-cavatappi actuation ▶.

Movie A5. Fifth digit flexion and extension of a robotic hand ▶.

Movie A6. Strain potential energy storage ▶.

Movie A7. High controllability ▶.

A.1 Device Fabrication and Processing

This section presents the fabrication process of cavatappi artificial muscles in their linear actuator form, as well as their torsional actuator form. The straight torsional form can be thought of as an elemental unit of the helical linear actuator form. The fabrication process for the cavatappi tested herein begins with precursor (untwisted) tubes with a 3.18 mm OD and a 1.58 mm ID, which were reinforced with a lubricated 0.8 mm diameter nylon monofilament. This reinforcement was used to keep the opening of the tube from collapsing during fabrication and to give the final structure a higher dimensional/structural rigidity (Fig. A.1(a)). The monofilament was lubricated with a small amount of mineral oil in order to aide insertion through the tube. A solid red line in Fig. A.1 is used to highlight how the internal microstructure of the material is reoriented during fabrication.

The first stage of fabrication consists of stretching the tube with a draw ratio of approximately 3:1. The result is a lengthened tube with reduced OD and ID of 1.8 mm and 0.85 mm, respectively (Fig. A.1(b)). The drawing process induces a plastic deformation that is maintained throughout the remainder of the fabrication process. The initial length of the reinforcing monofilament is longer than that of the tube, such that during drawing, the tube is drawn over some exposed reinforcement. The result is a drawn tube that contains internal reinforcement throughout its length. At this point the nylon reinforcement
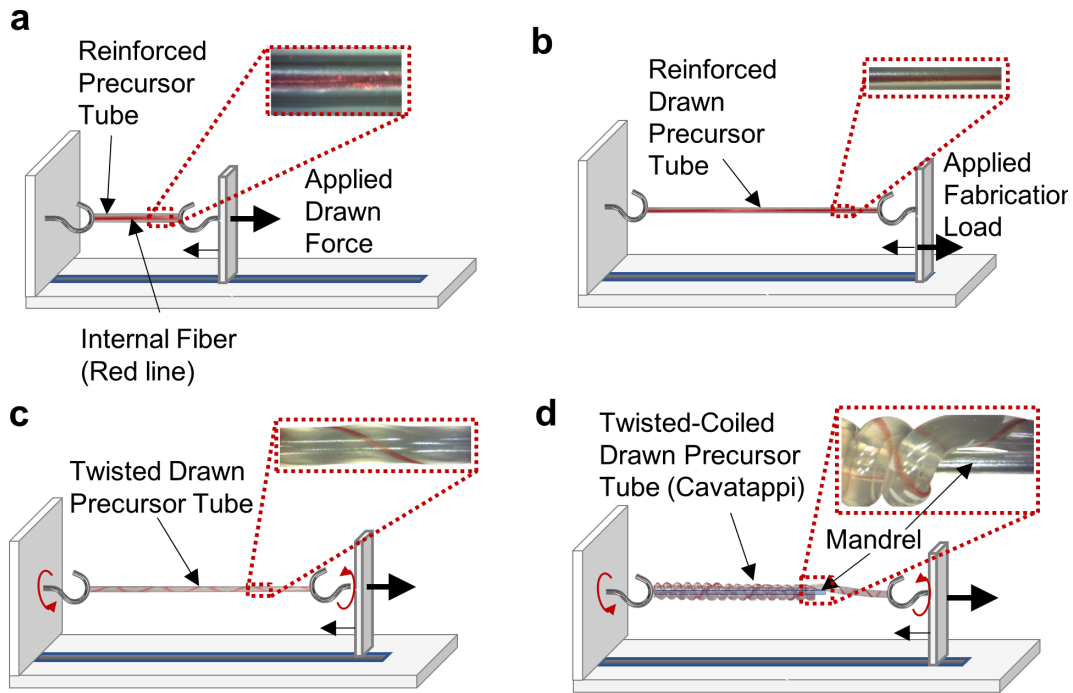
FIGURE A.1: Fabrication and processing of a cavatappi artificial muscle and its elemental unit

is detached from the spool of nylon and along with the drawn tube attached to the hooks which will be used for twisting.

After drawing and reinforcing, initial twists are inserted into the drawn precursor tube as well as the nylon reinforcement, as shown in Fig. A.1(c). A small tensile load is maintained on the sample during twisting to keep it straight, at least initially. This straight twisted configuration can be annealed at 190°F for 30 minutes and cooled down to room temperature to release internal stresses and then used as a torsional actuator when internal pressure is applied. However, if the sample keeps twisting, it will eventually buckle in torsion to start coiling to create a linear cavatappi artificial muscle. In order to maintain a uniform geometry of the coiled shape, a 1 mm OD mandrel was inserted at the center of the helix (Fig. A.1(d)). Different size mandrels can be used to create cavatappi artificial muscles with different diameter sizes of the coiled structure, which may be a way to tune the stiffness of the cavatappi spring. Finally, the sample can be annealed and
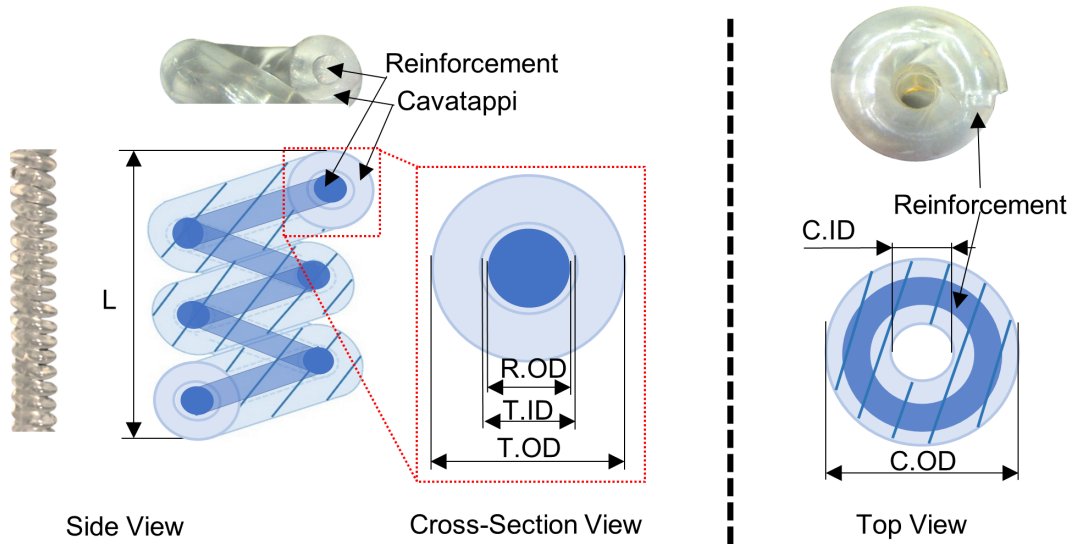
Reference	Definition	Dimension
R.OD	Reinforcement monofilament outer diameter	0.8 mm
T.ID	Tube inner diameter	0.85 mm
T.OD	Tube outer diameter	1.8 mm
C.ID	Coil inner diameter	1 mm
C.OD	Coil outer diameter	4.6 mm
m_c/L	Linear density. (m_c is the mass of the cavatappi)	0.014 g/mm

FIGURE A.2: Side, cross-sectional, and top views of a cavatappi along with its dimensions.

cooled to room temperature using the aforementioned heat treatment protocol to release internal stresses and keep the new shape.

Fig. A.2 shows the dimensions of the cavatappi artificial muscle used in this work. Fig. A.2 also shows real images of the side, cross-section, and top views of a cavatappi. Although the dimensioning of cavatappi can differ by using different extruded tubes and mandrel sizes, this work uses the cavatappi dimensions given in this figure. However, various lengths (L in Fig. A.2) have been used in this work, and since they all have the same cross-sectional dimensions, their mass and length can be directly related by the linear density value provided in Fig. A.2. Note that all actuation metrics have been reported

as specific or non-dimensional values to facilitate a comparison with other technologies and account for the various lengths used.

A.2 Experimental Methods

To measure axial and radial strain, as well as torsional and linear displacement in actuation tests, we used a Polytec OFV-5000 Vibrometer controller with the OFV 534 optics head. To apply and measure pressure in these tests, we used a RG1262-1500 pressure regulator along with QB1T closed loop servo system and a DS series pressure transducer from PROPORTION-AIR. The voltage outputs of these systems are linearly related to a change of position of the object on which it focuses (vibrometer) and change in pressure (pressure transducer) (Fig. A.3). This voltage was recorded by a National Instruments PXI-6361 multifunction data acquisition card and subsequently analyzed to develop the data in the primary manuscript.

Fig. A.3(a) shows the set-up used to measure the axial strain of the precursor tubes. In this set-up, the precursor tube was clamped vertically with the top end fixed to a beam and the bottom end hanging freely with a 2-gram mass (light weight) to ensure the sample stayed straight. The vibrometer was positioned directly below the sample with the laser reflecting off the attached mass to measure position. Pressure inputs were controlled with the gas pressure regulator.

Fig. A.3(b) shows the set-up used to measure radial strain of the precursor tubes. Here, the precursor tube was placed within a grooved frame. This design allowed the sample to expand symmetrically in the radial direction while contracting/expanding in the axial direction. In this set-up, the sample was only constrained by the quick connector at end of the tube. The vibrometer laser focused at a point along the midline of the tube far
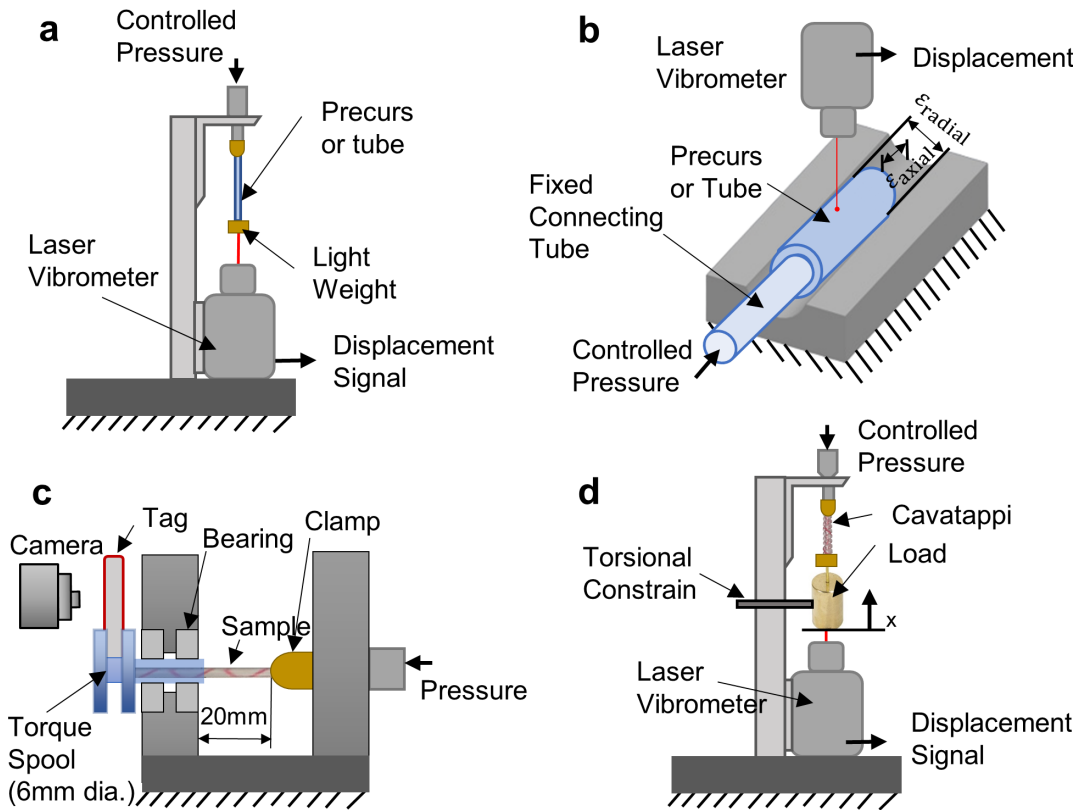
FIGURE A.3: Experimental setups used to measure axial strain of the precursor tube, radial strain for the precursor tube, the torsional actuation of an elemental unit of a cavatappi, and the axial actuation of a cavatappi artificial muscle.

away from the fixed connecting tube. Radial displacement of the precursor tube was measured while pressure inputs were controlled by the pressure regulator.

Fig. A.3(c) shows the experimental set-up used to measure torsional actuation under no load. In this set-up, we used an aluminum frame, two ball bearings, a torque spool, and a clamp. Fig. A.3(c) shows the torsional actuator fixed on the right by the clamp and connected to a pressure regulator. On the left, the actuator was glued into a torque spool which is set in the bearing pair and free to rotate and move in the axial direction. The sample was plugged on the left side, keeping the actuator from leaking during actuation. The angular position of a 2 cm actuator was measured using imaging processing of a video that was filmed during the actuation test, while the input pressure was applied,

controlled, and measured by the pressure regulator and transducer. The displacement video was manually synchronized with the pressure inputs to obtain torsional actuation data.

To measure linear actuation of cavatappi as a function of pressure under various loads, once again, the vibrometer, pressure regulator, and pressure transducer were used. Fig. A.3(d) shows a very similar set-up as seen in Fig. A.3(a) but with a cavatappi muscle connected in place instead of a precursor tube. In addition, during the cavatappi actuation tests, the samples were also constrained from rotation at the end of the sample by adding a small rod to the hanging weight which contacted the vertical beam, which served as a mount for the entire rig (Fig. A.3(d)). In theory, this rod added some friction to the actuation, but that was considered negligible.

A.3   Metrics Calculations

This section presents a more detailed explanation of how we calculated some of the metrics used to compare cavatappi to other actuators in Fig. 4.7 and Table 4.1 of the main manuscript. The inputs for these calculations were all determined using the cavatappi shown in Fig. A.2 and set-up in Fig. A.3(d). For this setup a hanging mass, m was suspended by the cavatappi of mass, m_c. The tensile force on the cavatappi from the hanging mass depends on the gravitational load and acceleration of the mass via $F(t) = m(\ddot{x} + g)$. Here g is the acceleration due to gravity and $\ddot{x}$ is the acceleration of the mass, with positive x up.

Peak specific power

Instantaneous power is calculated as $P(t) = F(t)\dot{x}(t)$. Therefore, instantaneous specific power can be calculated to be:

$$P^* (t) = \frac{P(t)}{m_\mathrm{c}} = \frac{m}{m_\mathrm{c}} \left(\ddot{x} + g \right) \dot{x}. \tag{A.1}$$

Here, the cavatappi with dimension shown in Fig. A.2 and a mass of approximately 0.4 grams was used. Velocity was measured by the vibrometer and acceleration calculated therefrom. The data used for this calculation is shown in Fig. 4.4(d). The time weighted average was calculated with a simple average of the instantaneous specific power values, as the velocity readings were made at regularly spaced time intervals. The maximum specific power was found for the 0.2 kg hanging mass to be 1.42 kW/kg (Fig. 4.7) by using the equation of motions, Eq. (A.1).

We also calculated the specific power ignoring the acceleration of the mass during actuation as:

$$P^* (t) = \frac{P(t)}{m_\mathrm{c}} = \frac{mg}{m_\mathrm{c}} \dot{x}. \tag{A.2}$$

Using Eq. (A.2), the maximum specific power obtained was 1.3 kW/kg. Comparing these specific power calculations, we see that the increase in specific power by including acceleration is only about 8%. Nonetheless, the calculations with inertia were used for the results presented in Fig. 4.4(d), Fig. 4.7, and Table 4.1. For comparison, it is worth mentioning that the specific work for mammalian muscles is 0.32 kW/kg [203].

Specific work

The specific work, being time integral of instantaneous power, was calculated using trapezoidal integration (using the function *trapz.m* in MATLAB). The sample rate of the data acquisition system for these tests was 100 Hz, which is approximately 10x higher than the transient dynamics captured in testing. The viscoelastic response evident in Figs. 4.4(b) and (c) of the manuscript shows that the actuator has both, a short and a long

period response. The initial response occurs within the first ~0.25 s, but if the pressure is maintained, the contraction continues to grow continuously at least out to the 5 min mark as shown in Fig. 4.4(c). Therefore, the specific work reported here must be prefaced by a reporting of time used as the upper limit of integration of power. When processing the specific work here, we defined the short response as that from $t = 0$ to the time of where strain rate first became negative (~0.25 s in Fig. 4.4(b)), which is the beginning of the ringing response to the step change in internal pressure. As our testing only extended out to 5 minutes, we defined the long period response from $t = 0$ to $t = 5$ min.

The specific work was calculated for the short response by integrating the instantaneous specific power, which was found using Eq. (A.1), from $t = 0$ to $t = 0.25$ using the data in Fig. 4.4(b). Note that the intermediate calculation for specific power found using the data in Fig. 4.4(b) well matched that found using the velocity data in Fig. 4.4(d). The resulting specific work was equal to 0.11 kJ/kg. Similarly, we calculated the specific work from $t = 0$ to $t = 0.25$ with the data from Fig. 4.4(b) ignoring the dynamics of the actuator, i.e. using Eq. (A.2), which gave a specific work equal to 0.105 kJ/kg Comparing these two results for short-term work, we can assume that the acceleration generated on the lifted mass during actuation does not have major effects on the specific work. The specific work of cavatappi was also calculated for the long response (from $t = 0$ to $t = 5$ min) using the data in Fig. 4.4(d) and neglecting the acceleration of the lifted mass (since we saw minor effects on the short response specific work calculation). The cavatappi with dimension shown in Fig. A.2 and a mass of ~0.4 grams (90 mm length under a load of 0.4 kg) was used to obtained short-term specific work and a mass of ~0.2 grams (45 mm length under a load of 0.4 kg) was used to obtain long-term specific work. The result is a specific work of 0.38 kJ/kg for the long actuation response. For comparison, the specific work for mammalian muscles is 0.039 kJ/kg [203].

Actuator Contractile Efficiency

TABLE A.1: Values obtained from Fig. A.4

Thermodynamic Parameter	Value
Initial Pressure (p_o)	0.1 MPa
Final Pressure (p_f)	2.15 MPa
Final Volume ($\forall_\text{f}$)	350 mm^3 or 3.5×10^{-7} m^3
Work-out (W_out)	0.183 J

The contractile efficiency of a cavatappi was calculated by accounting for the total energy that was put into the actuator divided by the work generated by the actuator during the muscle contraction. Similar to the experimental set-up used for cavatappi actuation testing shown in Fig. A.3(d), the laser vibrometer was used to measure change in position of a 0.3 kg hanging mass. The work output developed by a cavatappi of 0.52 grams was obtained by calculating the area under the load-displacement line shown in Fig. A.4(a). The input energy was calculated by characterizing the pressure-volume relationship of the cavatappi. The pressure input was manually applied and measured with a pressure transducer using a graduated water screw-syringe that was also used to measure the internal volume change in the inside of the cavatappi. The change in volume was directly related to the amount of water that was pumped from the graduated syringe cylinder. Fig. A.4(b) shows the change in pressure as a function of internal volume. Calculating the area under the curve shown in Fig. A.4(b), we obtained the energy input during muscle contraction. Finally, the contractile efficiency was calculated as

$$\eta_\text{cavatappi} = \frac{W_\text{out}}{E_\text{in}},\tag{A.3}$$

where W_out is the contractile work and E_in is the input energy in the cavatappi during muscle contraction. The efficiency obtained for a cavatappi was found to be approximately 45%.
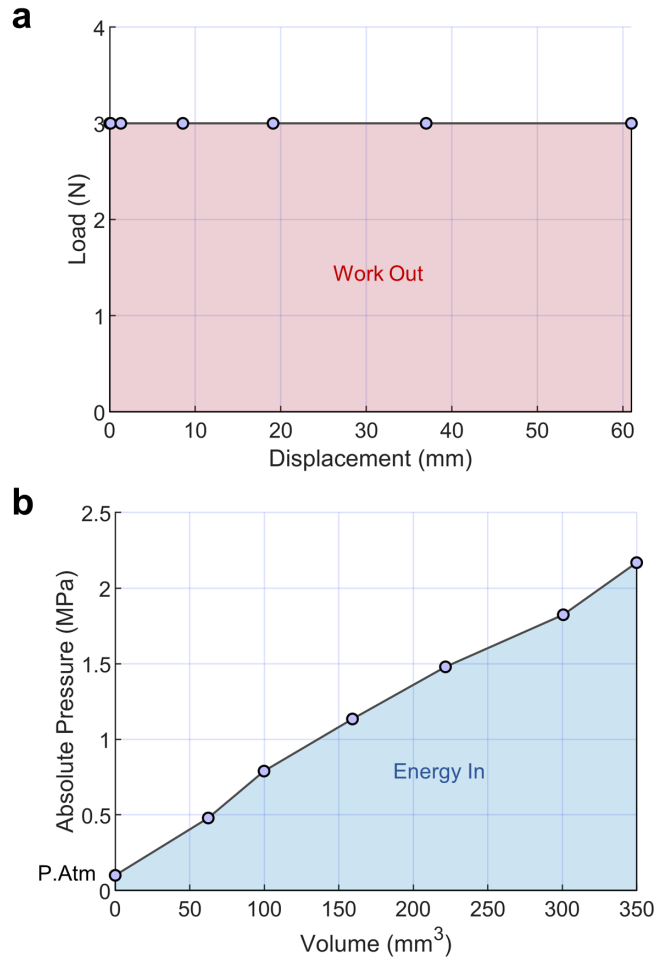
FIGURE A.4: Pressure-volume curve used to calculate the energy in during an actuation contraction and forcedisplacement used to calculate the work generated during an actuation contraction.

As previously mentioned, a contractile actuator efficiency of 45% was calculated when using water as the working fluid. In order to provide an estimate of the actuator efficiency using air as the working fluid, we used thermodynamics, assuming an isotropic isothermal process, to calculate the fluid input energy into the system (cavatappi). An isothermal assumption is reasonable given the low total mass of air that is used relative to the surface area and mass of the tubing and internal monofilament, both of which begin at ambient temperature. In this calculation, we used some thermodynamic parameters (volume and pressure) as well as the work-out that were already collected from the previous efficiency (Fig. A.4) using water. These parameters are the initial and final state properties in the

actuation test presented in Fig. A.4 and they are assumed to be the same for air as the main efficiency drop is expected to be due to air compressibility effects. These parameters are presented in Table A.1.

We assume that air behaves as an ideal gas given that the compressibility factor is approximately equal to 1 during this process. Using the ideal gas law for an isothermal (slow) process, Boyle's law can be derived as

$$p_\text{f} \, \forall_\text{f} = p_\text{o} \, \forall_\text{o}. \tag{A.4}$$

Substituting the initial, p_o, and final, p_f, pressures, as well as the final volume, $\forall_\text{f}$, from Table A.1 in Eq. (A.4), the initial volume, $\forall_\text{o}$, of air needed to inflate the cavatappi to the requisite volume and pressure would be 7.3×10^{-6} m^3. Similarly, Boyle's law is also used to obtain the final specific volume, v_f, in Eq. (A.5), which later is used to calculate the mass of air involved in the process (Eq. (A.6)):

$$p_\text{f} \, v_\text{f} = p_\text{o} \, v_\text{o} \tag{A.5}$$

and

$$m_\text{air} = \frac{\forall_\text{f}}{v_\text{f}}. \tag{A.6}$$

In Eq. (A.5), v_o is the specific volume of air at atmosphere pressure, which is equal to 0.83 m^3/kg. The obtained final specific volume, v_f, (0.04 m^3/kg) is used in Eq. (A.6) to calculate the air mass, m_air, which is 8.75×10^{-6} kg. Following the equation of an isothermal polytropic process for an ideal gas,

$$W_\text{in} = \int_{\forall_1}^{\forall_2} p \, d\forall = m_\text{air} \, R \, T \ln\frac{\forall_2}{\forall_1} \quad, \tag{A.7}$$

work-in, W_{in}, is calculated to be – 2.21 J, where the negative sign indicates that the work is being done on the gas (work-in). In Eq. (A.7), R is the universal gas constant for air (287 J/kgK) and T is the room temperature (293 K). Similar to Eq. (A.3), the contractile efficiency of the actuators is

$$\eta_{\text{cavatappi}} = \frac{W_{\text{out}}}{W_{\text{in}}}, \tag{A.8}$$

where W_{out} is the contractile work done by the cavatappi and W_{in} is the fluid input work or energy into the cavatappi during muscle contraction. Using the work-out from Table A.1 and work-in calculated from Eq. (A.7) we obtain a contractile actuator efficiency of approximately 9%.

In addition to the actuator contractile efficiency, we have also estimated a range for the total electric-mechanical efficiency of an overall system using the datasheets of three minipumps available in the market [38, 327, 328, 351]. The first one is an Inc M-Series brushless gear minipump, available from Flight Works. While the efficiency of these small high-pressure pump is not directly published on their datasheets, the MODELS 2232-M04C10/C12/C15 pressure-flowrate curves have been used to calculate a pumping efficiency of approximately 50-60% [351], which matches the electrical to flow energy conversion efficiency that were quoted by the company President/CEO [38]. The second pump considered was a new GAF series pump from MICROPUMP. From the datasheet of this pump, we have calculated an efficiency of approximately 0.3 when using water as the working fluid [327]. Finally, a minipump under the brand name MG 230XK Series provided by Fluid-o-Tech along with a DC motor of 24 V has also been used to calculate a third efficiency value. The combination of this pump with the 24 V DC motor is sold by TOPSFLO, which is the company that provides the datasheet [328]. Considering the pressure-flow rate curves and the input power provided at 3000 rpm in their datasheet, an efficiency of approximately 0.21 has been obtained for this pump.

The lower efficiency as compared to larger gear pumps is expected, as viscous losses are more significant for these smaller pumps. Taking the electrical to pumped fluid efficiency to be η_{pump}, the total system efficiency would be

$$\eta_{\text{total}} = \eta_{\text{pump}}\eta_{\text{cavatappi}}\eta_{\text{plumbing}}. \qquad (A.9)$$

Here η_{plumbing} is the efficiency of the tube network used to plumb the actuator related to head loss. If the micropump is directly connected to the cavatappi, this value could be assumed to be 1. The $\eta_{\text{cavatappi}}$ term is the contractile efficiency for tuning PV work into mechanical work. Assuming an efficiency range of $0.21 < \eta_{\text{pump}} < 0.5$ and $\eta_{\text{plumbing}} = 1$, we estimate an electric-mechanical system efficiency range from 10 to 22%. This number would be application specific, as particular plumbing and pump efficiencies would need to be considered. The typically quoted energy conversion efficiency of mammalian skeletal muscles is about 20% [203].

Time response

In this work, we have assumed that the time response of cavatappi is the time that it takes the actuator to react under a pressure stimulus. Thus, the time response is the same as the time-lag defined in Fig. A.4(b), i.e. approximately 20 milliseconds.

Maximum actuation stress and strain

To compare the maximum stress of cavatappi with that of other actuator technologies, we used the maximum load that a cavatappi was capable of lifting divided by the cross-sectional area of the cavatappi coil (Fig. A.2). Note that this does not represent stress on the material, but rather a normalized lifting force of the overall actuator. In this case, the force is normalized by cross-sectional area:

$$A = \frac{\pi \ (C.OD^2)}{4}, \tag{A.10}$$

where $C.OD$ is the outer diameter of the coil (Fig. A.2). Note that this area includes the air space at the center of the coil (where the mandrel was in Fig. A.1(d)), while this is technically not part of the actuator, it is also not usable space and is part of the overall volume occupied by the actuator. The stress on the material would be much larger because the cross-sectional area of the cavatappi coil given by Eq. (A.10) is much larger than the cross-sectional area of the PVC material and includes PVC material, air space, and reinforcing fiber, which is not part of the load path.

The maximum actuation force can be seen in Fig. A.5(a) wherein two actuation cycles of a cavatappi artificial muscle under an axial load of 1.1 kg are presented. This load was found to be close to the blocked force capacity of the actuator; the actuation strain developed under this condition was very small ($\sim$0.5%). This force divided by the area given in Eq. (A.10) gives the actuator stress listed in Table 4.1. Note that Fig. A.5(a) also shows how the cavatappi creeps between cycles due to the high applied load.

In order to calculate the maximum actuation strain, a lifting test was performed with a small mass attached to the actuator. In theory, the maximum strain should be reported with zero attached load, but a small load was attached to increase the pitch of the helical configuration. Fig. A.5(b) shows two actuation cycles for a pre-stretched cavatappi artificial muscle under a load of 0.1 kg. Under this load the cavatappi was able to contract approximately 55% of its initial length. We defined actuator strain as the contraction divided by the initial actuator length under a given applied tensile load.

Actuator Lifetime
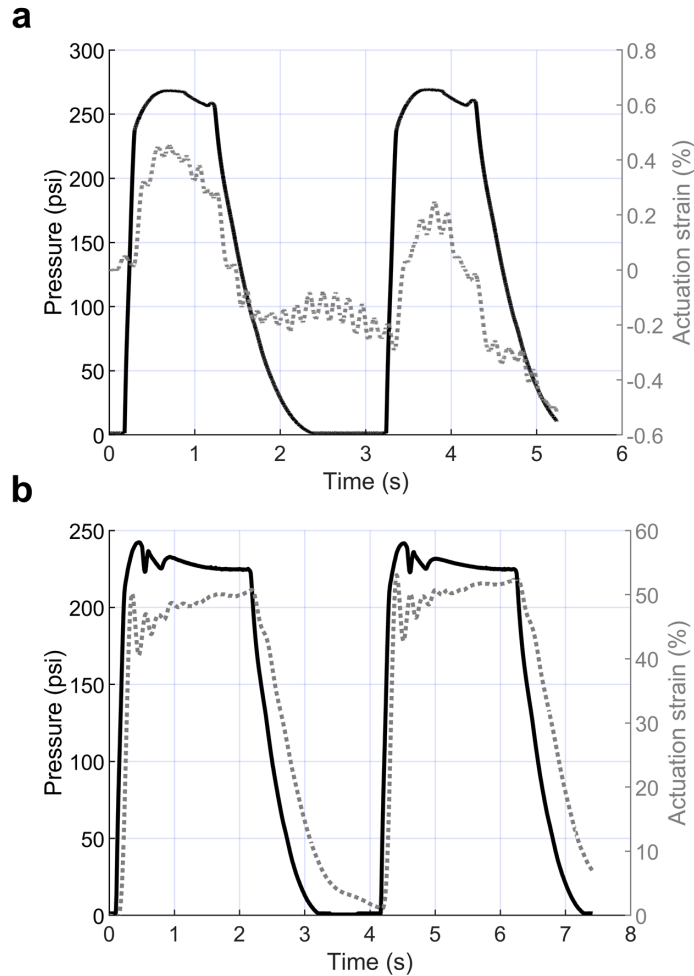
FIGURE A.5: Actuation under a load of 1.1 kg to show the maximum stress and under a load of 0.1 kg to show maximum strain.

To test the lifetime of cavatappi artificial muscles, a sample was cycled from zero to 220 psi, with increasing pressure taking approximately one second and, decreasing pressure requiring approximately 3.5 seconds (regulator limited). A 0.2 kg load was chosen for this experiment because Fig. 4.4 showed that the maximum peak specific power was developed near this load and thus the test would closely simulate real operating conditions. Fig. 4.4(e) shows the first 500 of the 10,000 cycles, along with an inset for the first 25 cycles. Actuation creep over ten-thousand cycles was not observed. Similar lifetime tests were conducted with a cavatappi artificial muscles without the nylon monofilament reinforcement at the core. Those experiments showed significant actuation creep, thus the almost

null creep effect shown in the lifetime actuation responses is attributed to the restorative force imposed by the internal nylon. We also found the monofilament reinforcement increased the lifetime of cavatappi by eliminating burst failures that occurred at the ends of the cavatappi. Prior to the monofilament addition, premature failures in life testing occurred in the straight section of tubing between the terminus of the helical section and the connector at the end of the tube. It was thought that these failures resulted from stress concentrations/pinching at the coupling, and it was hypothesized that the addition of a reinforcing monofilament may help to reduce any localized stresses. The addition of the core monofilament increases lifetime from ∼500 cycles to over 10,000 cycles. Fig 4.4(e) also shows a first cycle effect wherein the first actuation cycle does not recover to the initial state; however, after this first cycle, the actuation response is consistent.

A.4 Cavatappi Elemental Unit Actuation Demonstration

In order to highlight how cavatappi linear actuators contract, we developed a test to show how the elemental section (see Fig. 4.3, Fab. stage 3) untwists during internal pressurization. A 2 cm long elemental unit was fabricated with an outer pitch angle (α) of 45° and thermally annealed at 190°F for 30 minutes. After clamping one end and adding a dial indicator to the other, the tube section was internally pressurized (0-200 psi) to show the torsional actuation response. Fig. A.6 plots the angular displacement per unit length as a function of time and internal pressure. Pressure was stepped in 20 psi increments every four seconds. Previous testing showed the drawn tubes would burst at pressures above 300 psi, but pressures up to 250 psi were tolerated well when actuating. The angular displacement results show a nearly linear relationship with pressure. The maximum angular displacement was 70° (35°/cm of length), at a pressure of 200 psi. Angular recovery upon removal of the internal pressure occurred after approximately 40 s but is important to mention that a significant fraction of this angular recovery occurred
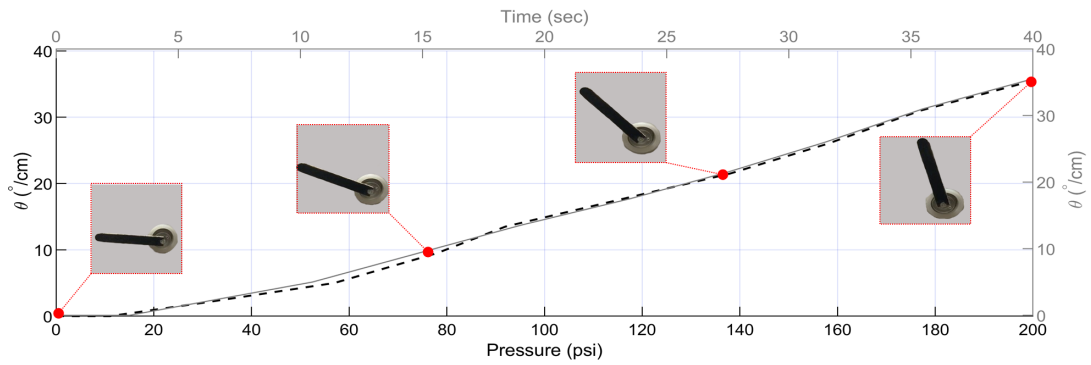
FIGURE A.6: The torsional actuation of a cavatappi artificial muscle elemental unit

within a second of depressurization highlighting the viscoelastic nature of the polymer. Movie A1 ▶ shows an illustrative animation of the torsional actuation of the elemental unit and how this is related to the axial actuation in cavatappi artificial muscles.

APPENDIX B

Material-based modeling of cavatappi artificial muscles. Supplementary Materials

B.1 Samples Preparation and Fabrication.

Previous characterizing the material properties of the precursor tubes used for fabrication or testing cavatappi artificial muscles, a consistent samples preparation and fabrication procedure is required. This section explains the preparation sample procedure for testing the precursor material properties, as well as cavatappi torsional actuators and artificial muscles, because their preparation procedures mirror the drawing and annealing processes. Here, we follow the fabrication process described by Higueras-Ruiz et al. [140].

Fig. B.1(a) and B.1(b) shows the precursor tube before and after drawing. The drawing process was shown by Higueras-Ruiz et al. to enhance the anisotropic properties of the precursor material and, in turn, the contraction actuation of cavatappi artificial muscles. During this process, a piece of Soft ND-100-65 Tygon PVC tubing with a 3.2 mm OD and a 1.6 mm ID is internally reinforced at the core with a lubricated 0.8 mm diameter nylon monofilament. This reinforcement is used to keep the opening of the tube from collapsing during annealing or kinking during twisting and coiling. Furthermore, it also provides the final structure a higher dimensional/structural rigidity (Fig. B.1(a)). The monofilament was lubricated with a small amount of mineral oil to aid insertion through the tube. A solid red line in Fig. B.1 is used to highlight how the internal microstructure of the material is reoriented during fabrication. The initial length of the reinforcing monofilament is longer than that of the tube, such that during drawing, the tube is drawn over some exposed reinforcement. After cold drawing with a ratio of approximately 3:1, the OD and ID of the tube is reduced to $\sim$2 mm and $\sim$0.8 mm, respectively, while

197

containing internal reinforcement throughout its length (Fig. B.1(b)). At this point, the nylon reinforcement is detached from the spool of nylon and along with the drawn tube attached to the hooks. At this stage (Fig. B.1(b)), the material can be annealed at 190°F for 30 minutes, cooled down to room temperature to release internal stresses, and used to test the drawn untwisted tube material properties. The resulting precursor tube will be cut in strips, blocks, or stay as a tube, depending on the experimental test to be performed (Section 5.2).
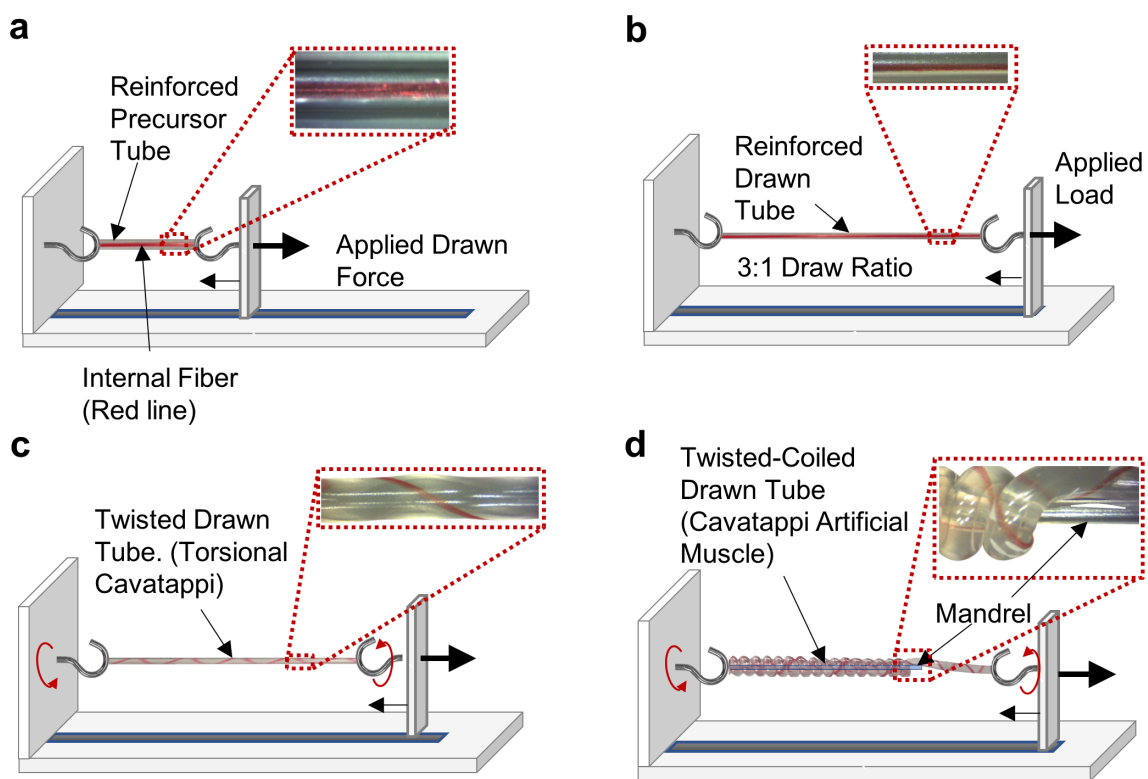
FIGURE B.1: Different states through the fabrication process of cavatappi artificial muscles. (a) Undrawn straight (untwisted) precursor polymer tube. (b) Drawn straight (untwisted) precursor polymer tube. (c) Cavatappi elemental unit; straight twisted polymer tube torsional actuator. (d) Cavatappi artificial muscles; axial actuator.

When the goal is to fabricate a cavatappi torsional actuator or artificial muscle, after drawing and reinforcing, initial twists are inserted into the drawn precursor tube as well as the nylon reinforcement under a small tensile load to keep the tube straight (Fig. B.1(c)). Similarly, as before, the sample can be annealed at 190°F for 30 minutes and

cooled down to room temperature to fabricate a cavatappi torsional actuator. However, if the sample keeps twisting, it will eventually buckle in torsion to start coiling to create a linear cavatappi artificial muscle. In order to maintain a uniform geometry of the coiled shape, a ~1 mm OD mandrel is inserted at the center of the helix (Fig. B.1(d)). Finally, the sample can be annealed and cooled to room temperature using the aforementioned heat treatment protocol to release internal stresses and keep the new shape.

Figure SB.2 shows the dimensions of the cavatappi artificial muscle used in this work along with real images of the side, cross-section, and top views of a cavatappi. Various lengths (L in Figure SB.2) have been used in this work; however, all strain actuation results have been reported as the amount of contraction divided by the initial length.

B.2 Precursor Material Properties. Testing Methods

As the model presented in this work uses the precursor drawn material properties for convenient design of cavatappi, methods for acquiring the physical properties of the material are needed. Drawn polymers can be classified as transversely isotropic—different properties in the axial (1-dir) and radial directions (2 and 3-dir) (see Fig. 5.2 in the manuscript)—the mechanical properties that are required are:

- Axial modulus, E_1.

- Radial modulus, E_2.

- Shear moduli: G_{12} and G_{23}.

- Poisson's ratios: ν_{12}, ν_{23}, and ν_{21}.

In this section, we present the methods used to obtain: axial modulus, E_1, shear modulus, G_{12}, radial modulus, E_2, and Poisson's ratios, ν_{12} and ν_{23}.
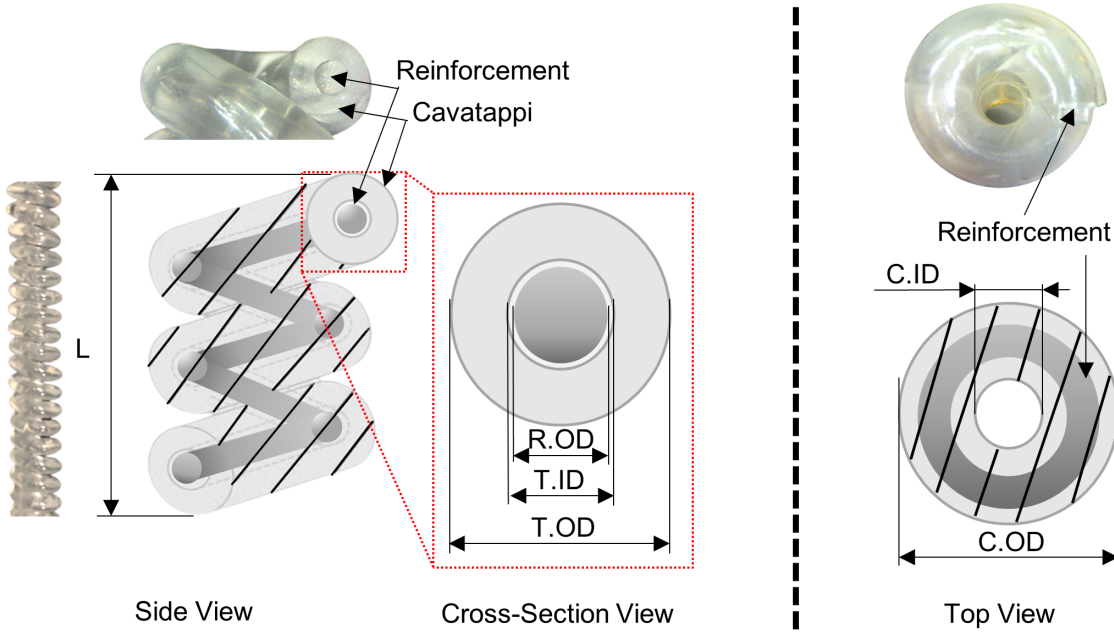
FIGURE B.2: Side, cross-sectional, and top views of the cavatappi artificial muscle used in this work along with its dimensions.

Reference	Definition	Dimension
R.OD	Reinforcement monofilament outer diameter	0.8 mm
T.ID	Tube inner diameter	0.8 mm
T.OD	Tube outer diameter	2 mm
C.ID	Coil inner diameter	1 mm
C.OD	Coil outer diameter	5 mm

B.2.1 Axial Modulus, E_1, and Shear Modulus, G_{12}, Set-up

A TA Instruments Hybrid Discovery Rheometer 2 (HR-2), along with a torsional or axial tool, were used to obtain the axial, E_1, and shear modulus, G_{12}, under the assumption of linear elasticity at room temperature (Fig. B.3(a)). The HR-2 allows for measurement resolutions of 0.1 nN-m in torque, 0.5 mN in force, 10 nrad in angular displacement, and 0.1 μm in axial displacement, making this piece of equipment suitable for the presented experimental testing.

Fig. B.3(a) shows the HR-2 with the torsional tool on the left and axial tool on the right used to clamp the sample. For each property, a total of three different samples were tested. The mechanical load was measured while gap distance was applied (for axial modulus), and angular displacement was measured while torque was applied (for shear modulus) by the HR-2. In order to remove first cycle effects [192], the samples were pre-cycled under the same testing conditions. After the first cycle, the consecutive results showed convergence. To calculate E_1, a 15 mm long sample prepared by axially cutting and unwrapping the tube was placed in the HR-2 using the flat tool and conducted to axial loading/unloading cycles (four cycles in total) with a maximum strain of approximately 5% while recording the force. To assume the short-term testing conditions (elasticity), the applied strain rate was 3.5%/s. As a result, the axial modulus, E_1, at a given stress-strain point can be defined as

$$E_1 = \frac{\sigma_{11}}{\varepsilon_{11}} = \frac{\left(\frac{4F}{\pi(D_0^2 - D_i^2)}\right)}{\left(\frac{\Delta L}{L_0}\right)}, \tag{B.1}$$

where σ_{11} is the mechanical axial stress, ε_{11} is the mechanical axial strain, F is tensile axial force, D_0 is the outer diameter (2 mm for the drawn tube in this work), D_i is the inner diameter (0.8 mm for the drawn tube in this work), ΔL is the change in length of the sample, and L_0 is the initial sample length. Note that even the tube was unwrapped for this test, the cross-section area still remains the same. Finally, for simplification, the axial modulus was calculated by using a linear fit on the last converged axial stress-strain cycle (see Fig. 5.2 in the manuscript).

To calculate shear modulus, a total of five stress-strain/torque-angular displacement experiments were conducted on a tubular sample of 7 mm in length. Here, the shear stress rate was 0.75 MPa/s and the maximum applied load 0.5 MPa. Similar to E_1, the last converged cycle was used to obtain stress-strain results. The shear modulus, G_{12}, at a

given stress-strain point can be defined as

$$G_{12} = \frac{\tau_{12}}{\gamma_{12}} = \frac{\left(\frac{D_0 T}{2J}\right)}{\left(\frac{D_0 \theta}{2L}\right)} = \frac{TL}{\theta J},$$ (B.2)

where τ_{12} is the mechanical shear stress, γ_{12} is the mechanical shear strain, T is the torque, L is the sample length, θ is the angular displacement, and J is the polar moment of inertia, which is equal to $\pi(D_0^2 - D_i^2)/32$ for a circular hollowed cross-section, with D_0 and D_i equal to the drawn tube outer and inner diameter, respectively. Similar to axial modulus, an estimate for shear modulus was calculated by using a linear fit on the last converged shear stress-strain.

B.2.2   Radial Modulus, E_2, Set-up

To obtain the radial modulus, E_2, of the precursor drawn tube, a square sheet of material obtained from unwrapping the tube was loaded under compression. We assume that the material presents the same stress/strain relationship during compression and extension, which seems to be a fair assumption for most polymers. For this method, the precursor drawn material was compressed between two flat parallel plates under the condition of plane strain. Figure B.3(b) shows the experimental set-up.

During this test, a total of three square sheets of material with a side length of approximately 5 mm and 0.6 mm in thickness were compressed while controlling displacement and recording the compressive force by the HR-2. A total of four cycles were conducted to ensure repeatability in the results. Every cycle was compressed to a maximum strain of 10% with a strain rate of 5%/s.
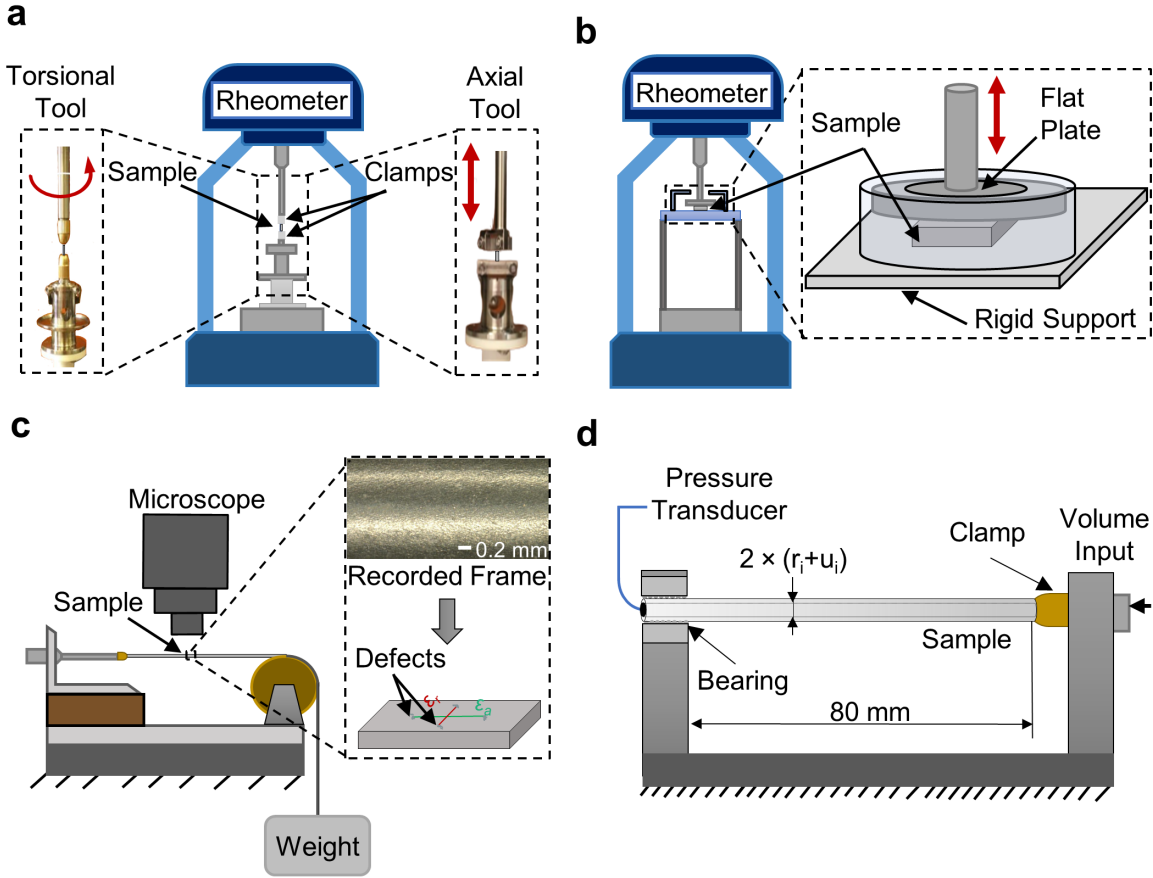
FIGURE B.3: Experimental set-ups for the acquisition of the mechanical properties of precursor drawn tube. (a) HR-2 along with the torsional and axial tool used to obtain the axial and shear modulus, respectively. (b) Radial modulus set-up with the HR-2 and flat plate accessory. (c) Posisson's ratio, ν_{12}, set-up with Keyence Digital Microscope under a 300x magnification. (d) Posisson's ratio, ν_{23}, set-up with a pressure transducer and controlled volume input.

This experimental methodology allowed the radial modulus to be calculated by,

$$E_2 = \frac{\sigma_2}{\varepsilon_2} = \frac{\left(\frac{F}{l^2}\right)}{\left(\frac{\Delta L}{L_0}\right)} \tag{B.3}$$

where E_2 is the radial modulus, F is the applied load, l is the length of the square block, ΔL is the change in thickness of the sample in compression, and L_0 is the initial sample thickness. Finally, we used a linear approximation to calculate the elastic radial modulus.

B.2.3 Poisson's Ratio, ν_{12}, Set-up

In order to determine Poisson's ratio in the plane of anisotropy, ν_{12}, radial and axial strains of the precursor material were measured using a digital microscope camera under different tensile loads. With this data for radial/axial strains, Poisson's ratio can be calculated by

$$\nu_{12} = -\frac{\varepsilon_{Radial}}{\varepsilon_{Axial}}. \tag{B.4}$$

During this test, similar to the sample preparation for E_1, the tube was cut in the axial direction to unwrap it in order to obtain a long sheet of material that could be used to track axial and radial deformations simultaneously. Fig. B.3(c) shows a diagram of the Poisson's ratio (12-dir) set-up where the sample is attached to a fixed point at one end and under a tensile load at the other with the use of a pulley to change the load direction. The deformation produces by the mechanical load was recorded as a function of axial load in the radial and axial direction at the material surface by using the Keyence Digital Microscope under a 300x magnification. One more time, the samples were precycled by applying the highest tested load to the samples before testing. Then microscopic imperfections were identified on a region on the flat surface close to the center, defined as reference points, and tracked by the microscope in radial and axial directions. Measuring the change in position of the radial points was a challenging process since displacement in this direction is minimal, and a high mechanical load was needed to produce significant deformation in the radial direction. As a result, a total of three samples were tested, and ν_{12} was calculated using the results under the final/highest load as they provide the maximum axial and radial deformation, which minimizes the human error during the measuring.

B.2.4 Poisson's Ratio, ν_{23}, Set-up

Finally, the Poisson's ratio in the plane of inisotropy, ν_{23}, was calculated using the thick-walled vessel stress analysis presented in Section 5.3 in the manuscript. More specifically, we used Eq. 5.13 in the manuscript to solve for

$$\nu_{23} = \frac{u_i E_2}{r_i p}, \tag{B.5}$$

where u_i is the radial displacement at r_i and p is the gauge pressure. Fig. B.3(d) shows the experimental set up for the ν_{23} test. Here, a total of three samples of approximately 80 mm in length were set under an internal volume input using a graduated water syringe. During the test, the sample was free to deform axially and radially. The input volume inside a tube that was already filled, ΔV, was used to calculate u_i as $\Delta V/(2 l_t \pi)$, where l_t is the length of the tube during the test. In addition, to solve Eq. B.5, the pressure was also recorded for every single volume input using a OMEGA PX319-100GV pressure transducer. As a result, the gauge pressure, internal volume, radial modulus, and tube dimensions were used to calculate the ν_{23}.

Furthermore, we checked the collected Poisson's ratio results for ν_{12} and ν_{23} using the strain energy analysis presented by Lempriere for the special case of transverse isotropy [187], where ν_{12} and ν_{23} are successfully checked to meet the following condition,

$$-1 < \nu_{23} < 1 \quad \text{and} \tag{B.6}$$

$$-\left(\frac{E_1}{E_2}\right)^{3/2} < \nu_{12} < \left(\frac{E_1}{E_2}\right)^{3/2} \tag{B.7}$$

B.3 Cavatappi Artificial Muscles and Torsional Actuator. Testing Methods

We used a Polytec OFV-5000 vibrometer controller with the OFV 534 optics head to measure torsional and linear displacement in actuation tests. We used a manually actuated graduated water syringe and an OMEGA PX319-100GV pressure transducer to apply and measure pressure in these tests. The voltage outputs of these systems are linearly related to a change of position of the object on which it focuses (vibrometer) and change in pressure (pressure transducer) (Fig. B.4). This voltage was recorded by a National Instruments PXI-6361 multifunction data acquisition card and subsequently, analyzed to develop the data in the primary manuscript.

Fig. B.4(a) shows the experimental set-up used to measure torsional actuation under no load (when weight 1 = weight 2) but also under different constant torque loads (when weight 1 < weight 2). In this set-up, we used an aluminum frame, two ball bearings, a torque spool, and a clamp to build the torsional actuator testing fixture. Fig. B.4(a) shows the torsional actuator fixed on the right by the clamp. On the left, the outside surface of the actuator was glued into a torque spool which is set in the bearing pair and free to rotate (when no torque is applied) and move in the axial direction. The sample was plugged on the left side, keeping the actuator from leaking during actuation. The angular position of a ~2 cm actuator was calculated by measuring the weight's displacement with the vibrometer under the settings of 0.2 mm/V (slow tracking filter) and the radius of the torque spool. For those tests under not torque, two masses of the same weight were wrapped around the spool in opposite directions. Thus the torques produced by both masses cancel out, and the free torsion condition was met. Fig. B.4(a) also shows how the displacements of the weights are related to the torsional actuation of the STPA. Finally, the torsional actuators were internally pressurized using manually controlled volume ramp inputs while measuring the internal pressure with the pressure

transducer. After a total of four torsional actuator cycles, the last cycle's data was used to obtain the results in the manuscript.
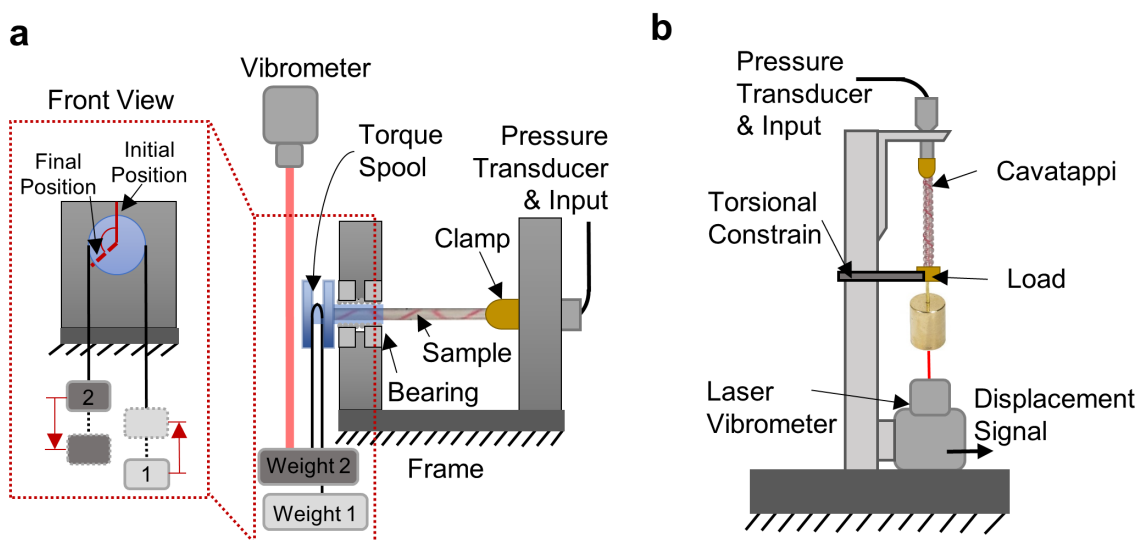
FIGURE B.4: Experimental set-ups for testing torsional cavatappi actuators and cavatappi artificial muscles. (a) Free torsion or isotorque set-up used to measure torsional actuation. Left-side shows a diagram of the experimental set-up with a cavatappi torsional actuator set in place along with the torsional actuation response (front view). (b) Experimental set-up used to measure axial contraction of cavatappi artificial muscles.

To measure linear actuation of cavatappi artificial muscles as a function of pressure under various loads, once again, the vibrometer, water graduated syringe, and pressure transducer was used. Fig. B.4(b) shows the set-up used to measure the axial strain actuation of cavatappi. In this set-up, the cavatappi artificial muscle was clamped vertically with the top end fixed to a beam and the bottom end hanging freely with a mass use to apply axial isotonic loading. In addition, during the cavatappi actuation tests, the samples were also constrained from rotation at the end of the sample by adding a small rod to the hanging weight, which contacted the vertical beam, which served as a mount for the entire rig (Fig. B.4(b)). In theory, this rod added some friction to the actuation, but that was considered negligible. The vibrometer was positioned directly below the sample, with the laser reflecting off the attached mass to measure position. Volume inputs were

controlled by the graduated syringe while recording the internal pressure with the pressure transducer. Finally, internal pressure and the axial contraction of cavatappi were combined to present the results in the main manuscript.

BIBLIOGRAPHY

[1] Atlas. `https://www.bostondynamics.com/atlas`. Accessed: 2021-07-03.

[2] Hydraulic cylinder. mill type. cdl2 type. re 17326. version: 2013-06. replaces:12.12. `https://docs.rs-online.com/c870/0900766b812c4444.pdf`. Accessed: 2021-07-03.

[3] Spot. `https://www.bostondynamics.com/spot`. Accessed: 2021-07-03.

[4] When to select an electric or pneumatic rotary actuator with quarter turn valves. `https://assuredautomation.com/news-and-training/wp-content/uploads/2016/08/electric-vs-pneumatic-rotary-actuators`. Accessed: 2021-07-03.

[5] *Weather and Climate. Relative Humidity*, 2008 (accessed March 2, 2020). `https://weather-and-climate.com/average-monthly-Humidity-perc,phoenix,United-States-of-America`.

[6] A. Abbas and J. Zhao. A physics based model for twisted and coiled actuator. In *2017 IEEE International Conference on Robotics and Automation (ICRA)*, pages 6121–6126, 2017.

[7] B. C. Abbott and X. M. Aubert. The force exerted by active striated muscle during and after change of length. *The Journal of Physiology*, 117(1):77–86, 1952.

[8] E. Acome, S. K. Mitchell, T. G. Morrissey, M. B. Emmett, C. Benjamin, M. King, M. Radakovitz, and C. Keplinger. Hydraulically amplified self-healing electrostatic actuators with muscle-like performance. *Science*, 359(6371):61–65, 2018.

[9] M. Adami and A. Seibel. On-board pneumatic pressure generation methods for soft robotics applications. *Actuators*, 8(1), 2019.

[10] G. Agarwal, N. Besuchet, B. Audergon, and J. Paik. Stretchable materials for robust soft actuators towards assistive wearable devices. *Scientific Reports*, 6:34224, 10 2016.

[11] S. Agarwal, S. Jiang, and Y. Chen. Progress in the field of water- and/or temperature-triggered polymer actuators. *Macromolecular Materials and Engineering*, 304(2):1800548, 2019.

[12] I. Agnarsson, A. Dhinojwala, V. Sahni, and T. A. Blackledge. Spider silk as a novel high performance biomimetic muscle driven by humidity. *Journal of Experimental Biology*, 212(13):1990–1994, 07 2009.

[13] P. Aigner and B. McCarragher. Human integration into robot control utilising potential fields. In *Proceedings of International Conference on Robotics and Automation*, volume 1, pages 291–296 vol.1, 1997.

[14] A. Ajoudani, S. B. Godfrey, M. Catalano, G. Grioli, N. Tsagarakis, and A. Bicchi. Teleimpedance control of a synergy-driven anthropomorphic hand. *2013 IEEE/RSJ International Conference on Intelligent Robots and Systems*, pages 1985–1991, 2013.

[15] A. Ajoudani, N. Tsagarakis, and A. Bicchi. Tele-impedance: Teleoperation with impedance regulation using a body–machine interface. *The International Journal of Robotics Research*, 31:1642 – 1656, 2012.

[16] Y. Akiyama, T. Hoshino, K. Iwabuchi, and K. Morishima. Room temperature operable autonomously moving bio-microrobot powered by insect dorsal vessel tissue. *PLOS ONE*, 7(7):1–6, 07 2012.

[17] A. Albu-Schäffer, S. Wolf, O. Eiberger, S. Haddadin, F. Petit, and M. Chalon. Dynamic modelling and control of variable stiffness actuators. *2010 IEEE International Conference on Robotics and Automation*, pages 2155–2162, 2010.

[18] J. Alcazar, R. Csapo, I. Ara, and L. M. Alegre. On the shape of the force-velocity relationship in skeletal muscles: The linear, the hyperbolic, and the double-hyperbolic. *Frontiers in Physiology*, 10:769, 2019.

[19] V. A. Alvarez, A. N. Fraga, and A. Vázquez. Effects of the moisture and fiber content on the mechanical properties of biodegradable polymer–sisal fiber biocomposites. *Journal of Applied Polymer Science*, 91(6):4007–4016, 2004.

[20] M. Amjadi and M. Sitti. Self-sensing paper actuators based on graphite–carbon nanotube hybrid films. *Advanced Science*, 5(7):1800239, 2018.

[21] K. Amundson, J. Raade, N. Harding, and H. Kazerooni. Hybrid hydraulic-electric power unit for field and service robots. *2005 IEEE/RSJ International Conference on Intelligent Robots and Systems*, pages 3453–3458, 2005.

[22] F. C. Anderson and M. G. Pandy. Storage and utilization of elastic strain energy during jumping. *Journal of Biomechanics*, 26(12):1413–1427, 1993.

[23] G. Andrikopoulos, G. Nikolakopoulos, and S. Manesis. A survey on applications of pneumatic artificial muscles. *2011 19th Mediterranean Conference on Control & Automation (MED)*, pages 1439–1446, 2011.

[24] R. Arridge and P. Barham. A theory for the drawing of oriented crystalline polymers. *Journal of Polymer Science Part B: Polymer Physics*, 16(7):1297–1319, 1978.

[25] Y. Asano, K. Okada, and M. Inaba. Design principles of a human mimetic humanoid: Humanoid platform to study human intelligence and internal body system. *Science Robotics*, 2(13), 2017.

[26] G. Askew, I. Young, and J. Altringham. Fatigue of mouse soleus muscle, using the work loop technique. *The Journal of experimental biology*, 200:2907–12, 12 1997.

[27] G. Asuni, G. Teti, C. Laschi, E. Guglielmelli, and P. Dario. Extension to end-effector position and orientation control of a learning-based neurocontroller for a humanoid arm. *2006 IEEE/RSJ International Conference on Intelligent Robots and Systems*, pages 4151–4156, 2006.

[28] S. Aziz, S. Naficy, J. Foroughi, H. R. Brown, and G. M. Spinks. Controlled and scalable torsional actuation of twisted nylon 6 fiber. *Journal of Polymer Science Part B: Polymer Physics*, 54(13):1278–1286, 2016.

[29] G. Bao, H. Fang, L. Chen, Y. Wan, F. Xu, Q. Yang, and L. Zhang. Soft robotics: Academic insights and perspectives through bibliometric analysis. *Soft Robotics*, 5(3):229–241, 2018. PMID: 29782219.

[30] Y. Bar-Cohen. Electroactive polymers as artificial muscles-capabilities, potentials and challenges. *Handbook on Biomimetics*, 11, 09 2000.

[31] Y. Bar-Cohen. Biologically inspired intelligent robots using artificial muscles. volume 41, pages 2– 8, 08 2003.

[32] F. O. Barroso, D. Torricelli, F. Molina-Rueda, I. M. Alguacil-Diego, R. C. de-la Cuerda, C. Santos, J. C. Moreno, J. C. Miangolarra-Page, and J. L. Pons. Combining muscle synergies and biomechanical analysis to assess gait in stroke patients. *Journal of Biomechanics*, 63:98–103, 2017.

[33] K. Basel. *Principles of Exercise Biochemistry.*

[34] R. H. Baughman, C. Cui, A. A. Zakhidov, Z. Iqbal, J. N. Barisci, G. M. Spinks, G. G. Wallace, A. Mazzoldi, D. De Rossi, A. G. Rinzler, O. Jaschinski, S. Roth, and M. Kertesz. Carbon nanotube actuators. *Science*, 284(5418):1340–1344, 1999.

[35] R. H. Baughman, A. A. Zakhidov, and W. A. de Heer. Carbon nanotubes–the route toward applications. *Science*, 297(5582):787–792, 2002.

[36] G. Belforte, G. Eula, A. Ivanov, and S. Sirolli. Soft pneumatic actuators for rehabilitation. *Actuators*, 3(2):84–106, 2014.

[37] A. Berens and H. Hopfenberg. Diffusion and relaxation in glassy polymer powders: 2. separation of diffusion and relaxation parameters. *Polymer*, 19(5):489 – 496, 1978.

[38] D. E. Besnard. *Quoting M-Series Brushless micro-pumps efficiency (On-line meeting).*

[39] P. Beyl, K. Knaepen, S. Duerinck, M. V. Damme, B. Vanderborght, R. Meeusen, and D. Lefeber. Safe and compliant guidance by a powered knee exoskeleton for robot-assisted rehabilitation of gait. *Advanced Robotics*, 25(5):513–535, 2011.

[40] S. S. P. A. Bishe, T. Nguyen, Y. Fang, and Z. F. Lerner. Adaptive ankle exoskeleton control: Validation across diverse walking conditions. *IEEE Transactions on Medical Robotics and Bionics*, 3(3):801–812, 2021.

[41] D. Bombara, V. Mansurov, R. Konda, S. Fowzer, and J. Zhang. Self-sensing for twisted string actuators using conductive supercoiled polymers. 2019.

[42] P. Boyraz, G. Runge, and A. Raatz. An overview of novel actuators for soft robotics. *Actuators*, 7(3), 2018.

[43] P. Brochu and Q. Pei. Advances in dielectric elastomers for actuators and artificial muscles. *Macromolecular Rapid Communications*, 31(1):10–36, 2010.

[44] C. E. Browning, G. E. Husman, and J. M. Whitney. Moisture effects in epoxy matrix composites. 1977.

[45] J. A. O. Bruno, N. L. Allan, T. H. K. Barron, and A. D. Turner. Thermal expansion of polymers: Mechanisms in orthorhombic polyethylene. *Phys. Rev. B*, 58:8416–8427, Oct 1998.

[46] M. Bryant, M. A. Meller, and E. Garcia. Variable recruitment fluidic artificial muscles: modeling and experiments. *Smart Materials and Structures*, 23(7):074009, jun 2014.

[47] V. Bukošek and D. C. Prevoršek. Model of nylon 6 fibers microstructure microfibrillar model or "swiss-cheese" model? *International journal of polymeric materials*, 47(4):569–592, 2000.

[48] J. Burgner-Kahrs, D. C. Rucker, and H. Choset. Continuum robots for medical applications: A survey. *IEEE Transactions on Robotics*, 31(6):1261–1280, 2015.

[49] A. Calanca, R. Muradore, and P. Fiorini. A review of algorithms for compliant control of stiff and fixed-compliance robots. *IEEE/ASME Transactions on Mechatronics*, 21:613–624, 2016.

[50] D. G. Caldwell. Natural and artificial muscle elements as robot actuators. *Mechatronics*, 3(3):269–283, 1993. Special Issue Robot Actuators.

[51] M. Calisti, M. Giorelli, G. Levy, B. Mazzolai, B. Hochner, C. Laschi, and P. Dario. An octopus-bioinspired solution to movement and manipulation for soft robots. *Bioinspiration & Biomimetics*, 6(3):036002, jun 2011.

[52] M. C. Capolei, E. Angelidis, E. Falotico, H. H. Lund, and S. Tolu. A biomimetic control method increases the adaptability of a humanoid robot acting in a dynamic environment. *Frontiers in Neurorobotics*, 13:70, 2019.

[53] F. Carpi, G. Frediani, and D. De Rossi. Hydrostatically coupled dielectric elastomer actuators. *IEEE/ASME Transactions on Mechatronics*, 15(2):308–315, 2010.

[54] F. Carpi, G. Frediani, C. Gerboni, J. Gemignani, and D. De Rossi. Enabling variable-stiffness hand rehabilitation orthoses with dielectric elastomer transducers. *Medical Engineering Physics*, 36(2):205–211, 2014.

[55] F. Carpi, R. Kornbluh, P. Sommer-Larsen, and G. Alici. Electroactive polymer actuators as artificial muscles: are they ready for bioinspired applications? *Bioinspiration & Biomimetics*, 6(4):045006, nov 2011.

[56] E. M. Chapman and M. Bryant. Bioinspired passive variable recruitment of fluidic artificial muscles. *Journal of Intelligent Material Systems and Structures*, 29(15):3067–3081, 2018.

[57] B. Chen, B. Zi, L. Qin, and Q. Pan. State-of-the-art research in robotic hip exoskeletons: A general review. *Journal of Orthopaedic Translation*, 20:4–13, 2020. The Role of FEA and Other Imaging-based Assessment in Orthopaedics.

[58] N. Cheney, J. Bongard, and H. Lipson. Evolving soft robots in tight spaces. In *Proceedings of the 2015 Annual Conference on Genetic and Evolutionary Computation*, GECCO '15, page 935–942, New York, NY, USA, 2015. Association for Computing Machinery.

[59] N. Cheney, R. MacCurdy, J. Clune, and H. Lipson. Unshackling evolution: Evolving soft robots with multiple materials and a powerful generative encoding. In *Proceedings of the 15th Annual Conference on Genetic and Evolutionary Computation*, GECCO '13, page 167–174, New York, NY, USA, 2013. Association for Computing Machinery.

[60] G. Cheng, E. Dean-Leon, F. Bergner, J. Rogelio Guadarrama Olvera, Q. Leboutet, and P. Mittendorfer. A comprehensive realization of robot skin: Sensors, sensing, control, and applications. *Proceedings of the IEEE*, 107(10):2034–2051, 2019.

[61] G. Cheng, S. K. Ehrlich, M. Lebedev, and M. A. L. Nicolelis. Neuroengineering challenges of fusing robotics and neuroscience. *Science Robotics*, 5(49), 2020.

[62] G. Cheng, S.-H. Hyon, J. Morimoto, A. Ude, J. G. Hale, G. Colvin, W. Scroggin, and S. C. Jacobsen. Cb: a humanoid research platform for exploring neuroscience. *Advanced Robotics*, 21(10):1097–1114, 2007.

[63] V. C. K. Cheung, A. d'Avella, and E. Bizzi. Adjustments of motor pattern for load compensation via modulated activations of muscle synergies during natural behaviors. *Journal of Neurophysiology*, 101(3):1235–1257, 2009. PMID: 19091930.

[64] J.-B. Chossat, D. K. Y. Chen, Y.-L. Park, and P. B. Shull. Soft wearable skin-stretch device for haptic feedback using twisted and coiled polymer actuators. *IEEE Transactions on Haptics*, 12(4):521–532, 2019.

[65] C. Chou and B. Hannaford. Measurement and modeling of mckibben pneumatic artificial muscles. *IEEE Trans. Robotics Autom.*, 12:90–102, 1996.

[66] C.-P. Chou and B. Hannaford. Static and dynamic characteristics of mckibben pneumatic artificial muscles. In *Proceedings of the 1994 IEEE International Conference on Robotics and Automation*, pages 281–286 vol.1, 1994.

[67] A. M. Choube. Finite element analysis of helical spring in monosuspension systems. *International Journal of Engineering Science and Computing*, 6(5):4947–4950, 2016.

[68] C. Choy, F. Chen, and K. Young. Negative thermal expansion in oriented crystalline polymers. *Journal of Polymer Science: Polymer Physics Edition*, 19(2):335–352, 1981.

[69] M. Cianchetti, A. Arienti, M. Follador, B. Mazzolai, P. Dario, and C. Laschi. Design concept and validation of a robotic arm inspired by the octopus. *Materials Science*

and Engineering: C, 31(6):1230–1239, 2011. Principles and Development of Bio-Inspired Materials.

[70] S. Collins, A. Ruina, R. Tedrake, and M. Wisse. Efficient bipedal robots based on passive-dynamic walkers. *Science*, 307(5712):1082–1085, 2005.

[71] S. Coyle, C. Majidi, P. LeDuc, and K. J. Hsia. Bio-inspired soft robotics: Material selection, actuation, and design. *Extreme Mechanics Letters*, 22:51–59, 2018.

[72] P. Crago and G. haur Shue. Muscle-tendon model with length-history dependent activation-velocity coupling. In *Ann Biomed Eng.*, volume 26, pages 369–80, 1998.

[73] S. Cranford and M. J. Buehler. Twisted and coiled ultralong multilayer graphene ribbons. *Modelling and Simulation in Materials Science and Engineering*, 19(5):054003, jun 2011.

[74] F. Daerden and D. Lefeber. The concept and design of pleated pneumatic artificial muscles. *International Journal of Fluid Power*, 2(3):41–50, 2001.

[75] F. Daerden, D. Lefeber, B. Verrelst, and R. Van Ham. Pleated pneumatic artificial muscles: compliant robotic actuators. In *Proceedings 2001 IEEE/RSJ International Conference on Intelligent Robots and Systems. Expanding the Societal Role of Robotics in the the Next Millennium (Cat. No.01CH37180)*, volume 4, pages 1958–1963 vol.4, 2001.

[76] M. Daley and A. Biewener. Running over rough terrain reveals limb control for intrinsic stability. *Proceedings of the National Academy of Sciences*, 103:15681 – 15686, 2006.

[77] M. Daley and A. Biewener. Leg muscles that mediate stability: mechanics and control of two distal extensor muscles during obstacle negotiation in the guinea fowl. *Philosophical Transactions of the Royal Society B: Biological Sciences*, 366:1580 – 1591, 2011.

[78] M. Daley, A. S. Voloshina, and A. Biewener. The role of intrinsic muscle mechanics in the neuromuscular control of stable running in the guinea fowl. *The Journal of Physiology*, 587, 2009.

[79] M. V. Damme, B. Vanderborght, B. Verrelst, R. V. Ham, F. Daerden, and D. Lefeber. Proxy-based sliding mode control of a planar pneumatic manipulator. *The International Journal of Robotics Research*, 28(2):266–284, 2009.

[80] C. A. de Saint-Aubin, S. Rosset, S. Schlatter, and H. Shea. High-cycle electromechanical aging of dielectric elastomer actuators with carbon-based electrodes. *Smart Materials and Structures*, 27(7):074002, jun 2018.

[81] S. A. DeLaHunt, T. E. Pillsbury, and N. M. Wereley. Variable recruitment in bundles of miniature pneumatic artificial muscles. *Bioinspiration & Biomimetics*, 11(5):056014, sep 2016.

[82] C. Della Santina, R. K. Katzschmann, A. Biechi, and D. Rus. Dynamic control of soft robots interacting with the environment. In *2018 IEEE International Conference on Soft Robotics (RoboSoft)*, pages 46–53, 2018.

[83] K. Derrien and P. Gilormini. The effect of moisture-induced swelling on the absorption capacity of transversely isotropic elastic polymer–matrix composites. *International Journal of Solids and Structures - INT J SOLIDS STRUCT*, 46:1547–1553, 03 2009.

[84] J. Di, X. Zhang, Z. Yong, Y. Zhang, D. Li, R. Li, and Q. Li. Carbon-nanotube fibers for wearable devices and smart textiles. *Advanced Materials*, 28(47):10529–10538, 2016.

[85] A. Di Lallo, M. G. Catalano, M. Garabini, G. Grioli, M. Gabiccini, and A. Bicchi. Dynamic morphological computation through damping design of soft continuum robots. *Frontiers in Robotics and AI*, 6:23, 2019.

[86] T. Dick, A. Biewener, and J. Wakeling. Comparison of human gastrocnemius forces predicted by hill-type muscle models and estimated from ultrasound images. *Journal of Experimental Biology*, 220:1643 – 1653, 2017.

[87] M. H. Dickinson, C. T. Farley, R. J. Full, M. A. R. Koehl, R. Kram, and S. Lehman. How animals move: An integrative view. *Science*, 288(5463):100–106, 2000.

[88] L. Ding, N. Dai, X. Mu, S. Xie, X. Fan, D. Li, and X. Cheng. Design of soft multi-material pneumatic actuators based on principal strain field. *Materials Design*, 182:108000, 2019.

[89] A. Doria, S. Cocuzza, N. Comand, M. Bottin, and A. Rossi. Analysis of the compliance properties of an industrial robot with the mozzi axis approach. *Robotics*, 8(3), 2019.

[90] D. Drotman, S. Jadhav, D. Sharp, C. Chan, and M. T. Tolley. Electronics-free pneumatic circuits for controlling soft-legged robots. *Science Robotics*, 6(51), 2021.

[91] L. Duan, J.-C. Lai, C.-H. Li, and J.-L. Zuo. A dielectric elastomer actuator that can self-heal integrally. *ACS Applied Materials & Interfaces*, 12(39):44137–44146, 2020. PMID: 32926620.

[92] M. Duduta, E. Hajiesmaili, H. Zhao, R. J. Wood, and D. R. Clarke. Realizing the potential of dielectric elastomer artificial muscles. *Proceedings of the National Academy of Sciences*, 116(7):2476–2481, 2019.

[93] C. Duriez. Control of elastic soft robots based on real-time finite element method. In *2013 IEEE International Conference on Robotics and Automation*, pages 3982–3987, 2013.

[94] C. Duriez and T. Bieze. *Soft Robot Modeling, Simulation and Control in Real-Time*, volume 17, pages 103–109. 09 2017.

[95] S. Dutta, B. Nelson, M. Gage, and K. Nishikawa. Calcium dependent interaction between n2a-halo and f-actin: A single molecule study. *Biophysical Journal*, 114:353a, 02 2018.

[96] M. Ehsani, Y. Gao, and S. Gay. Characterization of electric motor drives for traction applications. In *IECON'03. 29th Annual Conference of the IEEE Industrial Electronics Society (IEEE Cat. No.03CH37468)*, volume 1, pages 891–896 vol.1, 2003.

[97] N. El-Atab, R. B. Mishra, F. Al-Modaf, L. Joharji, A. A. Alsharif, H. Alamoudi, M. Diaz, N. Qaiser, and M. M. Hussain. Soft actuators for soft robotic applications: A review. *Advanced Intelligent Systems*, 2(10):2000128, 2020.

[98] J. Elad and J. Schultz. Microstructural rearrangement during heat treatment of drawn nylon 66 fiber. *Journal of Polymer Science: Polymer Physics Edition*, 22(5):781–792, 1984.

[99] K. Elgeneidy, N. Lohse, and M. Jackson. Data-driven bending angle prediction of soft pneumatic actuators with embedded flex sensors. *IFAC-PapersOnLine*, 49:513–520, 2016.

[100] I. Emri and V. Pavsek. On the influence of moisture on the mechanical properties of polymers. *Materials Forum*, 16:123–131, 12 1992.

[101] X. Fan. Mechanics of moisture for polymers: Fundamental concepts and model study. pages 1 – 14, 05 2008.

[102] S. Ferrante, N. C. Bejarano, E. Ambrosini, A. Nardone, A. M. Turcato, M. Monticone, G. Ferrigno, and A. Pedrocchi. A personalized multi-channel fes controller based on muscle synergies to support gait rehabilitation after stroke. *Frontiers in Neuroscience*, 10, 2016.

[103] A. Firouzeh, M. Salerno, and J. Paik. Soft pneumatic actuator with adjustable stiffness layers for multi-dof actuation. *2015 IEEE/RSJ International Conference on Intelligent Robots and Systems (IROS)*, pages 1117–1124, 2015.

[104] R. H. Fitts, C. J. Brimmer, J. P. Troup, and B. R. Unsworth. Contractile and fatigue properties of thyrotoxic rat skeletal muscle. *Muscle & Nerve*, 7(6):470–477, 1984.

[105] J. Foroughi, G. M. Spinks, G. G. Wallace, J. Oh, M. E. Kozlov, S. Fang, T. Mirfakhrai, J. D. W. Madden, M. K. Shin, S. J. Kim, and R. H. Baughman. Torsional carbon nanotube artificial muscles. *Science*, 334(6055):494–497, 2011.

[106] Y. Forterre, J. M. Skotheim, J. Dumais, and L. Mahadevan. How the venus flytrap snaps. *Nature*, 433(7024):421—425, January 2005.

[107] M. Franz and H. Mallot. Biomimetic robot navigation. *Robotics and Autonomous Systems*, 30:133–153, 01 2000.

[108] F. Fu, L. Shang, Z. Chen, Y. Yu, and Y. Zhao. Bioinspired living structural color hydrogels. *Science Robotics*, 3(16):eaar8580, 2018.

[109] R. Full and K. Meijer. Artificial muscles versus natural actuators from frogs to flies [3987-01]. *PROCEEDINGS-SPIE THE INTERNATIONAL SOCIETY FOR OPTICAL ENGINEERING*, pages 2–11, 06 2000.

[110] I. Gaiser, R. Wiegand, O. Ivlev, A. Andres, H. Breitwieser, S. Schulz, and G. Bretthauer. Compliant robotics and automation with flexible fluidic actuators and inflatable structures. In G. Berselli, R. Vertechy, and G. Vassura, editors, *Smart Actuation and Sensing Systems*, chapter 22. IntechOpen, Rijeka, 2012.

[111] C. Galindo, J. Gonzalez, and J.-A. Fernandez-Madrigal. Control architecture for human–robot integration: Application to a robotic wheelchair. *IEEE Transactions on Systems, Man, and Cybernetics, Part B (Cybernetics)*, 36(5):1053–1067, 2006.

[112] L. Gao, M. U. Akhtar, F. Yang, S. Ahmad, J. He, Q. Lian, W. Cheng, J. Zhang, and D. Li. Recent progress in engineering functional biohybrid robots actuated by living cells. *Acta Biomaterialia*, 121:29–40, 2021.

[113] Z. Gao, Q. Shi, T. Fukuda, C. Li, and Q. Huang. An overview of biomimetic robots with animal behaviors. *Neurocomputing*, 332:339–350, 2019.

[114] G. M. Gasparri, M. O. Bair, R. P. Libby, and Z. F. Lerner. Verification of a robotic ankle exoskeleton control scheme for gait assistance in individuals with cerebral palsy. pages 4673–4678, 2018.

[115] T. George Thuruthel, Y. Ansari, E. Falotico, and C. Laschi. Control strategies for soft robotic manipulators: A survey. *Soft Robotics*, 5(2):149–163, 2018. PMID: 29297756.

[116] S. H. Ghaderi and E. Hajiesmaili. Molecular structural mechanics applied to coiled carbon nanotubes. *Computational Materials Science*, 55:344–349, 2012.

[117] M. Giorcelli and M. Bartoli. Carbon nanostructures for actuators: An overview of recent developments. *Actuators*, 8(2), 2019.

[118] M. Giorelli, F. Renda, G. Ferri, and C. Laschi. A feed-forward neural network learning the inverse kinetics of a soft cable-driven manipulator moving in three-dimensional space. *2013 IEEE/RSJ International Conference on Intelligent Robots and Systems*, pages 5033–5039, 2013.

[119] V. Giovinco, P. Kotak, V. Cichella, C. Maletta, and C. Lamuta. Dynamic model for the tensile actuation of thermally and electro-thermally actuated twisted and coiled artificial muscles (TCAMs). *Smart Materials and Structures*, 29(2):025004, dec 2019.

[120] M. Goldfarb, E. Barth, M. A. Gogola, and J. Wehrmeyer. Design and energetic characterization of a liquid-propellant-powered actuator for self-powered robots. *IEEE-ASME Transactions on Mechatronics*, 8:254–262, 2003.

[121] S. D. Gollob, C. Park, B. H. B. Koo, and E. T. Roche. A modular geometrical framework for modelling the force-contraction profile of vacuum-powered soft actuators. *Frontiers in Robotics and AI*, 8:15, 2021.

[122] A. M. Gordon, A. Huxley, and F. Julian. The variation in isometric tension with sarcomere length in vertebrate muscle fibres. *The Journal of Physiology*, 184, 1966.

[123] U. Goswami and J. Ziegler. Fluency, phonology and morphology: a response to the commentaries on becoming literate in different languages. 09 2006.

[124] S. Haddadin, S. Haddadin, A. Khoury, T. Rokahr, S. Parusel, R. Burgkart, A. Bicchi, and A. Albu-Schäffer. On making robots understand safety: Embedding injury

knowledge into control. *The International Journal of Robotics Research*, 31:1578 – 1602, 2012.

[125] S. Haddadin, M. Weis, S. Wolf, and A. Albu-Schaffer. Optimal control for maximizing link velocity of robotic variable stiffness joints. *IFAC Proceedings Volumes*, 44:6863–6871, 2011.

[126] D. Hagen, D. Padovani, and M. Choux. A comparison study of a novel self-contained electro-hydraulic cylinder versus a conventional valve-controlled actuator—part 1: Motion control. *Actuators*, 8(4), 2019.

[127] C. S. Haines, N. Li, G. M. Spinks, A. E. Aliev, J. Di, and R. H. Baughman. New twist on artificial muscles. *Proceedings of the National Academy of Sciences*, 113(42):11709–11716, 2016.

[128] C. S. Haines, M. D. Lima, N. Li, G. M. Spinks, J. Foroughi, J. D. W. Madden, S. H. Kim, S. Fang, M. Jung de Andrade, F. Göktepe, Ö. Göktepe, S. M. Mirvakili, S. Naficy, X. Lepró, J. Oh, M. E. Kozlov, S. J. Kim, X. Xu, B. J. Swedlove, G. G. Wallace, and R. H. Baughman. Artificial muscles from fishing line and sewing thread. *Science*, 343(6173):868–872, 2014.

[129] R. V. Ham, T. G. Sugar, B. Vanderborght, K. W. Hollander, and D. Lefeber. Compliant actuator designs. *IEEE Robotics Automation Magazine*, 16(3):81–94, 2009.

[130] M. Hamaya, T. Matsubara, T. Teramae, T. Noda, and J. Morimoto. Design of physical user–robot interactions for model identification of soft actuators on exoskeleton robots. *The International Journal of Robotics Research*, 40:397 – 410, 2021.

[131] A. H. Hansen, D. S. Childress, S. C. Miff, S. A. Gard, and K. P. Mesplay. The human ankle during walking: implications for design of biomimetic ankle prostheses. *Journal of Biomechanics*, 37(10):1467–1474, 2004.

[132] J. Hanson and H. Huxley. Structural basis of the cross-striations in muscle. *Nature*, 172:530–532, 1953.

[133] H. Hauser, R. Füchslin, and K. Nakajima. *Morphological Computation - The Body as a Computational Resource*, pages 226–. 10 2014.

[134] T. Helps and J. Rossiter. Proprioceptive flexible fluidic actuators using conductive working fluids. *Soft Robotics*, 5(2):175–189, 2018. PMID: 29211627.

[135] T. Helps and J. Rossiter. Proprioceptive flexible fluidic actuators using conductive working fluids. *Soft Robotics*, 5(2):175–189, 2018. PMID: 29211627.

[136] D. R. Higueras Ruiz. Characterizing material properties of drawn monofilament for twisted polymer actuation, 2018.

[137] D. R. Higueras-Ruiz, C. J. Center, H. P. Feigenbaum, A. M. Swartz, and M. W. Shafer. Finite element analysis of straight twisted polymer actuators using precursor properties. *Smart Materials and Structures*, 30(2):025005, dec 2020.

[138] D. R. Higueras-Ruiz, H. P. Feigenbaum, and M. W. Shafer. Moisture's significant impact on twisted polymer actuation. *Smart Materials and Structures*, 29(12):125009, oct 2020.

[139] D. R. Higueras-Ruiz, K. Nishikawa, H. P. Feigenbaum, and M. W. Shafer. What is an artificial muscle? a comparison of soft actuators to biological muscles. *Bioinpired and biomimetics*, 2021.

[140] D. R. Higueras-Ruiz, M. W. Shafer, and H. P. Feigenbaum. Cavatappi artificial muscles from drawing, twisting, and coiling polymer tubes. *Science Robotics*, 6(53), 2021.

[141] D. R. Higueras-Ruiz, M. W. Shafer, and H. P. Feigenbaum. Material-based modeling of cavatappi artificial muscles. *Transactions on Robotics (T-RO)*, Under Revision, 2022.

[142] A. Hill. The heat of shortening and the dynamic constants of muscle. *Proceedings of The Royal Society B: Biological Sciences*, 126:136–195, 1938.

[143] M. Hiraoka, K. Nakamura, H. Arase, K. Asai, Y. Kaneko, S. John, K. Tagashira, and A. Omote. Power-efficient low-temperature woven coiled fibre actuator for wearable applications. *Scientific Reports*, 6, 11 2016.

[144] N. Hogan. Adaptive control of mechanical impedance by coactivation of antagonist muscles. *IEEE Transactions on Automatic Control*, 29(8):681–690, 1984.

[145] J. Hollerbach, I. Hunter, and J. Ballantyne. A comparative analysis of actuator technologies for robotics. 1992.

[146] A. Holstov, B. Bridgens, and G. Farmer. Hygromorphic materials for sustainable responsive architecture. *Construction and Building Materials*, 98:570–582, 2015.

[147] N. Holt, T. Roberts, and G. Askew. The energetic benefits of tendon springs in running: Is the reduction of muscle work important? *The Journal of experimental biology*, 217, 11 2014.

[148] J. E. Huber, N. A. Fleck, and M. F. Ashby. The selection of mechanical actuators based on performance indices. *Proceedings of the Royal Society of London. Series A: Mathematical, Physical and Engineering Sciences*, 453(1965):2185–2205, 1997.

[149] A. Hunt, Z. Chen, X. Tan, and M. Kruusmaa. An integrated electroactive polymer sensor-actuator: Design, model-based control, and performance characterization. *Smart Materials and Structures*, 25:035016, 2016.

[150] I. Hunter and S. Lafontaine. A comparison of muscle with artificial actuators. In *Technical Digest IEEE Solid-State Sensor and Actuator Workshop*, pages 178–185, 1992.

[151] A. Huxley and R. Niedergerke. Structural changes in muscle during contraction: Interference microscopy of living muscle fibres. *Nature*, 173:971–973, 1954.

[152] A. F. Huxley. Muscle structure and theories of contraction. *Prog Biophys Biophys Chem.*, 7:255–318, 1957.

[153] H. Huxley and J. Hanson. Changes in the cross-striations of muscle during contraction and stretch and their structural interpretation. *Nature*, 173:973–976, 1954.

[154] M. Ishikawa, P. V. Komi, M. J. Grey, V. Lepola, and G.-P. Bruggemann. Muscle-tendon interaction and elastic energy usage in human walking. *Journal of Applied Physiology*, 99(2):603–608, 2005. PMID: 15845776.

[155] M. Ison, I. Vujaklija, B. Whitsell, D. Farina, and P. Artemiadis. Simultaneous myoelectric control of a robot arm using muscle synergy-inspired inputs from high-density electrode grids. *2015 IEEE International Conference on Robotics and Automation (ICRA)*, pages 6469–6474, 2015.

[156] R. James, J. Altringham, and D. Goldspink. The mechanical properties of fast and slow skeletal muscles of the mouse in relation to their locomotory function. *The Journal of experimental biology*, 198(Pt 2):491—502, February 1995.

[157] R. James, I. Young, V. Cox, D. Goldspink, and J. Altringham. Isometric and isotonic muscle properties as determinants of work loop power output. *Pflügers Archiv - European Journal of Physiology*, 432:767–774, 09 1996.

[158] T. E. Jenkins, E. M. Chapman, and M. Bryant. Bio-inspired online variable recruitment control of fluidic artificial muscles. *Smart Materials and Structures*, 25(12):125016, nov 2016.

[159] X. Ji, X. Liu, V. Cacucciolo, Y. Civet, A. El Haitami, S. Cantin, Y. Perriard, and H. Shea. Untethered feel-through haptics using 18-µm thick dielectric elastomer actuators. *Advanced Functional Materials*, n/a(n/a):2006639.

[160] X. Ji, X. Liu, V. Cacucciolo, M. Imboden, Y. Civet, A. E. Haitami, S. Cantin, Y. Perriard, and H. Shea. An autonomous untethered fast soft robotic insect driven by low-voltage dielectric elastomer actuators. *Science Robotics*, 4, 2019.

[161] T. Jia, Y. Wang, Y. Dou, Y.-W. Li, M. Andrade, R. Wang, M. Zhang, J. Li, Z. Yu, R. Qiao, Z. Liu, Y. Cheng, Y. Su, M. Minary-Jolandan, R. Baughman, D. Qian, and Z. Liu. Moisture sensitive smart yarns and textiles from self-balanced silk fiber muscles. *Advanced Functional Materials*, 29, 03 2019.

[162] H. Jiang, Z. Wang, Y. Jin, X. Chen, P. Li, Y. Gan, S. Lin, and X. Chen. Hierarchical control of soft manipulators towards unstructured interactions. *The International Journal of Robotics Research*, 40(1):411–434, 2021.

[163] R. Josephson. Mechanical power output from striated muscle during cyclic contraction. *The Journal of Experimental Biology*, 114:493–512, 1985.

[164] H. S. Jung, K. H. Cho, J. H. Park, S. Y. Yang, Y. Kim, K. Kim, C. T. Nguyen, H. Phung, P. T. Hoang, H. Moon, J. C. Koo, and H. R. Choi. Musclelike joint mechanism driven by dielectric elastomer actuator for robotic applications. *Smart Materials and Structures*, 27(7):075011, may 2018.

[165] F. Karami and Y. Tadesse. Modeling of twisted and coiled polymer (TCP) muscle based on phenomenological approach. *Smart Materials and Structures*, 26(12):125010, nov 2017.

[166] R. K. Katzschmann, A. D. Marchese, and D. Rus. Autonomous object manipulation using a soft planar grasping manipulator. *Soft Robotics*, 2(4):155–164, 2015. PMID: 27625916.

[167] N. Kellaris, V. Gopaluni Venkata, G. M. Smith, S. K. Mitchell, and C. Keplinger. Peano-hasel actuators: Muscle-mimetic, electrohydraulic transducers that linearly contract on activation. *Science Robotics*, 3(14), 2018.

[168] L. A. Kelly, D. J. Farris, A. G. Cresswell, and G. A. Lichtwark. Intrinsic foot muscles contribute to elastic energy storage and return in the human foot. *Journal of Applied Physiology*, 126(1):231–238, 2019. PMID: 30462568.

[169] Y. P. Khanna, W. P. Kuhn, and W. J. Sichina. Reliable measurements of the nylon 6 glass transition made possible by the new dynamic dsc. *Macromolecules*, 28(8):2644–2646, 1995.

[170] S. Kianzad, M. Pandit, J. Lewis, A. Berlingeri, K. Haebler, and J. Madden. Variable stiffness and recruitment using nylon actuators arranged in a pennate configuration.

Proceedings of SPIE - The International Society for Optical Engineering, 9430, 04 2015.

[171] J. Y. Kim, N. Mazzoleni, D. Vemula, and M. Bryant. Development and demonstration of an orderly recruitment valve for fluidic artificial muscles. ASME 2020 Conference on Smart Materials, Adaptive Structures and Intelligent Systems, 09 2020.

[172] K.-R. Kim, Y. Shin, K.-S. Kim, and S. Kim. Application of chemical reaction based pneumatic power generator to robot finger. *2013 IEEE/RSJ International Conference on Intelligent Robots and Systems*, pages 4906–4911, 2013.

[173] S. Kim, C. H. Kwon, K. Park, T. J. Mun, X. Lepro, R. Baughman, G. Spinks, and S. J. Kim. Bio-inspired, moisture-powered hybrid carbon nanotube yarn muscles. *Scientific Reports*, 6:23016, 03 2016.

[174] R. D. Kornbluh, R. Pelrine, Q. Pei, S. Oh, and J. Joseph. Ultrahigh strain response of field-actuated elastomeric polymers. 3987:51 – 64, 2000.

[175] P. Kotak, T. Weerakkody, and C. Lamuta. Physics-based dynamic model for the electro-thermal actuation of bio-inspired twisted spiral artificial muscles (tsams). *Polymer*, 222:123642, 2021.

[176] A. S. Kuenstler and R. C. Hayward. Light-induced shape morphing of thin films. *Current Opinion in Colloid Interface Science*, 40:70–86, 2019. Particle Systems.

[177] S. Kurumaya, H. Nabae, G. Endo, and K. Suzumori. Design of thin mckibben muscle and multifilament structure. *Sensors and Actuators A: Physical*, 261:66–74, 2017.

[178] S. Kurumaya, K. Suzumori, H. Nabae, and S. Wakimoto. Musculoskeletal lower-limb robot driven by multifilament muscles. *ROBOMECH Journal*, 3, 09 2016.

[179] C. Lamuta, S. Messelot, and S. Tawfick. Theory of the tensile actuation of fiber reinforced coiled muscles. *Smart Materials and Structures*, 27(5):055018, apr 2018.

[180] C. Laschi and M. Cianchetti. Soft robotics: New perspectives for robot bodyware and control. *Frontiers in Bioengineering and Biotechnology*, 2:3, 2014.

[181] C. Laschi, M. Cianchetti, B. Mazzolai, L. Margheri, M. Follador, and P. Dario. Soft robot arm inspired by the octopus. *Advanced Robotics*, 26(7):709–727, 2012.

[182] H. Lee, B.-K. Lee, W. Kim, J.-S. Han, K.-S. Shin, and C.-S. Han. Human–robot cooperation control based on a dynamic model of an upper limb exoskeleton for human power amplification. *Mechatronics*, 24, 03 2014.

[183] J. Lee, J. Hwangbo, L. Wellhausen, V. Koltun, and M. Hutter. Learning quadrupedal locomotion over challenging terrain. *Science Robotics*, 5(47), 2020.

[184] J. G. Lee and H. Rodrigue. Efficiency of origami-based vacuum pneumatic artificial muscle for off-grid operation. *International Journal of Precision Engineering and Manufacturing-Green Technology*, 6(4):789–797, 7 2019.

[185] J.-G. Lee and H. Rodrigue. Origami-based vacuum pneumatic artificial muscles with large contraction ratios. *Soft Robotics*, 6(1):109–117, 2019. PMID: 30339102.

[186] S. S. M. Lee, A. Arnold, M. de Boef Miara, A. Biewener, and J. Wakeling. Accuracy of gastrocnemius muscles forces in walking and running goats predicted by one-element and two-element hill-type models. *Journal of biomechanics*, 46 13:2288–95, 2013.

[187] B. M. Lempriere. Poisson's ratio in orthotropic materials. *AIAA Journal*, 6(11):2226–2227, 1968.

[188] Z. F. Lerner, G. M. Gasparri, M. O. Bair, J. L. Lawson, J. Luque, T. A. Harvey, and A. T. Lerner. An untethered ankle exoskeleton improves walking economy in a pilot study of individuals with cerebral palsy. *IEEE Transactions on Neural Systems and Rehabilitation Engineering*, 26(10):1985–1993, 2018.

[189] S. Li, D. M. Vogt, D. Rus, and R. Wood. Fluid-driven origami-inspired artificial muscles. *Proceedings of the National Academy of Sciences of the United States of America*, 114:13132 – 13137, 2017.

[190] S. Li, C. Zhuang, C. M. Niu, Y. Bao, Q. Xie, and N. Lan. Evaluation of functional correlation of task-specific muscle synergies with motor performance in patients poststroke. *Frontiers in Neurology*, 8:337, 2017.

[191] T. Li, Y. Wang, K. Liu, H. Liu, J. Zhang, X. Sheng, and D. Guo. Thermal actuation performance modification of coiled artificial muscle by controlling annealing stress. *Journal of Polymer Science Part B: Polymer Physics*, 56(5):383–390, 2018.

[192] X. Li, Y. Wei, Q. Feng, and R. K. Luo. Mechanical behavior of nylon 66 tyre cord under monotonic and cyclic extension: Experiments and constitutive modeling. *Fibers and Polymers*, 18(3):542–548, 2017.

[193] Y. Li, Y. Chen, T. Ren, and Y. Hu. Passive and active particle damping in soft robotic actuators *this work is funded by a basic research grant from the university of hong kong. *2018 IEEE International Conference on Robotics and Automation (ICRA)*, pages 1547–1552, 2018.

[194] Z. Li, B. Huang, Z. Ye, M. Deng, and C. Yang. Physical human–robot interaction of a robotic exoskeleton by admittance control. *IEEE Transactions on Industrial Electronics*, 65(12):9614–9624, 2018.

[195] W. Liang, H. Liu, K. Wang, Z. Qian, L. Ren, and L. Ren. Comparative study of robotic artificial actuators and biological muscle. *Advances in Mechanical Engineering*, 12(6):1687814020933409, 2020.

[196] M. D. Lima, M. W. Hussain, G. M. Spinks, S. Naficy, D. Hagenasr, J. S. Bykova, D. Tolly, and R. H. Baughman. Efficient, absorption-powered artificial muscles based on carbon nanotube hybrid yarns. *Small*, 11(26):3113–3118, 2015.

[197] M. D. Lima, N. Li, M. Jung de Andrade, S. Fang, J. Oh, G. M. Spinks, M. E. Kozlov, C. S. Haines, D. Suh, J. Foroughi, S. J. Kim, Y. Chen, T. Ware, M. K. Shin, L. D. Machado, A. F. Fonseca, J. D. W. Madden, W. E. Voit, D. S. Galvão, and R. H. Baughman. Electrically, chemically, and photonically powered torsional and tensile

actuation of hybrid carbon nanotube yarn muscles. *Science*, 338(6109):928–932, 2012.

[198] S. Lindstedt and K. Nishikawa. Huxleys' missing filament: Form and function of titin in vertebrate striated muscle. *Annual review of physiology*, 79, 10 2016.

[199] L. Liu, C. Zhang, W. Wang, N. Xi, and Y. Wang. Regulation of c2c12 differentiation and control of the beating dynamics of contractile cells for a muscle-driven biosyncretic crawler by electrical stimulation. *Soft Robotics*, 5(6):748–760, 2018. PMID: 30277855.

[200] A. D. Luca and B. Siciliano. Trajectory control of a non-linear one-link flexible arm. *International Journal of Control*, 50(5):1699–1715, 1989.

[201] J. Madden, J. Barisci, P. Anquetil, G. Spinks, G. Wallace, R. Baughman, and I. Hunter. Fast carbon nanotube charging and actuation. *Advanced Materials*, 18(7):870–873, 2006.

[202] J. Madden and S. Kianzad. Twisted lines: Artificial muscle and advanced instruments can be formed from nylon threads and fabric. *Pulse, IEEE*, 6(1):32–35, 2015.

[203] J. Madden, N. Vandesteeg, P. Anquetil, P. Madden, A. Takshi, R. Z. Pytel, S. Lafontaine, P. Wieringa, and I. Hunter. Artificial muscle technology: physical principles and naval prospects. *IEEE Journal of Oceanic Engineering*, 29:706–728, 2004.

[204] J. D. Madden. Mobile robots: Motor challenges and materials solutions. *Science*, 318(5853):1094–1097, 2007.

[205] C. Majidi. Soft robotics: A perspective—current trends and prospects for the future. *Soft Robotics*, 1:5–11, 03 2014.

[206] N. Hogan. The mechanics of multi-joint posture and movement control. *Biological Cybernetics*, 52:315–331, 1985.

[207] A. F. Huxley. A note suggesting that the cross-bridge attachment during muscle contraction may take place in two stages. *Proceedings of the Royal Society of London. Series B. Biological Sciences*, 183(1070):83–86, 1973.

[208] K. Man and A. Damasio. Homeostasis and soft robotics in the design of feeling machines. *Nature Machine Intelligence*, 1:446–452, 2019.

[209] M. Manti, V. Cacucciolo, and M. Cianchetti. Stiffening in soft robotics: A review of the state of the art. *IEEE Robotics Automation Magazine*, 23(3):93–106, 2016.

[210] A. D. Marchese, R. K. Katzschmann, and D. Rus. A recipe for soft fluidic elastomer robots. *Soft Robotics*, 2(1):7–25, 2015. PMID: 27625913.

[211] J. H. Marden and L. R. Allen. Molecules, muscles, and machines: Universal performance characteristics of motors. *Proceedings of the National Academy of Sciences*, 99(7):4161–4166, 2002.

[212] K. Meijer, Y. Bar-Cohen, and R. Full. *Biologically Inspired Intelligent Robots*. 2003.

[213] M. Meller, M. Bryant, and E. Garcia. Energetic and dynamic effects of operating fluid on fluidic artificial muscle actuators. volume 2, 09 2013.

[214] M. Meller, J. Chipka, M. Bryant, and E. Garcia. Modeling of the energy savings of variable recruitment mckibben muscle bundles. *Proceedings of SPIE - The International Society for Optical Engineering*, 9429, 03 2015.

[215] M. Meller, J. Chipka, A. Volkov, M. Bryant, and E. Garcia. Improving actuation efficiency through variable recruitment hydraulic McKibben muscles: modeling, orderly recruitment control, and experiments. *Bioinspiration & Biomimetics*, 11(6):065004, nov 2016.

[216] M. A. Meller, M. Bryant, and E. Garcia. Reconsidering the mckibben muscle: Energetics, operating fluid, and bladder material. *Journal of Intelligent Material Systems and Structures*, 25(18):2276–2293, 2014.

[217] A. Menges and S. Reichert. Material capacity: Embedded responsiveness. *Architectural Design*, 82(2):52–59, 2012.

[218] J. Mersch, M. Koenigsdorff, A. Nocke, C. Cherif, and G. Gerlach. High-speed, helical and self-coiled dielectric polymer actuator. *Actuators*, 10(1), 2021.

[219] M. Miao. In M. Miao, editor, *Carbon Nanotube Fibers and Yarns*, The Textile Institute Book Series, pages 1–10. Woodhead Publishing, 2020.

[220] T. Mirfakhrai, J. D. Madden, and R. H. Baughman. Polymer artificial muscles. *Materials Today*, 10(4):30–38, 2007.

[221] S. M. Mirvakili, A. R. Ravandi, I. W. Hunter, C. S. Haines, N. Li, J. Foroughi, S. Naficy, G. M. Spinks, R. H. Baughman, and J. D. Madden. Simple and strong: Twisted silver painted nylon artificial muscle actuated by joule heating. In *SPIE Smart Structures and Materials+ Nondestructive Evaluation and Health Monitoring*, pages 90560I–90560I. International Society for Optics and Photonics, 2014.

[222] A. K. Mishra, T. J. Wallin, W. Pan, P. A. Xu, K. Wang, E. Giannelis, B. Mazzolai, and R. Shepherd. Autonomic perspiration in 3d-printed hydrogel actuators. *Science Robotics*, 5, 2020.

[223] S. K. Mitchell, X. Wang, E. Acome, T. Martin, K. Ly, N. Kellaris, V. G. Venkata, and C. Keplinger. An easy-to-implement toolkit to create versatile and high-performance hasel actuators for untethered soft robots. *Advanced Science*, 6(14):1900178, 2019.

[224] A. A. Mohd Faudzi, J. Ooga, T. Goto, M. Takeichi, and K. Suzumori. Index finger of a human-like robotic hand using thin soft muscles. *IEEE Robotics and Automation Letters*, 3(1):92–99, 2018.

[225] G. Moretti, A. Cherubini, R. Vertechy, and M. Fontana. Experimental characterization of a new class of polymeric-wire coiled transducers. In *SPIE Smart Structures and Materials+ Nondestructive Evaluation and Health Monitoring*, pages 94320P–94320P. International Society for Optics and Photonics, March 8-12 2015.

[226] M. Mori, K. Suzumori, S. Seita, M. Takahashi, T. Hosoya, and K. Kusumoto. Development of very high force hydraulic mckibben artificial muscle and its application to shape-adaptable power hand. *2009 IEEE International Conference on Robotics and Biomimetics (ROBIO)*, pages 1457–1462, 2009.

[227] Y. Morimoto, H. Onoe, and S. Takeuchi. Biohybrid robot powered by an antago-
nistic pair of skeletal muscle tissues. *Science Robotics*, 3(18):eaat4440, 2018.

[228] P. Moseley, J. M. Florez, H. A. Sonar, G. Agarwal, W. Curtin, and J. Paik. Mod-
eling, design, and development of soft pneumatic actuators with finite element
method. *Advanced Engineering Materials*, 18(6):978–988, 2016.

[229] A. A. Moustafa, E. Mfoumou, D. Roman, V. Nerguizian, I. Stiharu, and A. Yas-
meen. Impact of single-walled carbon nanotubes on the embryo: a brief review. *Int
J Nanomedicine*, 11:349–355, 2016.

[230] J. Mu, G. Wang, H. Yan, H. Li, X. Wang, E. Gao, C. Hou, A. Pham, L. Wu,
Q. Zhang, Y. Li, Z. Xu, Y. Guo, E. Reichmanis, H. Wang, and M. Zhu. Molecular-
channel driven actuator with considerations for multiple configurations and color
switching. *Nature Communications*, 9, 02 2018.

[231] T. Mulla, S. Kadam, and V. Kengar. Finite element analysis of helical coil compres-
sion spring for three wheeler automotive front suspension. *International Journal of
Mechanical and Industrial Engineering (IJMIE), ISSN No. 2231 –6477*, Vol-2,:74–
77, 06 2012.

[232] K. Nakajima, H. Hauser, R. Kang, E. Guglielmino, D. Caldwell, and R. Pfeifer. A
soft body as a reservoir: case studies in a dynamic model of octopus-inspired soft
robotic arm. *Frontiers in Computational Neuroscience*, 7:91, 2013.

[233] K. Nakajima, T. Li, H. Hauser, and R. Pfeifer. Exploiting short-term memory in
soft body dynamics as a computational resource. *Journal of The Royal Society
Interface*, 11(100):20140437, 2014.

[234] C. Nancy, B.-B. Hattie, H. Tatjana, L. John, G.-M. Anthony, B. Emily, A. Stephen,
L. Maja, W. Timothy, and W. Alan. Remarkable muscles, remarkable locomotion
in desert-dwelling wildebeest. *Nature*, 11 2018.

[235] K. Nguyen and M. Venkadesan. Rheology of tunable materials, 05 2020.

[236] K. D. Nguyen, N. Sharma, and M. Venkadesan. Active viscoelasticity of sarcomeres. *Frontiers in Robotics and AI*, 5:69, 2018.

[237] T. R. Nichols and J. C. Houk. Improvement in linearity and regulation of stiffness that results from actions of stretch reflex. *Journal of Neurophysiology*, 39(1):119–142, 1976. PMID: 1249597.

[238] A. Nicolau-Kuklińska, P. Latko-Durałek, P. Nakonieczna, K. Dydek, A. Boczkowska, and J. Grygorczuk. A new electroactive polymer based on carbon nanotubes and carbon grease as compliant electrodes for electroactive actuators. *Journal of Intelligent Material Systems and Structures*, 29(7):1520–1530, 2018.

[239] R. Niiyama, X. Sun, C. Sung, B. An, D. Rus, and S. Kim. Pouch motors: Printable soft actuators integrated with computational design. *Soft Robotics*, 2(2):59–70, 2015.

[240] K. Nishikawa. Letter to the editor: "titin-actin interaction: The report of its death was an exaggeration". *American Journal of Physiology - Cell Physiology*, 310:C622–C622, 04 2016.

[241] K. Nishikawa. Titin: A tunable spring in active muscle. *Physiology*, 35(3):209–217, 2020. PMID: 32293234.

[242] K. Nishikawa, A. A. Biewener, P. Aerts, A. N. Ahn, H. J. Chiel, M. A. Daley, T. L. Daniel, R. J. Full, M. E. Hale, T. L. Hedrick, A. K. Lappin, T. R. Nichols, R. D. Quinn, R. A. Satterlie, and B. Szymik. Neuromechanics: an integrative approach for understanding motor control. *Integrative and Comparative Biology*, 47(1):16–54, 05 2007.

[243] K. Nishikawa and T. Huck. Toward achieving muscle-like function 1 in robotic prosthetic devices. *In revision for Journal of Experimental Biology*, 2021.

[244] K. Nishikawa, J. Monroy, and U. Tahir. Muscle function from organisms to molecules. *Integrative and comparative biology*, 58 2:194–206, 2018.

[245] K. Nishikawa, J. Monroy, T. E. Uyeno, S. Yeo, D. Pai, and S. Lindstedt. Is titin a 'winding filament'? a new twist on muscle contraction. *Proceedings of the Royal Society B: Biological Sciences*, 279:981 – 990, 2011.

[246] K. C. Nishikawa, J. A. Monroy, K. L. Powers, L. A. Gilmore, T. A. Uyeno, and S. L. Lindstedt. A molecular basis for intrinsic muscle properties: Implications for motor control. In M. J. Richardson, M. A. Riley, and K. Shockley, editors, *Progress in Motor Control*, pages 111–125, New York, NY, 2013. Springer New York.

[247] I. Ogneva, D. Lebedev, and B. Shenkman. Transversal stiffness and young's modulus of single fibers from rat soleus muscle probed by atomic force microscopy. *Biophysical journal*, 98:418–24, 02 2010.

[248] N. Oh, Y. J. Park, S. Lee, H. Lee, and H. Rodrigue. Design of paired pouch motors for robotic applications. *Advanced Materials Technologies*, 4(1):1800414, 2019.

[249] P. Ohta, L. Valle, J. King, K. Low, J. Yi, C. G. Atkeson, and Y.-L. Park. Design of a lightweight soft robotic arm using pneumatic artificial muscles and inflatable sleeves. *Soft Robotics*, 5(2):204–215, 2018. PMID: 29648951.

[250] P. Ohta, L. Valle, J. King, K. Low, J. Yi, C. G. Atkeson, and Y.-L. Park. Design of a lightweight soft robotic arm using pneumatic artificial muscles and inflatable sleeves. *Soft Robotics*, 5(2):204–215, 2018. PMID: 29648951.

[251] C. Onal. System-level challenges in pressure-operated soft robotics. page 983627, 05 2016.

[252] C. D. Onal, X. Chen, G. M. Whitesides, and D. Rus. *Soft Mobile Robots with onboard Chemical Pressure Generation*, volume 100, pages 525–540. Springer, 2017. 1296.

[253] C.-C. Pai, R.-J. Jeng, S. J. Grossman, and J.-C. Huang. Effects of moisture on thermal and mechanical properties of nylon-6,6. *Advances in Polymer Technology*, 9(2):157–163, 1989.

[254] A. Pal, D. Goswami, and R. V. Martinez. Elastic energy storage enables rapid and programmable actuation in soft machines. *Advanced Functional Materials*, 30:1906603, 2020.

[255] S. Park, H. Lee, Y.-J. Kim, and P. S. Lee. Fully laser-patterned stretchable microsupercapacitors integrated with soft electronic circuit components. *NPG Asia Materials*, 10:959–969, 2018.

[256] Y. Park and X. Chen. Water-responsive materials for sustainable energy applications. *J. Mater. Chem. A*, 8:15227–15244, 2020.

[257] Y.-L. Park and R. Wood. Smart pneumatic artificial muscle actuator with embedded microfluidic sensing. pages 1–4, 11 2013.

[258] Q. Pei, M. Rosenthal, R. Pelrine, S. Stanford, and R. Kornbluh. Multifunctional electroelastomer roll actuators and their application for biomimetic walking robots. In *SPIE Smart Structures and Materials + Nondestructive Evaluation and Health Monitoring*, 2003.

[259] R. Pelrine and R. Kornbluh. Variable-stiffness–mode dielectric elastomer devices. *Advances in Science and Technology*, 61:192 – 201, 2008.

[260] R. J. Peterka. Comparison of human and humanoid robot control of upright stance. *Journal of Physiology-Paris*, 103(3):149–158, 2009. Neurorobotics.

[261] A. Peterlin. Plastic deformation and structure of extruded polymer solids. *Polymer Engineering & Science*, 14(9):627–632, 1974.

[262] H. Pettermann and A. Desimone. An anisotropic linear thermo-viscoelastic constitutive law: Elastic relaxation and thermal expansion creep in the time domain. *Mechanics of Time-Dependent Materials*, 22, 09 2017.

[263] R. Pfeifer. Morphological computation: Connecting brain, body, and environment. In A. J. Ijspeert, T. Masuzawa, and S. Kusumoto, editors, *Biologically Inspired Approaches to Advanced Information Technology*, pages 2–3, Berlin, Heidelberg, 2006. Springer Berlin Heidelberg.

[264] R. Pfeifer and J. Bongard. *How the Body Shapes the Way We Think: a New View of Intelligence*. 01 2007.

[265] R. Pfeifer, M. Lungarella, and F. Iida. Self-organization, embodiment, and biologically inspired robotics. *Science*, 318(5853):1088–1093, 2007.

[266] G. Pogany. Anomalous diffusion of water in glassy polymers. *Polymer*, 17(8):690 – 694, 1976.

[267] E. A. Pohlmeyer, M. Fifer, M. Rich, J. Pino, B. Wester, M. Johannes, C. Dohopolski, J. Helder, D. D'Angelo, J. Beaty, S. Bensmaia, M. McLoughlin, and F. Tenore. Beyond intuitive anthropomorphic control: recent achievements using brain computer interface technologies. In T. George, A. K. Dutta, and M. S. Islam, editors, *Micro- and Nanotechnology Sensors, Systems, and Applications IX*, volume 10194, pages 292 – 305. International Society for Optics and Photonics, SPIE, 2017.

[268] D. Prevorsek, P. Harget, R. Sharma, and A. Reimschuessel. Nylon 6 fibers: changes in structure between moderate and high draw ratios. *Journal of Macromolecular Science, Part B: Physics*, 8(1-2):127–156, 1973.

[269] G. Qiao, G. Liu, Z. Shi, Y. Wang, S. Ma, and T. C. Lim. A review of electromechanical actuators for more/all electric aircraft systems. *Proceedings of the Institution of Mechanical Engineers, Part C: Journal of Mechanical Engineering Science*, 232(22):4128–4151, 2018.

[270] G. Rahman, Z. Najaf, A. Mehmood, S. Bilal, A. u. H. A. Shah, S. A. Mian, and G. Ali. An overview of the recent progress in the synthesis and applications of carbon nanotubes. *C*, 5(1), 2019.

[271] A. Rajappan, B. Jumet, and D. J. Preston. Pneumatic soft robots take a step toward autonomy. *Science Robotics*, 6(51), 2021.

[272] A. Rathore, M. Wilcox, D. Z. Morgado Ramirez, R. Loureiro, and T. Carlson. Quantifying the human-robot interaction forces between a lower limb exoskeleton

and healthy users. In *2016 38th Annual International Conference of the IEEE Engineering in Medicine and Biology Society (EMBC)*, pages 586–589, 2016.

[273] I. Rayment, H. Holden, M. Whittaker, C. Yohn, M. Lorenz, K. Holmes, and R. Milligan. Structure of the actin-myosin complex and its implications for muscle contraction. *Science*, 261 5117:58–65, 1993.

[274] L. Ricotti, B. Trimmer, A. W. Feinberg, R. Raman, K. K. Parker, R. Bashir, M. Sitti, S. Martel, P. Dario, and A. Menciassi. Biohybrid actuators for robotics: A review of devices actuated by living cells. *Science Robotics*, 2(12):eaaq0495, 2017.

[275] J. A. Rieffel, F. J. Valero-Cuevas, and H. Lipson. Morphological communication: exploiting coupled dynamics in a complex mechanical structure to achieve locomotion. *Journal of The Royal Society Interface*, 7(45):613–621, 2010.

[276] J. Riemenschneider. Characterization and modeling of CNT based actuators. *Smart Materials and Structures*, 18(10):104003, sep 2009.

[277] M. A. Robertson, O. C. Kara, and J. Paik. Soft pneumatic actuator-driven origami-inspired modular robotic "pneumagami". *The International Journal of Robotics Research*, 40(1):72–85, 2021.

[278] R. Robinson, C. S. Kothera, and N. M. Wereley. Variable recruitment testing of pneumatic artificial muscles for robotic manipulators. *IEEE/ASME Transactions on Mechatronics*, 20:1642–1652, 2015.

[279] R. M. Robinson, C. S. Kothera, B. K. S. Woods, I. Robert D. Vocke, and N. Wereley. High specific power actuators for robotic manipulators. *Journal of Intelligent Material Systems and Structures*, 22(13):1501–1511, 2011.

[280] C. E. Rogers, V. Stannett, and M. Szwarc. The sorption, diffusion, and permeation of organic vapors in polyethylene. *Journal of Polymer Science*, 45(145):61–82, 1960.

[281] S. Rosset, C. de Saint-Aubin, A. Poulin, and H. R. Shea. Assessing the degradation of compliant electrodes for soft actuators. *Review of Scientific Instruments*, 88(10):105002, 2017.

[282] D. Rus and M. Tolley. Design, fabrication and control of soft robots. *Nature*, 521:467–475, 2015.

[283] M. M. Sadeghi, H. S. Kim, R. L. B. Peterson, and K. Najafi. Electrostatic micro-hydraulic systems. *Journal of Microelectromechanical Systems*, 25(3):557–569, 2016.

[284] L. Saharan, M. Andrade, W. Saleem, R. Baughman, and Y. Tadesse. igrab: Hand orthosis powered by twisted and coiled polymer muscles. *Smart Materials and Structures*, 26, 08 2017.

[285] R. Saito, G. Dresselhaus, and M. S. Dresselhaus. *Physical Properties of Carbon Nanotubes*. PUBLISHED BY IMPERIAL COLLEGE PRESS AND DISTRIBUTED BY WORLD SCIENTIFIC PUBLISHING CO., 1998.

[286] C. D. Santina, M. Bianchi, G. Grioli, F. Angelini, M. Catalano, M. Garabini, and A. Bicchi. Controlling soft robots: Balancing feedback and feedforward elements. *IEEE Robotics & Automation Magazine*, 24:75–83, 2017.

[287] A. D. Santis, B. Siciliano, A. D. Luca, and A. Bicchi. An atlas of physical human-robot interaction. *Mechanism and Machine Theory*, 43:253–270, 2008.

[288] U. Scarfogliero, C. Stefanini, and P. Dario. The use of compliant joints and elastic energy storage in bio-inspired legged robots. *Mechanism and Machine Theory*, 44:580–590, 2009.

[289] P. Schaeffer and S. Lindstedt. How animals move: comparative lessons on animal locomotion. *Comprehensive Physiology*, 3 1:289–314, 2013.

[290] L. Schiller, A. Seibel, and J. Schlattmann. A gait pattern generator for closed-loop position control of a soft walking robot. *Frontiers in Robotics and AI*, 7:87, 2020.

[291] L. Schwarz, M. Medina-Sánchez, and O. G. Schmidt. Hybrid biomicromotors. *Applied Physics Reviews*, 4(3):031301, 2017.

[292] S. Seok, A. Wang, M. Y. Chuah, D. Otten, J. Lang, and S. Kim. Design principles for highly efficient quadrupeds and implementation on the mit cheetah robot. In

2013 IEEE International Conference on Robotics and Automation, pages 3307–3312, 2013.

[293] A. Seth, J. Hicks, T. K. Uchida, A. Habib, C. L. Dembia, J. Dunne, C. F. Ong, M. S. DeMers, A. Rajagopal, M. Millard, S. R. Hamner, E. M. Arnold, J. R. Yong, S. K. Lakshmikanth, M. A. Sherman, J. P. Ku, and S. Delp. Opensim: Simulating musculoskeletal dynamics and neuromuscular control to study human and animal movement. *PLoS Computational Biology*, 14, 2018.

[294] A. Seth, M. A. Sherman, J. Reinbolt, and S. Delp. Opensim: a musculoskeletal modeling and simulation framework for in silico investigations and exchange. *Procedia IUTAM*, 2:212–232, 2011.

[295] M. Shafer, H. Feigenbaum, and D. Higueras Ruiz. A novel biomimetic torsional actuator design using twisted polymer actuators. *Smart Materials, Adaptive Structures and Intelligent Systems*, 1:1–7, 2017.

[296] M. W. Shafer, H. P. Feigenbaum, D. Pugh, and M. Fisher. First steps in modeling thermal actuation of twisted polymer actuators using virgin material properties. In *ASME 2016 Conference on Smart Materials, Adaptive Structures and Intelligent Systems*, pages V002T06A017–V002T06A017. American Society of Mechanical Engineers, 2016.

[297] S. Sharafi and G. Li. A mutliscale approach for modeling actuation response of polymeric artificial muscle. *Soft Matter*, (12):1–18, 2015.

[298] R. F. Shepherd, F. Ilievski, W. Choi, S. A. Morin, A. A. Stokes, A. D. Mazzeo, X. Chen, M. Wang, and G. M. Whitesides. Multigait soft robot. *Proceedings of the National Academy of Sciences*, 108(51):20400–20403, 2011.

[299] H. Shim, K. Sim, F. Ershad, P. Yang, A. Thukral, Z. Rao, H.-J. Kim, Y. Liu, X. Wang, G. Gu, L. Gao, X. Wang, Y. Chai, and C. Yu. Stretchable elastic synaptic transistors for neurologically integrated soft engineering systems. *Science Advances*, 5(10), 2019.

[300] H. Shin, S. Ikemoto, and K. Hosoda. Constructive understanding and reproduction of functions of gluteus medius by using a musculoskeletal walking robot. *Advanced Robotics*, 32(4):202–214, 2018.

[301] A. V. Singh, Z. Hosseinidoust, B.-W. Park, O. Yasa, and M. Sitti. Microemulsion-based soft bacteria-driven microswimmers for active cargo delivery. *ACS Nano*, 11(10):9759–9769, 2017. PMID: 28858477.

[302] G. Singh, A. Singla, and G. Virk. Modeling and simulation of a passive lower-body mechanism for rehabilitation. 01 2016.

[303] I. D. Sirbu, G. Moretti, G. Bortolotti, M. Bolignari, S. Dire, L. Fambri, R. Vertechy, and M. Fontana. Electrostatic bellow muscle actuators and energy harvesters that stack up. *Science Robotics*, 6(51):eaaz5796, 2021.

[304] J. Sorvari and M. Malinen. Determination of the relaxation modulus of a linearly viscoelastic material. *Mechanics of Time-Dependent Materials*, 10:125–133, 2006.

[305] G. M. Spinks, N. D. Martino, S. Naficy, D. J. Shepherd, and J. Foroughi. Dual high-stroke and high–work capacity artificial muscles inspired by dna supercoiling. *Science Robotics*, 6(53):eabf4788, 2021.

[306] K. M. Steele, A. Rozumalski, and M. H. Schwartz. Muscle synergies and complexity of neuromuscular control during gait in cerebral palsy. *Developmental Medicine & Child Neurology*, 57(12):1176–1182, 2015.

[307] C. Stefanini, S. Orofino, L. Manfredi, S. Mintchev, S. Marrazza, T. Assaf, L. Capantini, E. Sinibaldi, S. Grillner, P. Wallén, and P. Dario. A compliant bioinspired swimming robot with neuro-inspired control and autonomous behavior. In *2012 IEEE International Conference on Robotics and Automation*, pages 5094–5098, 2012.

[308] C. Stephen, R. Selvam, and S. Suranjan. A comparative study of steel and composite helical springs using finite element analysis. In *2019 Advances in Science and Engineering Technology International Conferences (ASET)*, pages 1–6, 2019.

[309] J. Sun, B. Tighe, Y. Liu, and J. Zhao. Twisted-and-coiled actuators with free strokes enable soft robots with programmable motions. *Soft Robotics*, 8(2):213–225, 2021. PMID: 32584186.

[310] J. Sun and J. Zhao. Integrated actuation and self-sensing for twisted-and-coiled actuators with applications to innervated soft robots. 08 2020.

[311] L. Sun, Y. Yu, Z. Chen, F. Bian, F. Ye, L. Sun, and Y. Zhao. Biohybrid robotics with living cell actuation. *Chem. Soc. Rev.*, 49:4043–4069, 2020.

[312] D. Surovik, K. Wang, M. Vespignani, J. Bruce, and K. E. Bekris. Adaptive tensegrity locomotion: Controlling a compliant icosahedron with symmetry-reduced reinforcement learning. *The International Journal of Robotics Research*, 40(1):375–396, 2021.

[313] D. Sutton and J. Kimm. Reaction time of motor units in biceps and triceps. *Experimental Neurology*, 23(4):503–515, 1969.

[314] A. M. Swartz. Characterization and modeling of drawn polymers and twisted polymer actuators, 2019.

[315] A. M. Swartz, D. R. Higueras Ruiz, M. Shafer, H. Feigenbaum, and C. C. Browder. Experimental characterization and model predictions for twisted polymer actuators in free torsion. *Smart Materials and Structures*, 27(11):1–12, 2018.

[316] J. Taborri, V. Agostini, P. Artemiadis, M. Ghislieri, D. A. Jacobs, J. Roh, and S. Rossi. Feasibility of muscle synergy outcomes in clinics, robotics, and sports: A systematic review. *Applied Bionics and Biomechanics*, 2018, 2018.

[317] M. Taghavi, T. Helps, and J. Rossiter. Electro-ribbon actuators and electro-origami robots. *Science Robotics*, 3(25):eaau9795, 2018.

[318] U. Tahir, A. L. Hessel, E. R. Lockwood, J. T. Tester, Z. Han, D. J. Rivera, K. L. Covey, T. G. Huck, N. A. Rice, and K. C. Nishikawa. Case study: A bio-inspired control algorithm for a robotic foot-ankle prosthesis provides adaptive control of level walking and stair ascent. *Frontiers in Robotics and AI*, 5:36, 2018.

[319] K. Takagi, C. Oiwa, K. Masuya, K. Tahara, T. Irisawa, K. Asaka, T. Yamauchi, E. Tanaka, and M. Shioya. Gray-box modeling and control of torsional fishing-line artificial muscle actuators. page 79, 03 2018.

[320] L. Tang, F. Li, S. Cao, X. Zhang, D. Wu, and X. Chen. Muscle synergy analysis in children with cerebral palsy. *Journal of Neural Engineering*, 12(4):046017, jun 2015.

[321] Y. Tang, Y. Chi, J. Sun, T.-H. Huang, O. H. Maghsoudi, A. Spence, J. Zhao, H. Su, and J. Yin. Leveraging elastic instabilities for amplified performance: Spine-inspired high-speed and high-force soft robots. *Science Advances*, 6(19), 2020.

[322] S. Tawfick and Y. Tang. Stronger artificial muscles, with a twist. *Science*, 365(6449):125–126, 2019.

[323] D. Thelen. Adjustment of muscle mechanics model parameters to simulate dynamic contractions in older adults. *Journal of biomechanical engineering*, 125 1:70–7, 2003.

[324] M. T. Tolley, R. F. Shepherd, B. Mosadegh, K. C. Galloway, M. Wehner, M. Karpelson, R. J. Wood, and G. M. Whitesides. A resilient, untethered soft robot. *Soft Robotics*, 1(3):213–223, 2014.

[325] B. Tondu. What is an artificial muscle? a systemic approach. *Actuators*, 4(4):336–352, 2015.

[326] B. Tondu and P. Lopez. The mckibben muscle and its use in actuating robot-arms showing similarities with human arm behaviour. *Industrial Robot: An International Journal*, 24, 12 1997.

[327] TOPSFLO. *MICROPUMP, Health Science. Series GAF (External Gear Pumps) (Vancouver, WA)*, (accessed February 7, 2021). `https://micropump.com/support_documents/gaf_tech_specs.pdf`.

[328] TOPSFLO. *TOPSFLO, MG200XKDC24, (Magnetic Drive Gear Pumps) (Changsha City, Hunan)*, (accessed February 7, 2021). `http://topsflo.com/micro-gear-pump/mg200xk-dc24.html`.

[329] D. Trivedi, C. Rahn, W. Kier, and I. Walker. Soft robotics: Biological inspiration, state of the art, and future research. *Applied Bionics and Biomechanics*, 5:99–117, 2008.

[330] M. Tschiersky, E. Hekman, D. Brouwer, J. Herder, and K. Suzumori. A compact mckibben muscle based bending actuator for close-to-body application in assistive wearable robots. *IEEE Robotics and automation letters*, 5(2):3042–3049, Apr. 2020. International Conference on Robotics and Automation, ICRA 2020, ICRA 2020 ; Conference date: 31-05-2020 Through 31-08-2020.

[331] M. Tyagi, J. Pan, and E. Jager. Novel fabrication of soft microactuators with morphological computing using soft lithography. *Advanced Functional Materials*, 5, 2019.

[332] J. van der Weijde, H. Vallery, and R. Babuška. Closed-loop control through self-sensing of a joule-heated twisted and coiled polymer muscle. *Soft Robotics*, 6(5):621–630, 2019. PMID: 31145024.

[333] B. Vanderborght, A. Albu-Schaeffer, A. Bicchi, E. Burdet, D. Caldwell, R. Carloni, M. Catalano, O. Eiberger, W. Friedl, G. Ganesh, M. Garabini, M. Grebenstein, G. Grioli, S. Haddadin, H. Hoppner, A. Jafari, M. Laffranchi, D. Lefeber, F. Petit, S. Stramigioli, N. Tsagarakis, M. Van Damme, R. Van Ham, L. Visser, and S. Wolf. Variable impedance actuators: A review. *Robotics and Autonomous Systems*, 61(12):1601–1614, 2013.

[334] A. J. Veale and S. Q. Xie. Towards compliant and wearable robotic orthoses: A review of current and emerging actuator technologies. *Medical Engineering Physics*, 38(4):317–325, 2016.

[335] B. Verrelst, R. V. Ham, B. Vanderborght, F. Daerden, D. Lefeber, and J. Vermeulen. The pneumatic biped "lucy" actuated with pleated pneumatic artificial muscles. *Autonomous Robots*, 18:201–213, 2005.

[336] D. Villegas, M. V. Damme, B. Vanderborght, P. Beyl, and D. Lefeber. Third–generation pleated pneumatic artificial muscles for robotic applications: Development and comparison with mckibben muscle. *Advanced Robotics*, 26(11-12):1205–1227, 2012.

[337] L. Visser, R. Carloni, and S. Stramigioli. Energy-efficient variable stiffness actuators. *IEEE transactions on robotics*, 27(5):865–875, 2011. 10.1109/TRO.2011.2150430.

[338] A. Wahl. *Mechanical Springs*. Machine design series. Penton Publishing Company, 1944.

[339] J. Wakeling, C. Tijs, N. Konow, and A. Biewener. Modeling muscle function using experimentally determined subject-specific muscle properties. *Journal of Biomechanics*, 117:110242, 01 2021.

[340] J. Walker, T. Zidek, C. Harbel, S. Yoon, F. S. Strickland, S. Kumar, and M. Shin. Soft robotics: A review of recent developments of pneumatic soft actuators. *Actuators*, 9(1), 2020.

[341] H. Wang, M. Totaro, and L. Beccai. Toward perceptive soft robots: Progress and challenges. *Advanced Science*, 5, 2018.

[342] T. Wang, M. Farajollahi, Y. S. Choi, I.-T. Lin, J. E. Marshall, N. M. Thompson, S. Kar-Narayan, J. D. W. Madden, and S. K. Smoukov. Electroactive polymers for sensing. *Interface Focus*, 6(4):20160026, 2016.

[343] W. Wang, L. Yao, C.-Y. Cheng, T. Zhang, H. Atsumi, L. Wang, G. Wang, O. Anilionyte, H. Steiner, J. Ou, K. Zhou, C. Wawrousek, K. Petrecca, A. M. Belcher, R. Karnik, X. Zhao, D. I. C. Wang, and H. Ishii. Harnessing the hygroscopic and biofluorescent behaviors of genetically tractable microbial cells to design biohybrid wearables. *Science Advances*, 3(5):e1601984, 2017.

[344] weather-and climate. *TYGON ND 100–65 Medical Tubing, 2011. Saint-Gobain Performance Plastic*, 2008 (accessed April 4, 2020). `https://usplastic.com/catalog/files/specsheets/TYGON_ND_100-65.pdf`.

[345] M. Wehner, R. L. Truby, D. J. Fitzgerald, B. Mosadegh, G. M. Whitesides, J. A. Lewis, and R. J. Wood. An integrated design and fabrication strategy for entirely soft, autonomous robots. *Nature*, 536:451–466, 2016.

[346] P. White, S. Latscha, and M. H. Yim. Modeling of a dielectric elastomer bender actuator. *Actuators*, 3:245–269, 2014.

[347] P. Willems, G. Cavagna, and N. Heglund. External, internal and total work in human locomotion. *The Journal of experimental biology*, 198:379–93, 03 1995.

[348] M. Wilson. *Implementation of Robot Systems*. 2015.

[349] S. Wolf, T. Bahls, M. Chalon, W. Friedl, M. Grebenstein, H. Höppner, M. Kühne, D. Lakatos, N. Mansfeld, M. Özparpucu, F. Petit, J. Reinecke, R. Weitschat, and A. Albu-Schäeffer. Soft robotics with variable stiffness actuators: Tough robots for soft human robot interaction. 03 2015.

[350] E. G. Wolff. Moisture and viscoelastic effects on the dimensional stability of composites. 11 1990.

[351] F. WORKS. *Inc. M-Series (Magnetic Drive Gear Pumps), MODELS 2232-M04C10/ C12/C15 (Irvine, CA)*, (accessed February 7, 2021). `http://products.flightworksinc.com/Asset/Product%20Data%20Sheet%20(2232-M04C10.C12.C15).pdf`.

[352] C. Wu and W. Zheng. A modeling of twisted and coiled polymer artificial muscles based on elastic rod theory. *Actuators*, 9(2), 2020.

[353] L. Wu and Y. Tadesse. Musculoskeletal system for bio-inspired robotic systems based on ball and socket joints. *International Mechanical Engineering Congress and Exposition*, 4A:11–16, 2016.

[354] Y. Wu, D. U. Shah, B. Wang, J. Liu, X. Ren, M. H. Ramage, and O. A. Scherman. Biomimetic supramolecular fibers exhibit water-induced supercontraction. *Advanced Materials*, 30(27):1707169, 2018.

[355] C. Yang, K. Yuan, Q. Zhu, W. Yu, and Z. Li. Multi-expert learning of adaptive legged locomotion. *Science Robotics*, 5(49), 2020.

[356] Q. Yang and G. Li. A top-down multi-scale modeling for actuation response of polymeric artificial muscles. *Journal of the Mechanics and Physics of Solids*, 92(12):237–259, 2016.

[357] O. Yasa, P. Erkoc, Y. Alapan, and M. Sitti. Microalga-powered microswimmers toward active cargo delivery. *Advanced Materials*, 30(45):1804130, 2018.

[358] J. C. Yeo, H. K. Yap, W. Xi, Z. Wang, C.-H. Yeow, and C. T. Lim. Flexible and stretchable strain sensing actuator for wearable soft robotic applications. *Advanced Materials Technologies*, 1(3):1600018, 2016.

[359] F. Yin, C. Tang, X. Li, and X. Wang. Effect of moisture on mechanical properties and thermal stability of meta-aramid fiber used in insulating paper. *Polymers*, 9:537, 10 2017.

[360] M. C. Yip and G. Niemeyer. High-performance robotic muscles from conductive nylon sewing thread. *2015 IEEE International Conference on Robotics and Automation (ICRA)*, pages 2313–2318, 2015.

[361] Z. Yoder, N. Kellaris, C. Chase-Markopoulou, D. Ricken, S. K. Mitchell, M. B. Emmett, R. F. f. Weir, J. Segil, and C. Keplinger. Design of a high-speed prosthetic finger driven by peano-hasel actuators. *Frontiers in Robotics and AI*, 7:181, 2020.

[362] J.-H. Youn, S. M. Jeong, G. Hwang, H. Kim, K. Hyeon, J. Park, and K.-U. Kyung. Dielectric elastomer actuator for soft robotics applications and challenges. *Applied Sciences*, 10(2), 2020.

[363] E. Yousif and R. Haddad. Photodegradation and photostabilization of polymers, especially polystyrene: review. *SpringerPlus*, 2, 2013.

[364] J. Yu, M. Tan, S. Wang, and E. Chen. Development of a biomimetic robotic fish and its control algorithm. *IEEE Transactions on Systems, Man, and Cybernetics, Part B (Cybernetics)*, 34(4):1798–1810, 2004.

[365] M.-F. Yu, O. Lourie, M. J. Dyer, K. Moloni, T. F. Kelly, and R. S. Ruoff. Strength and breaking mechanism of multiwalled carbon nanotubes under tensile load. *Science*, 287(5453):637–640, 2000.

[366] D. Yue, X. Zhang, H. Yong, J. Zhou, and Y.-H. Zhou. Controllable rectification of the axial expansion in the thermally driven artificial muscle. *Applied Physics Letters*, 107(11):111903, 2015.

[367] M. C. Yuen, R. Kramer-Bottiglio, and J. Paik. Strain sensor-embedded soft pneumatic actuators for extension and bending feedback. In *2018 IEEE International Conference on Soft Robotics (RoboSoft)*, pages 202–207, 2018.

[368] L. Yun, X. Peng, N. Feng, L. Zhang, T. Zhang, S. Wang, W. Zhou, W. Lu, S.-W. Kuo, and T. Chen. Biomimetic underwater self-perceptive actuating soft system based on highly compliant, morphable and conductive sandwiched thin films. *Nano Energy*, 81:105617, 03 2021.

[369] D. Zambrano, M. Cianchetti, and C. Laschi. The morphological computation principles as a new paradigm for robotic design, 2014.

[370] I. V. Zaporotskova, N. P. Boroznina, Y. N. Parkhomenko, and L. V. Kozhitov. Carbon nanotubes: Sensor properties. a review. *Modern Electronic Materials*, 2(4):95–105, 2016.

[371] H. Zeng, P. Wasylczyk, D. S. Wiersma, and A. Priimagi. Light robots: Bridging the gap between microrobotics and photomechanics in soft materials. *Advanced Materials*, 30(24):1703554, 2018.

[372] R. Zhang, P. Iravani, and P. S. Keogh. Modelling dielectric elastomer actuators using higher order material characteristics. *Journal of Physics Communications*, 2(4):045025, apr 2018.

[373] P. Zhao, B. Xu, Y. Zhang, B. Li, and H. Chen. Study on the twisted and coiled polymer actuator with strain self-sensing ability. *ACS Applied Materials & Interfaces*, 12(13):15716–15725, 2020. PMID: 32141730.

[374] Q. Zhao, K. Nakajima, H. Sumioka, H. Hauser, and R. Pfeifer. Spine dynamics as a computational resource in spine-driven quadruped locomotion. *2013 IEEE/RSJ International Conference on Intelligent Robots and Systems*, pages 1445–1451, 2013.

[375] G. Zheng, Y. Kang, J. Sheng, Q. Qin, W. Huaiwen, and D. Fu. Influence of moisture content and time on the mechanical behavior of polymer material. *Science in China Series E Technological Sciences*, 47:595–607, 10 2004.

[376] G. Zhou, Y. P. Zheng, and P. Zhou. Measurement of gender differences of gastrocnemius muscle and tendon using sonomyography during calf raises: A pilot study. *BioMed Research International*, 2017, 2017.

[377] M. Zhu, T. N. Do, E. Hawkes, and Y. Visell. Fluidic fabric muscle sheets for wearable and soft robotics. *Soft Robotics*, 7(2):179–197, 2020. PMID: 31905325.